UNIVERSITÀ DI PARMA

UNIVERSITÀ DEGLI STUDI DI PARMA

DOTTORATO DI RICERCA IN FISICA

CICLO XXXV

Quantum Computing and Simulations:

from benchmarking existing devices to developing new platforms based on molecular spin qudits

Coordinatore:
Chiar.mo Prof. Stefano Carretta

Tutore:
Chiar.mo Prof. Stefano Carretta

Co-Tutore:
Chiar.mo Prof. Alessandro Chiesa

Dottorando: Luca Crippa

Anni Accademici 2019/2020 - 2021/2022

Supervisore IBM:
Dr. Ivano Tavernelli

This work has been performed in a collaboration path between the University of Parma and IBM, as an Executive PhD.

IBM, the IBM logo, and ibm.com are trademarks of IBM Corp., registered in many jurisdictions worldwide. Other product and service names might be trademarks of IBM or other companies. A current list of IBM trademarks is available at Copyright and trademark information.

© Copyright 2023 by Luca Crippa. All Rights Reserved.

To my wife and my daughter.

Cover illustration:

The illustration cover is an artistic representation of molecular spins used as fundamental unit of computation, and it has been created by the Author with Adobe Photoshop 2023.

Internal illustrations:

When necessary, Copyright Permissions for internal illustrations are reported inside the document. Details are reported in Copyright Permissions section at the end of the document.

Design:

This document was typeset by the Author using LaTeX markup language on Overleaf software, and with Atom and Visual Studio Code editors. The file in Portable Document Format was generated with pdfLaTeX.

MIUR subjects:

FIS/03

Contents

List of Figures ix

List of Tables xiii

Notations xiii

Abstract xvi
Motivation xvii
Thesis overview xviii

Part I : Introduction 3

1 Introduction to Quantum Computation 3
1.1 Introduction to Quantum Information Theory 3
1.2 Quantum simulation 11
1.3 Quantum noise 13
1.4 Error mitigation techniques 19
1.5 Quantum Error Correction 21
1.6 Final considerations 27

Part II : Approaches to Quantum Computation 31

2 Quantum Computing technology 31
2.1 Available and emerging hardware and software technologies 32
2.2 Challenges on technology implementation 34

3 Transmons approach 37
3.1 Transmons as superconducting qubits 37
3.2 IBM Quantum 46

4 Molecular approach **53**
4.1 Introduction to Molecular Nanomagnets 53
4.2 Spin Hamiltonian 55
4.3 Exploiting MNMs for Quantum Computation 56
4.4 Quantum noise in MNMs qudits 59
4.5 Quantum Error Correction with MNMs 61

Part III : Simulation of physical systems on IBM Quantum **67**

5 Simulation of static and dynamic properties of Magnetic Molecules **67**
5.1 Introduction to Variational Quantum Algorithms 68
5.2 The VQE algorithm 70
5.3 Study of spin 1/2 Heisenberg chains Ground State properties 72
5.4 Study of GS spin states mixing on spin 1/2 systems 88
5.5 Study of spin 1/2 chains Dynamic Correlation Functions 96
5.6 Conclusions 100

6 Quantum Simulation of Fermionic systems **103**
6.1 The Fermi-Hubbard model 103
6.2 Jordan-Wigner Transformation 104
6.3 Error mitigation approaches 107
6.4 Simulation of static properties 108
6.5 Simulation of dynamic properties 108

Part IV : Quantum computation with Molecular Nanomagnets **115**

7 Molecular Nanomagnets for qudit-based computation **115**
7.1 Model molecular systems 116
7.2 Description of decoherence 118
7.3 Quantum gates on qudit architectures: decomposition methods 122
7.4 Single-qudit gates 126
7.5 Two-qudit gates 132
7.6 Conclusions 136

8 Quantum Error Correction with molecular spin qudits **139**
8.1 Introduction 139
8.2 Molecular systems and methods 140
8.3 Quantum Error Correction scheme on qudits 142
8.4 Physical implementation 143
8.5 Performance improvements with pulse-shaping techniques 148
8.6 Conclusions 152

Conclusions and future perspectives **153**

Appendices **155**

A The Qiskit framework **159**
A.1 Introduction to Qiskit 159
A.2 Gates composition using Qiskit 159
A.3 Search for systematic errors of quantum gates on IBM Quantum 162
A.4 Qiskit Measurement Error Mitigation 169

B Quantum gates decomposition on qudits **171**
B.1 Hadamard Transform and QFT 171
B.2 Details of decomposition methods 172

C Technological innovation **177**
C.1 Automatic computation framework for quantum algorithms 177
C.2 A new framework for integrating Quantum into existing software architectures 179

Bibliography **185**

List of Publications **200**

Copyright Permissions **201**

Acknowledgments **204**

List of Figures

1.1 Bit versus Qubit 5
1.2 Classical versus quantum logic gates circuits 9
1.3 Details of a quantum circuit 10
1.4 Circuit for 3 qubits GHZ state 20
1.5 Effect of Qiskit Measurement Error Mitigation technique 21
1.6 3-Qubits bit flip error correction circuit 23
1.7 9-Qubits bit and phase flip error correction circuit 25
1.8 Non-Fault-Tolerant versus Fault-Tolerant CNOT implementation 26

3.1 Ideal and real harmonic oscillating circuit with energy levels 38
3.2 Ideal and real anharmonic oscillating circuit with energy levels 40
3.3 Josephson Junction section view 40
3.4 Effective circuit diagram of a transmon qubit 43
3.5 Implementation scheme of the transmon in a CWR 43
3.6 Simulations of decoherence times on transmons qubits made with Qiskit 45
3.7 Different IBM Quantum system topologies (2019) 47
3.8 First generation of IBM Quantum basic chip structure 47
3.9 IBM Quantum systems 48
3.10 IBM Quantum chip scaling techniques 50
3.11 IBM Quantum chip scaling techniques combined to reach $\sim$ 4000 qubits and beyond 51

4.1 Example of a Molecular Nanomagnet compound Cr_7Ni 54
4.2 Sketch of single ion and competing interaction molecular qudits 57
4.3 Sketch of an effective $S = 1/2$ Ni ion switch linked to two qudits 59
4.4 Error after QEC as a function of memory time t/T_2 for different S values 63

5.1 VQE process flow 70
5.2 Results of VQE noisy simulations with HA approach for Measurement Error Mitigation 73

5.3 Results of VQE noisy simulations with HA approach for Zero-Noise Extrapolation 74
5.4 Single layer of hardware heuristic ansatz for a 4 spins closed chain 76
5.5 Physically Motivated Ansatz building blocks 77
5.6 PMA initialisation for 4 spins 77
5.7 Statevector simulations of 4 sites spin closed ring 79
5.8 Noisy simulations of 4 sites spin closed ring 80
5.9 PMA initialisation for 6 spins 83
5.10 Statevector simulations of 6 sites spin closed ring 83
5.11 Noisy simulations of 6 sites spin closed ring 84
5.12 Even-odd open-closed MNM configurations 86
5.13 PMA initialisation for 5 spins 87
5.14 Finite-size and Parity effects, even-odd open-closed chains (noisy VQE simulations) 87
5.15 Heuristic ansatz for the spin $1/2$ trimer with DMI 90
5.16 Noisy simulations of 3 spins system with DMI in two different configurations (isosceles and scalene triangles) 91
5.17 Exact solution of 4 spins system with DMI 92
5.18 Different hardware heuristic approaches for 4 spins system with DMI 94
5.19 Noiseless results in proximity of anti-crossings 95
5.20 Noisy results in proximity of anti-crossings 97
5.21 Circuit for computing Dynamic Correlation Functions 97
5.22 Time evolution circuit of the target Hamiltonian in high field region 98
5.23 Real and Imaginary parts of the dynamic spin-spin correlations computed on IBM Quantum hardware, displaying raw and mitigated results 101

6.1 Mapping between Fermi-Hubbard model and Qubits used 105
6.2 Full ansatz used to calculate Fermi-Hubbard model 2-sites GS energy 108
6.3 Fermi-Hubbard model VQE noisy simulations performed with a custom noise model derived from IBM Quantum Montreal QV 128 device 109
6.4 Single Suzuki-Trotter step of the Fermi-Hubbard model Time Evolution circuit, consisting of the hopping term and of the interaction term, following the proposed mapping 110
6.5 Time evolution results for an initial state with both Fermions on the same lattice site $(1_\uparrow, 1_\downarrow)$ computed on a noisy simulator and on a real IBM Quantum device 111

7.1 Single spin $S > 1$ MNMs 117
7.2 Energy levels and molecule sketch of multi-spin triangular molecule **C1** with competing interaction 118
7.3 Energy levels and molecule sketch of multi-spin hypothetical double tetrahedron molecule **C2** with competing interaction 118
7.4 Different connectivity schemes between energy levels 123

7.5 Depth (i.e. number of subsequent pulses) to implement H_d as a function of qudit space dimension d 127
7.6 Error after the implementation of a single Hadamard gate on an initial state $|\psi_0\rangle$ on a $d = 4$ qudit for two different T_2 (3 μs and 10 μs), using PR decomposition, as a function of external B_1 field. Error ε after the implementation of a series of Hadamard gates, with a fixed $T_2 = 3$ μs and $B_1 = 100$ G 129
7.7 H_6 pulse sequence implemented with PR on **S2** system, assuming linear connectivity between levels, without considering decoherence ($T_2 = \infty$) 130
7.8 H_6 State Fidelity implemented with PR on **S2** system, assuming linear connectivity between levels, considering decoherence 130
7.9 Error $\varepsilon = 1 - \langle\psi_0|H_d \rho H_d|\psi_0\rangle$ implementing Generalized Hadamard gate H_4 (dots), H_6 (squares) and H_8 (triangles) on $d = 4, 6, 8$ levels as a function of T_2/t_{gate} 131
7.10 Two different implementations of the two-qudit with switch architecture 133
7.11 Energy levels of the **S1**+σ+**S1** system 135
7.12 Simulation of the time evolution of the three selected components of the two-qudit wavefunction for the Controlled-Phase gate 136

8.1 Quantum Error Correction scheme proposed to correct pure dephasing at first order with $S = 3/2$ qudit and an ancilla $S = 1/2$ qubit 144
8.2 Energy levels as a function of the external static B_0 magnetic field for e2-system. Performances of QEC scheme for e1-system and e2-system 146
8.3 Energy levels as a function of the external static B_0 magnetic field for n-system. Performances of QEC scheme, with both Gaussian and DRAG pulses 149
8.4 Structure of the pulse components for DRAG implementation, and the related frequency spectra 150
8.5 Performances of the DRAG technique on the proposed QEC scheme on n-system 151

A.1 Composition of two-qubit gates with elementary quantum gates 160
A.2 Composition of three-qubit gates with elementary quantum gates 161
A.3 Hardware behaviour of R_x from 0 to 2π on a single qubit of IBM Quantum Yorktown QV8 chip and its reconstruction with a noiseless parametrized simulation 163
A.4 Hardware behaviour of R_y from 0 to 2π on a single qubit of IBM Quantum Yorktown QV8 chip and its reconstruction with a noiseless parametrized simulation 164
A.5 CNOT tomography for IBM Quantum Yorktown QV8 device (late 2019), qubits 0-1 167
A.6 CNOT tomography for IBM Quantum Yorktown QV8 device (late 2019), qubits 2-3 168

A.7 Qiskit Measurement Error Mitigation example on a single rotation gate on IBM Quantum Armonk device (mid 2020) 170

C.1 Computation framework developed to handle IBM Quantum / Qiskit jobs and results 178
C.2 Positioning of the proposed integration framework in the Qiskit technological ecosystem 181

List of Tables

5.1 Custom noise parameters derived from QV 128 chip (early 2021) 81
5.2 Custom noise parameters derived from QV 128 chip (early 2021), further improved 96

6.1 Main details of the noise model for the IBM Quantum QV 32 device in February 2021. 111

A.1 Parameters set to correct systematic errors for IBM Quantum Yorktown QV8 quantum chip 162
A.2 Parameters set to correct systematic errors for IBM Quantum Montreal QV128 quantum chip 163

B.1 Parameters to decompose H_4 gate into PR (keeping three significant digits), assuming full connectivity 173
B.2 Parameters to decompose H_6 gate into PR (keeping three significant digits), assuming full connectivity 174
B.3 Parameters to decompose H_8 gate into PR (keeping three significant digits), assuming full connectivity 175
B.4 Parameters to decompose H_3, H_4, H_6 and H_8 gate into QHR (keeping three significant digits) 176

Notations

List of abbreviations:

API	Application Programming Interface
CLOPS	Circuit Layer Operations per Second
CNOT	Controlled-NOT
C-ϕ	Controlled-Phase
C-Z	Controlled-Z
CPB	Cooper-pair Box
CPU	Central Processing Unit
CSS	Cascading Style Sheets
CWR	Coplanar Waveguide Resonator
DBaaS	Database-as-a-Service
DMI	Dzyaloshinskii-Moriya Interaction
DRAG	Derivative Removal by Adiabatic Gate
DP	Depolarizing / Depolarization
FLOPS	Floating point Operations per Second
F-T	Fault-Tolerant
HA	Heuristic Ansatz
HHA	Hardware Heuristic Ansatz
HTML	HyperText Markup Language
HTTP	HyperText Transfer Protocol
IaC	Infrastructure-as-Code
IaaS	Infrastructure-as-a-Service
JJ	Josephson Junction
JS	JavaScript
MEM	Measurement Error Mitigation
MNM	Molecular Nanomagnet
NISQ	Noisy Intermediate-Scale Quantum
OCP	OpenShift Container Platform
PaaS	Platform-as-a-Service
PMA	Physically Motivated Ansatz

QC	Quantum Computer / Quantum Computation
QEC	Quantum Error Correction
QPU	Quantum Processing Unit
QS	Quantum Simulator / Quantum Simulation
QV	Quantum Volume
RAM	Random Access Memory
REST	Representational State Transfer
RO	Readout
SaaS	Software-as-a-Service
SDK	Software Development Kit
sH	Spin Hamiltonian
S-T	Suzuki-Trotter
SWIPHT	Speeding up Waveforms by Inducing Phases to Harmful Transitions
TR	Thermal Relaxation
VQE	Variational Quantum Eigensolver
ZFS	Zero-Field Splitting
ZNE	Zero-Noise Extrapolation

Abstract

Motivation

Since the beginning, in the late 40s, computation was based on classical principles such as mechanics, electromechanics and, nowadays, electronics: these principles represented the basic technology to implement numeric calculation, driven by the need to speed up and automatize the process. Important improvements have been achieved through the decades, and countless inventions and innovations have contributed to raise computational power while minimizing the size of computers. Although the classical computation has reached incredible peaks, such as IBM Summit with more than 200 quadrillion (short scale, 10^{15}) calculations per second [1], there are still many problems that cannot be addressed adequately by a classical computer in terms of required resources or computation time. This awareness started to grow since the early 80s, when the need of a computer able to simulate nature without approximations exposed the limits of a classical approach to computation, especially when simulating quantum mechanical systems.

Quantum Computation represents the new frontier of information science and could be a breakthrough to solve some kind of problems impossible to be solved with a classical computer. Nowadays we are in the NISQ (*Noisy Intermediate Scale Quantum*) Computing era, and some market players have released basic versions of quantum processors using different technologies: in this context, IBM is one of the most advanced player, as in 2016 was the first to release on the Cloud an open-source quantum platform called IBM Quantum [2][3], with superconducting qubits as basis of quantum hardware, and an initial open-source software stack.

Currently there are several technologies to build qubits, for example superconducting transmons, ion traps, molecules and photons. In the NISQ era, the available number of qubits of near-term quantum devices is $\sim 10^1 - 10^2$ and the errors are still important: to define Quantum Computers power, a new set of metrics called have been developed, such as Quantum Volume [4], taking into account not only the number of qubits available, but also their quality. One of the most useful steams is to understand how to use Quantum Computers to solve important problems, starting from simple but scalable models. While today's technology is constantly improving over the years in terms of

chip quality, speed and scalability, together with the software and application stack, it is clear that new approaches should be investigated in order to overcome current limitations. Investigations on possible paradigm changes are due to address some current problems, in particular related to noise reduction and Quantum Error Correction implementation.

Thesis overview

Main results

The first results of this work have been achieved by exploiting IBM Quantum technology to study and simulate the static and dynamic behaviour of small spin and Fermionic models, developing and applying error mitigation techniques. We used the small-sized currently available Quantum Computers to simulate the static properties (with Variational Quantum Algorithms) and dynamic properties (with Digital Quantum Simulations) of Magnetic Molecules consisting of open and closed spin $1/2$ chains with Heisenberg interaction, up to 6 spins, and to study Fermionic systems like a 2 sites Fermi-Hubbard model. In particular, finite-size spin systems are interesting models for fundamental physics and they represent, for instance, Molecular Nanomagnets (MNMs).

These MNMs are not only interesting physical systems to be studied, but also possible quantum systems to implement new qudit-based technologies. We therefore focused on developing possible new platforms for quantum computation, in which Molecular Nanomagnets can be used to implement a new prototype of Quantum Computers based on multi-level qudits rather than qubits. This approach based on molecular spins can be a promising way to create quantum computing architectures that leverage on rather unique features like protection from decoherence, embedding of Quantum Error Correction (QEC) in single objects, and performing efficient Quantum Simulations of models with many degrees of freedom. I worked on one of the proposed approaches for the simulation of a Universal set of quantum gates, and on the analysis of the performance of a previously proposed Quantum Error Correction scheme on realistic molecular systems.

Thesis structure and performed activities

Part I of this work aims to give an introduction to Quantum Computation theory, Quantum Simulation and quantum noise, together with Error Mitigation and Error Correction concepts.
Part II is focused on Quantum Computing hardware and software platforms, with a deep dive on currently available superconducting transmons qubits that I specifically exploited, together with an introduction on a new possible platform based on molecular spin qudits.
Part III reports the results obtained with IBM Quantum devices. I specifically worked on the Hamiltonian encoding and ansatz definition for simulating static Ground State properties of 4 and 6 spins Heisenberg closed chains, and on noisy simulations reported in Chap. 5; I performed noisy simulations to compute Finite-Size and Parity effects. I also worked on the heuristic ansatz approach to study spin states mixing, one of the two

main methods adopted. I finally worked on defining and optimizing the quantum circuits and hardware runs to compute the Ground State dynamic properties, and on the implementation of the error mitigation techniques previously developed. On Fermionic systems reported in Chap. 6, I worked specifically on both Ground State properties simulations and time evolution computation on real IBM Quantum hardware.
Part IV is focused on the above mentioned new approach to quantum computation, in which the Molecular Molecules are exploited to build the fundamental unit of computation, the qudit (multi-level qubit). I worked specifically on single spin molecular systems and on Planar Rotation gates decomposition approach, on both single- and two-qudit gates simulation reported in Chap. 7. On QEC with qudits, work reported in Chap. 8, I focused on nuclear spin qudits by simulating QEC scheme performances and optimizing them with pulse-shaping technique DRAG.

It is worth mentioning the work described in the Appendices. I worked on performing the tomography and the search for systematic errors on IBM Quantum gates, as reported in App. A. I report in App. B the calculations on Planar Rotations gate decomposition method on qudits. Finally, I worked on the technological innovations that developed to support this work: an automatic computation framework to compute, save, manage and visualize large amount of quantum simulations, and a way to integrate quantum workloads into existing software architectures, reported in App. C.

Organizational note

This work has been performed in a collaboration path between the University of Parma and IBM, as an Executive PhD.

Part I

Introduction

CHAPTER 1

Introduction to Quantum Computation

When in 1981 Richard Feynman, the well known Nobel Prize in Physics, stated that *"Nature isn't classical, ... and if you want to make a simulation of nature, you'd better make it quantum mechanical"* [5], the quantum computation era just began: in over 40 years, many research effort has been performed in order to achieve this technological breakthrough, *"because it doesn't look so easy"* [5]. Classical computers were already able to perform very useful and unthinkable calculations since decades, like all the calculations to support the landing on the Moon in July 1969; the arising interest in simulating physical phenomena at microscopic scale though, started to highlight the limits of this approach to computation, in which the resources needed to solve a problem scale exponentially with the size of the task itself. This applies in particular to quantum mechanics problems: nowadays it is possible to simulate the behaviour of a molecule in a specific environment, for example during drug research; however, several approximations need to be done, leading to a certain loss of accuracy. And, beyond a certain problem size, approximating the simulation would not be the solution since the needed resources (i.e. bits of memory) and computation time would exceed the human scale. Simulating such systems with a classical computer is an intrinsic failure, even if the effort to minimize components and to increase the performances has been unbelievable; moreover, Moore's law [6] stating in 1965 that the number of transistors into an integrated circuit would double every two years, is quickly approaching saturation [7]: a change on computing paradigm is therefore needed.

1.1 Introduction to Quantum Information Theory

A Classical Computer differs from a Quantum Computer from its foundations: the logic of the first one is based on Classical Mechanics laws, in particular the classical binary logic, while the logic of the second one is built directly from Quantum Mechanics laws. On a QC, each computation is governed and made possible by such laws [8].

A QC consists of a set of well distinct quantum bits (qubits) that can be set to an initial state, properly controlled and then measured; each qubit is a two-states quantum system such as a spin $1/2$. However, these are necessary but not sufficient conditions to build a QC: in order to build a working quantum platform that can be used to perform computation, there are five requirements (called *DiVincenzo Criteria* [9]) that must be fulfilled.

- Scalability of the system with well characterized qubits. As stated, a qubit is defined as a two-level quantum system with a certain energy gap: a well characterized qubit is therefore a system able to remain in the subspace of the selected two-levels.

- Initialisation of qubits to a simple and fiducial state. Each operation performed on a qubit is dependent on the initial state of the qubit itself: it is crucial to be able to prepare the qubits in an initial pure state such as $|000...0\rangle$

- Long and relevant coherence time. Decoherence is one of the major problems of qubits as quantum systems: any interaction between the qubits and the environment can corrupt the state of the qubit, that collapses destroying completely the computation. Longer decoherence time (much longer than the average time needed to perform a generic quantum gate) means that the qubits state would last longer in the defined superposition or entanglement, allowing to make more operations on them.

- Universal set of quantum gates: this is the smallest set of one- and two-qubits gates that can be used to compute any unitary transformation on a register of N qubits.

- Qubit-specific measurement capability: to get the results of a quantum computation it is important to be able to perform the measurement of the states of the qubits registry, for each qubit involved.

In the following sections we will introduce in more details some above mentioned components of a QC.

1.1.1 Qubits as unit of information

The simplest and most effective way to encode information is using only two states, that we can define as 0 and 1. The binary approach is used on classical computers to store information and to perform calculations on it, from smartphones to supercomputers: each bulk of information, from very small ones to very large ones, can be encoded in a set of bits with a certain length. Therefore, bits are the unit of information. Bits can be easily modeled as switches, implementing the "open" (0) and "close" (1) states; many different implementations have been implemented over the decades, from tube valves to microscale transistors. The quantum bits (qubits) are the corresponding unit of information for Quantum Computers: as the classical counterparts, they can store one bit of information as they are quantum systems in a 2-dimensional Hilbert space, spanned by two distinct orthogonal states $|0\rangle$ and $|1\rangle$, and they can be represented with Pauli matrices algebra. The main difference between bits and qubits is the fact that they can be in a **superposition** of the basis states; a very useful representation of the qubit is viewing it as a generic point on the surface of the Bloch Sphere, as depicted in Fig. 1.1.

A qubit can be defined as a vector on a 2-dimensional complex vector space, and together with states $|0\rangle$ and $|1\rangle$ (North and South Poles of the Bloch Sphere) it can be prepared in a generic superposition

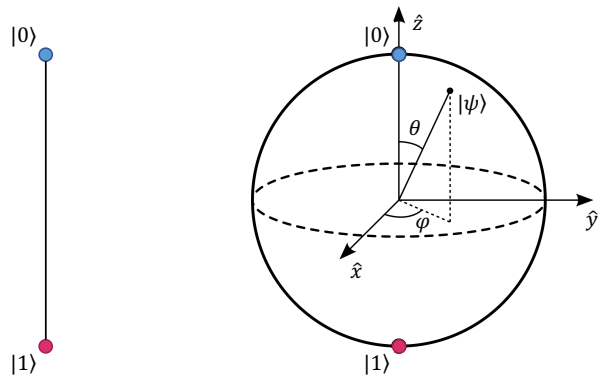

Figure 1.1: Representation of a bit (left) and of a qubit using the Bloch Sphere (right).

$$|\psi\rangle = \alpha|0\rangle + \beta|1\rangle \tag{1.1}$$

in an arbitrary combinations of them, where $\alpha, \beta \in \mathbb{C}$ and $|\alpha|^2 + |\beta|^2 = 1$. Another way to describe a qubit state $|\psi\rangle$ is using a geometric representation, that recalls the depicted state on the Bloch Sphere:

$$|\psi\rangle = \left(\cos\frac{\theta}{2}|0\rangle + e^{i\varphi}\sin\frac{\theta}{2}|1\rangle\right)e^{i\gamma} \tag{1.2}$$

where $\theta, \varphi, \gamma \in \mathbb{R}$. The factor $e^{i\gamma}$ is an overall phase, with no observable effects. The angles θ and φ are respectively the polar and the azimuth angles reported in Fig. 1.1, and are limited by $0 \leq \theta \leq \pi$ and $0 \leq \varphi \leq 2\pi$.

A QC is based on multiple qubits that can be used together to perform computations: we can enlarge and generalise the computational basis described above in Eq. 1.1 by considering n qubits. The computational basis would be then composed by 2^n states, and would have the form

$$|\psi_n\rangle = \alpha_{00\ldots0}|00\ldots0\rangle + \alpha_{00\ldots1}|00\ldots1\rangle + \ldots + \alpha_{11\ldots1}|11\ldots1\rangle \tag{1.3}$$

with 2^n different α values. The basis state would have the form $|x_1x_2\ldots x_n\rangle$; the n subspaces are thus coupled in a way that classical computers cannot achieve: the Hilbert space has size 2^n, almost impossible to be computed with the most powerful classical computers if n reaches ~ 50: let's recall that $2^{50} \sim 1.12 \cdot 10^{15}$, and classical computers yet struggle to handle this amount of information. Instead, Quantum Computers with 50 qubits are yet available in early 2022, so a computation made with these systems with 50 qubits can in theory outperform a classical computer on certain operations.

1.1.2 Quantum logic gates

In a classical computer, bit values are manipulated by the application of logic gates, such as NOT, AND, OR, XOR and the related NAND, NOR, XNOR. This set of classical logic gates can be used to build any boolean expression. Classical logic gates can be *reversible* or *irreversible*: for example, a NOT gate is logically reversible (the output can be inverted again), but a gate with 2 inputs and a single output is irreversible, as the two inputs cannot be uniquely reconstructed from the single output. It is possible to reduce the set of logic gates needed to build any boolean expression: these gates, such as AND, OR and NOT, are called "universal logic gates" [10]. An automatic machine with the ability to use an universal gate set to build any combination of every logic gates can than be defined "universal computer" . In late XIX Century it has been proven that by using NOR (or NAND) gates alone it is possible to construct any other logic gates. This simplification of notation had also an important impact on technology evolution, since the actual implementation of a NAND gate was simpler and more cost-effective than implementing the others; remarkably, it has been proven that it was more cost-effective to use several NAND gates to build any other gate, instead of building a single other gate itself [10].

The same concepts regarding computation on classical computers can be applied for quantum computing. Instead of classical logic gates there are the so called quantum logic gates, and, in contrast to classical computation, any quantum gate is represented by an unitary operator, since the qubit vector is normalized. It is worth noticing that unitary quantum gates are reversible gates, as the inverse of an unitary matrix is unitary itself: so it is possible to invert a quantum logic gate using another quantum logic gate, and this is impossible on a classical platform. As each quantum gate is represented by an unitary operation, it is theoretically possible to express an entire circuit using a unique unitary operation: this unitary operation, once applied to the initial state, returns the output state.

We define in the following paragraph the most common single-qubit and multi-qubit operations that have been used through all this work.

Single-qubit operations

As a single qubit is a two-levels system, a quantum gate acting on it can be defined as a 2×2 matrix. Hereby there is the definition of the most used single-qubit gates.

- Hadamard gate, creating superposition by transforming the computational basis state $|0\rangle$ and $|1\rangle$ into $|+\rangle = \frac{|0\rangle+|1\rangle}{\sqrt{2}}$ and $|-\rangle = \frac{|0\rangle-|1\rangle}{\sqrt{2}}$:

$$H = \frac{1}{\sqrt{2}} \begin{pmatrix} 1 & 1 \\ 1 & -1 \end{pmatrix} \tag{1.4}$$

- Pauli matrices, acting as π rotations along axes, from which we can obtain X, Y and Z rotations:

$$\sigma_x = \begin{pmatrix} 0 & 1 \\ 1 & 0 \end{pmatrix}, \ \sigma_y = \begin{pmatrix} 0 & -i \\ i & 0 \end{pmatrix}, \ \sigma_x = \begin{pmatrix} 1 & 0 \\ 0 & -1 \end{pmatrix} \tag{1.5}$$

- Generic θ rotations along an axis k:

$$R_k(\theta) = e^{-i\theta\sigma_k/2} = \cos\frac{\theta}{2} - i\sin\frac{\theta}{2}\sigma_k \tag{1.6}$$

reflecting on x, y and z axes as

$$R_x(\theta) = \begin{pmatrix} \cos\frac{\theta}{2} & -i\sin\frac{\theta}{2} \\ -i\sin\frac{\theta}{2} & \cos\frac{\theta}{2} \end{pmatrix} \tag{1.7}$$

$$R_y(\theta) = \begin{pmatrix} \cos\frac{\theta}{2} & -\sin\frac{\theta}{2} \\ \sin\frac{\theta}{2} & \cos\frac{\theta}{2} \end{pmatrix} \tag{1.8}$$

$$R_z(\theta) = \begin{pmatrix} e^{-i\theta/2} & 0 \\ 0 & e^{i\theta/2} \end{pmatrix} \tag{1.9}$$

- Generic rotation form in $SU(2)$ group:

$$U(\theta,\phi,\lambda) = \begin{pmatrix} \cos\frac{\theta}{2} & -e^{i\lambda}\sin\frac{\theta}{2} \\ e^{i\phi}\sin\frac{\theta}{2} & e^{i(\phi+\lambda)}\cos\frac{\theta}{2} \end{pmatrix} \tag{1.10}$$

Multi-qubit operations:
As described in Eq. 1.3, we would need to define operations acting on a system made of multiple qubits in order to expand computational possibilities using a Quantum Computer, making qubits interacting each others. Gates involving n-qubits can be defined as $2^n \times 2^n$ matrices. In general, the most common multiple-qubit gates are the controlled-operator operations; hereby we define the most important two-qubits gates, in general used to create entanglement between two qubits.

- Controlled-NOT, in which a NOT gate (X gate) is performed on the *target* qubit if the *control* qubit is in state $|1\rangle$: CNOT is therefore a Controlled-X operation. This gate is used to create *entanglement*: in particular, starting from a product state $(|0\rangle + |1\rangle) \otimes |0\rangle$, the application of the CNOT returns a maximally entangled state.

$$CNOT = \begin{pmatrix} 1 & 0 & 0 & 0 \\ 0 & 1 & 0 & 0 \\ 0 & 0 & 0 & 1 \\ 0 & 0 & 1 & 0 \end{pmatrix} \tag{1.11}$$

- SWAP, used to swap the state of two qubits. This is particularly useful during circuit transpiling, in order to rewrite the circuit in a way that can be run on a real hardware chip, where not all qubits are directly interconnected each others. SWAP gate does not create entanglement, and can be obtained using 3 CNOT gates:

$$SWAP = \begin{pmatrix} 1 & 0 & 0 & 0 \\ 0 & 0 & 1 & 0 \\ 0 & 1 & 0 & 0 \\ 0 & 0 & 0 & 1 \end{pmatrix} \tag{1.12}$$

- Controlled-Phase shift, adding a generic phase φ to the *target* qubit only if *control* qubit is on state $|1\rangle$. If $\varphi = \pi$, the C-φ gate acts as a Controlled-Z:

$$C - \varphi = \begin{pmatrix} 1 & 0 & 0 & 0 \\ 0 & 1 & 0 & 0 \\ 0 & 0 & 1 & 0 \\ 0 & 0 & 0 & e^{-i\varphi} \end{pmatrix} \tag{1.13}$$

- Generic multi-qubit operation, when one would apply a certain set of gates on a multiple qubits registry. Any multi-qubit gate can be decomposed into single-qubit Pauli matrices tensor products, for example:

$$ZZ = Z \otimes Z,\ XX = X \otimes X,\ YY = Y \otimes Y \tag{1.14}$$

and with more than 2 qubits

$$XZX = X \otimes Z \otimes X \tag{1.15}$$

and so on. It is also possible to define multi-controlled multi-qubit operations, leveraging on CNOT and on generic Controlled-U operations [11].

A more detailed description of multi-qubit gates and their composition is reported in Appendix A.

1.1.3 Universal gate set

As the classical computation lies on universal classical logic gate sets, it is possible to select a set composed by a finite number of quantum logic gates that can be used to perform arbitrary computations on a QC. It is possible to prove that any unitary operation can be built using a set of gates composed by CNOTs and single qubits rotations along two non-parallel axes of Bloch Sphere, or specific discrete gate set [11]. Each multi-qubit unitary operation can be decomposed in two-qubit gates, so on many platforms it is preferred to implement only them.

Although several universal gate sets composed of single-qubit and multiple-qubit gates can be defined [11], that can be used to implement any unitary operation, usually each hardware platform has its own best set of universal gates to achieve the most efficiency. For example, hardware technology based on superconducting qubits implement a coupling map with a small amount of inter-qubit interconnections, leveraging on software features to swap qubit states in order to implement entanglement on not directly interconnected qubits. Trapped ions technology has usually an all-to-all coupling map, so a different universal gate set could be more suitable.

1.1.4 Measurement and accuracy metrics

In order to collect the results of a computation of a quantum circuit it is necessary to implement a measurement of the final states of the required qubits. The probability to find a state $|\psi\rangle$ in a certain state $|z\rangle$ is:

$$p(|z\rangle) = |\langle z|\psi\rangle|^2 \tag{1.16}$$

Usually the measurement is performed by projecting along the basis of σ_z eigenstates, but it is possible to change the axis by performing the proper basis change: measuring in a different basis can be achieved by applying some rotations before the measurement operator, such as an Hadamard gate to measure on x basis, and a $R_x(\pi/2)$ to measure on y basis.

For many specific tasks is important to find a way to measure the accuracy of the calculation. In this work, we used as metric the fidelity $\mathcal{F}$. The fidelity can be used to compare the expected state $|\psi\rangle$ (if it is possible to compute it exactly with a classical computer) and the density matrix $\hat{\rho}$ (computed with a quantum computer):

$$\mathcal{F}(\hat{\rho}, |\psi\rangle\langle\psi|) = \sqrt{\langle\psi|\hat{\rho}|\psi\rangle} \tag{1.17}$$

Another useful metric is the error, defined as $\varepsilon = 1 - \mathcal{F}$.

1.1.5 Composing quantum gates: quantum circuits

A quantum circuit is a model used in Quantum Information to define a set of actions to be performed on the selected qubits. Basically, a quantum circuit consists of by a sequence of quantum logic gates, considering qubit initialization, one-qubit quantum gates, multi-qubit quantum gates and measurement operations. This concept is very similar to the classical logic circuit, in which a string of input bits is manipulated by a sequence of classical logic gates, obtaining the output bit string. In the same way, in a quantum circuit, a *registry* of qubit initialized in a proper state (usually $|0\rangle$) is manipulated by a sequence of quantum gates. Each quantum circuit must have at least one measurement gate in order to collapse the state of each measured qubit.

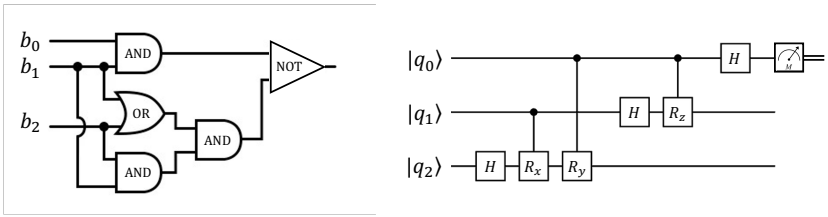

Figure 1.2: Different examples of classical logical gates circuit (left) and quantum logical gate circuit (right).

It is worth noticing that each quantum gate implements a unitary operation, and each operation takes a certain amount of time; usually, multiple-qubit operations are slower than single-qubit operations. Therefore, the total time for a quantum circuit to be executed can be computed with the sum of time length of all operations performed, considering that usually some operations are performed in parallel. Here we introduce the definition of *quantum circuit depth* as the number of gate layers that are performed in series, as depicted in Fig. 1.3.

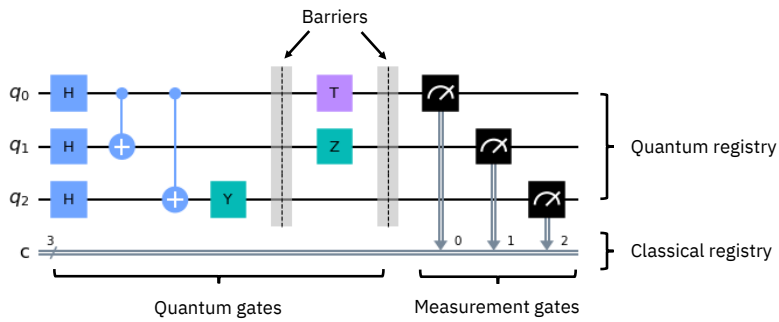

Figure 1.3: Details of a quantum circuit of depth 6 built with Qiskit [12].

Finally, a circuit or a set of circuits performing a certain task can be defined as *quantum algorithm*. These algorithms can be purely quantum, such as Shor's algorithm for numbers factorization, or hybrid classical-quantum, such as Variational Quantum Eigensolver, that leverages also on a classical optimizer to get the best set of parameters for a certain quantum circuit that is then prepared and measured by a Quantum Computer. The characteristic of hybrid algorithms is also to reduce the requirements on coherence times by performing many quantum calculations with less circuit depth.

1.1.6 Principles of quantum computation

Given the definition of qubits and quantum states, the next step is to implement a computation over a string of qubits $|q\rangle$. Performing a computation means properly changing the state of the input information, transforming it to the output information; the manipulation of the state of the qubits is represented by a generic operation:

$$|q\rangle \rightarrow \hat{U}|q\rangle \equiv |f(q)\rangle \tag{1.18}$$

where q is a string of binary numbers. A Quantum Computer is a machine designed to implement unitary operations $\hat{U}$ to work on qubit states. The real deal with Quantum Computers, however, lies in the combination of the above mentioned superposition and entanglement properties to enhance the computation. There is a wide class of quantum algorithms [13] whose circuits start with the application of Hadamard gates on the entire qubit register, preparing the qubits in a superposition of $|0\rangle$ and $|1\rangle$: in this way, the QC can compute in parallel all the final $f(q)$.

This implementation is however not valid for all functions. Indeed, all unitary transformations preserve the overlap between any pair of quantum states: taking two input states $|q_1\rangle \neq |q_2\rangle$ with $|f(q_1)\rangle = |f(q_2)\rangle$, we can prove that $\hat{U}|q\rangle \neq |f(q)\rangle$ for some q. To compute any function in a reversible way with a Quantum Computer, the introduction of a second bit string $|p\rangle$ is needed in order to compute the transformation:

$$|q\rangle \otimes |p\rangle \rightarrow \hat{U}|q\rangle \otimes |p\rangle \equiv |q\rangle \otimes |p \oplus f(q)\rangle \tag{1.19}$$

where $|p \oplus f(q)\rangle$ is a string of bits composed by modulo 2 addition of p and $f(q)$. It is

worth noticing that if the second bit string $y = 0$, the measurement of the final quantum state of the second string returns $f(q)$. Now, let's consider a state $|q\rangle$ defined as the following:

$$|q\rangle = H^{\otimes n}|0\rangle^{\otimes n} = \frac{1}{\sqrt{2^n}} \sum_{r=0}^{2^n-1} |r\rangle \tag{1.20}$$

and then use the defined state in Eq. 1.20 as one of the two states of Eq. 1.19.

$$\hat{U}|q\rangle \otimes |0\rangle = \frac{1}{\sqrt{2^n}} \sum_{r=0}^{2^n-1} |r\rangle \otimes |f(r)\rangle \tag{1.21}$$

It is worth to noting that, in general, the time needed to perform the operation in Eq. 1.19 scales up polinomially with the size n of the quantum register. However, the state prepared in Eq. 1.20 is a superposition of 2^n values, as per Hadamard gate (Eq. 1.4) application: in this case, the quantum processor has computed at the same time all $f(r)$ values for all r, and it is able to achieve an exponential speed up, for some class of problems.

A very important example of this implementation is the Quantum Fourier Transform (QFT). The QFT is a linear transformation on a set of qubits, that transforms an initial quantum state $|q\rangle = \sum_{i=0}^{N-1} q_i|i\rangle$ into a quantum state $|f\rangle = \sum_{i=0}^{N-1} f_i|i\rangle$ by applying n Hadamard gates and $n(n-1)/2$ C-φ gates:

$$|f\rangle \mapsto \hat{U}_{QFT}|f\rangle = \frac{1}{\sqrt{2^N}} \sum_{q=0}^{2^N-1} e^{i\frac{2\pi}{2^N}qf}|q\rangle \tag{1.22}$$

where q and f are strings of binary numbers. Finally, we can see that QFT is implemented with a number of gates that scales polinomially with qubit number.

1.2 Quantum simulation

One of the first applicable fields of quantum computation is the Quantum simulation. The simulation of the time evolution of a quantum system is a highly demanding process for a classical computer in terms of computational resources, as the number of bits required to store in memory all the possible system states (and to compute the corresponding time evolution) grows exponentially with the system size: due to its intrinsic features, a Quantum Computer is the most suitable platform to perform such simulations [14]. An interesting fact about quantum simulation is that the required amount of resources (qubit number, qubit quality and error correction) are limited, differently from a general purpose computation. This implies that current QC technology can be exploited to perform quantum simulations of rather complex physical systems: only a few tens of qubits with small error rate can outperform a classical computer in this field. There are two categories of Quantum Simulators:

- **Analog simulators**: the simulation is performed by a large quantum device globally addressable, that directly mimics the evolution of the target system; the hardware is composed by a large array of qubits geometrically reflecting the target system, with no local control [15]. In particular, the evolution of the target system is analogically emulated by an Hamiltonian that is equivalent to the Hamiltonian of the quantum device simulator. The quantum device properties can thus be studied instead of the properties of the target system.
- **Digital simulators**: the digital approach can be considered more flexible than the analog simulators. In particular, the physics of the target system is properly encoded in the quantum device qubits, then the system evolution is implemented using quantum gates: an Universal QC can be used as a digital simulator. This approach allows to encode various kind of physical systems into the quantum device, thus increasing the flexibility of such simulators [16].

During this work, Digital Quantum simulators have been used to study the dynamic properties of several physical systems.

1.2.1 Digital Quantum simulation

In general, an Hamiltonian describing a quantum system can be written in the form:

$$\mathcal{H} = \sum_{k}^{L} \mathcal{H}_k \tag{1.23}$$

where each Hamiltonian $\mathcal{H}_k$ is basically a tensor product of Pauli matrices; it is crucial that the Hamiltonian is the sum of local terms [17] to have an advantage on the quantum simulation.

The simulation of a time evolution of the Hamiltonian $\mathcal{H}$ corresponds to the implementation of the time evolution operator $\hat{U} = e^{-i\mathcal{H}t}$ (if $\mathcal{H}$ is not depending on time), where $\hat{U}$ is an unitary operation. As reported in more details in Appendix A, rotations and two-qubits gated needed to perform a digital simulation of a time evolution can be summarized as per Fig. A.1 and Fig. A.2.

Then, if $[\mathcal{H}_l, \mathcal{H}_{l'}] \neq 0$, in order to perform the time evolution of the Hamiltonian, the Suzuki-Trotter (S-T) decomposition [18] formula is needed (here reported using notation $\hbar = 1$):

$$e^{i(A+B)t} = \lim_{n\to\infty} (e^{i\frac{At}{n}} e^{i\frac{Bt}{n}})^n \tag{1.24}$$

where $\tau = t/n$ and n is the number of Trotter steps, to obtain, with a finite n, the approximated time evolution (with $\mathcal{O}(dt^2)$ error)

$$\hat{U}(t) = e^{-i\mathcal{H}t} \approx (e^{-i\mathcal{H}_1\tau} \dots e^{-i\mathcal{H}_L\tau})^n \tag{1.25}$$

The Suzuki-Trotter decomposition in Eq. 1.24 requires an approximation due to the finite number of Trotter steps possible to implement. A more general form of Eq. 1.24 is the following:

$$e^{-i\sum_l \mathcal{H}_l t} = \lim_{n\to\infty}\left(\prod_l e^{-i\mathcal{H}_l t/n}\right)^n \tag{1.26}$$

Unless all the $\mathcal{H}_l$ operators commute, in which case the ST identity is exact already for $n = 1$, the product of local unitaries will not be exactly equal to the total target unitary $\mathrm{U}(t) = \exp(-i\mathcal{H}t)$. However, it can be shown that $\forall n$:

$$\mathrm{U}(t) = e^{-i\sum_l \mathcal{H}_l t} = \left(\prod_l e^{-i\mathcal{H}_l t/n}\right)^n + O\left(\frac{t^2}{n}\right) \tag{1.27}$$

This means that we can approximate arbitrarily well the desired unitary operator by repeating n times the sequence of gates corresponding to the product of local terms for time slices t/n. The digitalization error due to S-T decomposition decreases by increasing the number of Trotter steps, but this implies using more noisy quantum gates: a trade-off is therefore needed.

We are finally able to break the original problem into smaller pieces $e^{-i\mathcal{H}_l t/n}$ which can now be implemented efficiently using only a limited set of elementary gates and which give the correct answer up to an arbitrarily small digitalization error. This technique has been applied in Chap. 5 and 6 to compute time evolution and dynamic properties of physical systems.

1.3 Quantum noise

Quantum Computers are very promising machines that could be used to perform computing tasks currently impossible for even classical supercomputers. However, as they are based on Quantum Mechanical laws, many noise sources are present: qubits are very fragile and prone to errors. Even if the QC technology is evolving very quickly, the current prototypes are still dramatically affected by noise. Currently we are in the era of *Noise Intermediate Scale Quantum (NISQ)* devices [19], where the rather small amount of qubits and the presence of noise make the use of Quantum Computers limited to certain areas of application; the main breakthrough would be the rise of the *Fault Tolerant* QCs, in which the errors caused by noise are corrected by the Quantum Error Correction and made acceptable by the computation itself; nowadays, we have still to face with noise by implementing error mitigation techniques in order to make current QCs useful for some kind of problems.

There are two kind of error sources, called coherent and incoherent:

- **Coherent errors**: in this case errors depend on an incorrect application of quantum gates, as a systematic control error. Let's consider an initial state prepared in $|0\rangle$ and apply to it a series of identity gates. The final state would be:

$$|\psi_f\rangle = \prod_i^N I_i|0\rangle = |0\rangle \tag{1.28}$$

An incorrect application of the identity gate due to coherent (systematic) errors leads to the application, each time, of a small rotation about a certain axis of the Bloch Sphere, for example the X axis. The result would be slightly different by Eq. 1.28:

$$|\psi_f\rangle = \prod_i^N e^{i\epsilon\sigma_x}|0\rangle = \cos(N\epsilon)|0\rangle + i\sin(N\epsilon)|1\rangle \tag{1.29}$$

The probability to measure $|0\rangle$ and $|1\rangle$ is then:

$$\begin{aligned} P_0 &= \cos(N\epsilon)^2 \approx 1 - (N\epsilon)^2 \\ P_1 &= \sin(N\epsilon)^2 \approx (N\epsilon)^2 \end{aligned} \tag{1.30}$$

where $(N\epsilon)^2 \ll 1$ can be defined as the error probability p.

The same concept can be applied to rotation gates. Let's consider a rotation of a certain angle along a certain axis: an incorrect application of the rotation gate can be due to a small tilt on the rotation axis, or an imprecise rotation angle.

- **Incoherent errors**: in this case errors depend on the interaction of the quantum system with the surrounding environment. As an example, we can consider the environment as an additional qubit with quantum state ($|e_0\rangle$, $|e_1\rangle$) coupled with the computational system during the idle stage of a quantum algorithm. Assuming an initial environment state $|E\rangle = |e_0\rangle$, we can couple it with the computational system on a coherent superposition: the system is entangled with the environment, and the calculation of the partial trace [11] results in a mixed state, i.e. due to the loss of coherence on the ρ.

1.3.1 Kraus decomposition

We need to introduce a method to modeling the above mentioned kind of errors, in order to understand and then mitigate and correct them. Quantum operations between quantum states introduced in the previous sections (Sec. 1.1.2) can be modeled using the *operator-sum representation*. Let's define a quantum operation as a transformation of the density operator $\rho' = f(\rho)$, where f is the quantum operation. Unitary transformations and measurements are thus defined as the following:

$$\begin{aligned} f(\rho) &= \hat{U}\rho\hat{U}^\dagger \\ f_m(\rho) &= \hat{M}\rho\hat{M}^\dagger \end{aligned} \tag{1.31}$$

where ρ is the initil state and $f(\rho)$ is the final state. We can now introduce the interaction with the environment during a quantum operation: we can define a general input state as a product state $\rho \otimes \rho_{env}$.

After the application of the transformation, the system is not interacting with the environment, so we can compute $f(\rho)$ as a partial trace:

$$f(\rho) = \mathrm{Tr}_{env}[\hat{U}(\rho \otimes \rho_{env})\hat{U}^\dagger] \tag{1.32}$$

Eq. 1.32 can be rewritten considering $\rho_{env} = |a_0\rangle\langle a_0|$, with $|a_k\rangle$ an orthonormal basis for the environment Hilbert space [11]:

$$f(\rho) = \sum_k \langle a_k|\hat{U}(\rho \otimes |a_0\rangle\langle a_0|)\hat{U}^\dagger|a_k\rangle = \sum_k E_k \rho E_k^\dagger \tag{1.33}$$

where $\sum_k E_k^\dagger E_k = \mathbb{I}$. The E_k operators are called *Kraus Operators*. This decomposition of quantum operations using Kraus Operators is very useful, and in particular can be applied to model quantum noise: these operators can be also called *Noise Operators* when the quantum operation represents the effect of the noise on the quantum state. The quantum state is thus described, after the effect of noise, with discrete operations.

With the above introduced formalism, we can take in consideration the main sources of quantum noise in order to modeling them. Each incoherent error derives from the interaction of the quantum state with the environment; in general, it is not possible to describe incoherent errors using unitary operations: an useful way to describe them is to assume the presence of incoherent errors on each gate implementation, and use the Kraus decomposition to describe them. Below there is a list of the main quantum noises.

- **Bit flip and phase flip errors**. The bit flip error flips the state of a qubit from $|0\rangle$ to $|1\rangle$, or from $|1\rangle$ to $|0\rangle$, with probability $(1-p)$. The related operation is:

$$\begin{aligned} E_0 &= \sqrt{p} \cdot \mathbb{I} \\ E_1 &= \sqrt{1-p} \cdot \sigma_x = \sqrt{1-p} \cdot \begin{pmatrix} 0 & 1 \\ 1 & 0 \end{pmatrix} \end{aligned} \tag{1.34}$$

  The related operation of the phase flip error, instead, is:

$$\begin{aligned} E_0 &= \sqrt{p} \cdot \mathbb{I} \\ E_1 &= \sqrt{1-p} \cdot \sigma_z = \sqrt{1-p} \cdot \begin{pmatrix} 1 & 0 \\ 0 & -1 \end{pmatrix} \end{aligned} \tag{1.35}$$

  The composition of the two errors, the bit-phase flip, has the following related operation:

$$\begin{aligned} E_0 &= \sqrt{p} \cdot \mathbb{I} \\ E_1 &= \sqrt{1-p} \cdot \sigma_y = \sqrt{1-p} \cdot \begin{pmatrix} 0 & -i \\ i & 0 \end{pmatrix} \end{aligned} \tag{1.36}$$

  where σ_x, σ_y and σ_z are the Pauli matrices, and $\mathbb{I}$ is the identity.

- **Depolarizing error**: this kind of noise represents the probability to find a qubit in a depolarized state (with probability p), where it is replaced by a mixed state. This is a generalisation of the above introduced errors, in which we assume the same probability for errors x, y and z. The related operation is, for a 2-dimensional quantum system:

$$f(\rho) = \frac{p \cdot \mathbb{I}}{2} + (1-p)\rho \tag{1.37}$$

where its generalisation to n qubits is achieved by substituting the denominator with 2^n. Considering a single qubit, with Pauli operators as computational basis, it is possible to rewrite the evolution of the density matrix ρ as the following:

$$f(\rho) = p_0 \mathbb{I}\rho\mathbb{I} + p_1 \sigma_x \rho \sigma_x + p_2 \sigma_y \rho \sigma_y + p_3 \sigma_z \rho \sigma_z \tag{1.38}$$

If we assume $p_1 = p_2 = p_3 = p/3 \rightarrow p_0 = (1-p)$, we can rewrite Eq. 1.38 as:

$$f(\rho) = (1-p)\rho + \frac{p}{3}(\sigma_x \rho \sigma_x + \sigma_y \rho \sigma_y) + \sigma_z \rho \sigma_z \tag{1.39}$$

- **Amplitude damping**: this error source describes energy dissipation effect to the quantum system. The operation describing the amplitude damping is:

$$f_{ad}(\rho) = E_0 \rho E_0^\dagger + E_1 \rho E_1^\dagger \tag{1.40}$$

where

$$\begin{aligned} E_0 &= \begin{pmatrix} 1 & 0 \\ 0 & \sqrt{1-\gamma} \end{pmatrix} \\ E_1 &= \begin{pmatrix} 1 & \sqrt{\gamma} \\ 0 & 0 \end{pmatrix} \end{aligned} \tag{1.41}$$

with $\gamma = (\sin\theta)^2$ is the probability of amplitude damping. The amplitude damping causes the decay with time of the diagonal elements of the density matrix, and it is related to the time T_1, the thermal relaxation time; the thermal relaxation is a stochastic and irreversible process related to the transition between two states. The effect of T_1 is represented basically by the qubits quantum state collapsing before finishing the computation, making the results inconsistent, or in the worst case losing entirely the information contained in the qubit state.

- **Phase damping**: this error source refers to the loss of information without loosing energy, but by changing of the relative phase between energy eigenstates. As per amplitude damping description, let's start from a quantum state as the one in Eq. 1.1 and apply random $R_z(\theta)$ rotations, originating from the interaction with the environment. The density operator defining the output state can be obtained by integrating on all θ random values:

$$\rho = \begin{pmatrix} |\alpha|^2 & \alpha\beta^* e^{-\lambda} \\ \beta\alpha^* e^{-\lambda} & |\beta|^2 \end{pmatrix} \tag{1.42}$$

where 2λ is the variance of the Gaussian distribution of random θ values, averaged on 0. The phase damping causes the decay with time of the off-diagonal elements of the density matrix, and it is related the T_2 time: it is called dephasing time, the time for the superposition state to lose its coherence. We can define the related operation as:

$$\begin{aligned} E_0 &= \sqrt{\mu} \cdot \mathbb{I} \\ E_1 &= \sqrt{1-\mu} \cdot \sigma_z = \sqrt{1-\mu} \cdot \begin{pmatrix} 1 & 0 \\ 0 & -1 \end{pmatrix} \end{aligned} \tag{1.43}$$

where $\mu = (1 + \sqrt{1-\lambda})/2$. It is worth noticing that this is the same effect of the phase flip, described above.

In superconducting transmon technology, introduced in Chap. 3, the effect of T_1 and T_2 is similar, as T_1 and T_2 are comparable, while in spin systems, introduced in Chap. 4, $T_1 \gg T_2$.

- The **Readout error** represents the probability to read $|1\rangle$ given an $|0\rangle$ state. Readout errors can be modeled as an environmental decoherence, acting as an incoherent error on the system. If a quantum circuit is long (i.e. composed by several quantum gates) and if there is a measurement only at the end of the algorithm, this kind of error is less relevant than other error sources. As reported in Section 1.1.4, the measurement operation on a single qubit can be defined by the application of *projection operators* $\hat{P}_0 = |0\rangle\langle 0|$ and $\hat{P}_1 = |1\rangle\langle 1|$; on a real hardware, the readout error distorts the projectors: we introduce the error parameters called p_{p1m0} and p_{p0m1}, that are respectively the probability to measure 0 on a state prepared in 1, and the probability to measure 1 on a state prepared in 0. The projection operators can be redefined by:

$$\begin{aligned} \hat{P}_{0_{generalized}} &= (1 - p_{p0m1})|0\rangle\langle 0| + p_{p1m0}|1\rangle\langle 1| \\ \hat{P}_{1_{generalized}} &= (1 - p_{p1m0})|1\rangle\langle 1| + p_{p0m1}|0\rangle\langle 0| \end{aligned} \tag{1.44}$$

1.3.2 Lindblad master equation

Another way to describe errors assuming to know their form, in particular decoherence, is to compute the continuum dynamics of the system by solving the Lindblad differential equation for the ρ. This approach is more precise than the Kraus decomposition, but also more demanding in terms of computation.

To describe this approach we first need to introduce the dynamics of open quantum systems, as the motion equation of the density matrix: the Lindblad master equation.

- **Closed and open quantum systems**: in case of closed quantum systems (i.e. not coupled to other quantum systems), the density matrix motion equation is:

$$\frac{d\hat{\rho}_S(t)}{dt} = -i[\hat{H}(t), \hat{\rho}(t)] = \mathcal{L}\hat{\rho}(t) \tag{1.45}$$

with $\hbar = 1$ and $\mathcal{L}$ is the Liouville superoperator [20]. Eq. 1.45 is called *Liouville-von Neumann* equation. If we want to describe the equation of motion for an open quantum system (where the computational system S is coupled with another quantum system, i.e. the environment E) we have to rewrite Eq. 1.45 as the following:

$$\frac{d\hat{\rho}_S(t)}{dt} = -i\,\mathrm{Tr}_E[\hat{H}_{tot}(t), \hat{\rho}(t)] \tag{1.46}$$

where H_{tot} is the total Hamiltonian of the system and the environment.

- **Evolution of open quantum system**: in the case of Markov approximation [21] (short correlation time with the environment), it is possible to write Eq. 1.46, the evolution of the open quantum system described by a generic transformation $W(t)$, as:

$$\frac{d\hat{\rho}}{dt} = \mathcal{L}\hat{\rho} \tag{1.47}$$

where $\mathcal{L}$ is a generator of the quantum dynamical semigroup $W(t) = e^{\mathcal{L}t}$ itself. A quantum dynamical semigroup, or *quantum Markovian semigroup*, describes the dynamic properties in a Markovian open quantum system [22]; one of the main properties of a quantum Markovian semigroup is that $W(t_1)W(t_2) = W(t_1 + t_2), \forall(t_1, t_2) > 0$ [20].

In general, in a N-dimensional Hilbert space, the $\mathcal{L}$ generator of the open quantum system can be written as:

$$\mathcal{L}_{\rho_S} = -i[\hat{H}, \hat{\rho}_S] + \sum_{i,j=1}^{N^2-1} a_{i,j}(\hat{F}_i\hat{\rho}_S\hat{F}_j^\dagger - \frac{1}{2}\hat{F}_j^\dagger\hat{F}_i\hat{\rho}_S - \frac{1}{2}\hat{\rho}_S\hat{F}_j^\dagger\hat{F}_i) \tag{1.48}$$

where $\hat{F}_i$ are the basis operators of the Liouville space of dimension N^2. By diagonalizing the coefficients $a_{i,j}$ with the unitary transformation u, it is possible to obtain:

$$\mathcal{L}_{\rho_S} = -i[\hat{H}, \hat{\rho}_S] + \sum_{k=1}^{N^2-1} \gamma_k(\hat{A}_k\hat{\rho}_S\hat{A}_k^\dagger - \frac{1}{2}\hat{A}_k^\dagger\hat{A}_k\hat{\rho}_S - \frac{1}{2}\hat{\rho}_S\hat{A}_k^\dagger\hat{A}_k) \tag{1.49}$$

where $\hat{A}_k$ are a set of operators related to the basis operators of the Liouville space of dimension N^2 by the following:

$$\hat{F}_i = \sum_{k=1}^{N^2-1} u_{k,i} \hat{A}_k \tag{1.50}$$

and γ_k are the relative non-negative eigenvalues [20]. $\hat{A}_k$ operators are called *Lindblad operators* and the density matrix is called *Lindblad equation*. We can finally introduce the *dissipator operator*

$$\mathcal{D}_{\rho_S} = \sum_{k=1}^{N^2-1} \gamma_k (\hat{A}_k \hat{\rho}_S \hat{A}_k^\dagger - \frac{1}{2} \hat{A}_k^\dagger \hat{A}_k \hat{\rho}_S - \frac{1}{2} \hat{\rho}_S \hat{A}_k^\dagger \hat{A}_k) \tag{1.51}$$

to obtain a more compact form for Eq. 1.49:

$$\frac{d\hat{\rho}_S(t)}{dt} = -i[\hat{H}(t), \hat{\rho}_S(t)] + \mathcal{D}_{\rho_S} \tag{1.52}$$

A more detailed view of this formalism can be found at Ref. [20].

1.4 Error mitigation techniques

In order to handle with these error sources that can compromise Quantum Computer calculations, several error mitigation techniques have been investigated, in particular leveraging on existing Quantum Computing platforms, i.e. IBM Quantum [2], with Qiskit [12] as software framework.

- **Systematic (coherent) error mitigation**: the first error mitigation technique implemented is related to a potential systematic error on Rotation Gates. This test has been performed on IBM Quantum chips: by using the Qiskit Aer noiseless simulator, we reproduced the behaviour of the real quantum hardware noisy rotations among respectively X and Y axes using a parametrization with a set of tilt angles $(\varepsilon_x, \varepsilon_y, \varepsilon_z)$, as reported in Appendix A, Sec. A.3. In December 2019 these ε angles were $\sim \pi/20$, but they have been progressively reduced to less than $\sim \pi/100$ with the new IBM Quantum hardware generation in May 2020.

- **Best qubit layout**: current Quantum Computing platforms, in particular superconducting ones (Chap. 3) provide many kind of quantum chips with different topologies (the actual positioning and coupling map between qubits on the chip, also called *coupling map*). When mapping a problem on a Quantum Computer it's important to select the right qubits layout, taking into account the needed entanglement. For example, with the Qiskit framework it is possible to create entanglement between qubits that are not directly interconnected, by an automatic addition of SWAP quantum gates. Each SWAP is however composed by 3 CNOTs, leading to an increase of the circuit length; by choosing the best problem mapping on the circuit, it is possible to slightly reduce the circuit length. However, as the number of qubits increases, it is useful to let a transpiler [23] choose the best qubit layout.

In this work, this error mitigation technique has been applied to mitigate results calculations made on several chip topologies.

- **Measurement error mitigation**: this method, whose implementation is based on Qiskit built-in functions, implies the computation of the calibration matrix of the chip on 0 states, to be used to correct results *a posteriori*. Such matrices are represented in Fig. 1.5(a), where an IBM Quantum chip with 5 qubits has been used: the difference between the noiseless and the noisy calibration matrix is evident, as the state mixing occurs in the second one. In Fig. 1.5(b) are then reported the results of a noiseless computation of a GHZ state (maximally entangled state with 3 qubits $|\psi\rangle = (|000\rangle + |111\rangle)/\sqrt{2}$), compared with the noisy simulation, noisy mitigated with Qiskit Measurement Error Mitigation, a real quantum hardware run and the mitigated hardware run on IBM Quantum platform. For this example we have chosen an hardware calibrated with a noise model allowing to clearly see the effect of the measurement error mitigation technique: the 3 qubits GHZ circuit (Fig. 1.4) is composed by 1 Hadamard gate, 2 CNOT gates and 3 measurement gates, so the effect of the measurement error is significant, compared to a circuit with hundreds of gates and only a couple of measurement gates at the end, in which the gate error would be dominant. The error is therefore largely mitigated by the application of the calibration matrix filter to the results. This technique is very useful to correct results on algorithms that require a large amount of measurements as the Variational Quantum Eigensolver algorithm, introduced later. The effort taken to build the calibration matrix increases exponentially with the system size, however in this work we applied this technique to a small amount of qubits, less than 10. A more detailed view of this method is described in Appendix A, Sec. A.4.

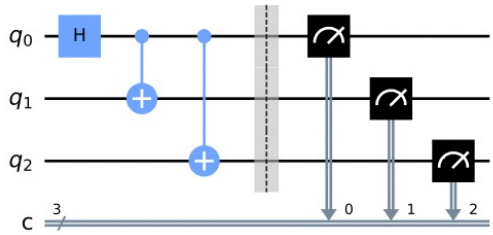

Figure 1.4: 3 qubits circuit for a GHZ state.

- **Zero-Noise Extrapolation**: this techniques can be used to correct the error of the gates [24]. The procedure is based on performing several calculations by adding gates each time, being sure to obtain an equivalent circuit, but each time with the introduction of additional error on the observable. It is thus possible to interpolate the value of the observable at zero noise implementing a fit on the results. Multiple-qubits gates are the most noisy ones, so we performed tests trying to mitigate the effect of CNOT gate errors. By adding CNOT pairs (identities) to our circuits, leading to equivalent circuits, we performed an interpolation to obtain the results without the effect of CNOT noise. It is worth noticing that this method re-

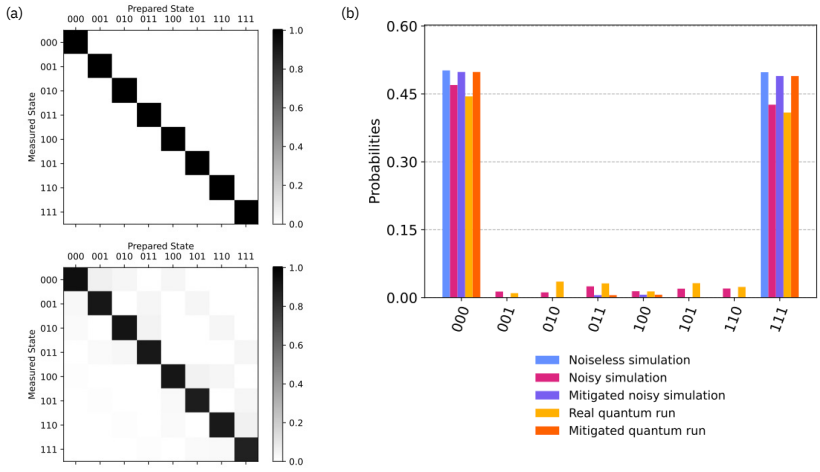

Figure 1.5: (a) Noiseless and noisy measurement error calibration matrices. (b) Noiseless, noisy raw, hardware raw and mitigated results.

lies on a linear interpolation, so it is applicable only if the error increases linearly with the application of the additional gates. A more complex fit (e.g. polynomial) would address the non linearity of the error increment, especially at high error rate, but it would be needed to deeply understand the behaviour of the trend.

- **Post selection**: in many cases, in particular on simple problems, some conservation laws (or symmetries of the investigated problem) can be exploited to correct the results *a posteriori*. As reported in Chap. 6, a post selection correction could consists on a rescaling of the results based only on these selected states, specifically for the studied system.

1.5 Quantum Error Correction

Quantum Error Correction and the Fault-Tolerant quantum computation are crucial aspects for the future of Quantum Computation. In the following section we will introduce the key aspects of QEC, but it is needed to introduce two main important points to be taken into account when considering error correction. Although classical computers are very robust regarding errors, their deployment in extreme environments such as outer space or radioactive zones, could lead to potential interactions between radiations and the hardware, causing a change of status of the hit bit. A solution to this bit flip error could be for example the use of multiple programmable hardware devices to perform the same calculation, such as Field Programmable Gate Arrays (FPGAs), that can be reprogrammed automatically if the majority of them notices differences in computed quantities. This approach is not directly applicable to quantum computers due to two main facts: the first is the impossibility to use results of a measurement of quantum state to help protect it from errors, since the measurement would destroy the quantum state itself; secondly, it is impossible to clone a quantum state in order to perform multiple

computation to correct errors, due to the *No-Cloning Theorem* [19]. It is clear that the only way to implement an error correction is by implementing codes regardless to the quantum state itself.

1.5.1 The Knill-Laflamme conditions

In their work [25], Knill and Laflamme introduced one of the first approaches for the QEC. A basic concept underlying QEC is the *redundant encoding*, where multiple physical qubits are used to generate logic qubits, thus expanding the overall Hilbert space: in this way, it turns out to be possible to correct quantum errors, or at least a subset of them. A single qubit of the form $|\psi\rangle = \alpha|0\rangle + \beta|1\rangle$ can be protected by the encoding on a larger Hilbert space as the following:

$$(\alpha|0\rangle + \beta|1\rangle)|000...0\rangle \rightarrow \alpha|0_L\rangle + \beta|1_L\rangle \tag{1.53}$$

where $|0_L\rangle$ and $|1_L\rangle$ are respectively the logical 0 and logical 1 of the protected qubit. Let's consider a quantum system interacting with the environment, with a density matrix of the form:

$$\rho_f = \sum_a A_a \rho_i A_a^\dagger \tag{1.54}$$

where A_a operators are called *interaction operators* and are built considering the environment basis $|\mu_a\rangle$, the environment state $|e\rangle$ and the time evolution operator $\hat{U}$

$$\hat{A}_a = \langle \mu_a | \hat{U} | e \rangle \tag{1.55}$$

with $\sum_a \hat{A}_a^\dagger A_a = \mathbb{I}$. Assuming a small number of errors occurring on the quantum system to be protected, the Knill-Laflamme necessary and sufficient conditions to recover the original state $|\psi\rangle$ from errors are the following:

$$\langle 0_L | A_a^\dagger A_b | 1_L \rangle = 0 \tag{1.56}$$

$$\langle 0_L | A_a^\dagger A_b | 0_L \rangle = \langle 1_L | A_a^\dagger A_b | 1_L \rangle \tag{1.57}$$

Eq. 1.56 imply that $|0_L\rangle$ and $|1_L\rangle$ must be projected to orthogonal states by the effect of errors; Eq. 1.57 states that the size and the inner product of the projected states after the effect of the errors must be the same.

In general, the Knill-Laflamme conditions state that any error operator $\hat{A}$ applied to an initial state, produce a distorted and corrupted image of the input state, where $|0_L\rangle$ and $|1_L\rangle$ are distorted in the same way, thus preserving the information: in this way, it is possible to implement the correction. In case of not satisfied K-L conditions, the distortion of α and β coefficients of Eq. 1.53 would be unknown, so the correction would not be possible.

1.5.2 QEC codes

An error correction code considering the above presented conditions can then be built by performing a measurement for a set of projections, then by applying a proper unitary operation depending on the measurement output. Proper basis change are required to perform measurements of the selected subspaces. It is worth mentioning the two assumptions made to let the quantum error correction code working as described below: errors occur only during idle time (when no quantum gates or QEC codes are applied), and quantum gate are not subject to systematic (coherent) errors [26]. Here we propose a brief description of the most famous QEC codes.

- **3-Qubit code**: one of the first introductive quantum error correction code, that performs single qubit bit and phase flip correction. The 3-Qubit code here described has been developed to correct a bit flip error on a single qubit, and the basis of this method lies in the encoding a logical qubit with three physical qubits. The 3-Qubit code is not a full quantum error correction code, as it can not correct bit flips and phase flips at the same time. If we consider a single-qubit superimposed state like the one in Eq. 1.1, it is possible to entangle the $|\psi\rangle$ state with other two qubits by using the circuit depicted in Fig. 1.4, obtaining a logical qubit encoded state:

$$|\psi_L\rangle = \alpha|0_L\rangle + \beta|1_L\rangle = \alpha|000\rangle + \beta|111\rangle \tag{1.58}$$

With this encoding, the 3-Qubit code is able to correct only a single bit flip error due to the binary distance between $|0_L\rangle$ and $|1_L\rangle$. If the distance between two encoded states in d, the number of bit flip errors that can be corrected is $t = \lfloor (d-1)/2 \rfloor$: with a distance $d = 3$, we obtain $t = 1$.

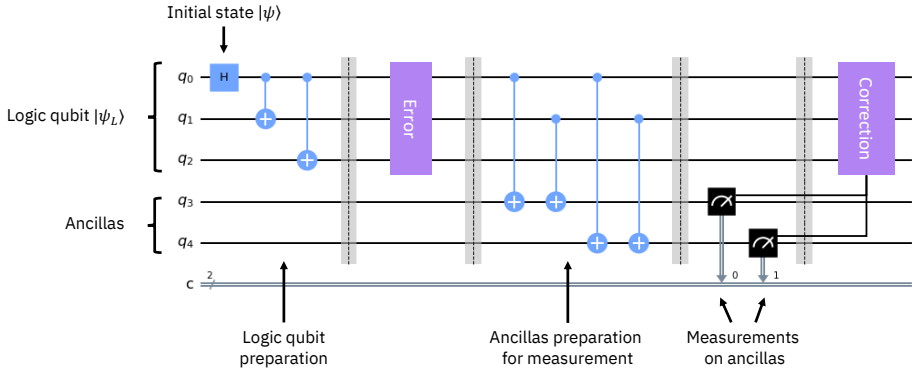

Figure 1.6: 3-Qubits bit flip error correction circuit.

Now, in order to detect a single bit flip acting on each of the three qubits, we need to measure the states without modifying the encoded superposition: this is done by adding two *ancillary qubits* (also called *ancillas*) properly entangled with the other qubits, where to perform parity measurement, as depicted in Fig. 1.6. It is then

possible to understand if something happened during the computation by reading the state of the measured ancillas. In particular:

$$\begin{aligned}
(\alpha|000\rangle + \beta|111\rangle) \otimes |00\rangle_{Ancillas} &\rightarrow \text{no bit flip} \\
(\alpha|100\rangle + \beta|011\rangle) \otimes |11\rangle_{Ancillas} &\rightarrow \text{bit flip q1} \\
(\alpha|010\rangle + \beta|101\rangle) \otimes |10\rangle_{Ancillas} &\rightarrow \text{bit flip q2} \\
(\alpha|001\rangle + \beta|110\rangle) \otimes |01\rangle_{Ancillas} &\rightarrow \text{bit flip q3}
\end{aligned} \tag{1.59}$$

When measuring the two ancillas, it is possible to detect in which state we are located during the computation without modifying encoded logical state. So, to correct the states we can apply the proper *recovery* algorithm, dependent by the values measured: this corresponds to a σ_x; a basis change is required to implement the error correction for phase flip and the combination of bit flip and phase flip. It is finally worth recall that this method cannot detect and correct errors on more than one qubit: more physical qubits implementing a logical qubit are needed to correct more errors, in example, a single error on more than one qubit, or a generic single qubit error. This method can be easily implemented on current Quantum Computers [27].

- **9-Qubit code**: developed by Shor in 1995 [28], this code is based on the 3-Qubit code with the difference that it can correct a bit flip, a phase flip, or both, on each of the 9 physical qubits involved. Thus, this code can be considered a full quantum error correction code, as it can correct an arbitrary single qubit error. Following and enlarging the same approach of the 3-Qubit code, in the 9-Qubit code the logical qubit encoding is performed as follow:

$$\begin{aligned}
|\psi_L\rangle = \alpha|0_L\rangle + \beta|1_L\rangle = \\
= \alpha[(|000\rangle + |111\rangle)(|000\rangle + |111\rangle)(|000\rangle + |111\rangle)] \\
+\beta[(|000\rangle - |111\rangle)(|000\rangle - |111\rangle)(|000\rangle - |111\rangle)]
\end{aligned} \tag{1.60}$$

In Fig. 1.7 is depicted the quantum circuit required to encode a quantum state using 9 physical qubits. The correction of bit flip (σ_x) errors can be achieved in the same way of the 3-Qubit code, while the correction of phase flip (σ_z) errors can be achieved by comparing the sign of the three code blocks, with the proper basis change application. This code is able to correct a single bit flip error in any of the three blocks, and a single phase flip error in any of the 9 qubits; a bit-phase flip on a single qubit can also be corrected. Despite being a full quantum error correction code, the 9-Qubit code can not handle and correct multiple occurring errors.

Other similar but more compact codes are available, using 5 and 7 qubits rather than 9.

Many other error correction codes and methods are available. However, we above introduced the ones that will be leveraged to implement QEC on qudits as reported in Chap. 8.

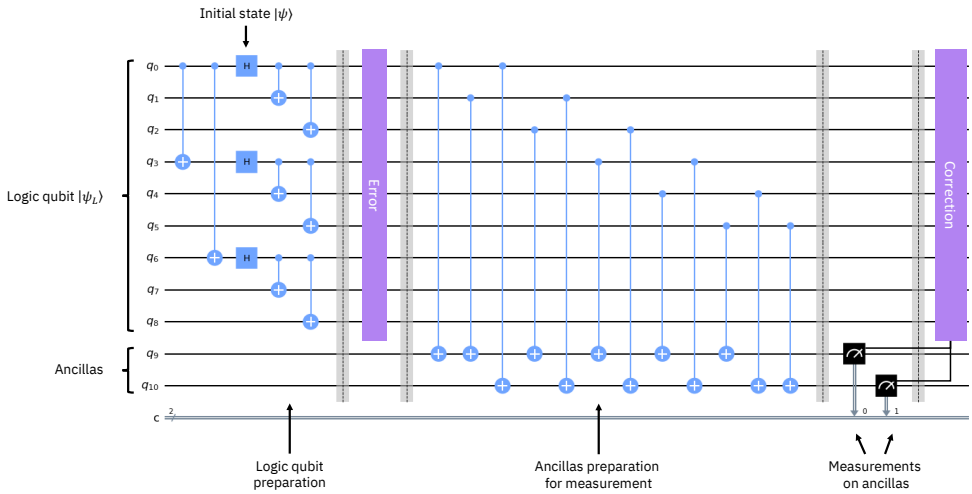

Figure 1.7: 9-Qubits bit and phase flip error correction circuit.

1.5.3 Fault-Tolerant computing

One of the ultimate goals for Quantum Computation is to achieve the Fault-Tolerant computing, a computing paradigm in which the primary computing circuits and the QEC circuits do not cause cascading errors through the entire computation process. In general, for F-T computation, the *Quantum Threshold Theorem* [29] states that if the physical qubit quantum error rate is below a certain threshold, a QC can suppress the logical error rate leveraging on QEC codes: in this way, Quantum Computation can achieve the Fault-Tolerance. So, in a F-T circuit element, a single error on a logical qubit would cause at most a single error on a logical qubit output state, if the QEC code corrects a single error: Fault-Tolerant computation, for a QEC code correcting $t = \lfloor (d-1)/2 \rfloor$ errors, requires that $n \leq t$ errors occurring during the computation execution would not create $n' > t$ errors in the output for each logically encoded qubit.

Let's consider a typical example in which a 2 logical qudit CNOT gate, mapping $|111\rangle|000\rangle \rightarrow |111\rangle|111\rangle$ is applied in a F-T way. In Fig. 1.8(a), a bit flip error on a single physical qubit of logical qubit $|\psi_1\rangle$ can propagate to more than 1 physical qubit on logical qubit $|\psi_2\rangle$. In Fig. 1.8(b) instead, the CNOT is implemented in a Fault-Tolerant way: the bit flip error can propagate only on a single physical qubit on the on logical qubit $|\psi_2\rangle$.

In order to achieve Fault-Tolerant computation with QEC, it is therefore needed to perform Fault-Tolerant operations directly on logical qubits. To do this, the *stabilizer formalism* [30] can be very helpful. Here, a quantum state is stabilized by an operator if the state itself is a $+1$ eigenstate of the operator:

$$K|\psi\rangle = |\psi\rangle \tag{1.61}$$

For example, $|0\rangle$ is stabilized by the operator σ_z, as $\sigma_z|0\rangle = |0\rangle$ [26]. To apply the formalism to N-qubits, we have to consider the group of operators called *Pauli group* $\mathcal{P}$,

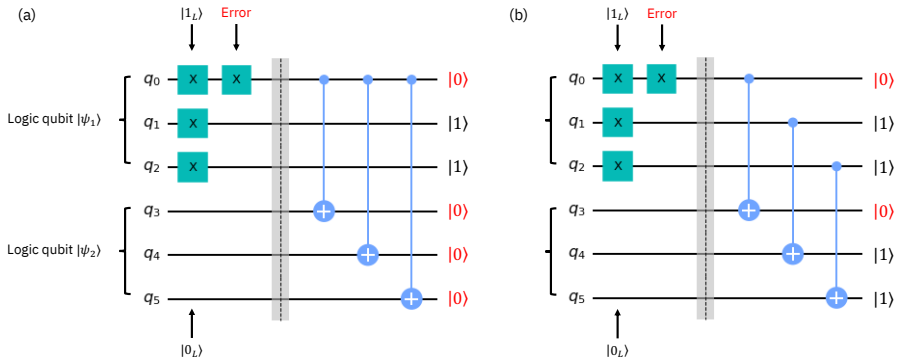

Figure 1.8: (a) Non-Fault-Tolerant CNOT implementation. (b) Fault-Tolerant CNOT implementation.

composed by $\{\pm I, \pm iI, \pm\sigma_x, \pm i\sigma_x, \pm\sigma_y, \pm i\sigma_y, \pm\sigma_z, \pm i\sigma_z\}$, and we have to expand it by taking the N tensor product of itself:

$$\mathcal{P}_N = \mathcal{P}^{\otimes N} \tag{1.62}$$

In order to stabilize a $|\psi_N\rangle$ state, we would need the group $\mathcal{G}$ of the N generators of the N-qubit Pauli group of Eq. 1.62:

$$\mathcal{G} = \{K^i | K^i|\psi\rangle, [K^i, K^j] = 0, \forall(i,j)\} \subset \mathcal{P}_N \tag{1.63}$$

It is possible now using the above introduced formalism to perform operations on logical qubits. For example, if a operation U is performed on a logical qubit $|\psi_L\rangle$ stabilized by the operator K, we can obtain:

$$UKU^\dagger U|\psi_L\rangle = UK|\psi_L\rangle = U|\psi_L\rangle \tag{1.64}$$

where the stabilizer set must be fixed. Thus, an X rotation acting on a logical qubit encoded using 3 physical qubits, would be:

$$X_L = XXX = X^{\otimes 3} \tag{1.65}$$

Two-qudit gates implemented on logically encoded qubits must follow a similar approach:

$$CNOT_L = CNOT^{\otimes 3} \tag{1.66}$$

This CNOT implementation is also intrinsically Fault-Tolerant, as represents exactly the circuit depicted in Fig. 1.8(b). The combination of gates applied directly on logically encoded qubits and a Fault-Tolerant implementation of them is thus a promising way to achieve Fault-Tolerant Quantum Computation with Quantum Error Correction. The above mentioned are only a subset of techniques that can be put in place to achieve F-T Quantum Computing: a more detailed view can be found on Ref. [26].

1.6 Final considerations

In this Chapter we introduced the theoretical framework underlying quantum gates, quantum circuit, quantum computation and simulation, together with an introduction and modeling of quantum noise and how to handle it through error mitigation and error correction. In the next chapters we will focus on some promising technologies that can be exploited to implement Quantum Computers based on the introduced theoretical elements.

Part II

Approaches to Quantum Computing

CHAPTER 2

Quantum Computing technology

In the previous Chapter we introduced the theory underlying quantum computation, together with an initial overview of noise mitigation techniques and some possible application areas. Now, the following part is focused on practical approaches to quantum computation, introducing technologies, applications, challenges and innovations exploited to build real Quantum Computers. Although the theoretical foundations of Quantum Computation started to be developed in the early 80s, there is not yet a well agreed and defined technology that can be exploited to mass produce such systems. Research is still in progress, even if the first prototypes hardware and software platforms are starting to arise. The first step on Quantum Computation implementation quest is to find a way to build the quantum systems to be controlled and measured to perform computation, and then to leverage on them to prove the advantage of the quantum approach for specific class of problems.

The first identified area of interest is the simulation of Quantum Systems, as the idea of a Quantum Computer originates from the need to perform a precise simulation of Nature through Quantum Mechanics, and as it is the closest to be realized with only tens of non-error corrected qubits. Quantum chemistry, material science and high energy physics fields can be the first to be significantly impacted by the rise of QC, as the digital quantum simulation requires a relatively small amount of qubits to obtain an advantage on computation. Possible applications could be new drug discovery, genomics analysis, chemical product design, high energy physics particles classification, identification of materials for battery improvements, and more. The second area of interest could be Artificial Intelligence [31][32], where a Quantum Computer could speed up the model training process and increase training quality. Example of this could be better product recommendation, better and quicker fraud detection, vehicle routing and better pattern recognition. Optimization area could be another field of interest, that could find application on finance and banking area. Optimization algorithms and Monte Carlo simulations are widely used in risk analysis and stock portfolio optimization, especially on high level Worldwide financial transactions: more speed and more accuracy on thousands of micro transaction could lead to significant earnings. Optimization field contains also more general areas such as schedule of transports, fabrication process, quality control, manufacturing supply chain, forecasting and data search [33]. Lastly, algorithms related to some mathematical problems like solving systems of linear equations, or factorization of large numbers (Shor's algorithm [34]) would achieve a huge speed up, as a

classical computer struggles to complete this task. This would have, at least in the next decades, an impact on cryptography and security [35] (when millions of qubits will be available on quantum chips), while the first quantum-safe systems are yet in production [36][37]. Many more fields of interests are still in development, and many others have to be discovered yet.

Since 2016, quantum technology field has seen important announcements from several research institutions and technology enterprises such as Google, IBM, Intel, Rigetti and many more: the race towards a practical implementation of Quantum Computers has started, reaching in November 2021 the release of a 127 qubits processor [38].

2.1 Available and emerging hardware and software technologies

2.1.1 Quantum hardware

The quest for real Quantum Computation starts obviously with the selection of the quantum system to be used to implement the fundamental unit of computation, the qubit. Here there is brief description of the available and emerging hardware platforms, each one carrying its own advantages and disadvantages.

- **Trapped ions**: this technology was one of the first used to create qubits with all needed features, such as initialization, quantum gates and measurement. It consists in a series of ions kept in position by rotating electromagnetic fields, that act as qubits with long coherence times. Although high fidelity of operations is achieved, these systems are currently having scalability issues [39]. Nevertheless, thanks to the high fidelity achievable and despite the limited amount of qubits that can be implemented, these machines are well suitable to perform quantum simulations, such as time evolution, and Variational quantum Algorithms implementation.

- **Quantum dots**: this way to build qubits is based on semiconductors, so can be supported by already developed industry best practices. Nanoscale points in a semiconductor substrate can trap and control single electrons using electric pulses, where the qubit is represented by the spin of the system, having a long coherence time [40]. This is also one of the first technologies proposed, as leverages on existing semiconductor techniques; scalability issues are still present.

- **Superconducting circuits**: they leverage on superconducting properties of materials to generate qubits as Cooper Pairs inside Josephson Junctions. Stability and quality of results has been proven up to more than hundred of qubits [38], and many players have started building software platforms to control such systems [41]. Superconducting transmons technology is described in Chap. 3, as it has been widely used in this work to simulate several spin and fermionic systems.

- **Photons**: a photon-based quantum computer uses photon spin states as qubits, controlled in example by phase shifters and beamsplitters. Photons are generated by single photon sources (lattices of resonators) and pass through optical wave

guides, then are finally measured by an array of detectors [42]: several networking systems are required to control photons and use them to create entanglement. There are various technologies almost ready to implement photonic quantum devices, based on state of art nanotechnologies and optoelectronics.

- **Topological encoding**: semiconductor nanoscale wires encode and host Majorana fermions inside them. They are however currently difficult to control and measure [43].

- **Neutral atoms**: trapped neutral atoms are manipulated by light pulses. Neutral atoms can be addressed individually, have long coherence times and can be organized in lattices, up to $\sim 10^2$ atoms [44].

- **Molecular spins**: some magnetic molecules can act as effective $S = 1/2$ quantum systems and can be exploited to encode qubits, where the $|0\rangle$ and $|1\rangle$ states are encoded in the two $m = \pm 1/2$ levels. Thanks to their multi-level structure, magnetic molecules can be also exploited to define multi-level qubits, called qudits [45][46]. This intrinsic feature of molecules increases the computational power, enabling integrated Quantum Error Correction (QEC) simplifying some algorithms [47] and allowing the execution of parallel operations within the same molecule. Moreover, with the proper chemical engineering process, customized molecules can be created in order to reduce decoherence errors and build systems that can be used together with other technologies such as superconducting transmons control systems [48]. A detailed description of such systems is provided in Chap. 4, and they will be exploited to create quantum gates (Chap. 7) and QEC (Chap. 8).

The most promising technology, used to build current most advanced Quantum Computers, is superconductivity; however, we are still in the NISQ era, but aiming to the "second quantum revolution" with a next generation of quantum devices, that could hopefully used for practical scope gaining advantage respect to classical computation in the proper fields of application. Other hardware technologies are still in development and will be probably explored for a practical implementation in the next years.

2.1.2 Quantum software

Together with hardware development, the software stack is an essential feature to enable the usage of Quantum Computers. There are several layers of software that need to be implemented in order to run applications on a quantum device.

- **Low-level access**: this is the lowest level of the software stack, communicating directly with the quantum hardware, and it is analogous to the classical Assembly language. At this level, instructions directly implementable by the Quantum Computer are managed, such as implementing a specific quantum gate to a specific set of qubits. Some examples of this low-level access programming are Qiskit Circuits (formerly Qiskit Terra) [49] and OpenQASM [50].

- **Transpilers**: on top of the basic low-level machine language there is the transpiler. This software performs a first translation of the original machine-level software, optimizing the quantum gate circuits considering mainly qubits topology and calibration. Moreover, transpiling a quantum circuit implies taking into account the connectivity in order to implement multi-qubit gates: if a quantum hardware does not have the right connectivity between qubits in order to implement the required two-qubit gates, this software layer introduces SWAP gates in order to properly rewrite the code. Several techniques can be leveraged to perform this circuit optimization, from a randomized optimization approach to machine learning.

- **Pre-built libraries**: the possibility to use a set of pre-built, automatically transpiled and optimized pieces of code is the first step towards an higher-level programming. Examples of this are the Qiskit Applications, in which several pre-built algorithms can be imported and used in a bigger program: the Variational Quantum Eigensolver library will be used during this work in Chap. 6 and in Chap. 5. In this case there is no need to manage the low-level programming structure of the algorithm: several functions are provided, each one with properties, flags and attributes to be set.

- **Compilers**: the next level of the software stack would be the program compiling. A *compiler* is a program that translates a code written in a certain language, called *source*, to a code written in another language, called *target*. An example of this is the translation of a program written using a high-level language to a low-level machine set of instructions.

- **High-level programming**: this layer of the software stack is a complete packaging of all core libraries and tools to enable developers to program Quantum Computers with the same skill set required for classical computation. With an high-level programming language, all the complexity related to quantum circuits, gates, error correction will be properly masked, and developing applications will be almost transparent. For this purpose, an architectural framework described in App. C has been designed and implemented [51].

- **Frictionless development**: the final stage of quantum software. When achieved, *frictionless development* will enable programmers to develop, test and run code without caring of the underlying platform. Each piece of code will be run automatically on the right platform, whether classical or quantum, considering several factors like performances required, type of algorithm, and so on [52].

2.2 Challenges on technology implementation

All the above mentioned hardware and software technologies would need, through their evolution, to face with some challenging problems.

2.2.1 Scalability and quality

The number of qubits available on quantum chips is the first crucial result that needs to be achieved. Although for some specific use cases such as quantum simulation a limited amount of qubits (~ 50) could lead to significant improvements, like the possibility to simulate time evolution of quantum systems impossible with classical computers, the majority of general quantum algorithms require thousands or million of qubits to become useful, for example the factorization of large numbers [34].

Beside the number of implemented qubits, the quality of themselves must be taken into account. The quality of qubits is primarily related to the ability of initialize, control and readout the states: the pursuit of quality qubits must pass through this improvement of these basic operations. Then, it is needed to improve the quality of the quantum system itself, in particular regarding coherence. Currently, available quantum computing platforms are limited by the number of quantum gates that can be performed: an improvement of T_1 and T_2 times, as well the reduction of the time taken to each gate to be performed, is crucial to be able to increase the complexity of algorithms.

In 2019, IBM proposed the Quantum Volume (QV) metric to define the quality of near-term quantum devices [4], being adopted also by other QC manufacturers. The Quantum Volume computation takes into account several quantum chip features, such as qubit number, connectivity, single-qubit and two-qubit gate error rates. In order to compute the QV of a certain chip, a specific algorithm must be run: a series made of d randomized modular circuits (depth) are applied to a set of m qubits (amplitude), then optimized by the software transpiler and let evolve. The final calculation is performed by the formula [53]:

$$\log_2 QV = \underset{m}{\operatorname{argmax}} \min(m, d(m)) \tag{2.1}$$

The Quantum Volume indicates the maximum size of square quantum circuits that a Quantum Circuit can implement considering the error rate. It can be considered an universal metrics, as it is independent from the QC architecture or topology: for example, with QV it is possible to compare the quality of superconducting transmons and ion trap devices, or other architectures.

2.2.2 Error mitigation and error correction

In order to help improving results quality, beside technological improvements, some error mitigation techniques can be exploited to reduce the effect of noise on the results. Some of them have been introduced in Chap. 1. The improvement on quantum hardware quality and the successful application of error mitigation techniques would be for sure a great achievement; however errors will still remain there, although heavily reduced. It is clear that a method of correcting them is desirable, achieving Fault-Tolerant computation, where operations are performed tolerating the errors, which are reduced by increasing the size of the logic qubits. Each quantum hardware technology should be assisted with the proper error correction codes, that should be applied in a reasonable

amount of time, not to extend significantly the overall computation time.

2.2.3 Demonstration of quantum advantage

The main goal of this technology research path is to obtain a solid way to build Universal Fault-Tolerant Quantum Computers, able to perform general purpose computation, with a significant amount of error corrected qubits. Quantum Computers will be a fundamental platform to gain access to the solution of problems that nowadays are impossible to handle with a classical computer; nevertheless, classical computers will remain the primary choice for some class of algorithms and problems. Thus, it is not fair considering valid the so called *quantum supremacy* concept. Quantum and classical computers will work together, each one on their specific class of problems: a more fair term is, in this case, the so called *quantum advantage*, where QCs will overcome classical systems on solving specific class of algorithm. In particular, considering the number of qubits as the sole comparing term, it is possible to notice that there is an exponential ramp-up of the coefficients involved in the calculation while increasing the size of the QC. It is worth noticing that 64 qubits will require ~ 75 EB (Exa-Byte) of memory to be encoded on a classical computer: for example, encoding 256 qubits on a classical computer would rather be simply impossible.

Although quantum supremacy/advantage is currently a controversial field [54][55], it is clear that Quantum Computation field is rapidly evolving in terms of number of available qubits, qubits quality and application use cases.

Taking into account the above introduced state of art of the available hardware and software technologies, together with the most promising ones for future developments, we now introduce in the following Chapters two different approaches to Quantum Computation. The first one, based on superconducting transmons qubits, has been used to perform simulations and real hardware runs on IBM Quantum platform; the second one, the molecular approach representing a possible next generation of Quantum Computers, has been exploited to create a set of simulated Universal Quantum Gates and a simulation of a Quantum Error Correction algorithm.

CHAPTER 3

Transmons approach

One of the most promising platforms used nowadays to build qubits are the superconducting transmons in terms of easiness to build, control, scale and, most of all performance [41]. They are implemented using a Niobium-Aluminum alloy: in particular, Niobium is a transition metal that enters in superconducting regime at relatively high temperature (~ 9.2 K), and it has some useful properties for superconducting technologies. Superconducting transmons qubits are basically anharmonic oscillators built using Josephson Junctions.

In the following sections the foundation theory is reported, along with a description of the physical implementation.

3.1 Transmons as superconducting qubits

Each modern classical computing hardware consists of basic components named transistors, elements capable to control electric charge flux with the application of an external electric field (FET, *Field Effect Transistor*) or current (BJT, *Bipolar Junction Transistor*). Transistors leverage electric concepts of capacitors (C), inductors (L) and resistors (R), that establish the basis of charge and current flow control; one of the most important combination of such electrical components is the LC oscillator, also called *resonant circuit*, that acts as an electrical resonator able to store and release energy.

3.1.1 The harmonic oscillator

A classical harmonic oscillator can be defined by the following equation:

$$H = \frac{p^2}{2m} + \frac{1}{2}m\omega^2 x^2 \tag{3.1}$$

where a particle of mass m is subject of the action of an harmonic potential, and where $[x, p] = i\hbar$ [56]. This can be translated in the electronic field as:

$$H = \frac{\phi^2}{2L} + \frac{q^2}{2C} \tag{3.2}$$

where ϕ is the magnetic flux and q is the electric charge. In Fig. 3.1(a) is reported a sketch of an ideal LC oscillator: the capacitor C is able to store energy by creating an

electric field between plates, while the inductor L by creating a magnetic field inside its coil. Connecting a capacitor and an inductor in a circuit can create an oscillation of energy through the two components, in terms of charge flux and induced currents. If this system is charged and then isolated, the oscillations would be damped until disappearing after a certain amount of time, as the resistance of the circuit dissipates energy; on the other hand, if an external generator is inserted in the LC circuit, oscillations can be controlled and maintained without damping. It is important now to introduce the main energy dissipation sources in an LC circuit oscillator, in order to understand the effect on energy storage. There are two main dissipation sources: internal and external.

- **Internal dissipation**: each LC circuit has an internal resistance, due to the physical implementation of the conductors (wires) and the dielectric of the capacitor. We can define this internal resistance as R_{int}.
- **External dissipation**: an LC circuit interacts with the external environment while oscillating, leading to radiation and coupling effects. We can define these external effects as R_{ext} and C_{ext}.

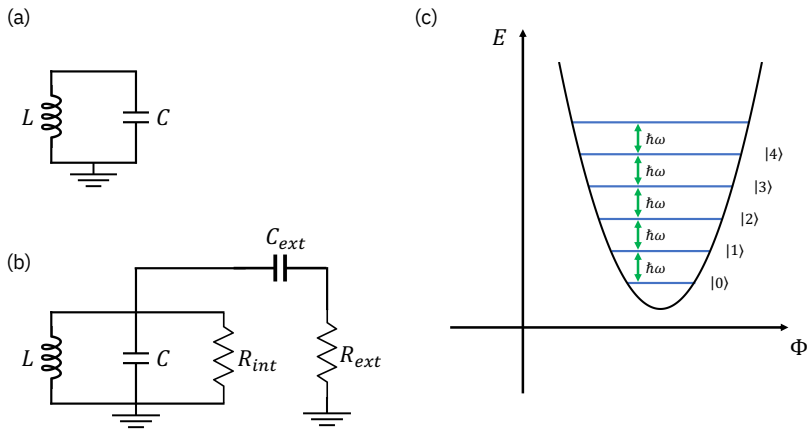

Figure 3.1: Ideal and real harmonic oscillating circuit with energy levels.

As depicted in Fig. 3.1(b), the external effects contribute to a decrease of the total resistance and an increase of the total capacitance, by following the laws regulating the series and parallel circuits. The total resistance and the total capacity can thus be defined as

$$\frac{1}{R_{tot}} = \frac{1}{R_{int}} + \frac{1}{R_{ext}} \tag{3.3}$$

$$C_{tot} = C_{int} + C_{ext} \tag{3.4}$$

leading to a energy decay time (and rate):

$$T_\tau = \frac{1}{\tau} = R_{tot} \cdot C_{tot} \tag{3.5}$$

We can then define a *resonance frequency* ω_0 for an oscillating LC circuit as $\omega_0 \equiv \frac{1}{\sqrt{LC}}$.

In Fig. 3.1(c) the energy levels of the harmonic oscillator built with an LC circuit after quantization are reported: in an harmonic oscillator, energy levels are equally separated by equal gaps. An oscillator with equal energy gaps is called *linear*.

3.1.2 Quantization of the harmonic oscillator

In order to use such theoretical basis to implement a quantum oscillating system to implement computation, we would need to address only a single gap, with $|0\rangle$ and $|1\rangle$ to be used to define qubit states.

First, the quantization of the harmonic oscillator is of course required. The classical harmonic oscillator Hamiltonian in Eq. 3.1 can be rewritten introducing a complex variable $A = m\omega x + ip$, resulting in the form $H = \frac{1}{2m}|A|^2$. This leads to the Hamiltonian of the quantum harmonic oscillator:

$$H = \frac{1}{4m}(A^\dagger A + AA^\dagger) = \frac{1}{2m}A^\dagger A + \frac{1}{2}\hbar\omega \tag{3.6}$$

that, with the introduction of the creation and annihilation operators a and $a^\dagger$, leads to [56]:

$$\mathcal{H} = a^\dagger a + \frac{1}{2} \tag{3.7}$$

The n-th energy level of the quantum harmonic oscillator is thus $E_n = (n + 1/2)\hbar\omega$, equal to the classic harmonic oscillator spectrum.

3.1.3 Josephson Junctions as non-linearity source

The most important feature now needed is a *non-linearity* source to make the energy gaps different each others in order to address specific levels to induce transitions between them, without inducing other unwanted transitions, as depicted in Fig. 3.2.

The introduction of a non-linear element in an harmonic oscillator is achieved using Josephson Junctions, the only circuit elements that are dissipation-free and nonlinear [57]. The LC circuit becomes an anharmonic oscillator with the introduction of Josephson Junctions working in the superconducting regime, as depicted in Fig. 3.3. This *artificial atom* would provide the anharmonicity needed to induce only the selected transitions. The Josephson Junction is a junction similar to what occurs on transistors, with the difference that two superconducting stripes (instead of semiconductors) are separated by an insulator [58]: the charge carriers, thus, are not electron-vacancy pairs, but Cooper Pairs acting like a Boson ($S = 0$) moving through the insulating layer by tunnel effect, condensed into a macroscopic wave function [59]. Several different uses of Josephson Junction are reported in Ref. [60]. The two main characteristics of Josephson Junctions essential to create qubits are reported below.

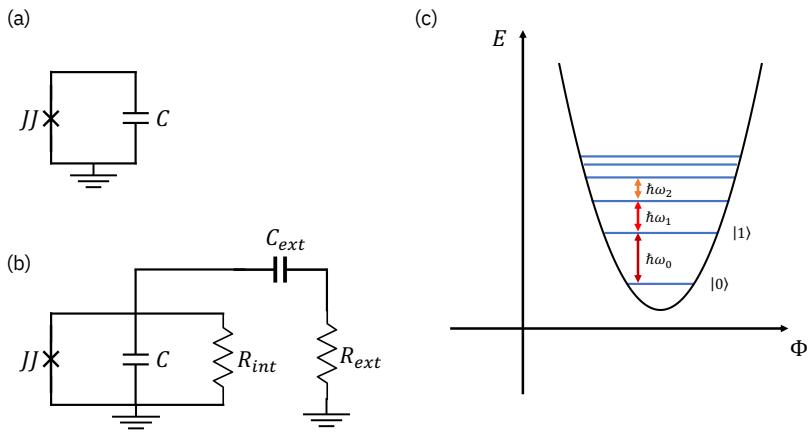

Figure 3.2: Ideal and real anharmonic oscillating circuit with energy levels.

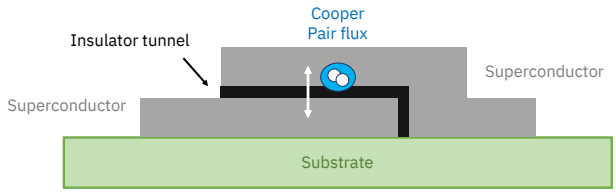

Figure 3.3: Josephson Junction section view.

- **Flux quantization and Josephson tunnelling**: when a ring-shaped superconducting material immersed in a magnetic field is cooled down below a certain temperature, in particular its superconducting transition temperature (usually a few degrees Kelvin dependant on the considered material), the repentine shut off of the magnetic field yields to the quantization of the magnetic flux through the ring; this is due to the supercurrents inside the ring. The magnetic flux takes values of:

$$\Phi_0 \equiv \frac{h}{2e} \tag{3.8}$$

In a Josephson Junction, as depicted in Fig. 3.3, an insulator tunnel lets Cooper Pairs pass: this supercurrent through the insulator is related to the different phases of the two superconducting layers:

$$I_{sup} = I_c \sin \phi(t) \tag{3.9}$$

where I_c is the critical current [61]. The phase time evolution can be represented by:

$$\frac{d\phi(t)}{dt} = \frac{2\pi}{\Phi_c} V = \frac{2e}{\hbar} V \tag{3.10}$$

as per Eq. 3.8, where V is the difference of potential between the two superconducting layers. Let's now represent the time evolution of supercurrent (Eq. 3.9) by using Eq. 3.10:

$$\frac{dI}{dt} = I_c \cos\phi(t) \frac{d\phi(t)}{dt} = \frac{2eVI_c}{\hbar} \cos\phi(t) = \frac{2\pi V I_c}{\Phi_c} \cos\phi(t) \tag{3.11}$$

Considering the Faraday's law of induction $\Delta V = -\frac{d\Phi}{dt}$ and $L = \Phi/I$, we can obtain:

$$|L_{jj}| = \frac{\Phi_c}{2\pi I_c \cos\phi(t)} = \frac{\Phi_c}{2\pi\sqrt{I_c^2 - I^2}} \tag{3.12}$$

in the $I < I_c$ regime. The Josephson Junction is thus a nonlinear inductance carrying an internal capacitance C_{int} as reported in Eq. 3.4.

- **Charge qubit**: in order to understand the different functioning regimes of a qubit made with Josephson Junctions, one needs to study the flux of Cooper Pairs that pass through the insulator. The characteristic energy contribution of the Josephson Junction is $E_{jj} \cos\hat{\phi}$, where $\hat{\phi}$ describes the phase difference across the junction. To study the Cooper Pairs flux we now introduce the number operator $\hat{n} = -\hat{q}/2e$ and the charging energy $E_c = q^2/2C_{int}$. Cooper Pairs energy can be represented by:

$$\hat{H} = 4E_c(\hat{n} - n_{off}) - E_{jj} \cos\hat{\phi} \tag{3.13}$$

where n_{off} represents an offset charge, when adding an external voltage source to the circuit depicted in Fig. 3.2(b). Hamiltonian in Eq. 3.13 can be rewritten on the charge basis:

$$\hat{H} = 4E_c \sum_{n=-N}^{N} (n - n_{off})^2 |n\rangle\langle n| - E_{jj} \sum_{n=-N}^{N-1} (|n+1\rangle\langle n| + |n\rangle\langle n+1|) \tag{3.14}$$

The number of Cooper Pairs tunnelling the insulator is then related to E_{jj}/E_c, and n are the eigenvalues of the operator $\hat{n}$.

3.1.4 Physical implementation

Superconducting qubits are physically implemented in many different ways. The nonlinear Josephson Junction, a crucial element that basically all implementations have in common, is usually built using an alloy of Niobium and Aluminum, with different critical temperatures to enter in superconducting regime, respectively $T_{C_{\mathrm{Nb}}} = 9.2$ K and $T_{C_{\mathrm{Al}}} = 1.2$ K. The insulating layer is usually built with Aluminum Oxide [62]. There are several regimes for implementing superconducting qubits, depending on the ratio E_{jj}/E_c, as reported in Eq. 3.14.

- **Cooper Pair Box (CPB)** regime: here we have $E_{jj}/E_c \sim 1$ [63], with a high anharmonicity of the system and a high Cooper Pairs flux, increasing decoherence.
- **Transmon** regime: here we have $E_{jj}/E_c \gg 1$ [41], where ahnarmonicity is only a small perturbation in a system dominated by harmonic characteristics. The system can then be described as a perturbed harmonic oscillator, with the Hamiltonian:

$$\hat{H} = \sqrt{8E_cE_{jj}}(\hat{\alpha}^\dagger\hat{\alpha} + \frac{1}{2}) - E_{jj} - \frac{E_c}{12}(\hat{\alpha} + \hat{\alpha}^\dagger)^4 \tag{3.15}$$

where $\hat{\alpha}^\dagger$ and $\hat{\alpha}$ are the canonical creation and annihilation operators of the harmonic oscillator. The latter part of the Eq. 3.15 is the leading order anharmonicity. The energy levels thus are not equally spaced as the harmonic oscillator, but a first order correction occurs:

$$E_l^{(1^{st})} = -\frac{E_c}{12}\langle l|(\hat{\alpha} + \hat{\alpha}^\dagger)^4|l\rangle = -\frac{E_c}{4}(2l^2 + 2l + 1) \tag{3.16}$$

where $|l\rangle$ are the harmonic oscillator eigenstates. They are mixed with $|l \pm 2\rangle$ and with $|l \pm 4\rangle$: resulting anharmonicity is $\sim -\sqrt{\frac{E_c}{8E_{jj}}}$. Cooper Pairs flux is thus limited, and also decoherence, while anharmonicity is reduced. The transmon qubit can be integrated on a superconducting transmission line resonator, also called Coplanar Wave guide Resonator (CWR). As depicted in Fig. 3.4, two Josephson Junctions with energy E_{jj} are coupled with a CWR and connected to a voltage source. Shunting capacitor C_B reduces E_c, increasing the ratio E_{jj}/E_c. Considering $C_r \ll C_{tot}$ (total capacitance), the system can be described by:

$$\hat{H}_{int} = 2e\frac{C_{off}}{C_{tot}}\sqrt{\frac{\hbar\omega_r}{2C_r}} \cdot \hat{n}(\hat{a} + \hat{a}^\dagger) \rightarrow \hbar\sum_{i,j} g_{i,j}|i\rangle\langle j|(\hat{a} + \hat{a}^\dagger) \tag{3.17}$$

where $\omega_r = 1/\sqrt{L_rC_r}$ is the resonator frequency, $\hat{a}$ and $\hat{a}^\dagger$ are respectively the annihilation and creation operators of the photons in the harmonic oscillator, and $\hat{n}$ is the number operator. The transmon qubits can be physically implemented and controlled by properly tuning the characteristic quantities E_{jj}/E_c, C_{off}/C_{tot}, C_r and ω_r. The latter notation is achieved by rewriting $\hat{H}_{int}$ on the basis of the uncoupled states $|i\rangle$, where:

$$\hbar g_{i,j} = 2e\frac{C_{off}}{C_{tot}}\sqrt{\frac{\hbar\omega_r}{2C_r}}\langle i|\hat{n}|j\rangle \tag{3.18}$$

Here we focus on the transmon regime, which is the most largely employed and studied. *Transmission-line Shunted Plasma Oscillation* qubits, also called *Transmon* qubits, are one of the most encouraging technological implementation of superconducting qubits: as said, some of their properties are that the energy gaps are very well defined, there is a low sensitivity to the noise due to the charge flux, and a large dipole moment.

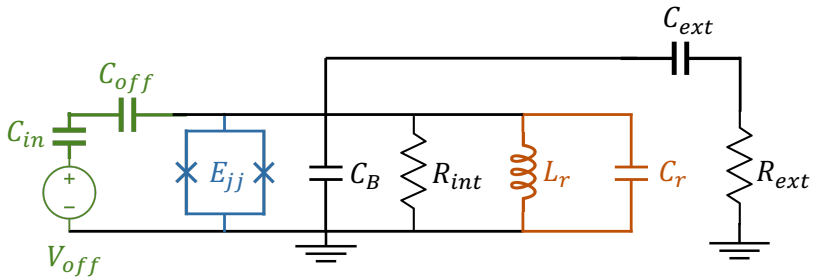

Figure 3.4: Effective circuit diagram of the transmon, with two Josephson Junctions (blue), an offset voltage source (green) and a CWR (orange).

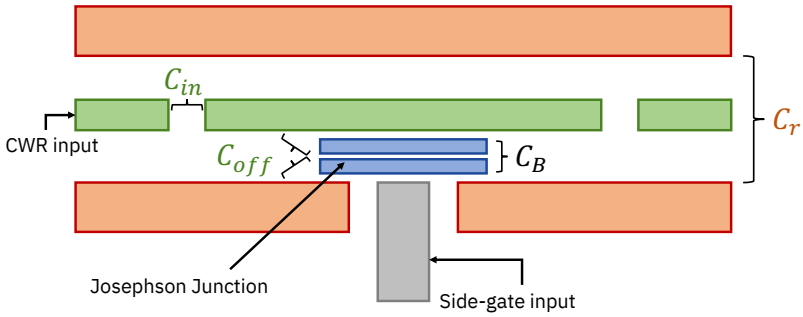

Figure 3.5: Implementation scheme of the transmon in a CWR. Typical scale of the overall CWR thickness is ~ 5 μm.

As compared to other superconducting qubit technologies, transmons are characterized by high anharmonicity and low charge noise. Increasing anharmonicity will increase charge noise, but while anharmonicity scales exponentially with E_{jj}/E_c, decoherence scales polinomially [41]. Most importantly, these systems can be controlled by introducing microwave-scale pulses, inducing transitions between the two lowest energy levels, defined as $|0\rangle$ and $|1\rangle$.

Taking into account all the above mentioned features, a quantum chip made of several transmons qubit is composed by the following elements.

- **Qubit processor**: the qubit itself is composed by a single Josephson Junction acting as non-linear inductor, introducing anharmonicity to the harmonic oscillator created by the transmission line resonator, with different gaps between energy levels. In there, the two states of the qubit can be accessed. To control the state of the qubits, the application of a resonant microwave pulses is required. To do this, some control lines inputs need to be installed on the chip [64]; the size of these resonators is due to the fact that they must resonate with a frequency ~ 5 GHz, thus with a scale length of 10^{-2} m. The external microwave pulse is tuned close to the resonating frequency, and it is sent through the resonator input or through the side-gate, properly varying their length, amplitude and phase. Single-qubit quantum gates are implemented with resonant microwave pulses; two-qubit gates are

implemented in various ways, always with resonant microwave pulses [14].

- **Qubit readout**: readout wave guides are used to obtain the qubit states after measurement. In general, the qubit readout is performed in the dispersive regime, where a large qubit-resonator detuning $\Delta = |\omega_r - \omega_0| \gg g$ is present, with g defined in Eq. 3.18 and ω_0 is the energy gap between level $|0\rangle$ and $|1\rangle$ (as depicted in Fig. 3.2). The Hamiltonian in the dispersive regime can be rewritten as the following [65]:

$$\hat{H}_{disp} \approx \hbar(\omega_r + \chi\hat{\sigma}_z)\hat{a}^\dagger\hat{a} + \frac{\hbar}{2}(\omega_0 + \chi)\hat{\sigma}_z \tag{3.19}$$

  where $\chi = g^2/\Delta$. The dispersive regime allows one to perform a non-demolition readout of the qubit state. The first term of Eq. 3.19 represents a state-dependent frequency shift of the resonator: the qubit performs a dispersive shift of the resonator frequency. The application of an external microwave pulse close to the resonance frequency ω_r on the CWR is required: then, a phase-sensitive measurement of the transmitted microwave is enough to gather the state of the qubit [65].

- **Refrigeration**: the entire chip containing qubit and resonating wave guides must be kept at very low temperature, to maintain superconductivity regime, and to cut down unwanted excitations from the external environment. To do so, a cooling system operating with liquid Helium isotopes ^{3}He and ^{4}He is required, capable to lower the temperature down to $\sim$ 10 mK. Superconductivity also carries the opportunity to lower the dissipation of energy and reduce excitations, due to the low temperature involved.

We can finally define the quality factor of the resonator as $Q \equiv \omega_r/\Delta\omega$, where $\Delta\omega$ is the half-power bandwidth [66]. The quality factor describes the resonator performance being inversely correlated to the energy damping rate. Exploiting Niobium properties to create Nb-based alloys superconducting transmons has improved the quality factor up to 10^7 [67].

3.1.5 Main noise sources

One of the major noise sources for transmons qubits are the decoherence errors, introduced in Section 1.3, and here recalled: the thermal relaxation time T_1 is the decay time of diagonal elements of the ρ, while T_2 time is the dephasing time, the decay time of the off-diagonal elements of the ρ ($T_1 \geq T_2$, in general). Transmon systems can be built with relaxation time $T_1 \sim 100$ μs and coherence time $T_2 \sim 100$ μs, as order of magnitude. As an example, below we simulated a measurement of relaxation time and coherence time on IBM's superconducting transmons qubits, using Qiskit simulators and fitters. In Fig. 3.6(a) it is reported the probability as a function of time to find the qubits in the state $|1\rangle$ after applying an X gate to the initially prepared state $|0\rangle$, for two different qubits. The slope is a decaying exponential, where T_1 is the decay time. In Fig. 3.6(b) are represented the probability as a function of time of Rabi oscillations between $|0\rangle$ and $|1\rangle$ states

obtained with a transition resonant pulse. The envelop is a decaying exponential, where T_2 is the decay time. Decoherence rates must be taken into account to be able to implement reliable computation. Each quantum gate composing a quantum circuit takes a certain time to be executed, usually single-qubit gates take ~ 30 ns and two-qubit gates take ~ 300 ns: the overall time taken to compute the entire circuit must be significantly shorter than T_1 and T_2.

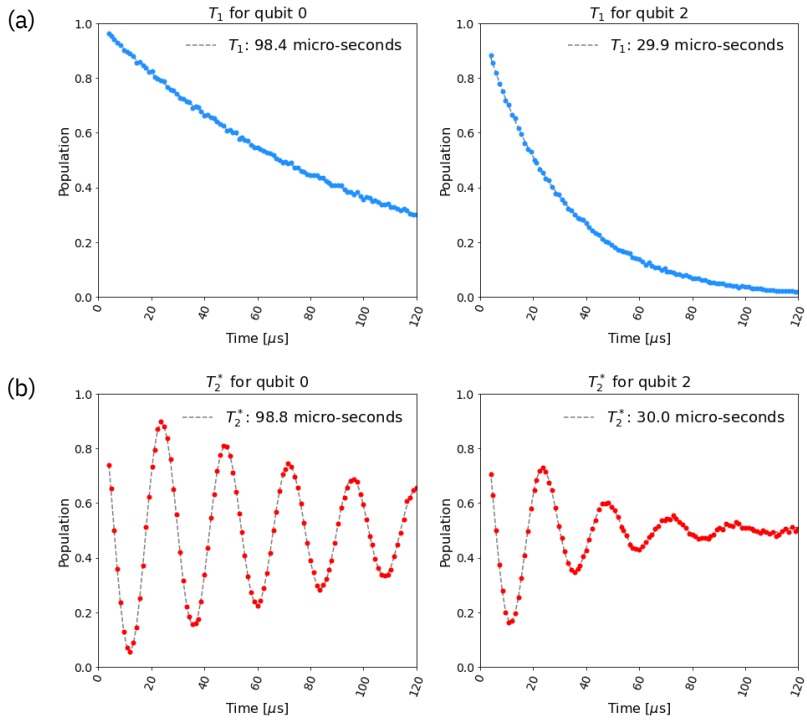

Figure 3.6: Simulations of decoherence times on transmons qubits made with Qiskit.

Another error source affecting superconducting transmons, but not limited to them, is related to the accuracy of rotations performed on the qubit states. Rotation gates theoretically are meant to implement rotations of a certain angles along a certain axes: in practice, this process is experiencing mainly two problems. The first one is a tilt on the rotation axis, not being precisely accurate; the second one is an incorrect implementation of the rotation angle, usually due to the fact that the transition frequency depends on the first-neighbour qubits, that are not completely decoupled (*cross-talk*). The combination of these two effects leads to an inaccurate implementation of the rotation gate, thus influencing the final state quality and the fidelity of the computation. An accurate characterization of IBM Quantum gates is reported in Appendix A.

3.2 IBM Quantum

A consistent part of this work has been developed using IBM Quantum technology, based on the above detailed superconducting transmon qubits. In the following sections we will give an overview of the main features of the IBM quantum computing platform. IBM was certainly [68] the first enterprise to start thinking about quantum computing, since the first quantum computing conference named "Physics of Computation Conference" was hosted in 1981 by IBM and the MIT [69], more than 40 years ago. During the following decades, a lot of theoretical and experimental research was performed by several research laboratories, academic institutions and enterprises, with the objective to create the foundations of quantum computing and to start thinking to possible implementations.

IBM's quantum devices are available in IBM Cloud since 2016 through the IBM Quantum Experience platform, then renamed IBM Quantum [2][3].

3.2.1 Hardware description

IBM Quantum systems are available for remote access via the Internet through IBM Cloud platform, and are released in different versions. The different architecture versions take the names of birds (e.g. Falcon, Hummingbird, Eagle) while the single devices take the name of cities (e.g. Nairobi, Toronto, Washington). Each chip architecture has different qubit topologies, as depicted in Fig. 3.7: it is clear that superconducting chips have a limited coupling, as only a few qubits are directly interconnected each other. However, the software stack is in charge to transpile the circuits in order to achieve the desired connectivity implementing SWAP gates, allowing the creation of entangled states using not directly interconnected qubits. This architectural choice is due to the fact that additional connectivity would introduce an higher cross-talk effect, leading to a more important noise impact on the chips. A detailed view of chip's calibration is provided on the user interface, or via API using the software stack. In Fig. 3.7 are reported the most common IBM Quantum chip topologies: the "brick-shape" topology is currently used to enable chip scalability, as more and more bricks can be attached together creating bigger chips. The different shades of purple color indicate the calibration data for both single-qubit gates and two-qubit gates.

These quantum devices are nowadays (late 2022) hosted on IBM facilities in the U.S., first of all due to the required highly skilled maintenance and operations personnel (Fig. 3.9(a)). For the production systems, all the hardware components, including the refrigerator, the classical read-out and control computing resources, are enclosed in a single glass case, as depicted in Fig. 3.9(b) photo: these machines are the World's first fully integrated universal quantum computing system "IBM Quantum System One" that can accomodate devices up to 127 qubits [38]. The future chips would require a bigger enclosure, with a more powerful cooling system, that will be called "IBM Quantum System Two" as depicted in Fig. 3.9(c) render [71].

IBM Quantum chips are constantly calibrated via software, and calibration data are available on both user interface on the portal and via programmatic access. Calibra-

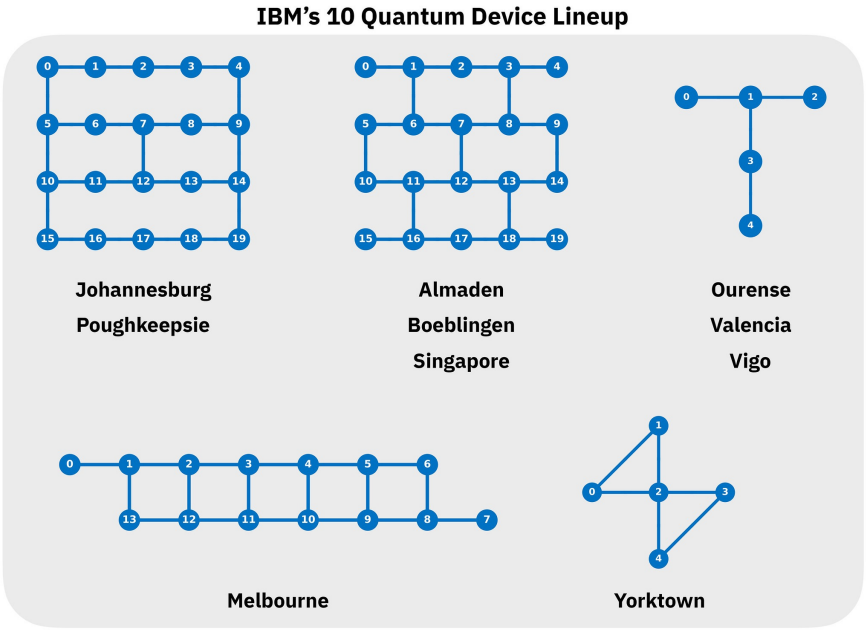

Figure 3.7: Different IBM Quantum system topologies (2019). Top-left: first version of brick-based topology. Top-center: current brick-based topology. Top-right: T-shaped topology. Bottom-left: first version of linear-brick topology. Bottom-right: first version of high-connectivity topology. The name of the Cities represent the different devices, with the relative topology. Not reported here: H-shaped and L-shaped topologies. Reproduced from Ref. [70] with permission from IBM (open access photo collection distributed under the terms and conditions of the Creative Commons Attribution (CC BY-ND 2.0) license Creative Commons).

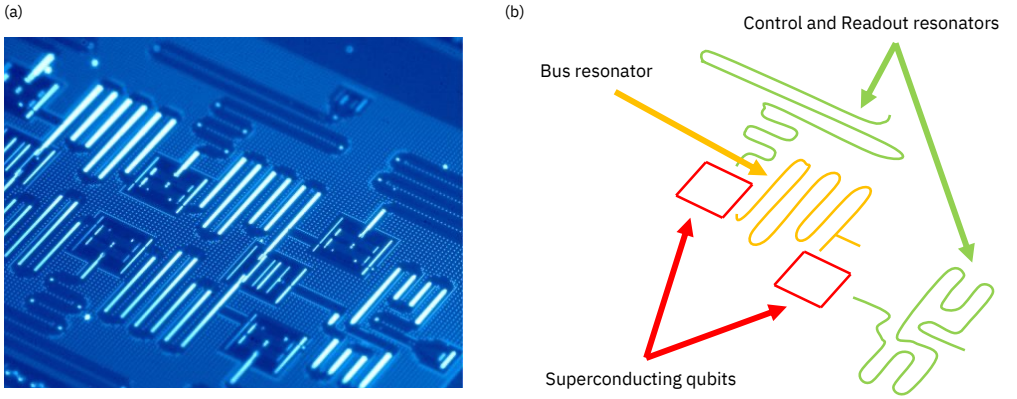

Figure 3.8: (a) First generation of IBM Quantum basic chip structure. Reproduced from Ref. [70] with permission from IBM (open access photo collection distributed under the terms and conditions of the Creative Commons Attribution (CC BY-ND 2.0) license Creative Commons). (b) Details of IBM Quantum chip components.

tion data (late 2022) contain the topology diagram depicting the coupling map between qubits, and a set of tables containing information on qubits themselves and on single-qubit and multi-qubit operations. The calibration includes the frequency and anharmonicity (both measured in GHz), T_1 and T_2 (measured in μs, readout error rate and length (in ns), and single qubit operation error rates. For connectivity calibration data, the CNOT error rates and the CNOT gate time length (in ns) are provided. It is possible to access the specific chip calibration data to perform noisy simulations reproducing the general behaviour of that chip; advanced error composition techniques also allow to build custom noise models to simulate custom calibrated chips, very useful to mimic technology improvements.

Figure 3.9: IBM Quantum systems. Reproduced from Ref. [70] with permission from IBM (open access photo collection distributed under the terms and conditions of the Creative Commons Attribution (CC BY-ND 2.0) license Creative Commons).

3.2.2 Metrics

There are currently three main metrics to define near-term quantum devices computational power [72].

- **Scale**: the number of available qubits in a quantum chip is an important feature, since more qubits mean more available states that can be accessed. Superconducting qubits are still the most promising for scalability purposes: for example, the IBM brick-shape connectivity would ensure a great improvement on qubits number, as they can be put together leveraging on their modular design. New strategies to constantly increase the number of qubits are in development (see Sec. 3.2.3).

- **Quality**: qubits quality refers to reducing the impact of noise on quantum computation. The metric defining the quality of quantum processors is Quantum Volume (QV) [53], introduced in 2019 by IBM and explained in Sec. 2.2.1.

- **Speed**: in 2021, IBM introduced the concept of Circuit Layer Operations per Second (CLOPS), that recalls the Floating Point Operations per Second (FLOPS) metric used for classical computers. CLOPS is a measure determining the number of circuit layers that the Quantum Processing Unit (QPU) is able to execute in a given unit of time. Properly, this metric is defined as the number of primitive circuits that can be processed in a second. Higher CLOPS means the ability to execute more circuits, allowing a Quantum Computer to perform more complex algorithms in a reasonable amount of time.

3.2.3 Development roadmap

As explained in the previous sections, superconducting transmons qubits are very promising technology to build Universal Quantum Computers. Several techniques to increase the number of qubits are in development, as per IBM Quantum roadmap [73][74]: *circuit knitting*, *real-time classical communication* between separate processors, and *chip-to-chip couplers* will be leveraged all together to break the barrier of 4000 qubits in the next years (2023 to 2026), reaching then 10k-100k qubits beyond 2026.

Circuit knitting is a software feature that will be used to break quantum circuits in chunks to be computed on separate quantum processors, then combined back by a classical controller: this is the main software feature that will enable all the scalability required to build the future devices. The next step, enabled by circuit knitting, is expected to allow the real-time communication between different quantum devices, that will work together in parallel to compute their chunk of circuit. This will be enabled by using hardware communicating links between quantum devices, with a scale length of $\sim 10^0$ m, as depicted in Fig. 7.4(a). In the meanwhile, quantum processors will be improved by introducing a chip-to-chip connectivity using small scale couplers ($\sim 10^{-3}$ m), enabling to put together several chips inside the same quantum device as depicted in Fig. 7.4(b). Each blue dashed block represents a separate quantum system. The last step will be the concurrent use of these technologies, building quantum devices connected with both real-time connections and chip-to-chip couplers, allowing to go beyond 4000 qubits. A scheme of this implementation is depicted in Fig. 3.11.

All IBM Quantum hardware is currently released remotely at IBM sites, for evident technology constraints such as refrigeration and highly skilled professionals required for maintenance. All quantum resources are available on the quantum portal in different flavours; in this work we used quantum chips up to 7 qubits to simulate static and dynamic properties of several quantum systems as reported in Chap 6 and Chap. 5. IBM's quantum devices are also available via IBM Cloud platform, integrating Qiskit Runtime services: this feature is described in Chap. C, where new architectural approaches are proposed to integrate quantum systems into current classical enterprise applications.

Although the significant effort put in place to develop this revolutionary technology, Quantum Computation is just at the beginning of its journey. Superconducting qubits,

as well as the other systems currently investigated, are probably only one of the first steps towards the large scale fault tolerant universal quantum computation. Fundamental research must continue to find new ways to build the future generation of Quantum Computers, hopefully mitigating all the issues experienced by current technology. In the next Chapter is thus introduced a different approach to Quantum Computation based on magnetic molecules, then exploited in Chap. 7 with several simulations.

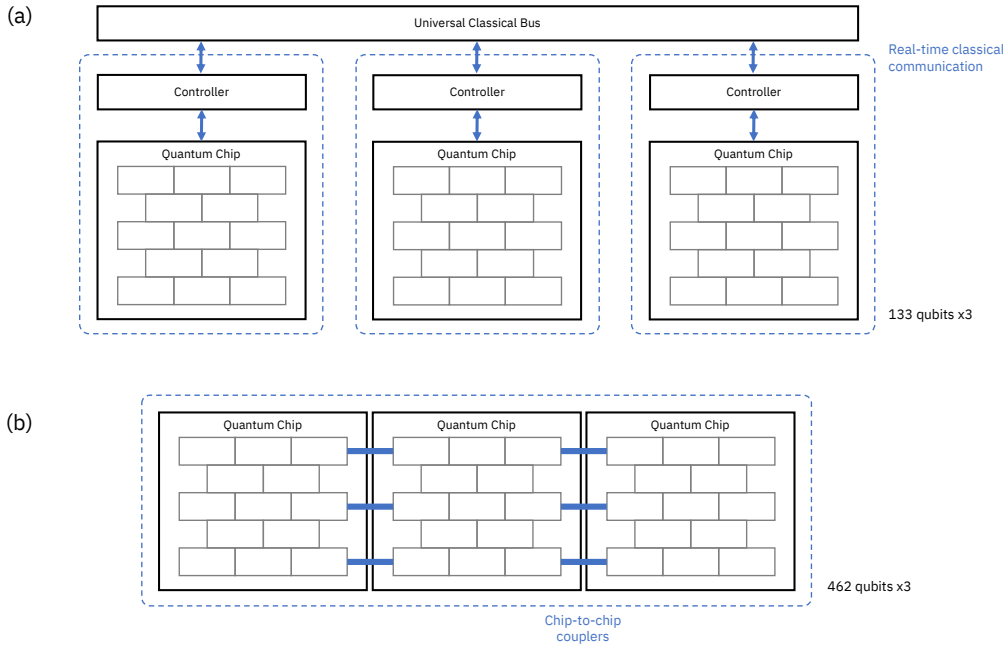

Figure 3.10: (a) Real-time classical communication scaling technique. (b) Chip-to-chip couplers scaling technique.

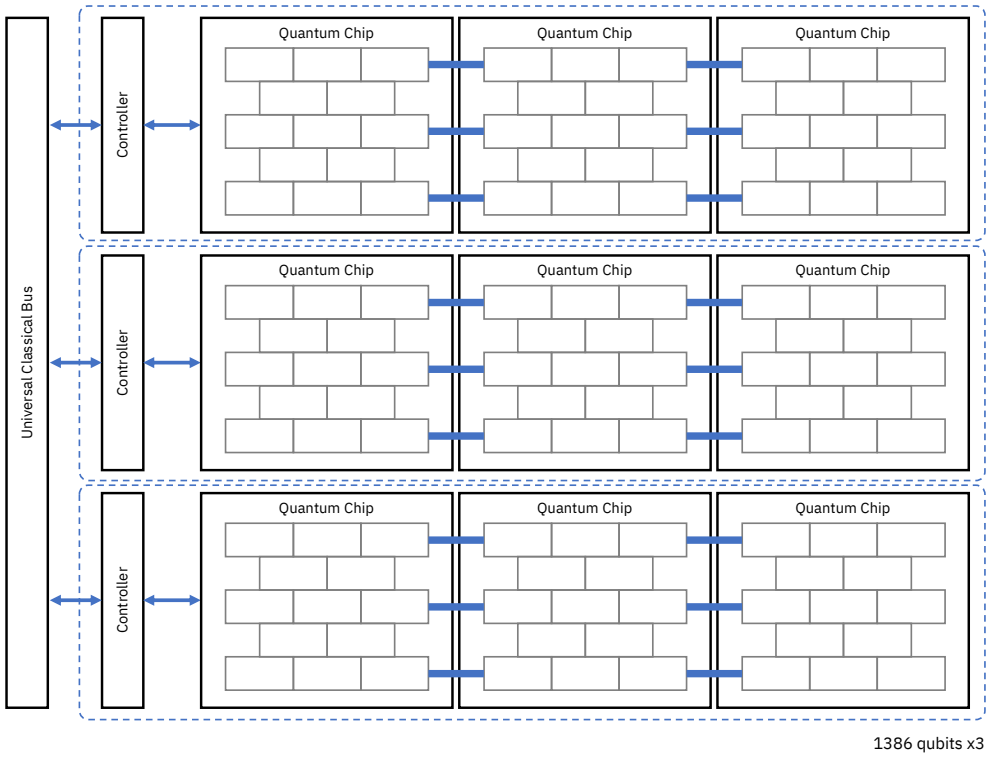

Figure 3.11: Putting together the two scaling technique to reach $\sim$ 4000 qubits and beyond.

CHAPTER 4

Molecular approach

The main issue preventing today's approaches to Quantum Computing to be considered good candidates for Fault-Tolerant computation is their intrinsic weakness to decoherence: current systems implementing qubits can be considered reliable only for a relatively small amount of time, thus cannot be used to achieve a real quantum advantage for applications in a production environment. Several ways are being studied and developed to improve Quantum Computer performances in terms of error correction, and will be available to next generations of Quantum Computers. One approach in development is the implementation of *block encoding*, where the fundamental unit of computation will be a logic unit composed by a certain amount of physical qubits: with this approach, the logical qubit becomes a collection of physical ones, which must then be corrected, as introduced in Chap. 1.5. The main drawback of this method is that a huge amount of physical qubits is needed: as million of logic qubits [75] will be probably needed to implement complex quantum algorithms, and each logical qubit would be composed by hundreds of physical qubits, a Quantum Computer would require chips implementing hundreds of millions of qubits [76]. This is not achievable with the currently available technology.

Fortunately, other approaches are arising for Quantum Error Correction: one of the most promising one is exploiting multi-level (*qudit*) systems to embed QEC into single objects. Molecular Nanomagnets provide one of the most promising implementation of such error-corrected units.

4.1 Introduction to Molecular Nanomagnets

Molecular Nanomagnets (MNMs) are molecules containing a small amount of transition metals or rare-earth ions in their core, surrounded by an organic ligand structure. The core ions are the source of the magnetic behaviour of the molecule: transition metal ions (usually V, Cr, Mn, Fe, Co, Cu) have a partially filled $3d$ shell, and are characterized by strong inter-spin Heisenberg interactions; rare-earth ions (usually lanthanides, Ce, Nd, Eu, Yb) have a partially filled $4f$ shell, and are characterized by a strong single-ion magnetic anisotropy. The incomplete orbital shells of the core ions are responsible for the magnetic effects, due to the Hund's Rules. The shell position respect to the ions nuclei are important to determine the most important interaction characterizing the molecule.

Such molecules composed by magnetic core ions and a ligand cage can be organized in crystal lattices, where each magnetic core acts as a single and isolated Molecular Nanomagnet: the surrounding ligand structure suppresses interactions between magnetic cores. This characteristic can be exploited to perform computation by accessing each magnetic ions singularly, while arranged in a solid and precise crystal structure.

Molecular Nanomagnets with an effective $S = 1/2$ have been proposed to implement qubits [77]: proper compounds have been selected and engineered to improve coherence time up to ~ 0.1 ms at low temperature and up to ~ 1 μs at room temperature [78], reaching values impossible to be achieved with currently implemented technologies such as superconducting transmons. Moreover, the molecular approach can lead to a relatively easy implementation of Quantum Error Correction algorithms by encoding logical qubits using the larger available Hilbert space. Unsurprisingly, the real power of Molecular Nanomagnets in the Quantum Computation field lays in a deeper use of such systems: complex and specific compounds can be properly synthesized to achieve highly stable and controllable multi level systems, with more than two levels: thus, the paradigm changes from *qubits - quantum bits* to *qudits - quantum digits*. This feature of such systems unlocks many computation possibilities: it is possible, for example, to encode multiple qubits into a single qudit molecule, firstly reducing the number of quantum objects required to achieve the same computational power, secondly allowing an embedded implementation of Quantum Error Correction. The above mentioned characteristics make Molecular Nanomagnets good candidates for the implementation of a new platform for next generation Quantum Computers.

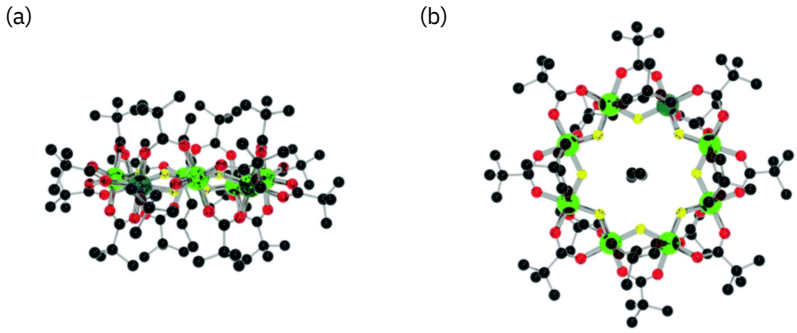

Figure 4.1: Example of a Molecular Nanomagnet compound Cr_7Ni. (a) Side view. (b) Top view. Reproduced from Ref. [79] with permission from the Royal Society of Chemistry (Creative Commons Attribution 3.0 Unported Licence).

In this work we first studied Molecular Nanomagnets static and dynamic properties with current available IBM Quantum Computers (Chap. 5), then we exploited specific Molecular Nanomagnets to simulate the implementation of an universal set of quantum gates (Chap. 7) and a specific QEC algorithm (Chap. 8), then as next step we plan to apply these techniques to study simple fermionic systems with qudits.

4.2 Spin Hamiltonian

Molecular Nanomagnets properties can be described with a single molecule spin Hamiltonian (sH), assuming that each magnetic ion at the core of the MNM can be represented by an effective spin S_{MNM}: this ensures that all magnetic properties of the system can be described using single-ion spin operators [80]. It is possible to express the contributions to the spin Hamiltonian of MNMs considering three main terms:

$$\hat{H}_{MNM} = \hat{H}_{ex} + \hat{H}_{ZFS} + \hat{H}_{B} \tag{4.1}$$

In the following sections we describe each term of Eq. 4.2.

4.2.1 Exchange interaction

The main contribution to the spin Hamiltonian of a MNM is the two-bodies interaction between core magnetic ions. This is described by:

$$\hat{H}_{ex} = \sum_{i>j} \hat{\mathbf{s}}_i \cdot \underline{\mathbf{J}}_{ij} \cdot \hat{\mathbf{s}}_j \tag{4.2}$$

A deeper analysis of this term leads to a further decomposition:

$$\hat{H}_{ex} = \hat{H}_{iso} + \hat{H}_{aniso} + \hat{H}_{antisym} \tag{4.3}$$

where:

$$\hat{H}_{iso} = \sum_{i>j} J_{ij} \hat{\mathbf{s}}_i \cdot \hat{\mathbf{s}}_j \rightarrow \text{Isotropic Heisenberg exchange} \tag{4.4}$$

$$\hat{H}_{aniso} = \sum_{i>j} \sum_{\alpha,\beta} J_{ij}^{\alpha,\beta} \hat{s}_{i,\alpha} \cdot \hat{s}_{j,\beta} \rightarrow \text{Anisotropic exchange} \tag{4.5}$$

$$\hat{H}_{antisym} = \sum_{i>j} \underline{\mathbf{G}}_{ij} \hat{\mathbf{s}}_i \times \hat{\mathbf{s}}_j \rightarrow \text{Antisymmetric exchange} \tag{4.6}$$

and i is the index identifying the magnetic ions, $\alpha, \beta = x, y, z$ are the coordinate axes, J_{ij} and $J_{ij}^{\alpha,\beta}$ are the isotropic and anisotropic exchange couplers, and $\underline{\mathbf{G}}_{ij}$ are antisymmetric parameters. The Hamiltonian of Molecular Nanomagnets based on transition metal ion cores are dominated by the isotropic Heisenberg exchange term, usually a superexchange (antiferromagnetic coupling between two neighbour cations through a non-magnetic anion): the incomplete $3d$ shells of magnetic ions interact via the non-magnetic organic ligands; on the other hand, MNMs with lanthanides magnetic cores interact with the incomplete $4d$ shells, leading to a much smaller interaction. In the first situation, with a leading $\hat{H}_{iso}$ term on the overall $\hat{H}_{ex}$, we can reach the so called *strong-exchange limit*. This imply the conservation of total spin S, and the fact that energy gaps within each multiplet are much smaller than the energy gaps between multiplets themselves. It is then possible to describe such MNMs considering only the ground state multiplet, reducing Hamiltonian complexity and Hilbert Space dimensions.

The magnetic ions are sufficiently separated to make the anisotropic exchange interaction including the dipolar intra-molecular interaction.

The latter term, the antisymmetric exchange, is the Dzyaloshinskii-Moriya Interaction, a contribution to the total magnetic interaction exchange between two neighbour magnetic ions sping s_i and s_j, which exists in pairs of spins lacking inversion symmetry.

4.2.2 Zero-Field Splitting

A Molecular Nanomagnet is composed by a magnetic core ion and a complex ligand structure: this contributing term to the spin Hamiltonian describes how the magnetic ion interacts with all the charges in which it is located. The surrounding charges create an electric field that influences the shape of the orbitals of the magnetic core ion, acting on spin multiplets caused by the spin-orbit interaction: this can introduce a strong anisotropy to the system. In the strong-exchange limit, this is described by:

$$\hat{H}_{ZFS} = \mu_B \sum_i \hat{\mathbf{s}}_i \cdot \underline{\mathbf{D}}_i \cdot \hat{\mathbf{s}}_i \tag{4.7}$$

where $\underline{\mathbf{D}}_i$ is a real symmetric tensor called *Zero-Field Splitting tensor* or *Fine-Structure tensor*. It is worth noting that, when no external magnetic field is applied, this term is the responsible for partially breaking the $(2s_i + 1)$ degeneration of the energy levels; this effect can be seen, also in case of the application of an external magnetic field as described in the following section, by exploring the splitting in proximity of $\mathbf{B} = 0$.

4.2.3 Zeeman interaction

As mentioned before, the latter interaction contributing to the spin Hamiltonian is related to the application of an external magnetic field. This is described by:

$$\hat{H}_B = \mu_B \sum_{i=1}^{N} \mathbf{B} \cdot \underline{\mathbf{g}}_i \cdot \hat{\mathbf{s}}_i \tag{4.8}$$

where μ_B is the Bohr Magneton and $\underline{\mathbf{g}}_i$ is the spectroscopic splitting tensor. The effect of the application of a generically oriented external magnetic field is double: to break the $(2s_i + 1)$ degeneration of the energy levels and to mix different spin states.

4.3 Exploiting MNMs for Quantum Computation

Molecular Nanomagnets are good candidates to implement fundamental units for Quantum Computation. Despite their fundamental characteristics, not all the theoretically ready ions are well suitable for a practical implementation of Quantum Computation: for example, transition metal ions (with the $3d$ shell partially filled) are better for their longer coherence [46].

4.3.1 Two-level systems using molecules

One of the first studies to create suitable compounds to implement qubits on Molecular Nanomagnets was based on molecular rings of Chromium ions. Proper chemical engineering of such compound, basically by replacing a Cr with a Ni ion on the ring, leads to Cr_7Ni molecule, with very promising characteristics to be exploited to create molecular qubits [81]. An array of such molecules, with an antiferromagnetic interaction between them, can be used to implement a set of qubits with a well separated ground doublet with $S = 1/2$ (as per DiVincenzo Criteria, Chap. 1.1), at low temperatures. The effective $S = 1/2$ spin on the ground state produces two different states, encoded by $m = \pm 1/2$, corresponding to the eigenvalues: those two states can be assigned to the qubit states $|0\rangle$ and $|1\rangle$, usable to perform quantum computation. However, the presence of a well defined two-states system is not enough to declare it useful for computation: a rather long coherence time would be required. Several different ions composing the magnetic core has been studied in order to find the right compounds implementing long spin-lattice relaxation time and long coherence time: Copper-based MNMs achieve $T_2 \sim 70\ \mu$s [82][83], while in certain conditions, Vanadium-based MNMs achieve up to ~ 1 ms [77][84]. Improvement of coherence time can be also achieved by a proper chemical engineering of molecules [85]: the structure of the ligands surrounding the magnetic core ion can be optimized to obtain a more robust lattice, obtaining longer coherence times, improving by an order of magnitude [85]. Finally, external electromagnetic pulses can be used to control the two states of such qubits, thus implementing quantum gates. It is worth noticing that such systems offer an intrinsic way to approach scalability: Molecular Nanomagnets can be in fact easily disposed in a structured way, forming arrays of well and solidly positioned qubits. These molecular structures can finally be easily scaled up, leveraging on current chemical engineering state of art, properly switching off the unwanted interactions that can cause *cross-talk*.

4.3.2 Multi-level systems using molecules

In general, Molecular Nanomagnets like Cr_7Ni have more than two accessible levels to be used to perform computation: the two-level systems introduced above are exploiting only two of them, and are the basis of a more complex (but more powerful) approach, in which more than two levels are used.

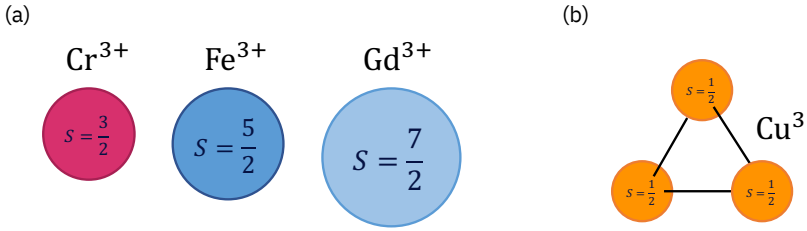

Figure 4.2: (a) Sketch of different single ion $S > 1$ qudits. (b) Sketch of competing interaction qudits, composed by three $S = 1/2$ interacting together.

There are two possible ways to exploit more than two levels on a molecular system in order to perform computation.

- The first one is to choose magnetic core ion with a spin $S > 1$. For instance, it is possible to use ions such Cr^{3+} with $S = 3/2$ and 4 accessible levels, or Fe^{3+} with $S = 5/2$ and 6 accessible levels, or Gd^{3+} with $S = 7/2$ and 8 accessible levels. Increasing the size of the spin of the single magnetic ion has some advantages and some disadvantages. They are very common compounds and there is a lot of literature about them, and well differentiated energy gaps can lead to high fidelity on quantum gates; they are also relatively easy to be synthesized. On the other hand, they have only a linear connectivity between energy levels, allowing only transitions with $\Delta m = \pm 1$, and decoherence gets worst by increasing S. Single spin $S > 1$ systems can also be "single giant spin molecules" where the fundamental multiplet could be generated by multiple spins interacting in the magnetic core.
- The second one is to create more complex compounds with several $S = 1/2$ states at low energy, originating from competing interactions between ions in the same molecule. Multiple magnetic ions with almost frustrated ground state energy levels have a very high connectivity between levels allowing all-to-all transitions, and they can be protected from decoherence, as reported in Chap. 7. However, even if many compounds are existing, chemical engineering effort to synthesize more complex and more suitable systems is needed.

Wrapping up, these molecular structures can be good candidates for qubits and qudits implementation, leveraging on the magnetic properties of the core ion and on the surrounding ligands. Besides electronic spins, also nuclear spins of the magnetic ions can be exploited [86]: they have a much important coherence (they are more protected from the environment than the electron spins), but their control is also slower. A combination of the two approaches (electronic and nuclear spins) can be leveraged to implement particular quantum computation, exploiting computation and memory features to improve results [87].

4.3.3 Switch between spin qubits

A crucial feature enabling scalability of such architecture is the possibility to implement a switchable interaction between the qudits (or qubits); in fact, a permanent interaction causes unwanted time evolution of the quantum states, while a switchable interaction can be turned off when not needed. A simple way to implement switchable interaction is to use external magnetic fields to induce the time evolution only when required: this can be done by exploiting auxiliary quantum states adding an ion between two qudits, acting as switch of the interaction of the two [88][89]. As depicted in Fig. 4.3, there are two different MNMs involved: the two lateral ones have the role to encode the qudit states, e.g. with an $S = 3/2$ each, while the central one is the ion switch, e.g. an effective $S = 1/2$.

The main condition that the switch must satisfy is that, when in the ground state, the effective exchange interaction between the qudits made possible through the switch

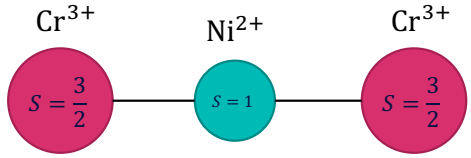

Figure 4.3: Sketch of an effective $S = 1/2$ Ni ion switch linked to two $S = 3/2$ Cr-based qudits.

is very small, and all the unwanted time evolution are thus minimal: the energy of the excited state of the switch must be much larger than the exchange between the qudit and the switch itself, but enough large to let the excitation energy of the switch dependent on the state of the qudits. In this way, it is possible to implement a conditional dynamic. An example of switch ion on Cr_7Ni MNMs is Ni^{2+}, that has $S = 1$ but only two levels can be exploited creating an effective $S = 1/2$ [90][91].

It is thus possible, using uniform pulses exciting the switch, to switch on and off the inter-qudit interaction, enabling scalability and making possible the implementation of two-qudit gates. This feature has been reported in Chap. 7, where two-qudit controlled gates have been simulated. This kind of gates require, as reported in Chap. 1.1.2, to implement rotations on a target qubit considering the state of the control qubit.

4.4 Quantum noise in MNMs qudits

When considering MNMs as quantum systems to implement qudits, an introduction to error sources can be outlined following the already introduced theoretical framework and modelization in Sec. 1.3.

4.4.1 Coherent errors

As introduced above, coherent errors are due to an incorrect implementation of quantum gates. This is basically due to a not perfect implementation of electromagnetic pulses required to implement transitions on the quantum system. In this case, especially when working with multi-level qudits, many transitions between energy levels are required to implement generic gates: pulse control is thus extremely important to induce highly reliable gates, even if energy levels could be very close together. As several transitions have similar energy gaps, one needs to be very selective with pulse frequencies: this can be done by making longer pulses, or with more complex pulse shaping techniques. Of course, a perfect pulse control is rather impossible to obtain.

Fine tuning and pulse engineering can improve pulse quality to obtain rather precise gates, approaching (but not reaching completely) the goal to implement almost perfect gates, addressing only the selected transition. The result of not perfectly monochromatic pulses is a population leakage between unwanted energy levels, reducing the accuracy of the quantum gates, making this kind of error source one of the most impacting on molecular qudits. It is worth noticing that MNMs can be precisely engineered by chemistry, obtaining compounds with optimized energy gaps between levels, slightly relaxing the requirements on pulse control.

4.4.2 Incoherent errors

Eq. 4.2 describes the main contributions to the spin Hamiltonian of a Molecular Nanomagnet considering the magnetic cores as non-interacting with the surrounding environment, *in primis* the ligands structure and the overall lattice. This description is very useful to comprehend the theoretical behaviour of a MNM and how to exploit its characteristics to perform quantum computation; however, there are some other contributions that come from the interaction of the core ions with the environment, leading to undesirable but still important effects.

As per other qubit technologies such superconducting transmons, decoherence is one of the main source of incoherent errors also on molecular spin systems [92]. An accurate description of decoherence is thus important to understand how to reduce its effect on computation. We recall that, if a quantum system described by an Hamiltonian has two possible states $|0\rangle$ and $|1\rangle$, these states can be put in superposition. This superimposed state, however, does not last forever when there is an interaction with the external environment. Another way to look at of this phenomenon is related to the description of a quantum system using a wave function: if the system interacts with the external environment, after a certain amount of time it would become impossible to describe it using a well defined wave function, as the phase would become unknown. This is the effect of decoherence. The system starts to loose coherence when computational time approaches T_2, when the interaction with the surrounding bath starts to become important after the initialization process. At low temperature, the main contribution to decoherence is the so called *pure dephasing*, and it is caused by interactions between the magnetic core and the neighbouring electronic and nuclear spins. Indeed the other contribution to decoherence, the so called *spin-lattice relaxation*, becomes negligible [93]. Moreover, at very low temperature the dipolar interaction between the magnetic ion and the electron and nuclear spins is suppressed, and the main contribution to pure dephasing is lead by an hyperfine coupling with the surrounding spin bath [94].

We describe incoherent errors such as pure dephasing by the Lindblad approximation for system dynamics, as introduced in Sec. 1.3.2: the first term of Eq. 1.52 is the time evolution of the density matrix of the computational quantum system, while the dissipator operator describes the effect of decoherence, causing the decay of the off-diagonal elements of the density matrix (as already discussed in Eq. 1.42). We can rewrite the dissipator operator in case of a spin S:

$$\mathcal{D}_{\rho_{\hat{S}_z}} = \hat{S}_z \rho \hat{S}_z^\dagger - \frac{1}{2}(\hat{S}_z^\dagger \hat{S}_z \rho + \rho \hat{S}_z^\dagger \hat{S}_z) \tag{4.9}$$

by using spin operators $\hat{S}_z$. Pure dephasing is induced by the interaction of the spins of the molecular qudit core with the spins of the surrounding environment.

An important implication of the Lindblad's equation form reported in Eq. 1.52 is that, with the expansion on S_z eigenstates $\{|m\rangle\}$, an exponential decay of the off-diagonal elements on ρ comes out, which is proportional to the squared difference of the eigenvalues of S_z:

$$\rho_S(t) = \sum_{m',m=-S}^{S} e^{-\gamma(m-m')^2 t} \langle m|\rho_S(0)|m'\rangle |m\rangle\langle m'| \tag{4.10}$$

where $\gamma = 1/T_2$ is the dephasing rate. Thus, systems with small differences between S_z eigenvalues can be protected by decoherence, as reported in Chap. 7.

4.5 Quantum Error Correction with MNMs

Quantum Error Correction represents a way to overcome the effect of errors, in particular incoherent ones, occurring during a computation on a Quantum Computer. We recall here the effect of incoherent errors on a quantum state. A qubit, for its nature of two-level quantum system, can encode two different states $|0\rangle$ and $|1\rangle$; we consider a superposition of these two states in the form $\alpha|0\rangle+\beta|1\rangle$. We recall here that an error, regardless its origin or nature, has the effect to corrupt this logical state: a change in the relative population of the two states $|0\rangle$ and $|1\rangle$ can occur, or also a decay of the superposition coherence. After this event, it is impossible to reconstruct the original information stored in α and β, as they are deformed: the error occurs in the same two-dimensional space used for the computation (i.e. the encoding of the logical superimposed state). In order to be able to detect errors, a larger space is then required: if more than two levels are available, it is possible to choose specific code words to encode and protect the state, so that an error applied on this encoded state result to a symmetric translation of the superimposed state from the two original levels to other two levels, without deforming α and β coefficients, thus without corrupting the information stored. In this case, a proper Quantum Error Correction scheme can detect and correct the errors. It is worth recalling that a Quantum Error Correction scheme can recover the original state if and only if the Knill-Laflamme conditions are satisfied [25]:

$$\begin{aligned} \langle 0_L|E_k^\dagger E_j|1_L\rangle &= 0 \\ \langle 0_L|E_k^\dagger E_j|0_L\rangle &= \langle 1_L|E_k^\dagger E_j|1_L\rangle \end{aligned} \tag{4.11}$$

Incoherent errors have different effects on different platforms: while the effect of both T_1 and T_2 is equally important on superconducting transmon qubits, for molecular systems the most important error at low temperature is pure dephasing [95], as already introduced in Sec. 7.2, coming from the interaction between the magnetic ion of the Molecular Nanomagnet and the nuclear spin bath in which the core is located [96]. A strategy to face it is required to create reliable quantum devices based on Molecular Nanomagnets.

Due to their intrinsic multi-level structure, qudits built on Molecular Nanomagnets are good candidates for the implementation of QEC: logical states $|0_L\rangle$ and $|1_L\rangle$ can be defined leveraging on multiple energy levels of the MNM. Errors acting on logical states have the effect to let the system leave the computational subspace formed by the logical states: errors can be detected and corrected if K-L conditions are satisfied. QEC codes implementation on two-level qubits (Sec. 1.5.2) is currently challenging, due to the need of a huge number of physical qubits to create logical qubits. Systems with more than

two levels can lower the hardware requirements, as $(2S+1)$ levels (instead of only 2) are available on each qudit.

In order to understand the form of the error operator E_k (see Sec. 1.3.1), we recall the Lindblad equation:

$$\frac{d\rho(t)}{dt} = \frac{1}{T_2}(2S_z\rho S_z - S_z^2\rho - \rho S_z^2) \tag{4.12}$$

its solution at a certain time t can be expanded as $\rho(t) = \sum_k E_k\rho(0)E_k^\dagger$ where E_k is the error operator

$$E_k = \sqrt{\frac{(2t/T_2)^2}{k!}}e^{-S_z^2 t/T_2}S_z^k \tag{4.13}$$

For small t/T_2, we notice that $E_k \propto S_z^k$: the first order error E_1 is $\propto S_z$, while higher powers become significant at longer times. Details are reported in the original work in Ref. [95]. The QEC is possible only if K-L conditions are satisfied for the E^k operators in Eq. 4.13, and thus for S_z^k operators, since they are proportional each other. K-L conditions can be condensed in the form:

$$\langle a_L|S_z^k|b_L\rangle = \beta_k\delta_{a,b} \tag{4.14}$$

where $a, b = 0, 1$, $0 \leq k \leq 2n$ and β_k is a coefficient. We describe here the code words $|0_L\rangle$ and $|1_L\rangle$ that can be used to implement QEC on molecular spin S qudits, as proposed in Ref. [95]. The conditions expressed in Eq. 4.14 are satisfied by the code words:

$$\begin{aligned}
|0_L\rangle &= \frac{1}{\sqrt{2^{2S-1}}}\sum_{k=1,\text{odd}}^{2S}\sqrt{\binom{2S}{k}}|k-S\rangle \\
|1_L\rangle &= \frac{1}{\sqrt{2^{2S-1}}}\sum_{k=0,\text{even}}^{2S}\sqrt{\binom{2S}{k}}|k-S\rangle
\end{aligned} \tag{4.15}$$

Demonstration of K-L conditions satisfaction

We here report the demonstration of how code words in Eq. 4.15 satisfy the K-L conditions [95]. For the first condition we have:

$$\langle 0_L|S_z^l|1_L\rangle = \langle 1_L|S_z^l|0_L\rangle \tag{4.16}$$

$|0_L\rangle$ and $|1_L\rangle$ are superposition of different sets of orthonormal states, not mixed by dephasing: the first condition is thus satisfied.

For the second condition we have:

$$\langle 1_L|S_z^l|1_L\rangle - \langle 0_L|S_z^l|0_L\rangle = \frac{1}{2^{2S-1}}\sum_{k=0}^{2S}(-1)^k\binom{2S}{k}\langle k-S|S_z^l|k-S\rangle = 0 \tag{4.17}$$

$$\frac{1}{2^{2S-1}}\sum_{k=0}^{2S}(-1)^k\binom{2S}{k}\langle k-S|S_z^l|k-S\rangle=\frac{1}{2^{2S-1}}\sum_{k=0}^{2S}(-1)^k\binom{2S}{k}(k-S)^l \tag{4.18}$$

recalling the binomial expansion $(1+x)^{2S}=\sum_{m=0}^{2S}\binom{2S}{m}x^m$ and with the assumption $l<2S$:

$$\sum_{m=0}^{2S}\binom{2S}{m}(-1)^m(m-S)^l=\left[\left(x\frac{d}{dx}\right)^l\sum_{m=0}^{2S}(-1)^m\binom{2S}{m}x^{m-S}\right]_{x=1} \tag{4.19}$$

and

$$\left[\left(x\frac{d}{dx}\right)^l\frac{1}{x^S}(1-x)^{2S}\right]_{x=1}=0 \tag{4.20}$$

Thus also the second condition is satisfied.
This demonstration is reported in details in Ref. [95].

■

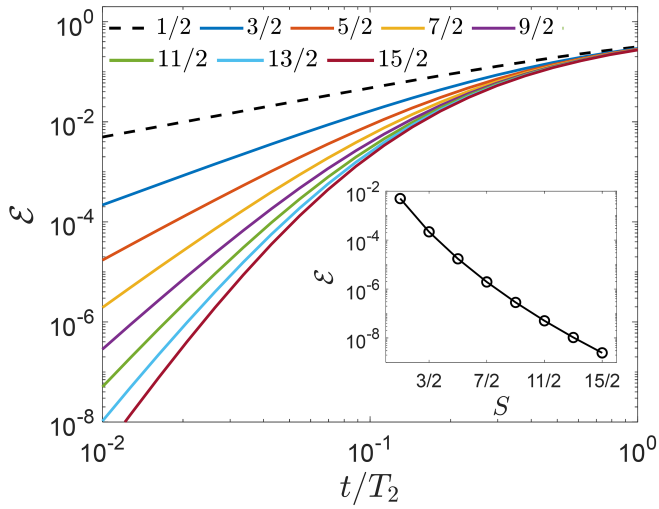

Figure 4.4: Error ε after QEC as a function of memory time t/T_2 for different S values. System is prepared in $|\psi(0)\rangle=(|0_L\rangle+|1_L\rangle)/\sqrt{2}$ superposition and its evolution is subject to decoherence (pure dephasing) for a certain time t/T_2. Inset: error ε decreases monotonically with the size of the qudit spin S, for a fixed $t/T_2=10^{-2}$. Reproduced from Ref. [47] with permission from the Royal Society of Chemistry (licensed under a Creative Commons Attribution-NonCommercial 3.0 Unported Licence).

Fig. 4.4 shows the error $\varepsilon=1-\langle\psi(0)|\rho(t)|\psi(0)\rangle$ occurring on a logically encoded state $|\psi(0)\rangle=(|0_L\rangle+|1_L\rangle)/\sqrt{2}$ as a function of a *memory time* t/T_2 (described in Sec. 8.3.2): the capacity of the QEC code increases with the size of the spin of the involved Molecular

Nanomagnet. We also noticed that, for a fixed t/T_2, the error decreases monotonically by increasing S. Lastly, it is worth noticing that code words in Eq. 4.15 work for powers of S_z up to $2S-1$: K-L conditions must be satisfied for powers of S_z up to $2n$ (Eq. 4.14) to correct to the order $(\gamma t)^n$. To be able to detect and correct n different errors, we thus would need to use a spin system with $2(n+1)$ addressable levels.

4.5.1 Embedding QEC into MNMs qudits

As reported in Chap. 1, Quantum Error Correction is based on encoding logical qubit states using multiple physical qubits. It is possible for example to implement the above mentioned code on a spin S with an ancillary spin $S = 1/2$ for error detection.

It has been shown that a class of molecules with the following Hamiltonian:

$$\mathcal{H} = g_z \mu B S_z + g_z^a \mu_B B \sigma_z^a + D S_z^2 + \mathbf{S} \cdot \mathbf{\Gamma} \cdot \sigma^{\mathbf{a}} \tag{4.21}$$

can be used to embed error protected states in the S qudit spin and to detect errors using the ancilla qubit σ^a. Hamiltonian in Eq. 4.21 recalls the above introduced in Eq. 4.2, and is composed by two Zeeman interaction terms, a single-ion anisotropic term, and a weak exchange (hyperfine) ancilla-qudit coupling; a practical implementation of such class of molecules is by exploiting compounds with a single magnetic ion with a nuclear spin S interacting with an electronic spin $1/2$, or also using two electronic spins, the first spin S and the second spin $S = 1/2$ (or an effective spin $1/2$, using compounds with spin $S > 1/2$ but using only 2 levels). Using the error operators introduced in Eq. 4.13 and implementing the code words reported in Eq. 4.15, it is possible to implement proper error correction codes [95].

Results of the implementation of this error correction code on realistic molecular compounds are reported on Chap. 8.

Part III

Simulation of physical systems on IBM Quantum

CHAPTER 5

Simulation of static and dynamic properties of Magnetic Molecules

Simulating static and dynamic properties of spin systems can be very challenging for classical computers when increasing the system size in terms of number of spins; Quantum Computers have an advantage above classical computers for their intrinsic nature that fits well to describe systems such as anti-ferromagnetic spin chains and rings. Prototype Quantum Computers, in particular IBM Quantum systems up to QV 32 and 7 qubits, are here exploited to perform simulations and real hardware runs on small-sized spin systems, with the help of proper error mitigation techniques on finite-size spin systems. The systems studied are Molecular Nanomagnets, finite-size spin systems, here explored as test-beds for the current generation of Quantum Computers. Such systems are also very interesting for fundamental phenomena investigation. Moreover, they are very interesting for their technological applications to implement new approaches to quantum computation (see Chap. 4, and Chap. 7) and for QEC (see Chap. 8): being able to explore all their static and dynamic properties will be very useful to better understand their technological potential.

Quantum Computers, and in particular their application to Quantum Simulation and Variational Algorithms as described in Chap. 1, can simulate the static and dynamic properties of the target system handling linearly the scaling of computational resources with the size of the target system [97]. The potential applications in physics and chemistry fields are thus very interesting. As already introduced in Chap. 2, there are many different technologies available, each one with its own features: the most promising ones for Quantum Simulation and for the implementation of Variational Algorithms are the superconducting [98][99] and the ion trap platforms [100]. In the last few years, the size and quality of such platform have seen a quick rise [19], together with the development of error mitigation techniques [101][97]. The devices used in this work, IBM Quantum systems, have been upgraded several times from mid 2020 to mid 2021 in terms of available chips, Quantum Volume and number of qubits: we had the possibility to use better devices over time, and using Qiskit simulators to simulate the technological evolution in terms of device noise rate.

We study here two classes of MNMs: anti-ferromagnetic open chains with open boundary conditions [102], and closed rings with closed (periodic) boundary conditions [103][104], both composed by spins $S = 1/2$; we are using these systems as ideal test-

beds for IBM Quantum superconducting devices [99], that can be hard to simulate classically by increasing the size [97]. As the publicly available systems are limited in terms of qubits number, we will evaluate systems with up to 6 spins, but with a theoretically scalable approach to larger systems. Further investigations can be performed on $S = 1$ systems, properly mapped on pairs of qubits.

We exploit the Variational Quantum Eigensolver (VQE) [105][106], a method part of the class of Variational Quantum Algorithms (VQA) [107][108], to find the ground state. Different approaches are put forward to apply VQE to explore the ground state of the target MNMs, mainly due to the high level of entanglement: we leverage on an heuristic approach, where the exploited quantum gates reflect the chip topology and characteristics instead of the target model properties, and also on a physically motivated approach, that exploits system's symmetries and properties of the target Hamiltonian. Dynamic properties of target MNMs are also investigated, in particular the dynamic spin-spin correlation functions, with a Digital Quantum Simulation of the system time evolution [109].

5.1 Introduction to Variational Quantum Algorithms

The Variational Quantum Algorithm (VQA) methods are a very useful near-term class of algorithms that can be used in many fields, from spin systems [106] to optimization [110] and machine learning [111]; NISQ devices are able to implement such algorithms as they require rather simple (small-depth) circuits with a limited amount of qubits. VQA algorithms are in general called "hybrid quantum-classical" algorithms, as they consist of a quantum-computed part and by a classical counterpart. In order to explain how this class of algorithms work, considering also the Variational Quantum Eigensolver (VQE), several theorem must be introduced.

5.1.1 Variational theorem

The variational method is a way to estimate the energy of the ground state (GS) of a physical system; it can also be applied to compute the energy of some excited states. This method is based on the variational principle stating that, for a given Hamiltonian, its expectation value on a $|\psi\rangle$ state is always greater (or equal) to the energy of the GS. The variational method has been developed basically to solve problems where the perturbative theory can not be applied. The outcome of the variational method applied to the GS of a system is an approximation of the energy E_0 and the state $|0\rangle$, respectively the eigenvalue and the relative eigenvector. The variational theorem [112] states that the computed energy is always approximated upwards:

$$\langle H \rangle \equiv \frac{\langle \psi(\vec{\theta}) | H | \psi(\vec{\theta}) \rangle}{\langle \psi(\vec{\theta}) | \psi(\vec{\theta}) \rangle} \tag{5.1}$$

$$\langle H \rangle \geq E_0 \tag{5.2}$$

It is possible to demonstrate the variational theorem in the following way. We decompose $|\psi\rangle$ into the basis of H eigenvectors:

$$|\psi(\vec{\theta})\rangle = \sum_{k=0}^{\infty} |k\rangle\langle k|\psi(\vec{\theta})\rangle \tag{5.3}$$

and using the definition of eigenvector and eigenstate $H|k\rangle = E_k|k\rangle$

$$\begin{aligned} \langle H\rangle &= \frac{\sum_{k=0}^{\infty} |\langle k|\psi(\vec{\theta})\rangle|^2 E_k}{|\langle k|\psi(\vec{\theta})\rangle|^2} \\ &= \frac{\sum_{k=0}^{\infty} |\langle k|\psi(\vec{\theta})\rangle|^2 (E_k - E_0)}{|\langle k|\psi(\vec{\theta})\rangle|^2} + E_0 \\ &\geq E_0 \end{aligned} \tag{5.4}$$

we find that, as $(E_k - E_0) \geq 0$, $\langle H\rangle \geq E_0$.

■

These quantities are computed recursively: an initial parametric ansatz defining the eigenstate $|\psi(\vec{\theta})\rangle$ is used to compute the eigenvalue (the energy), then an optimization is performed to minimize the energy, finding the related parameters $\vec{\theta}$.

5.1.2 Hellmann-Feynman theorem

Another foundational theorem that can be used for the computation of the observables is the Hellmann-Feynman theorem. It relates the energy derivative with respect to a certain parameter λ to the expectation value of the Hamiltonian derivative with respect to the same parameter.

$$\frac{\partial E_\lambda}{\partial \lambda} = \left\langle \psi_\lambda \middle| \frac{\partial \hat{H}_\lambda}{\partial \lambda} \middle| \psi_\lambda \right\rangle \tag{5.5}$$

where $\hat{H}_\lambda$ is the Hamiltonian depending on a certain parameter λ, $|\psi_\lambda\rangle$ is an eigenstate of the Hamiltonian (depending on the same parameter) and E_λ is the related eigenvalue. It is possible to simply proof this theorem:

$$\begin{aligned} \frac{\partial E_\lambda}{\partial \lambda} &= \frac{\partial}{\partial \lambda}\langle \psi_\lambda|\hat{H}_\lambda|\psi_\lambda\rangle \\ &= \left\langle \frac{\partial \psi_\lambda}{\partial \lambda} \middle| \hat{H}_\lambda \middle| \psi_\lambda \right\rangle + \left\langle \psi_\lambda \middle| \hat{H}_\lambda \middle| \frac{\partial \psi_\lambda}{\partial \lambda} \right\rangle + \left\langle \psi_\lambda \middle| \frac{\partial \hat{H}_\lambda}{\partial \lambda} \middle| \psi_\lambda \right\rangle \\ &= E_\lambda \left\langle \frac{\partial \psi_\lambda}{\partial \lambda} \middle| \psi_\lambda \right\rangle + E_\lambda \left\langle \psi_\lambda \middle| \frac{\partial \psi_\lambda}{\partial \lambda} \right\rangle + \left\langle \psi_\lambda \middle| \frac{\partial \hat{H}_\lambda}{\partial \lambda} \middle| \psi_\lambda \right\rangle \\ &= E_\lambda \frac{\partial \langle \psi_\lambda|\psi_\lambda\rangle}{\partial \lambda} + \left\langle \psi_\lambda \middle| \frac{\partial \hat{H}_\lambda}{\partial \lambda} \middle| \psi_\lambda \right\rangle \\ &= \left\langle \psi_\lambda \middle| \frac{\partial \hat{H}_\lambda}{\partial \lambda} \middle| \psi_\lambda \right\rangle \end{aligned} \tag{5.6}$$

as $\langle \psi_\lambda|\psi_\lambda\rangle = 1$, so its derivative with respect to λ is equal to 0.

■

5.2 The VQE algorithm

The Variational Quantum Eigensolver algorithm [105] is based on the variational theorem and allows one to obtain, when applied to physics systems, an approximation of the the energy of the ground state. It is an hybrid algorithm, as demands to a quantum computer all the operations whose cost increases exponentially on a classical computer, while retaining on a classical computer the optimization process. In the following subsections, all the steps of the VQE algorithm are introduced.

The VQE approach is based on an hybrid calculation that consists in the approximation of the exact target Hamiltonian ground state $|\psi_0\rangle$ with the construction of a parametrized quantum state $|\psi(\vec{\theta})\rangle$, whose E expectation value $\langle\mathcal{H}\rangle_\theta = \langle\psi(\vec{\theta})|\mathcal{H}|\psi(\vec{\theta})\rangle$, obtained measuring the quantum states on a QC, is minimized by a classical optimizer.

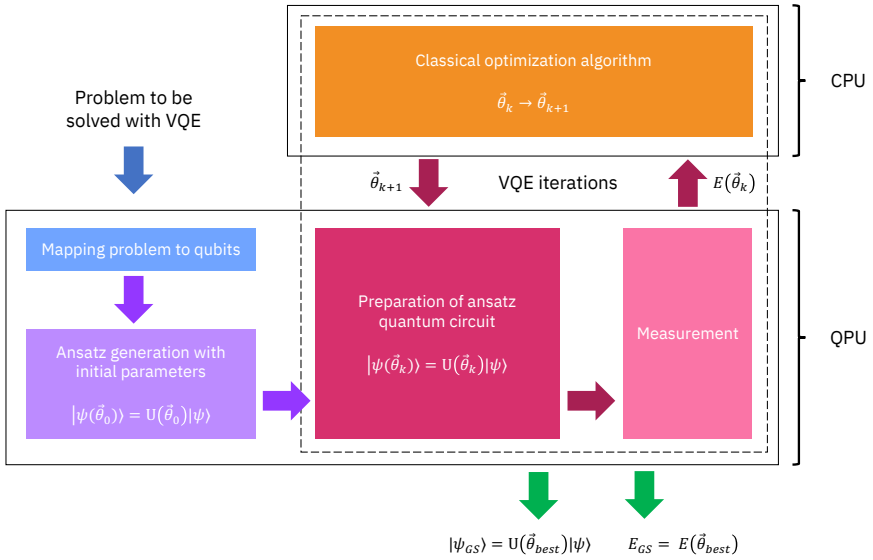

Figure 5.1: VQE process flow.

5.2.1 Quantum part

The first part of the VQE process is performed on a QPU (Quantum Processing Unit), and it consists of the encoding of the target Hamiltonian into an *operator* function and the creation of a *variational ansatz* via a sequence of quantum gates. The operator, namely the encoded Hamiltonian of the target system, is created by mapping the problem on the qubit topology: in case of systems made by spin $1/2$ objects, the mapping is quite trivial, as qubits themselves are spin $1/2$ objects. Details of the encoding method are reported in Sec. 5.3.1, taking advantage of the first explorative model studied.

The trial waveform, or the variational ansatz, contains a set of parameters $\vec{\theta}_k$, which number impacts on the performances of the VQE itself: these parameters are continu-

ously updated to minimize the energy of the system using the operator (the encoded Hamiltonian), obtaining at the end a set of parameters that, applied to the ansatz, represent the ground state itself. It is crucial to build the ansatz with the right amount of parameters: on the one hand, a number of parameters increasing polynomially with the system size can be computed efficiently on the QC; on the other hand, a limited set of parameters allow the ansatz to explore only a subset of the whole Hilbert space in which the problem lies. It is worth noting that, in principle, the exploration of the whole Hilbert space is possible using many parameters; however, the classical optimization process would fail, making this approach impracticable. The objective of a good ansatz building strategy is to select the relevant Hilbert space to be spanned with the right set of variational parameters. The estimation of the target Hamiltonian energy on the $|\psi(\vec{\theta})\rangle$ is then performed by measuring $\langle\mathcal{H}\rangle_\theta$.

5.2.2 Classical part

The parametrized wavefunction is then sent to a classical optimizer that minimizes the energy, obtaining a new set of parameters θ'. This new set is then used to build a new parametrized wavefunction by the Quantum part of the algorithm. The subsequent iteration of this method is required until reaching a proper convergence, where $|\psi(\theta_{opt})\rangle \simeq |\psi_0\rangle$. The classical optimization algorithms have been widely studied and developed, and a lot of literature is present [105][113]. In this work, two algorithms have been exploited: COBYLA (*Constrained Optimization By Linear Approximation*) [114] and SPSA (*Simultaneous Perturbation Stochastic Approximation*) [115].

The first one is a gradient-based algorithm, and can be initialized with three parameters: the maximum number of optimizing iterations, the tolerance of the optimization approximation, and the length of the parameters optimization steps.

The second one is a stochastic algorithm based only on the measurements of the cost function to determine the next optimization steps. This algorithm is not gradient-based, so a tolerance is not included in the parameters; it will continue optimizing until reaching the maximum number of iterations set. It is consequently more costly from a computational resources point of view; however, its stochastic nature makes it more robust when dealing with quantum noise and with the measurement statistics.

5.2.3 Computation of observables of interest

The computation of the physical quantities can be performed in two ways. The first one is leveraging directly on VQE outcomes, measuring the expectation value using the ansatz with the optimized parameters. The second method is based on the Hellmann-Feynman theorem (Eq. 5.5): observables can be obtained by deriving the energy with respect to the proper parameter.

In the next Sections, we make use of the VQE algorithm to compute physical properties of several spin systems.

5.3 Study of spin $1/2$ Heisenberg chains Ground State properties

We investigate several different systems, from 2 up to 6 spin $1/2$, in order to simulate their static properties: in the considered systems, the dominant interaction linking the spins on chains and rings is the Heisenberg interaction, with an uniform strength J and an uniform external magnetic field B. To study the static GS properties of these systems, we build the variational ansatz, introduced in Sec. 5.2.1, using two different approaches.

- **Heuristic approach**: the simplest way to implement the ansatz is following an hardware heuristic approach, in which no information about the physical system under investigation is required. The ansatz is built via a sequence of standard parametrized rotations and entanglement blocks, organized in layers. Usually, single qubit rotation gates, containing the variational parameter as rotation angle, and CNOT gates to create entanglement, are the only needed ingredients. A possible choice is to leverage on the single-qubit rotation implemented using the general U_3 gate, represented by the form:

$$U_3(\theta, \phi, \lambda) = \begin{pmatrix} \cos(\theta/2) & -e^{i\lambda}\sin(\theta/2) \\ e^{i\phi}\sin(\theta/2) & e^{i(\lambda+\phi)}\cos(\theta/2) \end{pmatrix} \tag{5.7}$$

  An hardware heuristic ansatz takes into account the hardware features and topology: as a knowledge of the target system is not required, entanglement is created by putting CNOT gates on the required positions in a flexible way, leaving to the transpiler to adapt them on the hardware configuration, i.e. adding SWAP gates considering the coupling map (see Fig. 3.7). An heuristic ansatz is usually built by concatenating a certain amount of layers, consisting of a set of rotations (with embedded variational parameters) and two-qudits entangling gates. Although its high flexibility and adaptivity, HA are unaware of the actual Hamiltonian of the system, usually having the need to implement an high number of layers (thus variational parameters) to be able to converge to the optimal solution: an higher number of parameters implies a difficult optimization process, increasing the chance to fall into local minima [116].

- **Physically motivated approach**: this ansatz building technique takes into account the properties and symmetries of the system's Hamiltonian. This ansatz class lies on methods and techniques able in theory to better approximate the quantum state, obtaining better results overall. An example of PMA is the Unitary Coupled Cluster (UCC) ansatz [113][117].

5.3.1 Test model: spin $1/2$ Heisenberg dimer

Before starting to investigate different spin configuration for MNMs, I contributed to perform an initial test of the methods and techniques on a simpler model, consisting of a 2 spins $1/2$ chain with Heisenberg interaction and an external field along z. This model is characterized by an energy levels crossing as a function of B, ideally dividing in two regions: the low field and the high field regions. The Hamiltonian is reported in Eq. 5.8.

$$\begin{aligned}\mathcal{H} = J_1(\sigma_x \otimes \sigma_x) + J_2(\sigma_y \otimes \sigma_y) + J_3(\sigma_z \otimes \sigma_z) \\ +B\left[\cos\theta(\sigma_z \oplus \sigma_z) + \sin\theta(\sigma_x \oplus \sigma_x)\right]\end{aligned} \tag{5.8}$$

In order to implement the VQE algorithm to be able to get the GS properties of the target system, we need to first encode the system Hamiltonian on the qubits. A variational ansatz (i.e. a parametrized trial wavefunction) is then varied by the classical optimizer, with the objective to get the minimum expectation value of the input Hamiltonian. The Hamiltonian in Eq. 5.8 can be, for example, traduced into an input *operator* for VQE by leveraging on Qiskit Operators [118], representing the Pauli matrices (taking into account the normalizing factor). The obtained result is then:

$$\begin{aligned}\hat{H}_{op}^{(dimer)} = J_1(X \otimes X) + J_2(Y \otimes Y) + J_3(Z \otimes Z) \\ +B_z(Z \otimes I + I \otimes Z) + B_x(X \otimes I + I \otimes X)\end{aligned} \tag{5.9}$$

where X, Y and Z are the Qiskit Operators, and the magnetic field is acting on the xz plane, with B_z and B_x its components along respectively the z and the x axes. It is worth noting that, since the studied systems are composed by $S = 1/2$, it is possible to natively encode the Hamiltonian on the spin $1/2$ qubits: an interaction between two spins is mapped on the quantum chip as an interaction between two qubits. Details on the actual implementation of $X \otimes X$ and similar gates are reported in App. A.

We test the heuristic ansatz approach on this simple system in order to compute GS energy, where the Hamiltonian is isotropic ($J_1 = J_2 = J_3 = J$); the HA is composed by R_y and R_z, with a simple CNOT entanglement layer.

We also apply and test several error mitigation techniques on noisy simulations, in particular the Qiskit Measurement Error Mitigation [119] and the Zero-Noise Extrapolation [120][24], together with performing multiple VQE calculations keeping the best result for each point.

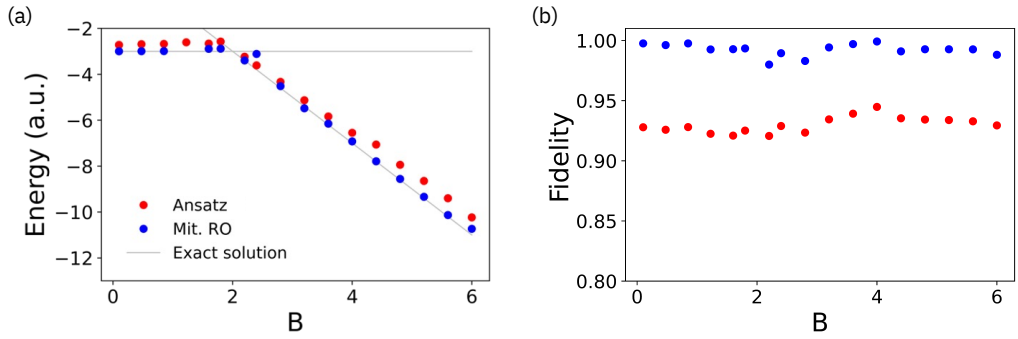

Figure 5.2: Results of VQE noisy simulations with HA approach for Measurement Error Mitigation. (a) Effect of Measurement Error Mitigation for the mitigation of Readout error (RO). (b) Corresponding state fidelity.

In Fig. 5.2 and Fig. 5.3 the results of the VQE noisy simulations for the target model are reported, with different noise source active, leveraging on Qiskit features [121], and

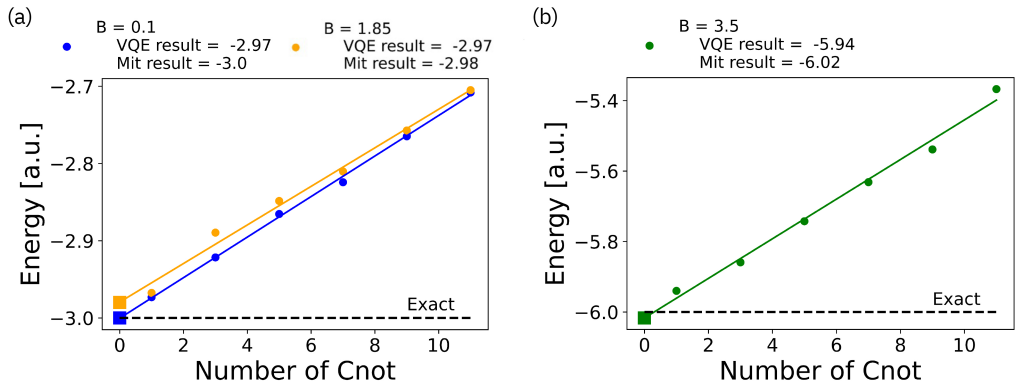

Figure 5.3: Results of VQE noisy simulations with HA approach for Zero-Noise Extrapolation. Squared markers: extrapolated zero-noise result. (a) Effect of ZNE for the Gates Error in low field region. (b) Effect of ZNE for the Gates Error in intermediate field region.

based on QV 8 IBM Quantum chips. In Fig. 5.2(a), only the Readout Error is active: due to the simplicity of the model, an heuristic approach is able to reconstruct well the GS, however the application of the Measurement Error Mitigation is able to further improve the results, almost completely correcting the data. A significant improvement on state fidelity is evident in Fig. 5.2(b).

In Fig. 5.3, only the Gates Error is active: the Zero-Noise Extrapolation technique is applied by recursively increasing the number of involved CNOTs in the variational ansatz, leaving unchanged the circuit outcome, and assuming a linear increment of the noise. We are able to extract the energy by performing a linear fit of the data series, in this case for some different B values on low and intermediate field regions. The squared mark on each data series represents the extrapolated zero-noise value for the relative GS energy.

The VQE approach, together with the two main error mitigation techniques, is thus validated and ready to be used for more complex systems. It is worth noting that the ZNE is quite demanding in terms of computation, as it requires several VQE runs by incrementing ansatz depth, to extrapolate the exact value for a single point; moreover it is applicable only in presence of low noise rate, due to the need of linear increasing errors. So, this technique will not be used for complex systems, but can still represent a possible improvement on the results.

5.3.2 Four spins $1/2$ Heisenberg closed ring

We now consider as target system a chain of spin $1/2$, with the following Hamiltonian:

$$\mathcal{H} = 2J \sum_i \vec{s}_i \cdot \vec{s}_{i+1} + B \sum_{i=1}^{N} s_i^z \tag{5.10}$$

where s_i^α are spin $1/2$ operators and the magnetic field is along z axis. In the following sections the results are reported for the different systems studied, in terms of number

of spins and open or closed boundary conditions. VQE noiseless and noisy simulations are performed on IBM Quantum devices and simulators with Qiskit.

The first studied system is a MNM composed by four $S = 1/2$ spins in a closed ring, arranged in a squared shape. The general target Hamiltonian in Eq. 5.10 (isotropic) is completed with the proper boundary conditions, assumed to be periodic; the following commutation relations are thus valid: $[\mathcal{H}, S^2] = 0$ and $[\mathcal{H}, S_z] = 0$. This implies that the Hamiltonian eigenstates can be related to the quantum numbers S (associated to the total spin $\vec{S} = \sum_i \vec{s}_i$) and $m = -S, -S+1, ..., S$ (associated to the projection of S along z axis).

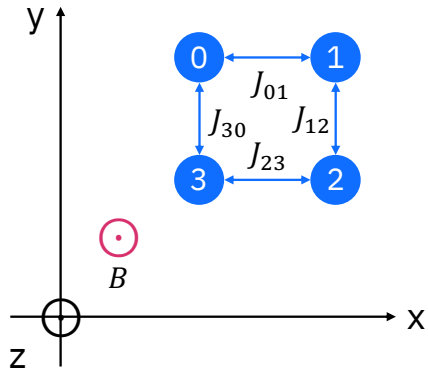

The exact solution of the ground state is characterized by several crossings, which identify several different regions corresponding to $S = 0, 1, 2$ and $m = -S$. In order to implement the VQE, we focus our search on low and intermediate external magnetic field conditions, since for high B all the spins are known to be aligned in a factorized ground state $|\downarrow\downarrow ... \downarrow\rangle$.

Hamiltonian encoding

Hamiltonian in Eq. 5.10 of this 4 sites closed chain can be encoded on the spin $1/2$ qubits following the same approach introduced in Eq. 5.9. It is possible to build the following operator, introducing the general notation $MM...M = M \otimes M \otimes ... \otimes M$ (used from here onward):

$$\begin{aligned} \hat{H}_{op}^{(4\ closed)} = & J_z(ZZII + IZZI + IIZZ + ZIIZ) \\ & + J_y(YYII + IYYI + IIYY + YIIY) \\ & + J_x(XXII + IXXI + IIXX + XIIX) \\ & + B(ZIII + IZII + IIZI + IIIZ) \end{aligned} \tag{5.11}$$

where, as stated, the B field is acting only on the z axis, and we assume $J_{\alpha_{01}} = J_{\alpha_{12}} = J_{\alpha_{23}} = J_{\alpha_{30}}$ (where $\alpha = x, y, z$). It is possible to notice the application of periodic boundary conditions, as the Hamiltonian is representing a closed chain, in the latter element of the first three lines of Eq. 5.11.

Construction of the variational ansatz

As introduced in Sec. 5.3, both hardware heuristic (HA) and physically motivated (PMA) approaches are put in place to build the variational ansatz.

For the HA approach, the building blocks of the ansatz are composed by the structure depicted in Fig. 5.4, and built as:

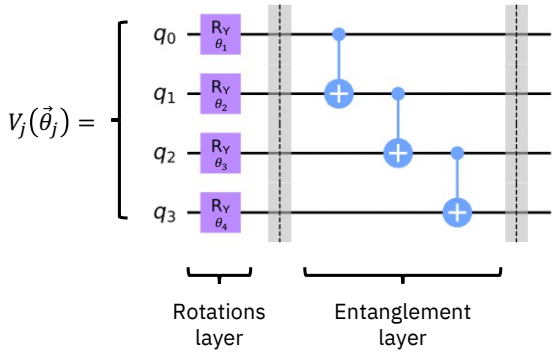

Figure 5.4: Single layer of hardware heuristic ansatz for a 4 spins closed chain, consisting of a single block of parametrized rotations and a linear entanglement pattern.

$$U_{HA}(\vec{\theta}) = \prod_{j=1}^{L} V_j(\vec{\theta}_j) \tag{5.12}$$

Since the target Hamiltonian in Eq. 5.10 is real and symmetric, also the GS wavefunction is real: we can then make use of R_y rotations, specializing the form in Eq. 5.7, avoiding ϕ and λ parameters (controlling relative phases), obtaining $R_y(\theta) = U_3(\theta, 0, 0)$. Considering the target hardware linear coupling map that will be simulated, the entangling layer consists of CNOT gates connecting only the nearest neighbouring qubits. It is worth noting that, although the Heisenberg chain considered is a closed ring, the entanglement layer is not composed by a closed configuration (i.e. there is no entanglement between qubit 3 and qubit 0): this is done to optimize the number of CNOTs involved while preserving a sufficient reconstruction precision of the GS, as the heuristic ansatz approach lies on the fitting of the circuit on the considered hardware, which has a linear connectivity. A final layer of $R_y(\theta)$ rotations is put at the end of the ansatz circuit.

For the above introduced PMA approach, we know that the target Hamiltonian in Eq. 5.10 has well defined S and m, total spin quantum numbers: this property allows to explore only a subspace of the entire Hilbert space by initializing the ansatz with a well defined S and m, while implementing only parametrized rotations that preserve the symmetries of the system [122][123]. In this case, the initial state could have the form:

$$W_{ij}(\theta) = e^{-i\theta \mathbf{s}_i \cdot \mathbf{s}_j} \tag{5.13}$$

This operation is the so called eSWAP [122][123], preserving S and m. The implementation of this eSWAP operation using quantum gates is depicted in Fig. 5.5 [122][14].

Hence, an eSWAP preserving S and m values following the form in Eq. 5.13 can be implemented with the circuit reported in Fig. 5.5(a). The resulting physically motivated ansatz (PMA) layer can be built alternating the circuit blocks of Eq. 5.13. The circuit depth can be reduced by implementing in parallel operations not sharing common qubits, implementing a $V_k(\vec{\theta}_k)$ circuit block (Fig. 5.5(b). The nearest neighbours

connectivity applied on the HA is suitable also for the PMA. The overall PMA ansatz is then built, in general, with several layers:

$$U_{PMA}(\vec{\theta}) = \prod_{k=1}^{K} V_k(\vec{\theta}_k) \tag{5.14}$$

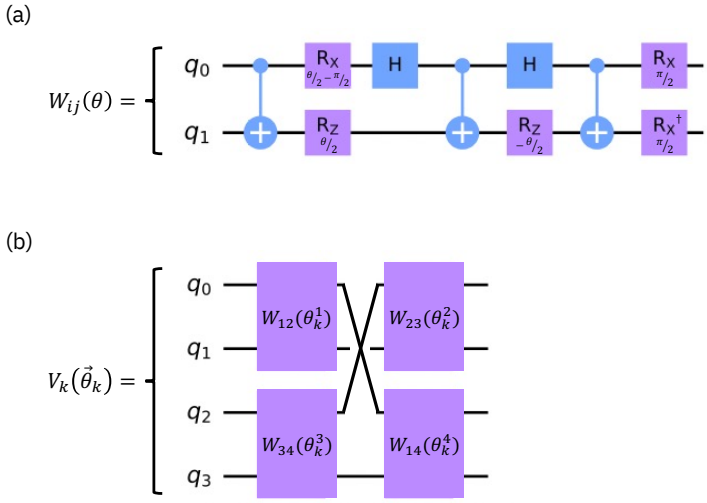

Figure 5.5: (a) Physically motivated ansatz building block with 1 parameter, preserving S and m quantum numbers. (b) PMA ansatz layer with 4 parameters, built by composing 4 ansatz blocks.

$U_{PMA}(\vec{\theta})$ preserves S and m: hence, so a proper initialization of the qubit states is required, respecting the symmetries of the GS for the different regions corresponding to $S = 0, 1, 2, ...$ and $m = -S$.

Initialisation of the ansatz

Ansatz initialisations depending by the B field region are prepended to the ansatz circuit, where the qubits are initially set to $|0\rangle$. In the following list there are examples of possible ansatz initialisations.

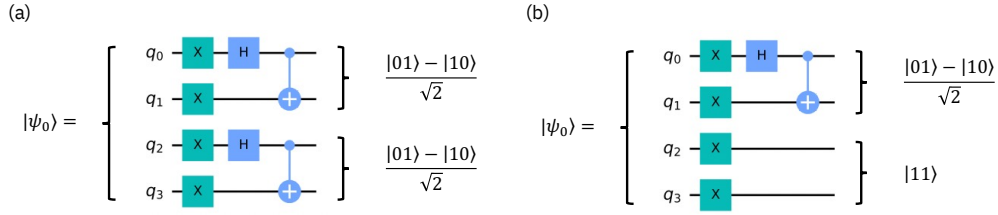

Figure 5.6: PMA initialisation, 4 spins: (a) low B ($S = 0, m = 0$ region), (b) intermediate B ($S = 1$, $m = -1$ region).

- Low B (before the first crossing): for even-numbered spin $1/2$ open or closed chains with anti-ferromagnetic interactions, the S is minimized [104], so the GS has $S = 0$ and $m = 0$. For this region, initialization is then reported in Fig. 5.6(a) [122]. This state is called *resonating-valence-bond* (RVB) [123][124][125], and it is one of the possible choices to obtain a $S = 0$ state.

- Intermediate B (after the first crossing): the ground state becomes $S = 1$, $m = -1$ due to the Zeeman contribution to the Hamiltonian. For this region, initialization is then reported in Fig. 5.6(b): we start from $S = 0$ and we change one of the pairs to $S = 1$.

- High B: the Zeeman contribution dominates, so the GS becomes ferromagnetic ($|\downarrow\downarrow\downarrow\downarrow\rangle$). For this region, initialisation is done by setting all qubits to $|1\rangle$ with an array of X gates.

The parametrized wavefunction is then:

$$|\psi(\vec{\theta})\rangle = U_{PMA}(\vec{\theta})|\psi_0\rangle \tag{5.15}$$

It is worth noting that the initial states reported in Fig. 5.6, in case of closed chain (periodic boundary conditions), break the spatial symmetry of the target system (Fig. 5.3.3), together with the $U_{PMA}(\vec{\theta})$ having four independent variational parameters, one for each bond: this asymmetry could lower the performance of the ansatz itself in the VQE calculation, leading to an increment of optimization cycles required. Although results show a good recovery of the symmetry with the proposed ansatz, improvements can be achieved by changing the order of the building blocks of Fig. 5.5(b), applying first the block on the bond connecting the local singlet (for low B) or triplet (for higher B): this approach balances the initial state structure, making the recovering of the symmetry faster. Circuit depicted in Fig. 5.5(b) becomes, in the correct order, $W_{23}(\theta_k^1)$, $W_{14}(\theta_k^3)$, then $W_{12}(\theta_k^2)$ and $W_{34}(\theta_k^4)$.

Noiseless statevector VQE results

Here we report the results of the numerical simulation of the VQE process performed with Qiskit `statevector_simulator` [126], to which I contributed by helping to define VQE parameters. This process is done by performing direct matrix multiplication evaluating the results of the quantum circuits and using COBYLA [114] as classical optimizer.

The heuristic ansatz (HA) results, corresponding to dark green dots in Fig. 5.7(a), are in good accordance with the exact ground state solution. At low field, 3 layers (16 parameters and 9 CNOT gates) are required, due to an higher entanglement when Heisenberg interaction is dominant; at intermediate field, only 2 layers (12 parameters and 6 CNOTS) are sufficient to exactly reconstruct the GS. The PMA results, corresponding to light green stars, are still in good agreement with the exact GS solution, while requiring only 1 layer (with 4 parameters and 12 CNOTs, some of them parallelisable leading to a total of 6 CNOTs) for both low and intermediate field regions.

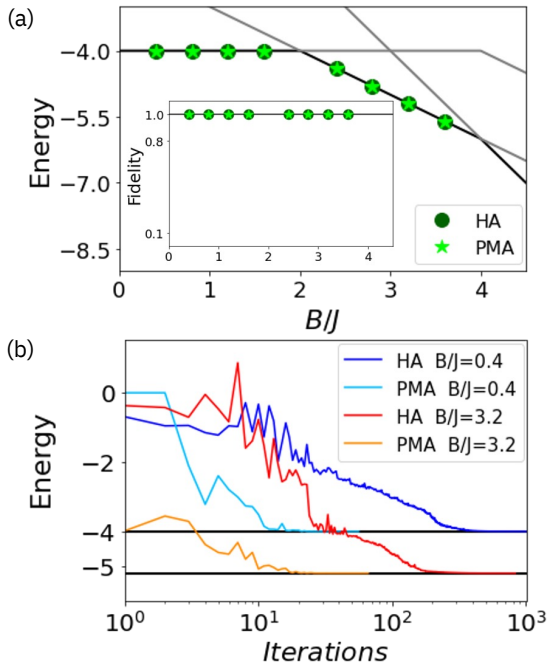

Figure 5.7: Statevector simulations of 4 sites spin closed ring. (a) GS energy. Inset: corresponding fidelity. (b) VQE energy convergence. Reproduced from Ref. [127] with permission from MDPI (open access article distributed under the terms and conditions of the Creative Commons Attribution (CC BY 4.0) license Creative Commons).

Each computed point represents the minimal achieved energy from 5 independent VQE runs with random initial parameters. The Fig. 5.7(a) inset is the state fidelity of each point relative to the exact GS solution (black solid line). In Fig. 5.7(b) the computed energies as a function of the VQE iteration are reported, for two different B/J points on the two regions of interest (low and intermediate field), showing the convergence to the two exact solutions (black solid lines): despite having a similar number of gates involved, PMA shows much faster convergence rather than HA, due to the lower number of variational parameters involved. Increasing the number of layers (thus the number of parameters and of quantum gates involved) leads to better results; however, ah high number of parameters makes impractical the classical optimization, while an high number of quantum gates makes very noisy the execution, especially on the near-term quantum devices used.

Noisy VQE simulation results

In the previous section we presented the results regarding ansatzes performances in absence of noise. In the NISQ era, a crucial point is to verify the robustness and the performances of the defined strategy in presence of realistic quantum noise. Here we simulate the VQE process using Qiskit noisy simulators with realistic noise models, representing the mid-term status of the available quantum technology, especially IBM Quantum

devices. As introduced in Sec. 1.3, the expected errors of currently available devices are:

- incoherent errors like thermal relaxation (T_1) time and coherence (T_2) time of the qubits, with the effect of amplitude damping and phase damping;
- gate errors of single-qubit and two-qubit gates, due to systematic (coherent) error on the implementation of the gates themselves, and due to other incoherent errors such as depolarizing error;
- measurement (readout) error, due to an imperfect measurement process.

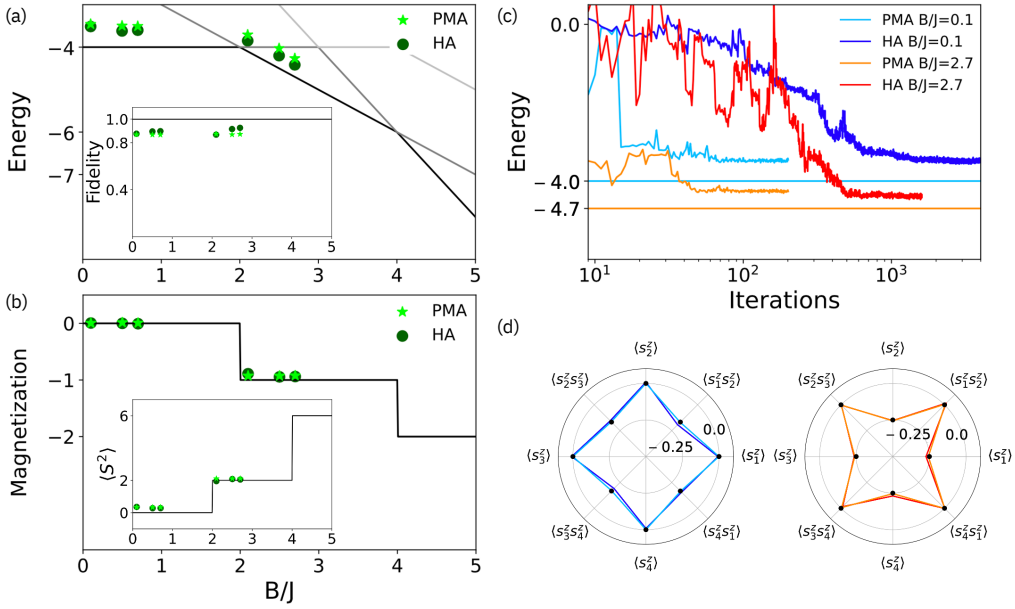

Figure 5.8: Noisy simulations of 4 sites spin closed ring. (a) GS energy, both HA and PMA are able to reconstruct well the expected results. Inset: corresponding fidelity. (b) Expectation value of magnetization and total spin S^2: both ansatz perform well to reconstruct GS observables. (c) VQE convergence, showing that PMA is able to let the optimization process to converge quicker. (d) Expectation values of the local one- and two-body spin operators. Reproduced from Ref. [127] with permission from MDPI (open access article distributed under the terms and conditions of the Creative Commons Attribution (CC BY 4.0) license Creative Commons).

The main effect of noise on VQE calculations is lowering the precision of the estimation of the observables, in this case the ground state energy; moreover, also the optimization process itself is affected by the effect of noise, increasing the number of iterations required to reach convergence [128].

In Fig. 5.8 we report the VQE results simulated with Qiskit `qasm_simulator` [119], considering the custom noise rates reported in Table 5.1, derived from IBM Quantum `ibmq_kolkata` chip (QV 128) in early 2021. SPSA optimizer [129] is used for all noisy

simulations, as its stochastic approach is more effective in presence of fluctuations of the observables due to the noise. Qiskit Measurement Error Mitigation technique [119], already introduced in Sec. 1.4, is applied to improve the results by correcting the readout error [130], increasing the accuracy of the observables evaluation. In Fig. 5.8(a) we report the GS energies in the low and intermediate field regions: both HA and PMA are able to reconstruct well the observable, together with an high state fidelity, averaged around 0.9. In Fig. 5.8(b) are reported the other two GS global observables: the expectation value of the magnetization along z axis $M = \sum_i S_z$ and the expectation value of the total spin S^2. Despite the presence of noise, the GS energy and both the expectation values of magnetization and total spin are well reconstructed.

The effect of the noise is clearly visible in Fig. 5.8(c): VQE struggles to converge to the right value of the GS energy (solid lines), here reported for two different B/J values, each one in a region of interest (low and intermediate field). It is also worth noting that convergence is reached with an higher number of iterations, in particular $\sim 10^2$ for the PMA (respect to $\sim 10^1$ in the noiseless statevector case, as reported in Fig. 5.7(b)) and $> 10^3$ for the HA (respect to $> 10^2$ in the noiseless statevector case). The physically motivated approach is thus much faster than the heuristic approach. In Fig. 5.8(d) we report two local observables, i.e. the expectation value of s_i^z and $s_i^z s_{i+1}^z$: the black dots indicate the exact solution, hence both ansatzes are able to reconstruct well the correct translational invariance of the model.

T_1	135 μs
T_2	125 μs
Single-qubit Gate Error	$\sim 2.5 \times 10^{-4}$
Two-qubit Gate Error	$\sim 8 \times 10^{-3}$
Readout Error	$\sim 10^{-2}$

Table 5.1: Custom noise parameters derived from QV 128 chip (early 2021).

5.3.3 Six spins $1/2$ Heisenberg closed ring

The same approach is applied for a more complex system, consisting of six spins $1/2$ arranged in a closed hexagon chain described by Eq. 5.10 (isotropic in J) and periodic boundary conditions, with an external B field parallel to z axis. Despite being still easy to compute classically, it represents a good test to study ansatz scalability and performances.

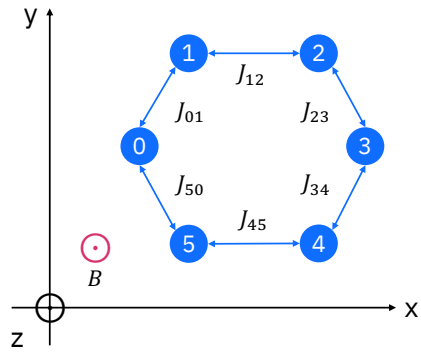

Hamiltonian encoding

Hamiltonian in Eq. 5.10 of this 4 sites closed chain can be encoded on the spin $1/2$ qubits following the same approach introduced in Eq. 5.9. It is possible to build the following operator:

$$\begin{aligned}\hat{H}_{op}^{(6\ closed)} = J_z(ZZIIII + IZZIII + IIZZII + IIIZZI + IIIIZZ + ZIIIIZ)\\ +J_y(YYIIII + IYYIII + IIYYII + IIIYYI + IIIIYY + YIIIIY)\\ +J_x(XXIIII + IXXIII + IIXXII + IIIXXI + IIIIXX + XIIIIX)\\ +B(ZIIIII + IZIIII + IIZIII + IIIZII + IIIIZI + IIIIIZ)\end{aligned} \tag{5.16}$$

where the B field is acting only on the z axis. Also in this case it is possible to notice the application of periodic boundary conditions, as the Hamiltonian is representing a closed chain, in the latter element of the first three lines of Eq. 5.16.

Construction and initialisation of the ansatz

Both HA and PMA approaches are here extended to a 6 sites configuration. For the HA, we just add two qubits to the circuit represented in Fig. 5.4, both initialized with an $R_y(\theta_l)$ and linearly entangled with the next neighbour. Each variational ansatz layer thus includes 6 different parameters instead of 4, and 5 CNOTs instead of 3.

For the PMA approach, we can use the same building block introduced in Fig. 5.5(a) and a similar approach for the overall ansatz layer, with a slightly different initialisation for the different field regions, as reported in Fig. 5.9.

Noiseless statevector VQE results

Numerical simulations of the VQE performed with Qiskit `statevector_simulator` are reported in Fig. 5.10, as per 4 sites case, and using COBYLA as classical optimizer, to which I contributed by investigating the optimal configuration of VQE.

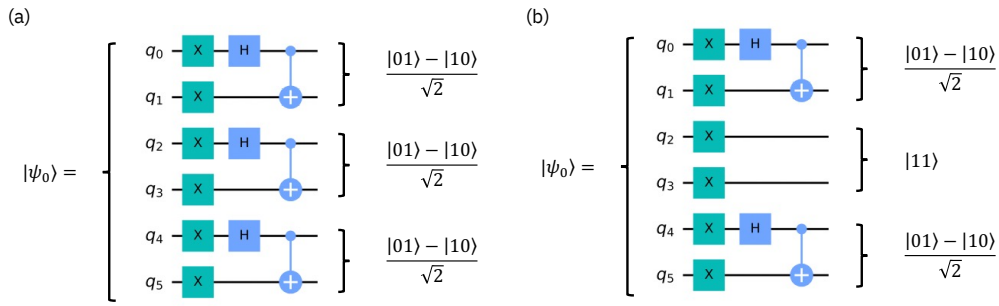

Figure 5.9: PMA initialisation, 6 spins: (a) low B ($S = 0$, $m = 0$ region), (b) intermediate B ($S = 1$, $m = -1$ region).

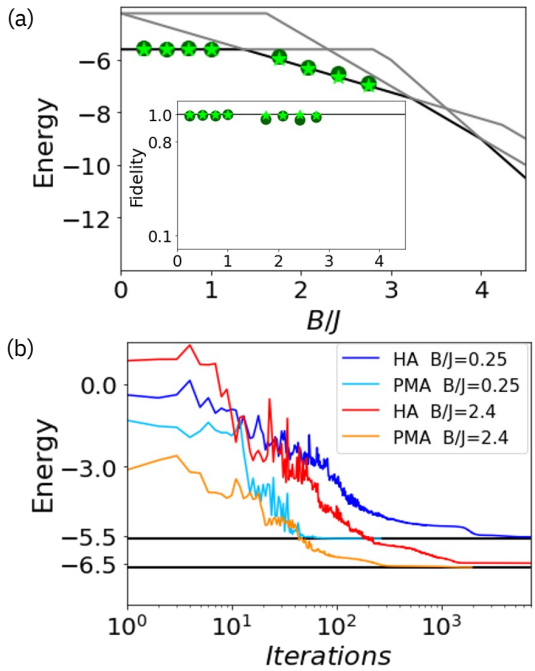

Figure 5.10: Statevector simulations of 6 sites spin closed ring. (a) GS energy. Inset: corresponding fidelity. (b) VQE energy convergence. Reproduced from Ref. [127] with permission from MDPI (open access article distributed under the terms and conditions of the Creative Commons Attribution (CC BY 4.0) license Creative Commons).

In this case, due to an increased system complexity, both ansatzes are more demanding in terms of parameters and quantum gates to be able to reconstruct the GS observables. The HA requires 5 layers (24 parameters and 15 CNOTs) for the low field region, and 4 layers (20 parameters and 12 CNOTs) for the intermediate field region. The PMA requires instead 2 layers, with 8 parameters and 36 parallelizable CNOTs. Also in the 6 spin case, we notice that the HA circuit is less complex than the PMA, but the PMA has

less parameters to be optimized, leading to a easier and quicker convergence.

Noisy VQE simulation results

The same noisy VQE simulations are performed also in the 6 spins case, using the same customized noise parameters reported in Table 5.1. A degradation in the performances of both ansatzes is evident, due to the more complex circuits.

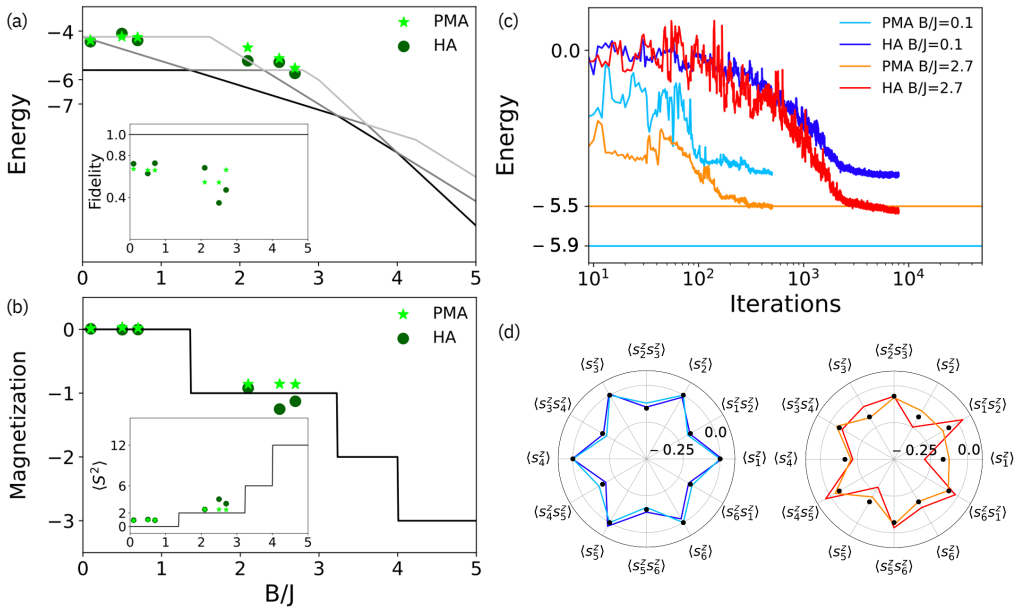

Figure 5.11: Noisy simulations of 6 sites spin closed ring. (a) GS energy. Inset: corresponding fidelity. (b) Expectation value of magnetization and total spin S^2. (c) VQE convergence. (d) Expectation values of the local one- and two-body spin operators: only PMA is able to reconstruct the local spin expectation values symmetries, in particular at intermediate B/J (orange solid line). Reproduced from Ref. [127] with permission from MDPI (open access article distributed under the terms and conditions of the Creative Commons Attribution (CC BY 4.0) license Creative Commons).

Fig. 5.11(a) shows the GS energy observable and the corresponding state fidelity. HA seems slightly better in reconstructing the GS energy in the intermediate field region, while the average fidelity is similar for both ansatzes.

A different trend is reported in Fig. 5.11(b): here the PMA is slightly better on reconstructing the expectation value of both magnetization and total spin S^2: this is due to the imposition of the symmetry constraints in the ansatz.

Fig. 5.11(c) reports the VQE convergence for two B/J values, one in each field region: while the energy is clearly not well reconstructed for the effect of noise, showing that with this system complexity we are close to the current limits of technology, we can confirm that PMA converges in $\sim 10^2$ iterations, while HA takes almost 10^4 iterations.

Perhaps the most interesting result is reported in Fig. 5.11(d): here the expectation value of s_i^z and $s_i^z s_{i+1}^z$ are shown. We notice the effect of symmetry breaking induced by

the noise, especially in the intermediate field region: only the PMA (light blue for low B, orange for intermediate B) preserves the star-shaped trend of the exact results, reported with the black dots. This leads to the possibility to design error mitigation techniques based on the system symmetry [131][132][133], in order to improve the variational ansatz performances.

In general, in case of 6 spins the PMA is able to better reconstruct the ground state with also the correct symmetry; the noisy simulations highlights that VQE is still demanding to be implemented on real quantum devices. Moreover, for complex systems requiring a more complicated entanglement-map, several SWAP operations would be included by the circuit transpiler in order to be implemented on the current chips: two ways are here available to overcome this issue, i.e. improving chips connectivity or lowering the error rate. The latter approach is more promising, as there are no future improvements on IBM Quantum roadmap for increasing intra-qubit connectivity due to cross-talk errors (see Sec. 3.2.3), while chips QV is constantly increasing [134]. Calculations of such static system properties will then be possibly implemented in the near-term future hardware devices. Additionally, other error mitigation techniques could be implemented, such as the Zero-Noise Extrapolation (ZNE) [120][24] and the above mentioned system symmetry-based techniques.

5.3.4 Finite-Size and Parity effects of local spin operators

In the previous sections we used both HA and PMA approaches to study GS static properties of the target systems; the PMA is the best of the two approaches, in terms of observables reconstruction accuracy, easiness of convergence and symmetry preservation. PMA can now be used to study how the local variables change by changing the topology of the system in terms of number of spins and boundary conditions (open or closed chains). The studied systems are reported in Fig. 5.12; in particular, a comparison of the expectation values of the local spin operators $\langle s_i^z \rangle$ on the GS is performed, with the objective to study finite-size effects and parity effects, as they are important quantities for MNMs characterization [102].

First, we need to introduce the Hamiltonian encoding on qubits for 4, 5 and 6 spins open chains, following a similar approach of 4 and 6 spins closed chains, already reported in Eq. 5.11 and Eq. 5.16:

$$\begin{aligned}\hat{H}_{op}^{(4\ open)} = J_z(ZZII + IZZI + IIZZ)\\ +J_y(YYII + IYYI + IIYY)\\ +J_x(XXII + IXXI + IIXX)\\ +B(ZIII + IZII + IIZI + IIIZ)\end{aligned} \tag{5.17}$$

$$\begin{aligned}\hat{H}_{op}^{(5\ open)} = J_z(ZZIII + IZZII + IIZZI + IIIZZ)\\ +J_y(YYIII + IYYII + IIYYI + IIIYY)\\ +J_x(XXIII + IXXII + IIXXI + IIIXX)\\ +B(ZIIII + IZIII + IIZII + IIIZI + IIIIZ)\end{aligned} \tag{5.18}$$

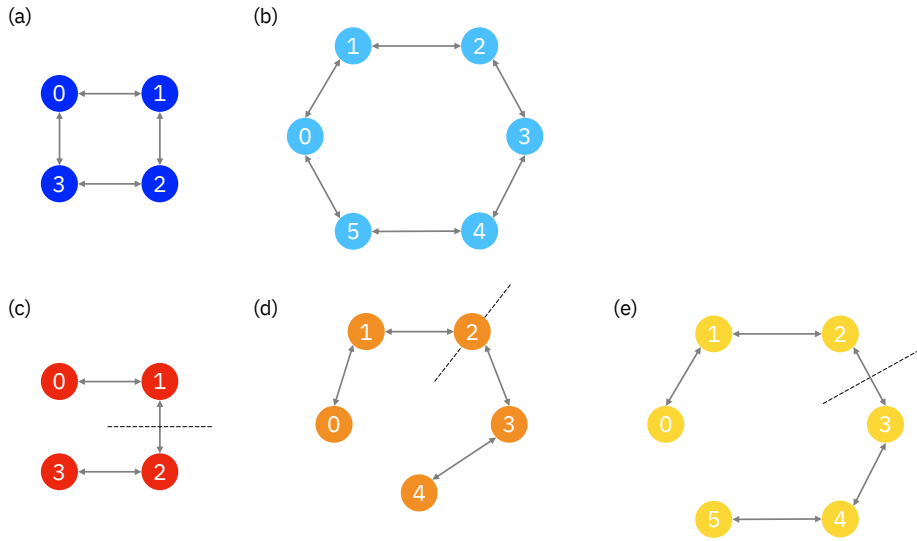

Figure 5.12: Even-odd open-closed MNM configurations. Dashed lines are an useful symmetry axis of the open chains.

$$\begin{aligned}\hat{H}_{op}^{(6\ open)} = J_z(ZZIIII + IZZIII + IIZZII + IIIZZI + IIIIZZ)\\ +J_y(YYIIII + IYYIII + IIYYII + IIIYYI + IIIIYY)\\ +J_x(XXIIII + IXXIII + IIXXII + IIIXXI + IIIIXX)\\ +B(ZIIIII + IZIIII + IIZIII + IIIZII + IIIIZI + IIIIIZ)\end{aligned} \tag{5.19}$$

where the periodic boundary conditions are here not present due to the open structure of the chain, and where the magnetic field is acting only on the z axis.

The VQE algorithm with PMA approach, considering the same noise configuration of the previous GS studies reported in Sec. 5.3.2 and in Sec. 5.3.3, is used to simulate the local spin expectation values for the configurations depicted in Fig. 5.12. It is worth noting that the initialisation of the PMA for a 5 spins chain follows the same approach of the 4 and 6 spins chains. In Fig. 5.13 is reported the initialisation for the low field region, as our investigation of odd-numbered chains is based on this range for simplicity reasons.

Results of the finite-size and parity effects exploration are reported in Fig. 5.14, where the different colors and symbols are related to the different MNM configurations introduced above; exact values are reported by the dashed lines. In Fig. 5.14(a) are reported the $\langle s_i^z \rangle$ in the low field region, for $B/J = 0.1$, while in Fig. 5.14(b) are reported the $\langle s_i^z \rangle$ in the intermediate field region, for $B/J = 2.7$. In the following list are listed the main outcomes.

- Even-numbered closed chains: due to their periodic boundary conditions, these rings show a translational invariance symmetry. Expectation values of the local

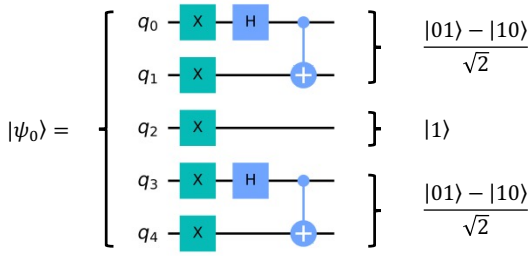

Figure 5.13: PMA initialisation, 5 spins, low B ($S = 0$, $m = 0$ region).

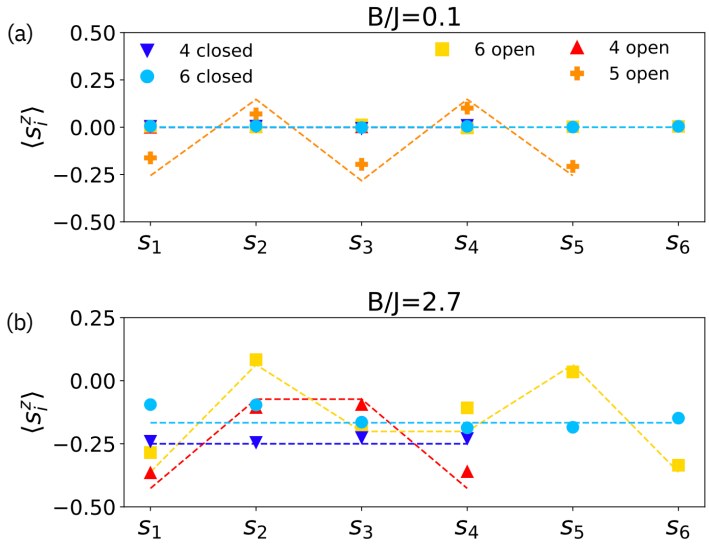

Figure 5.14: Finite-size and Parity effects, even-odd open-closed chains (noisy VQE simulations): (a) low B ($S = 0$, $m = 0$ region), (b) intermediate B ($S = 1$, $m = -1$ region). All noisy simulated results are in good agreement with expected behaviour of finite-size systems. Reproduced from Ref. [127] with permission from MDPI (open access article distributed under the terms and conditions of the Creative Commons Attribution (CC BY 4.0) license Creative Commons).

spin operators are uniform and equal to 0 in low field region, as the GS is $S = 0$ (Fig. 5.14(a), light blue circles and blue triangles). The same behaviour is visible also in intermediate field region, with the difference that as the GS is characterised by $S = 1$ and $m = -1$, the expectation value is $\langle s_i^z \rangle = -1/N$, where N is the number of spins in the ring (Fig. 5.14(b), light blue circles and blue triangles).

- Even-numbered open chains: due to their open boundary conditions and an even number of spins, these MNM are symmetrical to the central bond. Low field region results show a uniform (but still symmetric with respect to the central bond) $\langle s_i^z \rangle = 0$ behaviour (Fig. 5.14(a), yellow squares and red triangles), while in the intermediate field region this symmetry is evident (Fig. 5.14(b), yellow squares and

red triangles).

- Odd-numbered open chains: as per even-numbered open chains, odd-numbered open chains show an symmetric pattern, this time with respect to the central spin. Results for low B field are showing alternating positive and negative expectation values (Fig. 5.14(a), orange plus marks), as expected for $\langle m \rangle = \langle \sum_i s_i^z \rangle = -1/2$.

The VQE noisy simulations are in very good agreement with exact results; by increasing the MNM size, the symmetric behaviour is slightly worse reconstructed, but still in good accordance.

The obtained results show how the PMA approach can reconstruct the actual structure and symmetries of the target MNM ground state.

5.4 Study of GS spin states mixing on spin $1/2$ systems

I then helped investigating anti-ferromagnetic closed Heisenberg chains in which a small Dzyaloshinskii-Moriya Interaction (DMI) is added on top of the leading coupling. Such systems are interesting because, rather than the other systems studied, they present a mixing between different total spin states; this mixing is induced by the DMI itself, and induces anti-crossings between ground and first excited state ad specific magnetic field values. As the energy gap between ground state and the first excited state is very small in proximity of the anti-crossing, a proper variational ansatz must be built to be able to explore that particular area, in which observables like torque assume non-trivial behaviours.

5.4.1 Test-case: spin $1/2$ Heisenberg trimer with DMI

We first consider a rather simple test model, consisting of three spins $1/2$ arranged in a closed chain with a triangular shape. This system is subject to an external magnetic field along z axis, and is described by the general Hamiltonian in Eq. 5.20. The DMI is acting on all three bonds, and both J_{ij} and D_{ij} are considered in general different on each bonds: several configurations of have been explored. In Fig. 5.4.1 is reported a sketch of the target test model.

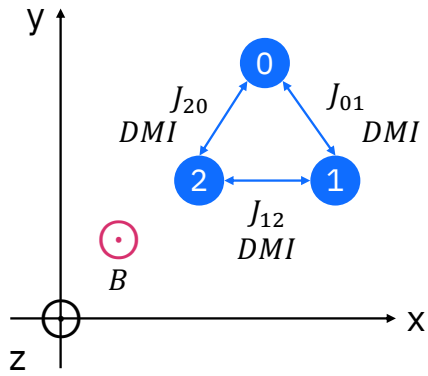

$$\begin{aligned}\mathcal{H} = \sum_i J_i \vec{s}_i \cdot \vec{s}_{i+1} + \sum_i \vec{B} \cdot \vec{s}_i \\ + \sum_{ij} D_{ij} \vec{s}_i \wedge \vec{s}_j\end{aligned} \tag{5.20}$$

The Hamiltonian in Eq. 5.20 has been implemented on the trimer configuration as:

$$\begin{aligned}\mathcal{H} = \mathcal{H}_0 + \mathcal{H}_1 \\ = J_1 \vec{s}_1 \cdot \vec{s}_2 + J_2 \vec{s}_2 \cdot \vec{s}_3 + J_3 \vec{s}_3 \cdot \vec{s}_1 + B(s_1^z + s_2^z + s_2^z) \\ + D(\vec{s}_1 \times \vec{s}_2 + \vec{s}_2 \times \vec{s}_3 + \vec{s}_3 \times \vec{s}_1)\end{aligned} \tag{5.21}$$

and it is composed by a leading term $\mathcal{H}_0$ and a perturbative term $\mathcal{H}_1$ representing the DMI (assuming $D \sim J/10$). For this first test model, a rather simple HA is adopted to explore several configurations of the spin triangle in terms of J_{ij} and D_{ij} values.

Hamiltonian encoding

The Hamiltonian in Eq. 5.21 is encoded on qubits as the following:

$$\begin{aligned}\hat{H}_{op}^{trimer\ DMI} = J_{01}(XXI + YYI + ZZI) \\ + J_{12}(IXX + IYY + IZZ) \\ + J_{20}(IXI + IYI + IZI) \\ + B(ZII + IZI + IIZ) \\ + D(ZXI - XZI + IZX - IXZ + XIZ - ZIX \\ + YXY - XYI + IYX - IXY + XIY - YIX \\ + ZYI - YZI + IZY - IYZ + XIZ - ZIY)\end{aligned} \tag{5.22}$$

where the magnetic field is acting only on z axis and DMI is acting on each bond.

Construction of the variational ansatz

We start studying these systems by leveraging on a heuristic approach for the variational ansatz. The circuit constructing the ansatz is depicted in Fig. 5.15, and it is composed by a set of parametrized R_y and by a linear entanglement layer; the ansatz block $V_j(\vec{\theta}_j)$ is then repeated two times, with a final rotation layer. Overall, this ansatz shows 9 variational parameters.

VQE results

The ansatz in Fig. 5.15 is exploited to perform noiseless and noisy VQE simulations. Due to the simplicity of this model, we found that the ansatz is able to reconstruct well the GS even close to the anti-crossing; the parallel magnetization however is not well reconstructed, in particular the behaviour induced by the anti-crossing. In Fig. 5.16 we report the results, where VQE was performed 5 times, getting the best results for each point. Noisy simulations have been performed with a noise model created from a QV 16 IBM Quantum chip (`ibmq_belem`).

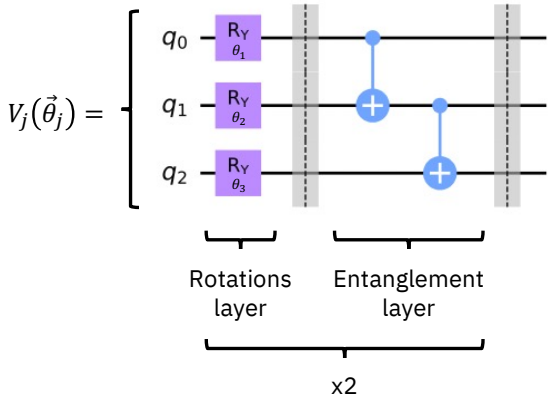

Figure 5.15: Heuristic ansatz for the spin $1/2$ trimer with DMI, containing 3 variational parameters per block.

Panel (a) and (b) of Fig. 5.16 are related to a spin $1/2$ trimer configuration representing an isosceles triangle, where $J_{01} = J_{20} \neq J_{12}$ (considering the sketch in Fig. 5.4.1). It is worth noting that, at $B = 0$, the energy difference between doublets depends on $J_{12} - J_{01}$. Noiseless, noisy (with the three noise sources active: Thermal Relaxation, Readout and Gate Errors) and noisy mitigated (using Qiskit Measurement Error Mitigation) quantum computations have been performed. The implemented error mitigation technique is able to increase the accuracy of the results.

Panel (c) and (d) of Fig. 5.16 are instead related to a spin $1/2$ trimer configuration representing a scalene triangle, where $J_{01} \neq J_{20} \neq J_{12}$. The same considerations of the isosceles triangle about noiseless, noisy and noisy mitigated results are due.

While the noise effect is evident, results show a rather good agreement between VQE simulations and the exact behaviour; a more complex heuristic ansatz would increase the accuracy, but also the error in the noisy simulations. In general, for small systems, a well balanced heuristic approach could lead to an accurate reconstruction of the GS static properties. Incrementing system complexity in terms of sites can be very challenging for a heuristic ansatz, as reported in the next Section.

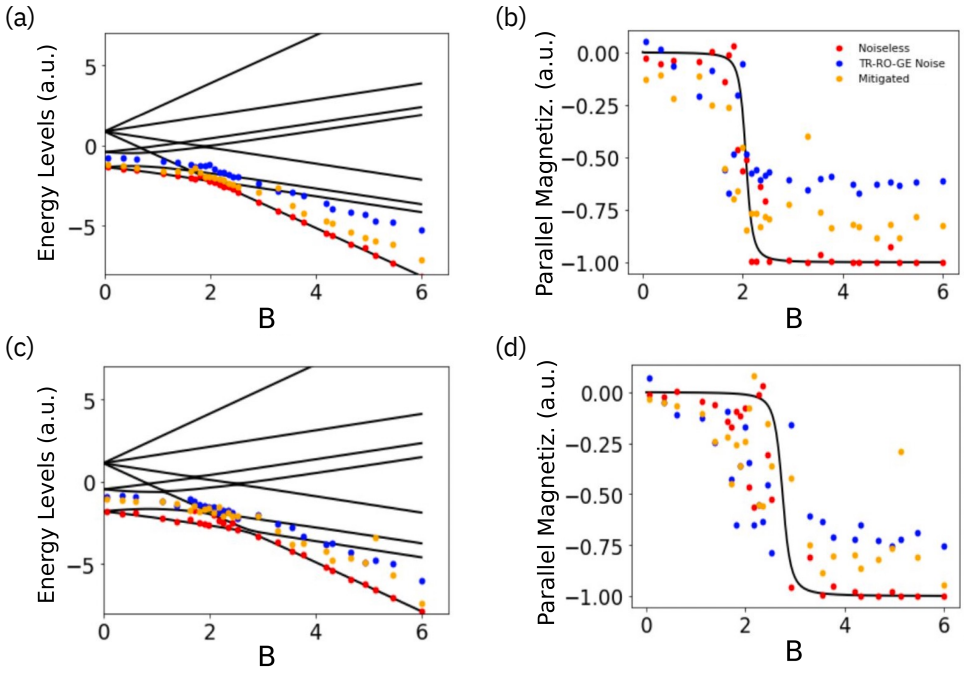

Figure 5.16: (a) VQE simulations for an isosceles ($J_{01} = J_{20} \neq J_{12}$) triangle of spins $1/2$ with DMI. (b) Related parallel magnetization simulations. (c) VQE simulations for a scalene ($J_{01} \neq J_{20} \neq J_{12}$) triangle of spins $1/2$ with DMI. (d) Related parallel magnetization simulations. HA is able to reconstruct quite well the expected behaviour of the GS, while approximates the parallel magnetization observable; the HA however struggles to reconstruct the observables in presence of noise. Error mitigation increases the performances significantly on the noisy simulation.

5.4.2 Four spins $1/2$ Heisenberg closed ring with DMI

Given the test model trimer results, I contributed to focus on a more complicated system consisting of four spins $1/2$, in which, as depicted in Fig. 5.4.2, we assume DMI acting only on the 0-1 and 2-3 bonds to make the Hamiltonian less symmetric. The Hamiltonian describing such systems is reported in Eq. 5.23, it is isotropic in both J_i and D_{ij}, and and it can be considered composed by a leading term $\mathcal{H}_0$ and a perturbative term $\mathcal{H}_1$ (assuming $D \sim J/10$).

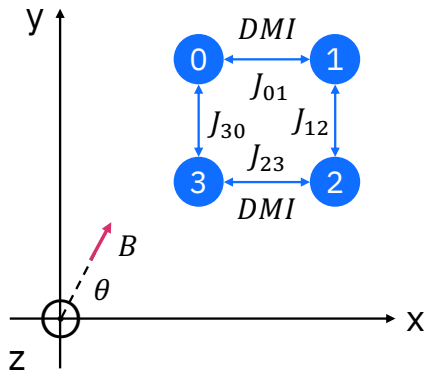

In order to create anti-crossings between states with $\Delta m = 1$, it is necessary to have a

magnetic field not null in the xz plane: we thus need to tilt its direction, assuming i.e. an angle θ between the magnetic field and the z axis. In this case we imposed $\theta = \pi/6$.

$$\begin{aligned} \mathcal{H} &= \mathcal{H}_0 + \mathcal{H}_1 \\ &= J\sum_{i=1}^{4}(\sigma_x^i\sigma_x^i + \sigma_y^i\sigma_y^i + \sigma_z^i\sigma_z^i) + B\sum_{i=1}^{4}(\sin\theta(\sigma_x^i + \sigma_x^i) + \cos\theta(\sigma_z^i + \sigma_z^i)) \\ &\quad + D(\sigma_x^0\sigma_y^1 - \sigma_x^1\sigma_y^0 + \sigma_x^2\sigma_y^3 - \sigma_x^3\sigma_y^2) \end{aligned} \tag{5.23}$$

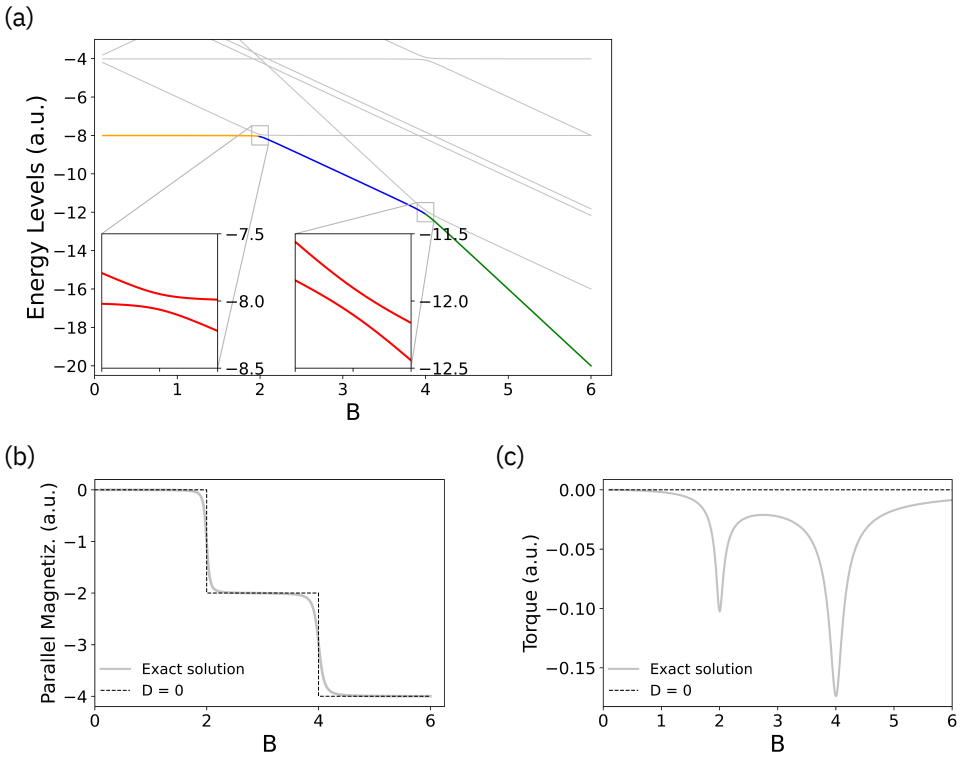

Figure 5.17: (a) Exact solution of energy levels of 4 spins system with DMI, with zoom on the anti-crossings. Yellow, blue and green colors represent respectively the low, intermediate and high field regions. (b) Parallel magnetization exact solution. (c) Torque exact solution. It is worth noting the effect of the DMI on the observables in panels (b) and (c), by comparing the exact solution and the solution with $D = 0$ (black dashed lines).

In Fig. 5.17(a) the exact energy levels of the target system described by Eq. 5.23 are reported, with the highlighted GS. The effect of the DMI on the energy levels is to mix different total spin states in proximity of the anti-crossings: while the spin eigenstates are well defined far away from the anti-crossings ($|S = 0, m = 0\rangle$ in the low field region, $|S = 1, m = -1\rangle$ in the intermediate field region, $|S = 2, m = -2\rangle$ in the high field region), where the effect of DMI is negligible, in proximity of the anti-crossings the spin

eigenstates are not well defined. Interestingly, parallel magnetization and torque are influenced by the DMI, leading to the behaviour reported in Fig. 5.17(b) and Fig. 5.17(c): magnetization shows a smoothed steps behaviour, and torque shows peaks. These observables require high precision to be computed accurately with a QC: a custom variational ansatz is thus needed to address explore the interesting but narrow part of the observables near the anti-crossings.

Hamiltonian encoding

The encoding of the Hamiltonian follows the Eq. 5.22 approach, with the proper modifications due to the system properties. We can obtain:

$$\begin{aligned}\hat{H}_{op}^{4\ closed\ DMI} = J_z(ZZII + IZZI + IIZZ + ZIIZ)\\ +J_y(YYII + IYYI + IIYY + YIIY)\\ +J_x(XXII + IXXI + IIXX + XIIX)\\ +B_z(ZIII + IZII + IIZI + IIIZ)\\ +B_x(XIII + IXII + IIXI + IIIX)\\ +D(XYII - YXII + IIXY - IIYX)\end{aligned} \tag{5.24}$$

where the magnetic field is acting on the xz plane, and the DMI is acting only on $0-1$ and $2-3$ bonds.

Construction of the variational ansatz

Three different approaches are adopted to build the variational ansatz. The first approach I specifically focused on is based on the HA: the ansatz is composed by a general rotation block (U_3 rotations) and a full entanglement block, forming a layer, repeated 3 times (Fig. 5.18(a)) and with a final rotation layer, for a total of 48 variational parameters. This is due to the complexity of the anti-crossing region.

A second heuristic approach I contributed to, based on symmetry considerations of the target system, aims to lower the number of parameters while preserving the performance of the ansatz (Fig. 5.18(b)). We first consider that the Hamiltonian in Eq. 5.23 with the same J for each bond, so we can assume R_y and R_z rotations instead of U_3 rotations, lowering the overall number of parameters. Moreover, due to system symmetry, it is possible to impose the variational parameters related to opposite spins (i.e. $0-2$ and $1-3$) to be equal, halving the number of parameters, achieving 16 parameters overall. In fact, also the Ground State of the system is expected to show the same Hamiltonian symmetries. The symmetric heuristic ansatz choice has also the effect to reduce the parameters space explored by the ansatz itself, forcing it to stay in a subspace conserving the symmetries of the system. The quantum circuit implementing this variational ansatz is composed by 32 single-qubit rotations and 18 CNOTs.

The third ansatz I contributed to is based on a PMA approach, and it is built in particular to explore the anti-crossings proximity. This approach has been developed considering that the dominant term of the Hamiltonian is isotropic, so all eigenstates are also S_{tot} eigenstates; then, the Heisenberg interaction is dominant, and commutes with the Zeeman part of the Hamiltonian, while the DMI is a perturbation. In these conditions,

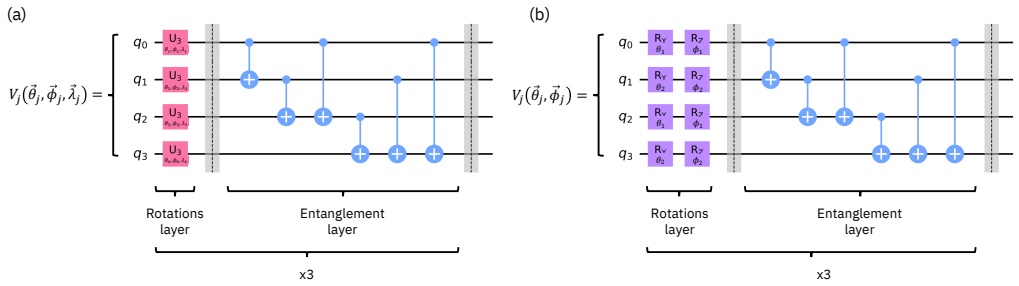

Figure 5.18: Different hardware heuristic approaches for 4 spins system with DMI. (a) Hardware heuristic ansatz with 48 parameters. (b) Hardware heuristic ansatz considering system symmetries, with 16 parameters. Both ansatzes require a final rotation layer after the 3 repetitions of the block.

as already said, it is possible to know the configuration of the GS far away from the anti-crossings. Near the anti-crossings, instead, we expect DMI to mix the states: near the first anti-crossing, $|S = 0, m = 0\rangle$ and $|S = 1, m = -1\rangle$ will be mixed, leading to the need of only 2 variational parameters for a VQE calculation to discriminate them. The same considerations can be done for the second anti-crossing, where $|S = 1, m = -1\rangle$ and $|S = 2, m = -2\rangle$ are mixed. So, as we know the eigenstates of the total spin, a quantum circuit to obtain them has been built, and then a linear combination of the two has been performed: the ansatzes created (S0S1 for the first and S1S2 for the second anti-crossing) are thus adapted to the area of interest. In this way, it is possible to simplify the overall VQE process.

$$\begin{aligned} S0S1 &= |S = 0, m = 0\rangle \cos\alpha + e^{i\beta}|S = 1, m = -1\rangle \sin\alpha \\ S1S2 &= |S = 0, m = -1\rangle \cos\alpha + e^{i\beta}|S = 2, m = -2\rangle \sin\alpha \end{aligned} \tag{5.25}$$

The ansatz with the forms in Eq. 5.25 is built using Qiskit `initialize` function [135][136]: the output is a circuit made of 15 single-qubit rotations and 22 CNOTs. Further optimizations of this build have been made in our joint research, especially for the S1S2 ansatz.

Noiseless VQE results

Several numerical noiseless simulations of the VQE process have been performed, and related results are reported in Fig. 5.19.

Panels (a) and (b) of Fig. 5.19 show the computed GS energy in proximity of the first and the second anti-crossings. The circles are calculated with the two HA approaches, while the squared markers are obtained by the PMA (S0S1 and S1S2). In particular, for the PMA two different optimization processes have been developed: the first one (green squared symbols) represent a regular VQE optimization performed with COBYLA, while the second one (blue squared symbols) represents a manual optimization of the two parameters of Eq. 5.25. While it is clear that the PMA approach works better than the HA, the manual optimization of the parameters achieves a remarkable State Fidelity.

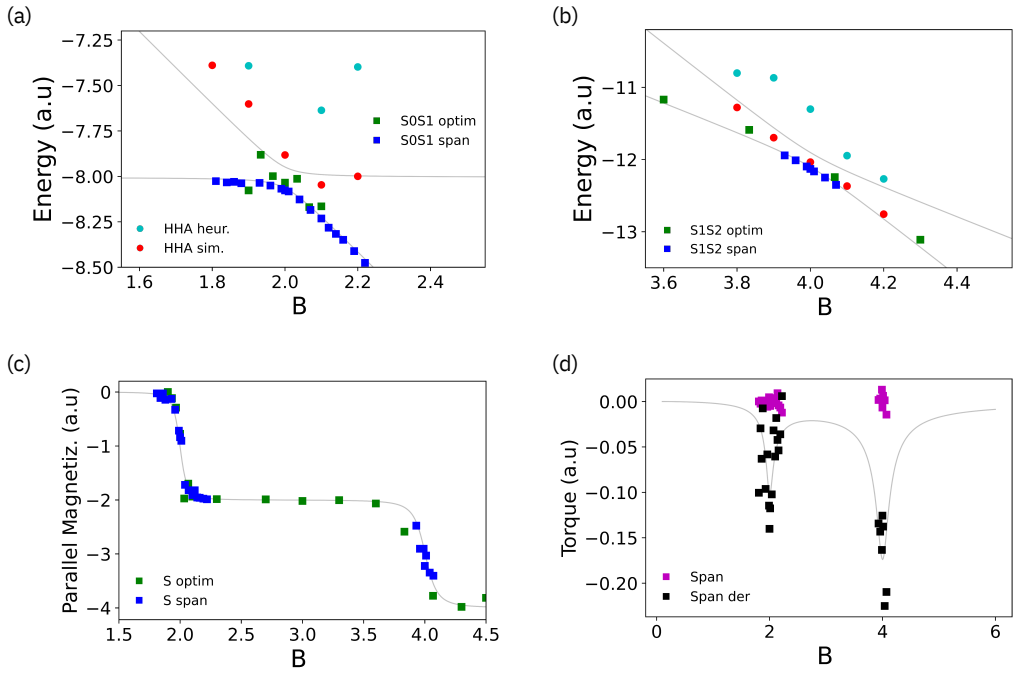

Figure 5.19: (a) GS energy computed in proximity of the first anti-crossing with noiseless simulations. (b) GS energy computed in proximity of the second anti-crossing. (c) Parallel magnetization. In all these three cases, the PMA (S0S1 for the first anti-crossing, S1S2 for the second anti-crossing, and in general S) with the manual parameters optimization is able to achieve a remarkable fidelity. (d) Torque, reconstructed with good agreement with a derivative approach based on Hellmann-Feynman theorem, developed in our joint research.

We then use the PMA approach to compute the parallel magnetization and the torque observables. Panel (c) shows the parallel magnetization computed with S0S1 and S1S2 ansatzes: the manual optimization leads to better results, and can be used in proximity of the anti-crossing. Panel (d) shows the torque results, computed exploiting the PMA approach with the manual optimization of the parameters, and with two different methods to extract the observable. In particular, the first one (purple squared symbols) represents the regular calculation using the results from the VQE process; the second one (black squared symbols) relies on the *derivative* method developed in our joint research, based on the Hellmann-Feynmann theorem (Eq. 5.5). Taking the target system Hamiltonian (Eq. 5.23) it is possible to compute:

$$\begin{aligned} \frac{\partial E_\theta}{\partial \theta} &= \left\langle \psi_\theta \middle| \frac{\partial \mathcal{H}}{\partial \theta} \middle| \psi_\theta \right\rangle \\ &= \left\langle \psi_\theta \middle| B \sum_{i=1}^{4} (-\cos\theta(\sigma_x^i + \sigma_x^i) + \sin\theta(\sigma_z^i + \sigma_z^i) \middle| \psi_\theta \right\rangle \\ &= B(M_z \sin\theta - M_x \cos\theta) \end{aligned} \tag{5.26}$$

thus it is possible to obtain the torque by calculating the derivative of the energy with respect to the direction θ of the magnetic field. Then, a discrete derivative is computed by slightly varying the θ between two points with similar B field.

The same calculation can be performed to compute the parallel magnetization:

$$\frac{\partial E_B}{\partial B} = \left\langle \psi_B \middle| \frac{\partial \mathcal{H}}{\partial B} \middle| \psi_B \right\rangle = M_{par} \tag{5.27}$$

It is worth noting that, while the technique reported in Eq. 5.26 is the best way we found to compute the rather small torque values, it is very sensible to fluctuations: it would be hard to be implemented on noisy simulations, especially with high noise rates.

Noisy VQE simulation results

Due to the complexity of the VQE calculation in the anti-crossings proximity already noticed in noiseless simulations, we report here the best results obtained by our joint research. In Table 5.2 are reported the custom noise parameters used in these simulations, which have been further improved from the parameters in Tab. 5.1 used in the other simulations.

T_1	200 μs
T_2	200 μs
Single-qubit Gate Error	$\sim 2 \times 10^{-4}$
Two-qubit Gate Error	$\sim 5 \times 10^{-3}$
Readout Error	$\sim 2.5 \times 10^{-3}$

Table 5.2: Custom noise parameters derived from QV 128 chip (early 2021), further improved.

Fig. 5.20 reports the VQE results of GS energy in proximity of the anti-crossings. In Panel (a), the PMA S0S1 approach leads to the best results, although the ansatz circuit is composed by an higher number of CNOT gates rather than the hardware heuristic symmetric ansatz (22 for the PMA, 18 for the HA symmetric). A similar behaviour is reported in Panel (b), in the proximity of the second anti-crossing: PMA S1S2 results are more stable rather than symmetric HA. Further improvements have been put in place, in particular to improve the S1S2 ansatz by lowering the number of gates, with the help of an ancillary qubit: these improvements are however not part of this work.

5.5 Study of spin $1/2$ chains Dynamic Correlation Functions

Dynamic properties of target Molecular Nanomagnets described by the Hamiltonian in Eq. 5.10 are here explored. The dynamic spin-spin correlation functions are very important physical quantities [137][138], as they are used to obtain other observables and to describe the propagation of external perturbations and excitations within the target system. We base our research on the approach developed in Ref. [109]; dynamic spin-spin correlation functions are defined as:

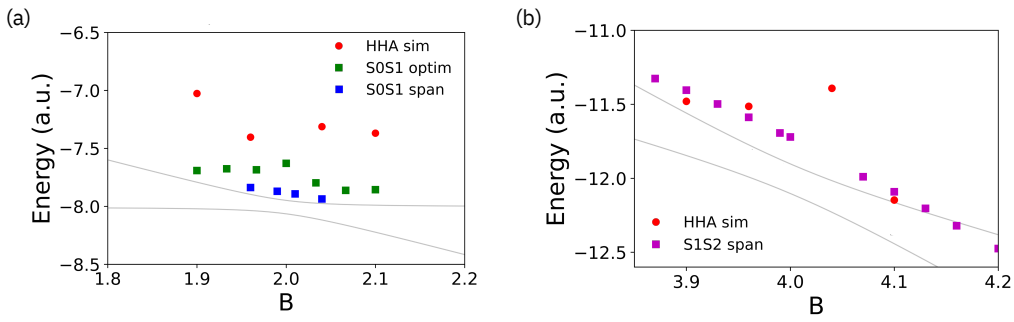

Figure 5.20: (a) Noisy VQE simulations of GS energy in proximity of the first anti-crossing. (b) Noisy VQE simulations of GS energy in proximity of the second anti-crossing.

$$\mathcal{C}_{ij}^{\alpha\beta}(t) = \langle s_i^\alpha(t) s_j^\beta \rangle_0 = \sum_p \langle 0|s_i^\alpha|p\rangle\langle p|s_j^\beta|0\rangle e^{-iE_p t} \tag{5.28}$$

where $|p\rangle$ are the system eigenstates with eigenvalues (energies) E_p, where $\alpha, \beta = x, y, z$ and i, j are the spin sites. The computation of such quantities is hard for classical computers. In order to compute dynamic correlations with a QC it is possible to use the class of quantum circuits depicted in Fig. 5.21 [14][109], in this case applied to the $N = 4$ spins $1/2$ closed chain. In particular, the quantum circuit reported is based on 4 qubits register $|\psi\rangle_R$ and an ancilla qubit a; the quantum register needs to be prepared in the ground state $|\psi_0\rangle$.

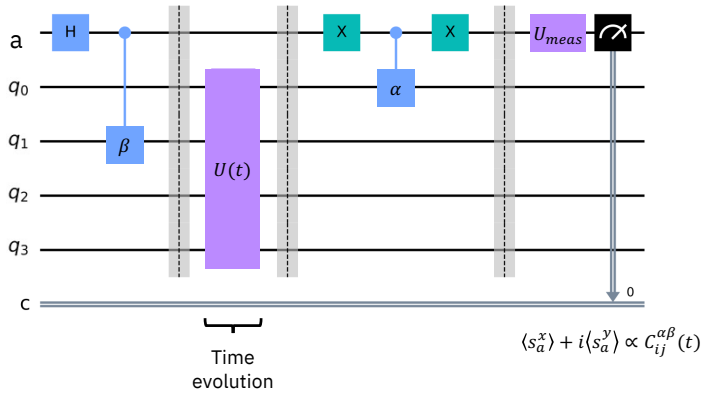

Figure 5.21: Circuit for computing Dynamic Correlation Functions, implementing time evolution $U(t)$ and conditional ancilla excitation to access the correlation functions.

- **Circuit preparation**. Qubits from 0 to 1 are used to simulate the time evolution of the target system, while the qubit a is an ancilla, prepared in a superposition $(|0\rangle + |1\rangle)/\sqrt{2}$ using an Hadamard gate.

- **First and second ancilla entanglement**. In order to compute the dynamic correlation functions $\mathcal{C}_{ij}^{\alpha\beta}$ between sites i and j, on axes α and β, we need to first entangle the ancilla with the j-th qubit with a c-β gate; a c-α gate is then required, after the time evolution simulation, to entangle the ancilla with the i-th qubit. The i and j choice represent the possibility to choose the pair of spins on which to compute the dynamic correlation function, including also autocorrelations if $i = j$.

- **System time evolution**. The central step is to perform a simulation of the time evolution of the target system. The operator $U(t) = e^{-i\mathcal{H}t}$ can be implemented [14] on the quantum device using a Digital Quantum Simulation (see Sec. 1.2.1). In this case, the time evolution has been performed at an high field region, where the Zeeman interaction is dominant; VQE process with PMA can be exploited to compute the ground state optimal variational parameters, then used to create the actual ground state, and its time evolution circuit is then represented in Fig. 5.22. In general, the S-T decomposition is needed, while in this situation a single Trotter step is enough to simulate the time evolution with a good level of approximation.

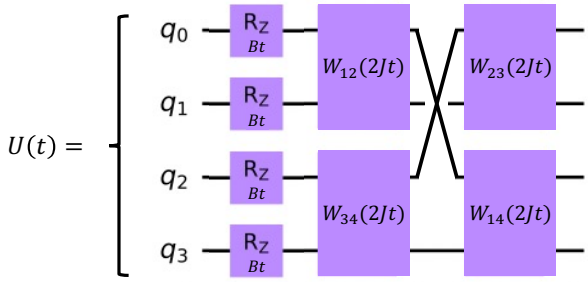

Figure 5.22: Time evolution circuit of the target Hamiltonian in high field region. The Ground State is represented by an array of R_z rotations.

- **Measurement process**. The measurement is then performed on the ancilla, and the process is conditioned by the quantities to be computed: both s_x and s_y are required, composing respectively the real and imaginary part of the function, so two different quantum computations are required as the two observables are incompatible and can not be computed at the same time. A basis change is required to measure on axes different than z, and the U_{meas} circuit implements just this choice: it is an Hadamard gate to measure s_x, and a $R_y(\pi/2)$ to measure s_y. In particular, a measurement of the observable σ_x on the ancilla qubit returns

$$\langle \sigma_x^\alpha \rangle = \mathrm{Tr}\left[\left(\sigma_x^\alpha \otimes \mathbb{I} \right) |\psi_{out}\rangle\langle\psi_{out}| \right] = \Re[\mathcal{C}_{ij}^{\alpha\beta}(t)] \tag{5.29}$$

and a measurement of σ_y on the ancilla qubit returns $\Im[\mathcal{C}_{ij}^{\alpha\beta}(t)]$. The overall dynamic correlation function is obtained by:

$$\langle 2\sigma_+^\alpha \rangle = \mathcal{C}^{\alpha\beta}(t) \tag{5.30}$$

where $2\sigma_+ = \sigma_x + i\sigma_y$ [14].

5.5.1 Error mitigation techniques

In order to compute the dynamic correlation functions on IBM Quantum real hardware devices, some error mitigation techniques should be applied.

Qubit topology
First, it is important to avoid unnecessary SWAP gates introduced in the circuit by the transpiler, having the objective to adapt the circuit to the selected hardware. We used IBM Quantum `ibmq_bogota` chip, with a linear connectivity (see Fig. 3.7 L-shape chip), and we adapted the circuit choosing the best position for the ancilla in each measurement case.

Phase and Scale
Observables of this kind computed on a real quantum superconducting transmons-based device are affected by a phase factor and a scale factor (due to incoherent error induced damping): these errors can be mitigated, without considering their origin, by applying to the raw results a physically motivated correction related to general properties of dynamic correlation functions.

- First, one can easily show from Eq. 5.28 that, for $t = 0$, the autocorrelation functions $\mathcal{C}_{ii}^{\alpha\alpha}(0)$ (same site, same axis) are a real quantity:

$$\mathcal{C}_{ii}^{\alpha\alpha}(0) = \sum_p |\langle 0|s_i^\alpha|p\rangle|^2 \tag{5.31}$$

  Raw results show a complex value for this quantity: here we apply to all t the same computed phase at $t = 0$, by imposing $\mathcal{C}_{ii}^{\alpha\alpha}(0)$ being real and positive.

$$\phi = \arg(\Re[\mathcal{C}_{ii}^{\alpha\alpha}(0)] + i\Im[\mathcal{C}_{ii}^{\alpha\alpha}(0)]) \tag{5.32}$$

$$\mathcal{C}_{ii_{mit}}^{\alpha\alpha}(0) = e^{-i\phi}\mathcal{C}_{ii}^{\alpha\alpha}(0) \tag{5.33}$$

- Second, we exploit a sum rule for autocorrelations in $t = 0$:

$$\langle (s_i)^2\rangle = s_i(s_i+1) = \sum_\alpha \mathcal{C}_{ii}^{\alpha\alpha}(0) \tag{5.34}$$

  where $(s_i)^2$ is related to the total spin operator of the i-th spin $1/2$. In this case, Eq. 5.34 implies:

$$\mathcal{C}_{ii}^{xx}(0) + \mathcal{C}_{ii}^{yy}(0) + \mathcal{C}_{ii}^{zz}(0) = s(s+1) = \frac{3}{4} \tag{5.35}$$

or, due to the isotropic model under investigation, $\mathcal{C}_{ii}^{\alpha\alpha}(0) = 1/4$. We can now find a scaling factor to correct the amplitude damping due to incoherent errors:

$$F_i = \frac{s_i(s_i+1)}{\sum_\alpha \mathcal{C}_{ii}^{\alpha\alpha}(0)} \tag{5.36}$$

This method has been developed in Ref. [109], and we apply it in order to mitigate the errors in the real hardware computation of the Dynamic Correlations Functions.

5.5.2 Dynamic Correlations Functions results

In order to test the above mentioned PaS procedure, we performed several noisy simulations for $\mathcal{C}_{11}^{xx}$, $\mathcal{C}_{11}^{yy}$, $\mathcal{C}_{11}^{zz}$, $\mathcal{C}_{22}^{xx}$, $\mathcal{C}_{22}^{yy}$, $\mathcal{C}_{22}^{zz}$, and $\mathcal{C}_{21}^{xx}$, $\mathcal{C}_{21}^{yy}$, $\mathcal{C}_{21}^{zz}$, with the same noise parameters used in the previous sections, reported in Table 5.1. Despite being close to the exact values due to the low noise rate, a significant mitigation is obtained by the PaS procedure by applying the computed phase and scaling factors through all the time evolution; we then performed the same calculations on IBM Quantum `ibmq_bogota` chip, with 5 qubit hardware and QV 32, with $n_{shots} = 8192$. Raw (experimental) and mitigated results using PaS [109] technique are reported in Fig. 5.23. Hardware (raw) results are depicted in light colors, while PaS (mitigated) in dark colors; black solid lines are the exact values. The computed correlations are $\mathcal{C}_{11}^{xx}$, $\mathcal{C}_{22}^{xx}$ and $\mathcal{C}_{21}^{xx}$, as the $\mathcal{C}_{ij}^{yy}$ show theoretically the same behaviour, and the $\mathcal{C}_{ij}^{zz}$ are theoretically flat to 0. The agreement is remarkably good after the error mitigation, in particular on $\mathcal{C}_{21}^{xx}$ cross-correlations. First, imaginary part of the dynamic correlation functions is rather different from zero, especially on auto-correlations; second, raw data are clearly damped in amplitude; third, it is possible to notice that the minima and the maxima are shifted with respect to the exact behaviour. The latter behaviour is especially evident in the cross-correlations $\mathcal{C}_{21}^{xx}$, for both real and imaginary part. For the considered system (4 spins closed chain), mid-sized QV 32 IBM Quantum chips are able to produce acceptable results; dynamic correlation functions of more complex systems are not investigated here, but as chip quality increases it would be possible to compute them on real hardware devices, with acceptable accuracy after error mitigation.

5.6 Conclusions

In conclusions, the work carried on exploiting IBM Quantum devices and simulators demonstrated the potential of this technology to describe small-sized molecular system properties; this approach, in particular the Physically Motivated one supported by the proper error mitigation techniques, will allow one to scale up the target system size when the number of qubits will increase, showing the possibility to reliably simulate relevant systems (i.e. chains consisting of at least tens of spins). It is finally worth noting that, although being very interesting physical models, Molecular Nanomagnets are quantum systems that can also be exploited to build fundamental units of quantum computation themselves: in Part IV we will deeply explore this possibility.

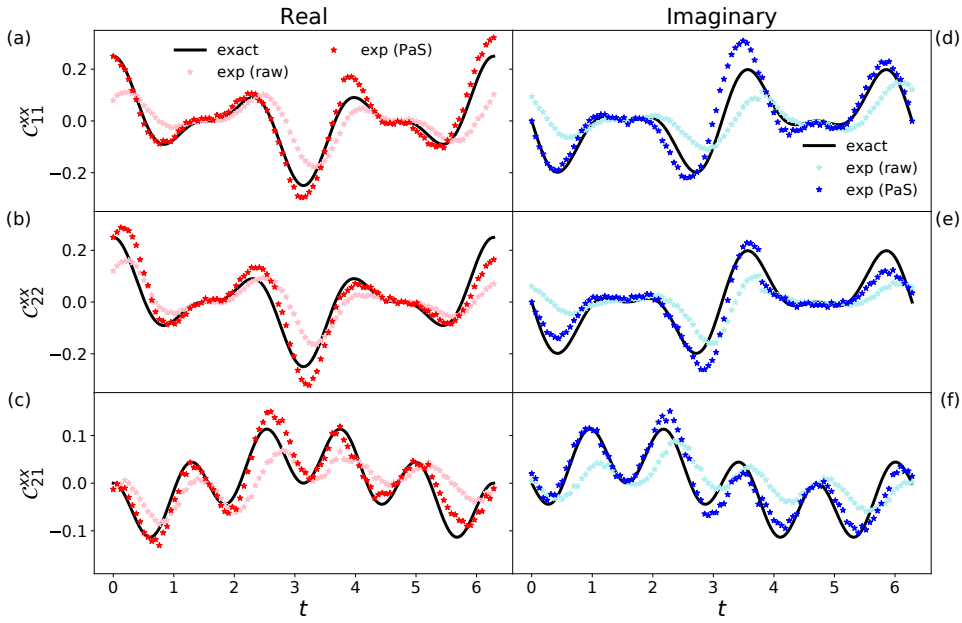

Figure 5.23: Real and Imaginary parts of the dynamic spin-spin correlations computed on IBM Quantum hardware, displaying raw and mitigated results. Computed dynamic correlation functions: $\mathcal{C}_{11}^{xx}$, $\mathcal{C}_{22}^{xx}$ and $\mathcal{C}_{21}^{xx}$, both real and imaginary parts. The computed results using a mid-sized QV 32 device show an amplitude damping and phase shift due mainly to incoherent errors of the real hardware; the Phase and Scale (PaS) error mitigation technique is able to correct well the results, obtaining a good agreement with the exact results (black solid lines). Reproduced from Ref. [127] with permission from MDPI (open access article distributed under the terms and conditions of the Creative Commons Attribution (CC BY 4.0) license Creative Commons).

Part of the content of this Chapter has been published in Magnetochemistry 2021, 7(8), 117 (Ref. [127]).

CHAPTER 6

Quantum Simulation of Fermionic systems

Strongly correlated quantum systems represent an interesting class of problems, in particular in Physics of Matter, that have been studied since last century [5][139]; they can not be solved using simple classic approximations, so a QC approach is needed. Nowadays, with the current prototype QC, they are taken as interesting test-beds for simulation on prototype Quantum Computers.

In this Chapter we describe the work performed on Fermionic systems, in particular simulating the static and dynamic properties of a one-dimensional Fermi-Hubbard model [140][141] by changing model parameters (i.e. one- and two-body terms), using currently available IBM Quantum real devices, with proper error mitigation techniques. Variational Quantum Eigensolver algorithm is exploited to compute the static properties of target system Ground State, while a Digital Quantum Simulation is performed to study the time evolution of the target system. The aim of the work reported in this Chapter is to leverage on a well known system to apply a similar approach to the one adopted for Chap. 5 in terms of simulation of static and dynamic properties, in particular a Physically Motivated approach to build the variational ansatz for VQE and the application of error mitigation techniques like Qiskit MEM [142] and the best qubit layout, specifically on quantum hardware calculations. In particular, coherent and incoherent errors are taken into account with a Post Selection error mitigation method, allowing us to simulate the time evolution of the model faithfully despite having circuits consisting on more than 300 two-qubit gates.

6.1 The Fermi-Hubbard model

The Fermi-Hubbard model is an approximate model that can be used to describe interacting particles in a lattice [141]. This model is one of the most studied in condensed matter, because it can be used to model many semiconductor and superconductor systems, and in general correlated systems like localized magnetic systems; in many cases, as the size of the lattice increases, classical algorithms cannot reproduce well the behaviour of this model, as the Hilbert's space dimension scales exponentially. In case of strongly correlated systems, it is difficult to compute the solution with classical approximations, as they are likely to fail.

The Hamiltonian describing the time evolution of this system consists of a kinetic (or hopping) term, describing the particle jumps between chain sites, and by a potential (or

interaction) term, describing the interaction between a pair of particles on the same site. The Fermi-Hubbard model under the second quantization formalism is described by the following Hamiltonian:

$$\mathcal{H} = -t \sum_{<i,j>}^{N} (\hat{b}_i^\dagger \hat{b}_j + \hat{b}_j^\dagger \hat{b}_i) + V \sum_{i}^{N} (\hat{n}_{i\uparrow} \hat{n}_{i\downarrow}) \tag{6.1}$$

with $\hat{n}_{i\uparrow} = (\hat{b}_i^\dagger \hat{b}_i)_\uparrow$ and $\hat{n}_{i\downarrow} = (\hat{b}_i^\dagger \hat{b}_i)_\downarrow$, and where $\hat{b}_i^\dagger$ and $\hat{b}_j$ are respectively the fermionic creation operator in site i and the fermionic annihilation operator in site j, with N the total sites number. In case of 2 sites:

$$\mathcal{H} = \left[-t \sum_{\sigma} (\hat{b}_{1,\sigma}^\dagger \hat{b}_{2,\sigma} + \hat{b}_{2,\sigma}^\dagger \hat{b}_{1,\sigma}) \right] + \left[V \sum_{i}^{2} (\hat{n}_{i\downarrow} \hat{n}_{i\uparrow} + \hat{n}_{i\uparrow} \hat{n}_{i\downarrow}) \right] \tag{6.2}$$

where the two square brackets highlight the hopping and the interaction terms $\mathcal{H} = \mathcal{H}_{hop} + \mathcal{H}_{int}$.

6.2 Jordan-Wigner Transformation

The Jordan-Wigner Transformation [11][143] is a transformation that maps spin operators in fermionic operators, in particular creation and annihilation operators. In Quantum Computing, it can be inverted to transform a fermionic Hamiltonian into a spin Hamiltonian, that can be encoded into a qubit registry. Among the steps that must be undertaken in order to practically design and realize a Digital Quantum Simulation of the Fermi-Hubbard model, the states mapping is the one that is most typically hardware-dependent [144]. It is also critical in terms of results and performance, particularly in the present era of NISQ devices, where the correlation between hardware properties and target features is stronger. With the J-W approach, spin $1/2$ states must be considered as empty ($|\downarrow\rangle \equiv |0\rangle$) or single-occupied fermionic states ($|\uparrow\rangle \equiv |1\rangle \equiv f^\dagger|0\rangle$), where $S^+ = f^\dagger$ and $S^- = f$. One can calculate:

$$\begin{cases} S_x = \frac{1}{2}(S^+ + S^-) = \frac{1}{2}(f^\dagger + f) \\ S_y = \frac{1}{2}(S^+ - S^-) = \frac{1}{2i}(f^\dagger - f) \\ S_z = \frac{1}{2}\Big[|\uparrow\rangle\langle\uparrow| - |\downarrow\rangle\langle\downarrow| \Big] \equiv f^\dagger f - \frac{1}{2} \end{cases} \tag{6.3}$$

The resulting J-W Transformations can be written as:

$$\begin{cases} S_j^+ = f_j^\dagger e^{i\pi \sum_{l<j} n_j} \\ S_j^- = f_j e^{-i\pi \sum_{l<j} n_j} \\ S_j^z = f_j^\dagger f_j - \frac{1}{2} \end{cases} \tag{6.4}$$

from which one can obtain $S^+ = \sigma^+ = \frac{\sigma^x + i\sigma^y}{2}$ and $S^- = \sigma^- = \frac{\sigma^x - i\sigma^y}{2}$.

In order to directly map onto a N-qubit quantum register the model of Eq. 6.2 we thus need to apply the J-W Transformations mapping fermionic operators $\hat{b}_i$ using spin states

S using the notation $\hat{b}^k \rightarrow S^+ e^{i\alpha_j}$, with $\alpha = \sum_i (\hat{n}_i)\pi$. In order to proceed with the Hamiltonian expression in spin notation, we can notice that:

$$\begin{aligned} \{\hat{b}_i^\dagger, \hat{b}_j\} &= \delta_{ij} \\ \{\hat{b}_i^\dagger, \hat{b}_j^\dagger\} &= 0 \\ \{\hat{b}_i^\dagger, \hat{b}_i\} = \{S_i^+, S_i^-\} &= \mathbb{I} \\ \{S^+, S^+\} &= 0 \\ \{S_2^+, S_1^-\} = \{\mathbb{I}, S^-\} \otimes \{S^-, \mathbb{I}\} \\ \{\sigma_z, S^+\} &= 0 \end{aligned} \tag{6.5}$$

where we define $S_2^+ = \mathbb{I} \otimes S^+$ the creation operator on a correlated system acting on site 2, and $S_1^- = S^- \otimes \mathbb{I}$ the annihilation operator acting on site 1. From the above relations one can obtain [145]:

$$\begin{aligned} \hat{b}_j &\rightarrow \left(\prod_{l=1}^{j-1} -\sigma_z^l \right) \sigma_-^j = (-1)^{j-1} \sigma_z^1 \sigma_z^2 \cdots \sigma_z^{j-1} \sigma_-^j \\ \hat{b}_j^\dagger &\rightarrow \left(\prod_{l=1}^{j-1} -\sigma_z^l \right) \sigma_+^j = (-1)^{j-1} \sigma_z^1 \sigma_z^2 \cdots \sigma_z^{j-1} \sigma_+^j \end{aligned} \tag{6.6}$$

6.2.1 Application of J-W Transformation to Fermi-Hubbard Hamiltonian

Here we apply the J-W Transformation with the objective to map the target two sites fermionic Hamiltonian into a 4-qubits registry. We first need to define a mapping for lattice sites and electronic spins on the qubit registry:

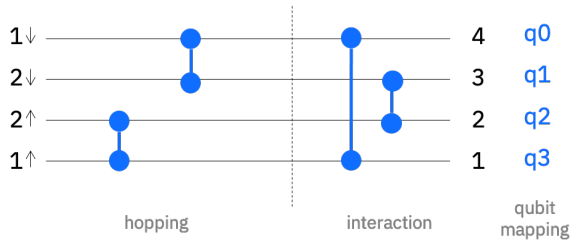

Figure 6.1: Mapping between Fermi-Hubbard model and Qubits used. Note on the left the numbers 1 and 2, representing the lattice sites, and the spin of the particles ↑ and ↓. The hopping (of kinetic) term represents the Fermions hopping between site 1 and site 2, with the same spin; the interaction term represents the interaction of different spin species in the same site.

Here we report the calculation of hopping and interaction terms of Fermi-Hubbard Hamiltonian of Eq. 6.2 using the spin notation, leveraging on the above defined transformations.

- **Hopping term**: using Eq. 6.6, the first term of Eq. 6.2 can be written in spin notation as:

$$\mathcal{H}_{hop} = -\frac{t}{2}\Big(\sigma_x \otimes \sigma_x + \sigma_y \otimes \sigma_y\Big) \tag{6.7}$$

Taking into account the mapping introduced in Fig. 6.1, this term becomes:

$$\begin{aligned}\mathcal{H}_{hop} = t\Big[&(\sigma_x \otimes \sigma_x \otimes \mathbb{I} \otimes \mathbb{I}) + (\sigma_y \otimes \sigma_y \otimes \mathbb{I} \otimes \mathbb{I}) \\ &+(\mathbb{I} \otimes \mathbb{I} \otimes \sigma_x \otimes \sigma_x) + (\mathbb{I} \otimes \mathbb{I} \otimes \sigma_y \otimes \sigma_y)\Big]\end{aligned} \tag{6.8}$$

- **Interaction term**: the transformation of the interaction term follows a similar approach. Starting from the latter term of Eq. 6.2, rewritten here as $\mathcal{H}_{int} = V(\hat{n}_{i\uparrow}\hat{n}_{i\downarrow}) = V(\hat{b}^{\dagger}_{i\uparrow}\hat{b}_{i\uparrow})(\hat{b}^{\dagger}_{i\downarrow}\hat{b}_{i\downarrow})$ it is possible to obtain a compact notation for the fermionic operators:

$$\begin{aligned}\hat{b}^{\dagger}_{1\uparrow} &= \sigma^{+} \otimes \mathbb{I} \otimes \mathbb{I} \otimes \mathbb{I} \\ \hat{b}^{\dagger}_{1\downarrow} &= \sigma_z \otimes \sigma^{+} \otimes \mathbb{I} \otimes \mathbb{I} \\ \hat{b}^{\dagger}_{2\uparrow} &= \sigma_z \otimes \sigma_z \otimes \sigma^{+} \otimes \mathbb{I} \\ \hat{b}^{\dagger}_{2\downarrow} &= \sigma_z \otimes \sigma_z \otimes \sigma_z \otimes \sigma^{+}\end{aligned} \tag{6.9}$$

$$\begin{aligned}\hat{b}_{1\uparrow} &= \sigma^{-} \otimes \mathbb{I} \otimes \mathbb{I} \otimes \mathbb{I} \\ \hat{b}_{1\downarrow} &= \sigma_z \otimes \sigma^{-} \otimes \mathbb{I} \otimes \mathbb{I} \\ \hat{b}_{2\uparrow} &= \sigma_z \otimes \sigma_z \otimes \sigma^{-} \otimes \mathbb{I} \\ \hat{b}_{2\downarrow} &= \sigma_z \otimes \sigma_z \otimes \sigma_z \otimes \sigma^{-}\end{aligned} \tag{6.10}$$

Thus, considering Eq. 6.9 and Eq. 6.10 together with the definition of σ^{+} and σ^{-}, and the mapping depicted in Fig. 6.1, the full interaction term can be written in a compact spin notation as:

$$\begin{aligned}\mathcal{H}_{int} = V\Big[&(\sigma_z \otimes \mathbb{I} \otimes \mathbb{I} \otimes \sigma_z) + (\mathbb{I} \otimes \sigma_z \otimes \sigma_z \otimes \mathbb{I}) \\ &+(\sigma_z \otimes \mathbb{I} \otimes \mathbb{I} \otimes \mathbb{I}) + (\mathbb{I} \otimes \sigma_z \otimes \mathbb{I} \otimes \mathbb{I}) \\ &(\mathbb{I} \otimes \mathbb{I} \otimes \sigma_z \otimes \mathbb{I}) + (\mathbb{I} \otimes \mathbb{I} \otimes \mathbb{I} \otimes \sigma_z)\Big]\end{aligned} \tag{6.11}$$

Combining the hopping term (Eq. 6.8) and the interaction term (Eq. 6.11) transformed according to the Jordan-Wigner Transformations, it is possible to obtain the full Fermi-Hubbard model Hamiltonian in spin notation. Here we report a compact notation, considering the qubit number (1 to 4, following the mapping of Fig. 6.1) on which to apply the quantum gates:

$$\begin{aligned} \mathcal{H} &= \mathcal{H}_{hop} + \mathcal{H}_{int} \\ &= \frac{t}{2}\left[(\sigma_x^1 \otimes \sigma_x^3 + \sigma_y^1 \otimes \sigma_y^3) + (\sigma_x^2 \otimes \sigma_x^4 + \sigma_y^2 \otimes \sigma_y^4)\right] \\ &+V\left[(\sigma_z^1 \otimes \sigma_z^2 + \sigma_z^3 \otimes \sigma_z^4) + (\sigma_z^1 + \sigma_z^2 + \sigma_z^3 + \sigma_z^4)\right] \end{aligned} \tag{6.12}$$

6.3 Error mitigation approaches

In order to be able to handle the requirements in terms of circuit depth (metric that calculates the longest path between the data input and the output in terms of single, two-qubits gate, where each gate counts as a unit) for both VQE and Digital Quantum Simulations on IBM Quantum devices, we apply a set of error mitigation techniques that can be classified in two different approaches.

- **Post Selection**: this technique is implemented iteratively inside the algorithm, and is based on the classification of the given output states in *allowed* and *unallowed* states. The time evolution of quantum mechanical systems follows the conservation laws for some physical quantities, i.e. the number of particles and the total spin for the Hubbard model: in this case, the two different spin species $\uparrow$ and $\downarrow$ are then both separately conserved. The same consideration can be done on VQE algorithm: in this case the ansatz can be structured in order to span just the subspace of the Hilbert space where the particles number and the total spin are conserved. Being this conservation ensured by the theory, the results violating the species conservation can be discarded. The Post Selection error mitigation technique has been implemented by computing the observable values selecting only the *allowed* states, and then normalizing the wave function. The best results obtained by this Post Selection technique take place when there is an almost uniform leakage of counts among the *allowed* states to the *unallowed* states. In this case, the shape of the wave function is unaltered, and both ground state and time evolution are scaled and corrected according to a normalization factor.

  This technique could be improved by demanding to proper quantum algorithm the computation of counts occurred in *allowed* states, e.g. the Quantum Counting algorithm [146]. This improvement is however not subject of this work.

- **Best qubit layout**: it is important to be aware of the actual calibration and configuration of the selected quantum chip. Is it possible to choose the best qubits to be used in terms of qubit calibration and quantum chip layout. The latter is particulary critical: being able to choose the best connected qubits considering the mapping in Fig. 6.1 can help to reduce the SWAP gates needed to transpile the circuit on the hardware to perform calculations. The best layout can be chosen programmatically by Qiskit [119] using the transpiler; however, for this kind of simulations on quite small systems, keeping the control on the qubits involved in the calculation could be required to further improve the results.

6.4 Simulation of static properties

We start the investigation of Fermionic systems by performing the Ground State energy calculation using VQE algorithm [147][148][149], for different V/T ratios. In order to let the VQE algorithm find the GS energy of this model, it is important to choose an ansatz that best fits the complexity of the problem [150]. A Physically Motivated Ansatz (PMA) [122] conserving the total number of Fermions has been built (as introduced above about error mitigation in Sec. 6.3) considering the chosen model mapping on the qubit registry; the circuit creating the ansatz is reported in Fig. 6.2.

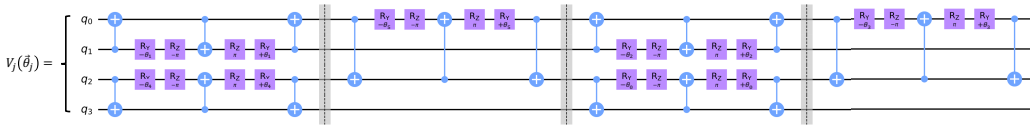

Figure 6.2: Full ansatz used to calculate Fermi-Hubbard model 2-sites GS energy. Note the 6 parameters (from θ_0 to θ_5) as the rotation angle in all R_y gates, with the proper sign, and the application of the mapping depicted in Fig. 6.1.

We make here a comparison between raw results and mitigated results, with Measurement Error Mitigation [130] technique applied. Results reported in Fig. 6.3(a) show a good accordance between calculated and expected GS energies, in particular for low V/T ratio. Fig. 6.3(b) show the noisy simulated GS components: the expected *allowed* states can be recognized as 0101, 0110, 1001, 1010 considering the problem mapping. Results are simulated using a noise model derived from IBM Quantum `ibmq_montreal` QV 128 device. It is worth noting that the Measurement Error Mitigation technique is able to reduce the effect of Readout Errors by lowering the probability to find the GS in an *unallowed* state.

6.5 Simulation of dynamic properties

Many studies on how to simulate Fermi-Hubbard model on current quantum device have been already carried on [140][139], together with works on how to reach a practical computational advantage [151][152] on this kind of computations. In order to test the hardware behaviour and the above mentioned error mitigation techniques [153], we present here the simulation of the time evolution of a initial state composed by two particles, with the objective to observe the behaviour of $n_{1\uparrow}$, $n_{1\downarrow}$, $n_{2\uparrow}$, $n_{2\downarrow}$ quantities, intended as the probability to find the particles in a specific site with a specific spin. In order to perform a Digital Quantum Simulation, it is needed to implement the Suzuki-Trotter decomposition for fixed V/T ratio.

6.5.1 Suzuki-Trotter decomposition

The best form of Fermi-Hubbard model Hamiltonian ready to be implemented on quantum processor is built from Eq. 6.9 and Eq. 6.10. An introduction of the Suzuki-Trotter

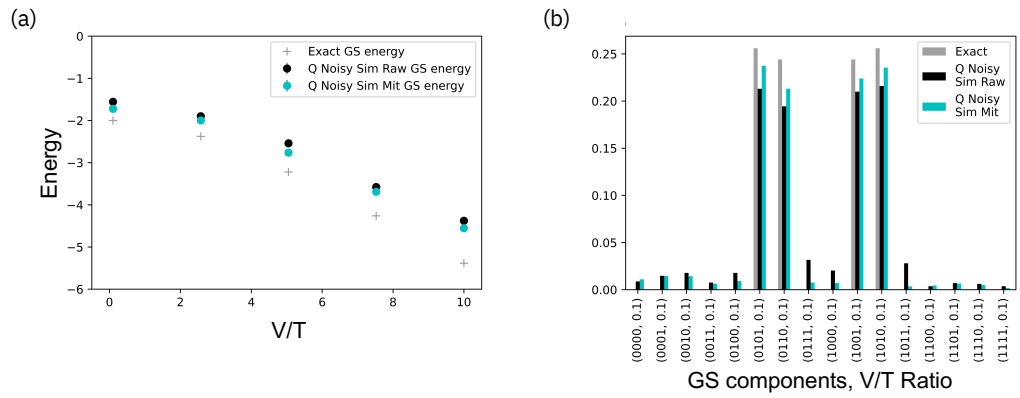

Figure 6.3: Fermi-Hubbard model VQE noisy simulations performed with a custom noise model derived from IBM Quantum Montreal QV 128 device. (a) GS energy for various V/T ratios. (b) GS components at fixed $V/T = 0.1$. Measurement Error Mitigation improves the GS components results, in particular by reducing the leakage to *unallowed* states.

decomposition is reported in Sec. 1.2.1; here we present an optimization of the Suzuki-Trotter approach by applying a second order decomposition on $\mathcal{H}_{hop}$ term (the same approach is possible on $\mathcal{H}_{int}$ term), obtaining:

$$\begin{aligned} e^{-i(\mathcal{H}_{hop}+\mathcal{H}_{int})t} &= e^{-i\mathcal{H}_{hop}t}e^{-i\mathcal{H}_{int}t} + O(t^2) \\ &\rightarrow e^{-i\frac{\mathcal{H}_{hop}}{2}t}e^{-i\mathcal{H}_{int}t}e^{-i\frac{\mathcal{H}_{hop}}{2}t} + O(t^3) \end{aligned} \tag{6.13}$$

This strategy allows one to optimize the S-T decomposition in terms of Trotter steps needed, but a trade-off analysis between quantum circuit length and digital error is still necessary. While a single σ^z can be easily implemented on a quantum computer using a standard rotation among z-axis, the implementation of $\sigma^x \otimes \sigma^x$, $\sigma^y \otimes \sigma^y$ and $\sigma^z \otimes \sigma^z$ require the application of a transformation of the reference coordinate system, as two-body terms require two-qubit gates. In particular, the relationships used are the following [14]:

$$\begin{aligned} \hat{X} &\rightarrow [R_y(-\frac{\pi}{2})\ Z\ R_y(\frac{\pi}{2})] \\ \hat{Y} &\rightarrow [R_x(-\frac{\pi}{2})\ Z\ R_x(\frac{\pi}{2})] \\ \hat{Z}\hat{Z} &\rightarrow [CNOT\ R_z(2\delta)\ CNOT] \end{aligned} \tag{6.14}$$

where the parameter δ is the angle related to the time evolution of the system. Hence, we can create the needed building blocks to map the spin Hamiltonian (Eq. 6.12) as reported in Fig. A.1. The quantum circuit describing the Fermi-Hubbard model Hamiltonian time evolution is reported in Fig. 6.4.

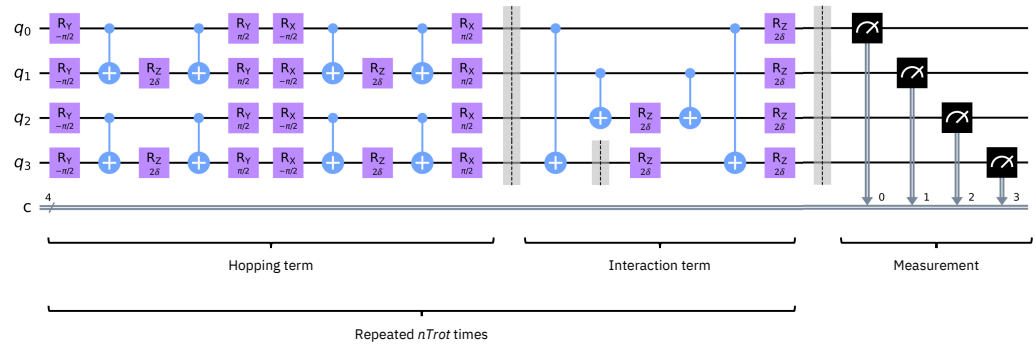

Figure 6.4: Single Suzuki-Trotter step of the Fermi-Hubbard model Time Evolution circuit, consisting of the hopping term and of the interaction term, following the above defined mapping. The angle 2δ in each R_z gates represents the time of the time evolution. The main circuit block needs to be repeated $n =$ Suzuki-Trotter steps times. A final measurement on each qubit is required to extract the observables; considering 3 S-T steps, obtaining an overall circuit depth ~ 90, the Readout error effect is negligible, making practically useless the Measurement Error Mitigation.

6.5.2 Time evolution

With the above introduced S-T decomposition, we now report the results of the time evolution of the system initialized in a well defined initial particle configuration. Several tests have been performed in order to find the best trade-off between the quality of the decomposition and the error introduced due to an increasing number of quantum gates involved: for the target model, current quantum devices are able to handle between 3 and 5 Suzuki-Trotter steps. It is worth noting that this limited amount of S-T steps introduces a difference between the exact time evolution and the actual (decomposed) one; quantum computed results are thus considered valid until the two slopes diverge (i.e. on $t \sim 3$ for 3 S-T steps, as reported in Fig. 6.5).

We report in Fig. 6.5 the results of the time evolution of a state starting from both Fermions on the same lattice site $(1_\uparrow, 1_\downarrow)$. Panel a) shows the noisy simulation for observable $n_{1\downarrow}$ with a noise model derived from the IBM Quantum Rome QV 32 (noise parameters reported in Tab. 6.1), while panel b) shows the results computes on the actual IBM Quantum Rome device. In both cases, the circuit consists of 242 gates (188 single-qubit gates 54 two-qubits gates), which sum up to an overall circuit depth of 89, approaching limits of prototype devices at the moment of computation (early 2021). The applied error mitigation techniques, in particular Post Selection (as the effect of Measurement Error Mitigation is negligible) are able to significantly correct the raw results (black series) obtaining a remarkable agreement between mitigated results (cyan series) and the expected behaviour of the spin Hamiltonian time evolution with 3 S-T steps (green solid line).

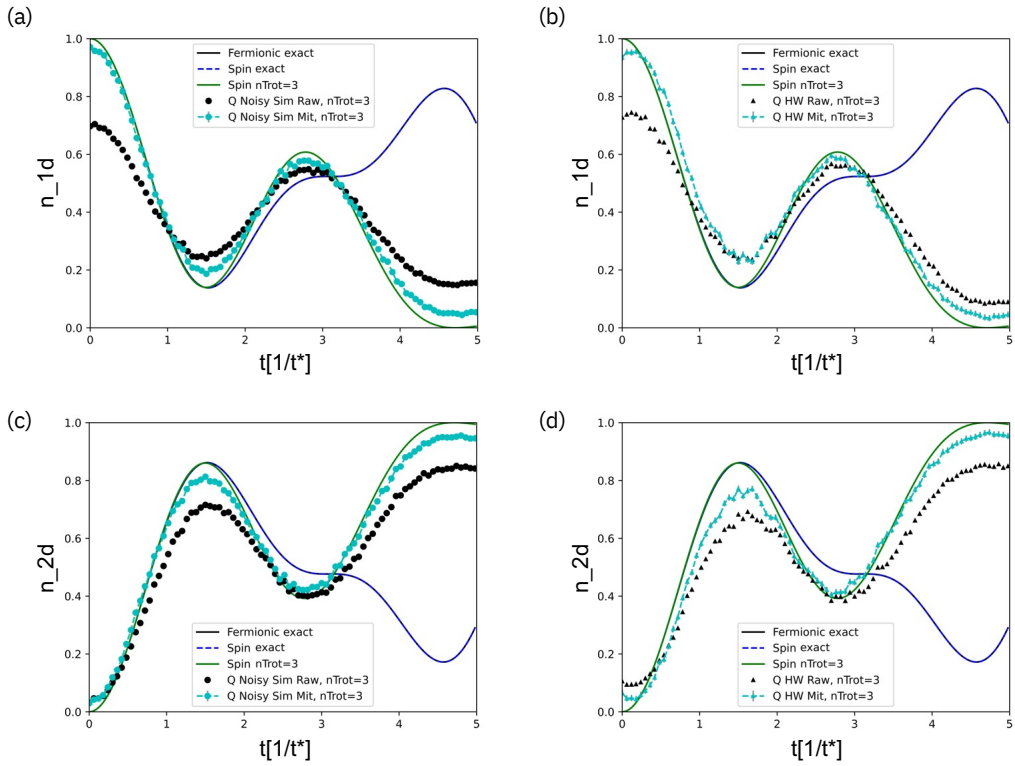

Figure 6.5: Time evolution results for an initial state with both Fermions on the same lattice site $(1_\uparrow, 1_\downarrow)$. (a) Noisy simulations with IBM Quantum Rome QV 32 noise model for $n_{1\downarrow}$ observable. (b) Real hardware computation on IBM Quantum Rome QV 32 device for $n_{1\downarrow}$ observable. (c)-(d) Noisy simulations and real hardware results for $n_{2\downarrow}$ observable, where the errorbars on hardware mitigated results are $1/\sqrt{shots}$, with $shots = 8192$. The applied error mitigation techniques (in particular Post Selection) are able to rescale well the results, achieving a remarkable agreement with the expected behaviour. The overall observables $n_{1\downarrow}$ and $n_{2\downarrow}$ should be symmetric with respect to the x axis, as shown by the exact simulations; however, differences in the qubits calibration at the moment of the calculation lead to an asymmetry: e.g. panel (a) $n_{1\downarrow}(t = 0) \sim 0.75$ (black dots) while panel (c) $n_{2\downarrow}(t = 0) \sim 0.1 \neq (1 - n_{1\downarrow}(t = 0))$ (black dots). However, the applied error mitigation techniques are able to correct this issue, as $n_{2\downarrow}(t = 0) \sim (1 - n_{1\downarrow}(t = 0))$ (cyan dots, panels (a) and (c)).

T_1	134.7 μs
T_2	105 μs
Single-qubit Gate Error	2.6×10^{-4}
Two-qubit Gate Error	$7.4 \cdot 10^{-3}$
Readout Error	$2.1 \cdot 10^{-2}$

Table 6.1: Main details of the noise model for the IBM Quantum QV 32 device in February 2021.

Part IV

Quantum computation with Molecular Nanomagnets

CHAPTER 7

Molecular Nanomagnets for qudit-based computation

In Part III of this document is reported the work performed using currently available Quantum Computers, in particular IBM Quantum devices, where simple spin and fermionic models have been used as test beds for both hardware and algorithms. The results reported in Chap. 5 and Chap. 6 show that current devices are able to reproduce well set of observables of this kind of systems; however, an important limitation is the effect of noise. Current Quantum Computers are intrinsically and largely affected by decoherence, limiting their potential and reliability. An interesting solution to overcome aforementioned limitations of current devices is to exploit systems with embedded Quantum Error Correction, or systems with many accessible levels, enabling the simplification of various algorithms. A specific class of quantum systems with many accessible energy levels are the Molecular Nanomagnets.

Molecular Nanomagnets (MNMs), as described in Chap. 4, are very promising fundamental units of computation to design the new generations of Quantum computing architectures [154][90][155]; this class of molecules can be manipulated with proper magnetic pulses [156], and can be deployed on surfaces [157][158] and in superconducting resonators [159], introduced in Chap. 3. Molecular Nanomagnets intrinsic possibility to display more than two levels with remarkable coherence [45][160] is a key feature enabling the implementation of a new kind of fundamental unit for quantum computation, namely *qudit* (quantum-digit). Also, the large number of accessible levels could simplify the the implementation of several algorithms, due to the large amount of computational states available.

In this Chapter we study two different MNM configurations. The first one is a class of iso-structural molecules with ferromagnetic exchange interactions, consisting of a single spin $S > 1$ (S-systems). They are very common compounds and there is a lot of literature about them, and well differentiated energy gaps can lead to high fidelity on quantum gates implementation; they are also relatively easy to be synthesized. On the other hand, they have only a linear connectivity between energy levels, allowing only transitions with $\Delta m = \pm 1$, and decoherence effect becomes larger by increasing the size of the qudits.

The second one is a class of artificial molecules consisting of multi-spin clusters with anti-ferromagnetic competing spin-spin interactions (C-systems) between different magnetic ions [161]. These molecules have many low-spin multiplets at low energy, an high

connectivity between levels allowing a more flexible approach to level transitions, and most importantly, a suppression of decoherence [162] even by increasing the size of the qudits. Several molecules with competing interactions exist: here we focus on Cu^3 triangle [163] with almost frustrated ground state, and on a class of molecule with a double-tetrahedron arrangement, like Ni^7 [164].

We tested these systems by implementing and simulating a generalized Hadamard gate [165], representing a Quantum Fourier Transform, with a proper decomposition into several elementary operations. This set of single-qudit gates, together with the realisation of a two-qudit Controlled-Phase gate, provide an universal set of quantum gates for molecular spin qudits.

7.1 Model molecular systems

Here we introduce the above mentioned MNM systems; as described in the below Sections, two key features of a candidate molecule to implement qudits are the presence of many low-energy eigenstates (mitigating decoherence), and the presence of magnetic dipole matrix elements among most of them (enabling efficient qudit state manipulation). These features have been take in consideration in the presented molecular system models.

7.1.1 Single spin systems

The first considered system to implement a qudit is a molecule containing a single magnetic ion, with a spin $> 1/2$; I specifically focused on these systems. The Hamiltonian describing such systems is the following:

$$\mathcal{H}_{single} = \mathcal{D}S_z^2 + g\mu_B B_0 S_z \tag{7.1}$$

where the first term is the the Zero-Field Splitting (ZFS) with coupling $\mathcal{D}$, and the second term is the Zeeman interaction of the ion with an external magnetic field B_0, parametrized by g. For simplicity, the axial anisotropy and the external magnetic field are assumed parallel [1]. Here, $\mathcal{H}_S$ and S_z itself share a common basis of eigenstates: $S_z|m\rangle = m|m\rangle$. We simulated three different S-systems with an increasing spin, depicted in Fig. 7.1, with real parameters:

- System **S1**: $S = 3/2$ ion, e.g. Cr^{3+}, with $\mathcal{D} = 30$ μeV and $g = 1.98$ [166][167].
- System **S2**: $S = 5/2$ ion, e.g. Fe^{3+} or Mn^{2+}, with $\mathcal{D} = 30$ μeV and $g = 2.0$ [166][167].
- System **S3**: $S = 7/2$ ion, e.g. Gd^{3+}, with $\mathcal{D} = 20$ μeV and $g = 2.0$ [168].

The above introduced single spin molecular systems are characterized by real parameters: it is possible to find more details in the reported References.

[1] The analysis can be extended to handle more complex situations.

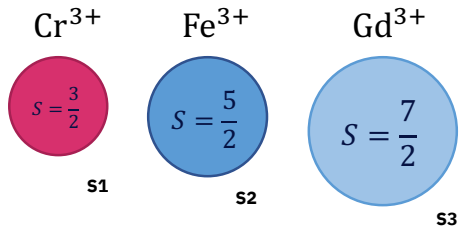

Figure 7.1: Single spin $S > 1$ MNMs [166][167][168].

7.1.2 Multi-spin systems with competing interactions

The second system that has been considered in order to implement a qudit is a molecule consisting of multi-spin with competing interactions, described by the following Hamiltonian:

$$\mathcal{H}_{c.i.} = \sum_{i>j}^{N} J_{i,j}\mathbf{s}_i \cdot \mathbf{s}_j + \sum_{i>j}^{N} \mathbf{D}_{i,j} \cdot \mathbf{s}_i \times \mathbf{s}_j + \mu_B \mathbf{B}_0 \cdot \sum_{i}^{N} \mathbf{g}_i \cdot \mathbf{s}_i \tag{7.2}$$

where the first term is the isotropic exchange interaction between the ions, coupled by $J_{i,j}$; the second term is the Dzyaloshinskii–Moriya interaction (DMI), coupled by $\mathbf{D}_{i,j}$; the third term is the Zeeman interaction of each single ion with the external magnetic field $\mathbf{B}_0$, parametrized by $\mathbf{g}_i$; $\mathbf{s}_i$ are the spin operators. I contributed to simulate two different systems, depicted in Fig. 7.2 and Fig. 7.3, with realistic parameters:

- System **C1**: existing frustrated triangular Cu^3 molecule, consisting of three $s_i = 1/2$ ions arranged in a triangular shape (almost isosceles), with parameters $J_{12} = 0.390$ meV, $J_{13} = J_{23} = 0.348$ meV, $g_1^{xx} = g_1^{yy} = 2.2$, $g_2^{xx} = g_2^{yy} = 2.1$, $g_3^{xx} = g_3^{yy} = 2.4$, $g_i^{zz} = 2.0$; $D_{12}^x = D_{12}^y = D_{12}^z = 0.045$ meV ($D \sim J/10$) [163]. The energy levels spectrum reported in Fig. 7.2 shows two low-energy doublets, splitted by the difference between J_{12} and J_{13}, and an higher energy multiplet. The presence of the DMI induces an anti-crossing at $B_0 \sim 0.8$ T, mixing the two multiplets. The simulations have been performed with a static magnetic field $B_0 = 1$ T, tilted by $\theta = 1$ rad with respect to the z axis in the xz plane.

- System **C2**: hypothetical system consisting of eight $S = 1/2$ low-energy multiplets, reported in Fig. 7.3, with $s_i = 1/2$ for $i = 1, ..., 6$, $s_7 = 3/2$, with parameters: $J_{i,7} = 0.95$ meV, $J_{1,2} = 1.29$ meV, $J_{2,3} = J_{3,1} = 1.25$ meV, $J_{4,5} = 1.41$ meV, $J_{5,6} = J_{6,4} = 1.36$ meV and g-factors $g_1 = g_2 = g_4 = g_5 = 2.1$, $g_3 = g_6 = 2.15$ and $g_7 = 2$, typical for Cu^{2+} (s_{1-6}) and Cr^{3+} (s_7) arranged in a double-tetrahedron shape, similar to Ni^7 [164]. The simulations have been performed with a static magnetic field of 2.7 T along z axis, and with only the z component of DMI vector ($D_{i,j}^z = J_{i,j}/10$), similar to **C1** system.

Panel a) of both Fig. 7.2 and Fig. 7.3 report the spectrum of energy levels: both considered molecules display low-spin multiplets at low energy, crucial feature to be taken into account when dealing with decoherence.

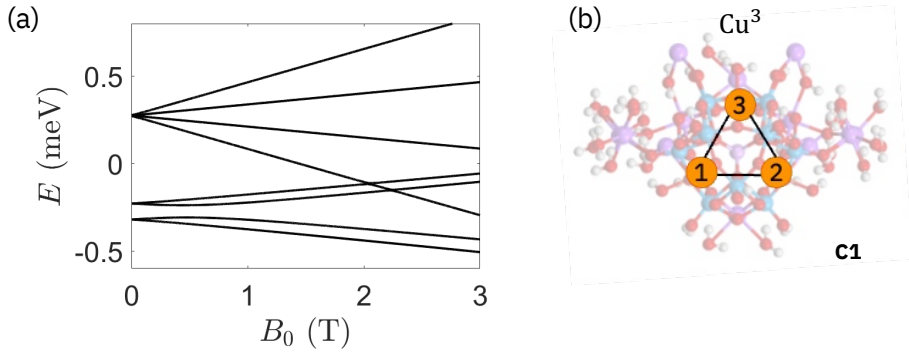

Figure 7.2: (a) Energy levels in function of external magnetic field B_0 (tilted by $\theta = 1$ rad with respect to the z axis in the xz plane) of multi-spin triangular molecule **C1** with competing interaction. (b) Scheme of the magnetic core structure, where solid black lines represent the interactions between the magnetic ions. Reproduced from Ref. [46] with permission from Phys. Rev. Research (available under the terms of the Creative Commons Attribution 4.0 International license).

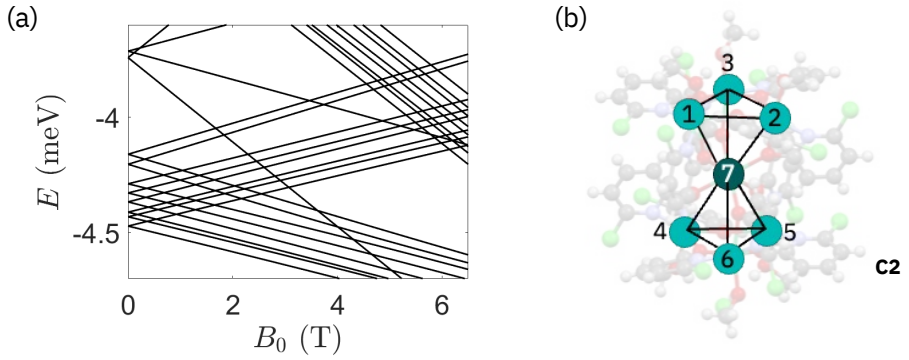

Figure 7.3: (a) Energy levels in function of external magnetic field B_0 (along the z axis) of multi-spin hypothetical double-tetrahedron molecule **C2** with competing interaction. (b) Scheme of the magnetic core structure, where solid black lines represent the interactions between the magnetic ions. Reproduced from Ref. [46] with permission from Phys. Rev. Research (available under the terms of the Creative Commons Attribution 4.0 International license).

7.2 Description of decoherence

Pure dephasing, induced by the coupling of the magnetic ions spins with the surrounding nuclear spins, is the main error influencing the quantum state of a MNM. As described in Sec. 1.3, solving Lindblad master equation for the density matrix leads to an exponential decay of the off-diagonal elements of local spin operators (i.e. the connectivity of levels does not affect it). In order to describe the effect of pure dephasing, we consider a markovian bath, and we use Lindblad approximation to describe the system dynamics, as already introduced in Sec. 1.3.2.

7.2.1 Derivation of the master equation

In order to describe the time evolution of the density matrix, we report here some details of the derivation of the master equation, already published in Ref. [162]. It is possible to write the Hamiltonian of the interaction between the system and the nuclear spin bath as the following:

$$\mathcal{H}_{SB} = \sum_{j=1}^{N}\sum_{n=1}^{M}\sum_{\alpha,\beta=x,y,z} d_{jn}^{\alpha\beta} s_j^{\alpha} \otimes I_n^{\beta} \tag{7.3}$$

where N is the number of the magnetic ions of the system, M is the number of nuclear spins in the bath, I_n^{β} are the bath spin operators and $d_{jn}^{\alpha\beta}$ are components of the dipole-dipole interaction tensor (in point dipole approximation, and for isotropic nuclear magnetic moments)

$$d_{jn}^{\alpha\beta} = \frac{\mu_B \mu_N g_N}{R_{jn}^3}\left[g_j^{\alpha\beta} - 3\frac{R_{jn}^{\beta}(\sum_\gamma g_j^{\alpha\gamma} R_{jn}^{\gamma})}{R_{jn}^2}\right] \tag{7.4}$$

with g_N the nuclear g-factor, μ_N the nuclear magneton and R_{jn}^{α} the α component of the distance between the j-th electronic spin and n-th nuclear spin ($\alpha = x, y, z$). Defining $\mathcal{H}_S$ as the Hamiltonian of the free system and $\mathcal{H}_B$ the Hamiltonian of the bath, it is possible to write the interaction picture in the form:

$$\begin{aligned}\mathcal{H}_{SB}(t) &= e^{i(\mathcal{H}_S+\mathcal{H}_B)t/\hbar}\mathcal{H}_{SB}e^{-i(\mathcal{H}_S+\mathcal{H}_B)t/\hbar} \\ &= \sum_{n=1}^{M}\sum_{\mu\nu}\sum_{\beta} L_{n,\mu\nu}^{\beta} e^{i(E_\mu - E_\nu)t}|\mu\rangle\langle\nu| \otimes I_n^{\beta}(t)\end{aligned} \tag{7.5}$$

where $|\mu\rangle$ is the basis of the system eigenstates ($\mathcal{H}_S = \sum_\mu E_\mu |\mu\rangle\langle\mu|$) and $I_n^{\beta}(t)$ are the nuclear spin operators in interaction picture

$$I_n^{\beta}(t) = e^{i\mathcal{H}_B t/\hbar} I_n^{\beta} e^{-i\mathcal{H}_B t/\hbar} \tag{7.6}$$

and the $L_{n,\mu\nu}^{\beta}$ are defined as

$$L_{n,\mu\nu}^{\beta} = \sum_{j=1}^{N}\sum_{\alpha=x,y,z} d_{jn}^{\alpha\beta}\langle\mu|s_j^{\alpha}|\nu\rangle \tag{7.7}$$

containing the structure of the system eigenstates in the matrix elements $\langle\mu|s_j^{\alpha}|\nu\rangle$. The dynamic of the system (in Born and Markov approximations) is described by the master equation [169]:

$$\frac{d\rho(t)}{dt} = -\int_0^{\infty} dt' \mathrm{tr}_B\Big[\mathcal{H}_{SB}(t), [\mathcal{H}_{SB}(t-t'), \rho(t)\otimes\rho_B]\Big] \tag{7.8}$$

where the reduced density matrix of the system (as per Eq. 1.46) has been used. It is then possible to obtain:

$$\frac{d\rho(t)}{dt} = -\sum_{n,n'=1}^{M}\sum_{\mu,\nu}\sum_{\beta\beta'}\left\{L^{\beta}_{n,\mu\mu}L^{\beta',*}_{n',\nu\nu}\zeta^{\beta\beta'}_{nn'}(\omega)\Big[|\mu\rangle\langle\mu|\nu\rangle\langle\nu|\rho(t) - |\mu\rangle\langle\mu|\rho(t)|\nu\rangle\langle\nu|\Big] + \text{h.c.}\right\} \tag{7.9}$$

where the $\zeta^{\beta\beta'}_{nn'}(\omega)$ are the bath spectral functions, in general unknown and hard to compute, defined as:

$$\zeta^{\beta\beta'}_{nn'}(\omega) = \int_0^{\infty} dt\ \text{tr}_B\left[I^{\beta}_n(t)I^{\beta'}_{n'}(0)\rho_B\right]e^{i\omega t} \tag{7.10}$$

It is worth noting that in Eq. 7.9 operators of the form $|\mu\rangle\langle\nu|$ (with $\mu \neq \nu$) have been neglected because the difference between $\Delta_{\mu\nu}$ and the energy gaps of the bath is much larger than the system-bath interaction. In this limit, only diagonal operators $|\mu\rangle\langle\mu|$ are considered (pure dephasing). Finally, it is possible to rewrite Eq. 7.9 in a more compact form:

$$\frac{d\rho(t)}{dt} = -i[\mathcal{H}_{LS}, \rho(t)] + \sum_{\mu\nu}\Gamma_{\mu\nu}\Big[2|\mu\rangle\langle\mu|\rho(t)|\nu\rangle\langle\nu| - |\mu\rangle\langle\mu|\delta_{\mu\nu}\rho(t) - \rho(t)|\nu\rangle\langle\nu|\delta_{\mu\nu}\Big] \tag{7.11}$$

where the coefficients $\Gamma_{\mu\nu}$ are defined as

$$\Gamma_{\mu\nu} = \sum_{n,n'=1}^{M}\sum_{\beta,\beta'}L^{\beta}_{n,\mu\mu}L^{\beta',*}_{n',\nu\nu}\chi^{\alpha\alpha'}_{nn'}(0) \tag{7.12}$$

with

$$\chi^{\alpha\alpha'}_{nn'}(0) = \frac{1}{2}\int_{-\infty}^{\infty} dt\ \text{tr}_B[I^{\alpha}_n(t)I^{\alpha'}_{n'}(0)\rho_B] \tag{7.13}$$

and where $\mathcal{H}_{LS} = \sum_{\mu} S_{\mu}|\mu\rangle\langle\mu|$ is the Lamb shift Hamiltonian, not considered in the simulations as it introduces a small renormalization of the energies. Hence, the final form of the dynamics of the density matrix is described by:

$$\frac{d\rho(t)}{dt} = -i[\mathcal{H} + \mathcal{H}_1, \rho] + \sum_{\mu\nu}\Gamma_{\mu\nu}\Big(2|\mu\rangle\langle\mu|\rho|\nu\rangle\langle\nu| - \delta_{\mu\nu}|\mu\rangle\langle\mu|\rho - \delta_{\mu\nu}\rho|\nu\rangle\langle\nu|\Big) \tag{7.14}$$

where the first term is the coherent time evolution of the Hamiltonian (with $\mathcal{H}_1$ is the driving pulse Hamiltonian), and the second term is the dissipator operator introduced in Eq. 1.51, modeling pure dephasing. $|\mu\rangle$ and $|\nu\rangle$ are the system eigenstates.

7.2.2 Pure dephasing

Eq. 7.14 implies the decay of the off-diagonal elements of the density matrix $\rho_{\mu\nu}(t) = e^{-\gamma_{\mu\nu}}\rho_{\mu\nu}(0)$ where $\gamma_{\mu\nu} = -2\Gamma_{\mu\nu} + \Gamma_{\mu\mu} + \Gamma_{\nu\nu}$. These coefficients are:

$$\Gamma_{\mu\nu} = \sum_{jj'=1}^{N} \sum_{\alpha\alpha'=x,y,z} \mathcal{C}_{jj'}^{\alpha\alpha'} \langle\mu|s_j^{\alpha}|\mu\rangle\langle\nu|s_{j'}^{\alpha'}|\nu\rangle \tag{7.15}$$

where the zero-energy bath spectral function $\mathcal{C}_{jj'}^{\alpha\alpha'}$ is defined as

$$\mathcal{C}_{jj'}^{\alpha\alpha'} = \sum_{nn'} \sum_{\beta\beta'} \chi_{nn'}^{\beta\beta'}(0) d_{jn}^{\alpha\beta} d_{j'n'}^{\alpha'\beta'} \tag{7.16}$$

where $\chi_{nn'}^{\beta\beta'}(0)$ is defined in Eq. 7.13, $d_{jn}^{\alpha\beta}$ and $d_{j'n'}^{\alpha'\beta'}$ is defined in Eq. 7.4. The pure dephasing described in Eq. 7.15 is thus mainly dependent on the difference between expectation values on local spin operators s_j^{α} on different eigenstates ($|\mu\rangle$ and $|\nu\rangle$). This is a general property of the system Hamiltonian: the eigenstates structure can be tuned to create e.g. ferromagnetic / anti-ferromagnetic interactions, or competing interaction patterns, by chemically engineering the ligand structure. Pure dephasing is also dependant on the structure of the molecule itself, in particular regarding the dipolar interactions between nuclear spins and electronic spins, involving the distances between them: this is dependant on the system itself. As we are mainly facing with model systems, we tested ~ 30 different random (but reasonable) configurations for nuclei positions: the general behaviour does not change significantly, having an impact only on T_2 times. Lastly, the bath spectral functions containing information about the intra-nuclei interactions, are unknown: we assumed them as constant.

We first consider the simplest case in order to understand the general behaviour: we describe how the form of the eigenstates can affect system decoherence considering the case of an axial Hamiltonian with an external magnetic field along z direction: in this case, we notice that $\langle\mu|S_\alpha|\mu\rangle \propto \delta_{\alpha z}$, with $S_\alpha = \sum_j s_j^{\alpha}$. The coefficients $\mathcal{C}_{jj'}^{\alpha\alpha'}$ are independent on j, j', thus $\Gamma_{\mu\nu} \propto \langle\mu|S_\alpha|\mu\rangle\langle\nu|S_\alpha|\nu\rangle$. Hence, the decay rate of the off-diagonal elements of the density matrix is:

$$\gamma_{\mu\nu} \propto \Big(\langle\mu|S_\alpha|\mu\rangle - \langle\nu|S_\alpha|\nu\rangle\Big)^2 \tag{7.17}$$

Decoherence is thus eliminated if subspaces are characterized by the same $\langle S_z\rangle$. Refer to Ref. [162] for more details.

7.2.3 Decoherence effect on considered molecular systems

As introduced in the previous Section, a molecular spin system is affected by decoherence depending on the structure of its eigenstates and its coupling with the surrounding nuclear spin bath. Here we describe this effect on the two above introduced molecular systems that have been exploited to simulate qudits, i.e. single spin (S-systems) and multi-spin with competing interaction systems (C-systems). In order to identify general properties of these systems to suppress decoherence, we first need to fix the position of nuclear and system spins in both cases. To do this, two iso-structural molecules are considered, in which we reverse the sign of the isotropic exchange. Indeed, we note that a multi-spin molecule with a ferromagnetic exchange as leading interaction, has a ground

state multiplet with total spin $S = \sum_{i=1}^{N} s_i$, independently from the actual values of $J_{ij} < 0$. This multiplet is characterized by the same eigenstates (namely $|m\rangle$) of a single spin ion, making it possible a comparison between S-systems and C-systems.

We can now compute the form of the $\langle m|s_j^\alpha|m\rangle$ of Eq. 7.15 [170]. In case of a ground state spin S multiplet with small anisotropy, we obtain:

$$\langle m|s_j^\alpha|m\rangle = \zeta_j \langle m|S_z|m\rangle \delta_{\alpha z} \tag{7.18}$$

where ζ_j are the projection coefficients. Is is possible to write the γ coefficients for both S-systems and C-systems:

$$\Gamma^S_{mm'} = \left(\sum_{jj'} \mathcal{C}^{zz}_{jj'} \zeta_j \zeta_{j'}\right) mm' = \frac{mm'}{T_2} \tag{7.19}$$

$$\Gamma^C_{mm'} = \frac{1}{T_2 \sum_{jj'} c^{zz}_{jj'} \zeta_j \zeta_{j'}} \sum_{jj'=1}^{N} \sum_{\alpha\alpha'} c^{\alpha\alpha'}_{jj'} \langle \mu|s_j^\alpha|\mu\rangle \langle \nu|s_j^{\alpha'}|\nu\rangle \tag{7.20}$$

where an effective dephasing rate has been introduced as $T_2^{-1} = \bar{\chi} \sum_{jj'} c^{zz}_{jj'} \zeta_j \zeta_{j'}$, that contains the information about the nuclear spin bath (i.e. the distribution of the nuclei and the bath spectral functions). The $\chi^{\beta\beta'}_{nn'}$ are considered constant (reported as $\bar{\chi}$) and factorized from the geometric factor $c^{zz}_{jj'}$; they are equal for both S-systems and C-systems. It is worth noting that Eq. 7.20 is written in terms of T_2 (i.e. dephasing time) and geometric factors $c^{\alpha\alpha'}_{jj'} = \sum_{nn'} \sum_{\beta\beta'} d^{\alpha\beta}_{jn} d^{\alpha'\beta'}_{j'n'}$.

A comparison between Eq. 7.19 and Eq. 7.20, respectively for S-systems and C-systems, suggests that the latter are protected by decoherence: the eigenstates of these systems are in fact characterized by a small total spin S and have small differences in the expectation values of the spins s_j^α; moreover, for S-systems the decoherence rate significantly changes by changing eigenstates, while is constant for C-systems.

In the following Sections we report the calculations performed to compare multi-spin systems with competing interactions **C1** and **C2** (see Fig. 7.2 and Fig. 7.3) with single spin systems **S1**, **S2** and **S3**, displaying substantial differences in the structure of the eigenstates. Refer to Ref. [46] for more details.

7.3 Quantum gates on qudit architectures: decomposition methods

Implementing the first quantum gates on the two introduced qudit architectures is the identified strategy to compare them in terms of performances and decoherence protection. To do this, a method to factorize generic unitary operations on a d-dimensional qudit into a sequence of elementary gates is required: here we exploit different existing methods [171]. The first one is called Planar Rotations (PR) [172][173][174][175], implementing Givens rotations between pairs of consecutive energy levels, that can be applied to any quantum system (both S-systems and C-systems, in this case). Transitions between consecutive energy levels (induced by electromagnetic pulses) need to be allowed by non-zero matrix elements (but are always present). The second method is

called Quantum Householder Reflection (QHR) and leverages on different connectivity between energy level (available on C-systems), allowing us to improve the efficiency of decomposition.

Before detailing the decomposition methods, we introduce in Fig. 7.4 the inter-level connectivity for qudit systems. The simplest connectivity is depicted in panel a), where levels are interconnected linearly. This is a specific feature of S-systems. Panel b) shows a pod connectivity, where an auxiliary level $|e\rangle$. Panel c) shows a full connectivity between energy levels. The reported $\omega_{\mu\nu}$ are the frequencies of the pulses used to implement the gate decomposition, addressing a pair of eigenstates $|\mu\rangle$ and $|\nu\rangle$. Systems with linear / full connectivity have been exploited for Planar Rotations decomposition, while systems with pod / full connectivity (with an extra level) have been exploited for Quantum Householder Reflection.

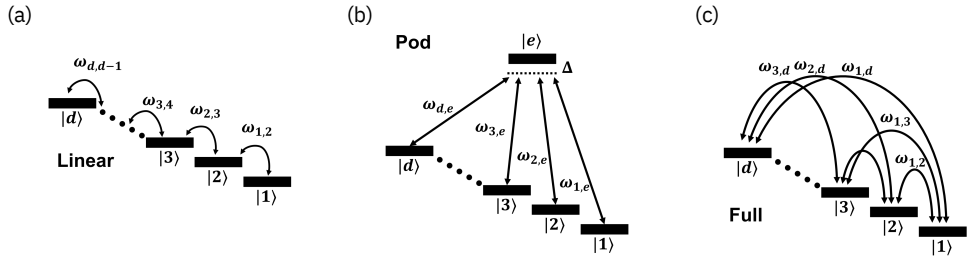

Figure 7.4: (a) "Linear" interconnected system, where only consecutive levels are interconnected. (b) "Pod" interconnected system, requiring an auxiliary level $|e\rangle$. (c) "Full" interconnected system. Reproduced from Ref. [46] with permission from Phys. Rev. Research (available under the terms of the Creative Commons Attribution 4.0 International license).

7.3.1 Planar Rotations

The basic rotation set between pairs of consecutive energy levels consists of $d\times d$ matrices of the form:

$$U_{\mu\nu}(\theta,\beta)=\cos\frac{\theta}{2}\Big(|\mu\rangle\langle\mu|+|\nu\rangle\langle\nu|\Big)+\sin\frac{\theta}{2}\Big(|\nu\rangle\langle\mu|e^{i\beta}-|\mu\rangle\langle\nu|e^{-i\beta}\Big)+\sum_{l\neq\mu,\nu}|l\rangle\langle l| \quad (7.21)$$

that is equal to the identity, except for the matrix elements identified by the intersection between μ-th row and ν-th column. Below we outline the algorithm for the decomposition of an arbitrary $W\in SU(d)$ in Planar Rotations.

- Multiply W on the right by $U_{d-1\,d}(\theta_{\frac{d(d-1)}{2}},\beta_{\frac{d(d-1)}{2}})$, with $\theta_{\frac{d(d-2)}{2}}$ and $\beta_{\frac{d(d-1)}{2}}$ such that the $(d,d-1)$ element of the resulting $W_1=WU_{d-1,d}(\theta_1,\beta_1)$ is zero.
- Compute $W_2=W_1U_{d-2,d}(\theta_{\frac{d(d-2)}{2}},\beta_{\frac{d(d-2)}{2}})$, fixing as before $\theta_{\frac{d(d-2)}{2}}$ and $\beta_{\frac{d(d-2)}{2}}$ angles to nullify the $W_2(d,d-2)$ element.

- Obtain the W_{d-1} matrix with all zeros on the d column and row, apart from the (d,d)-th element, which must have magnitude one (the matrix is unitary).
- Without affecting the d-th column and row, the same scheme is be repeated for all the others lines.

The resulting matrix is

$$\begin{gathered} WU_{d-1,d}U_{d-3,d}\dots U_{1,d}U_{d-2,d-1}\dots\dots U_{1,3}U_{1,2} = \\ \Lambda(e^{i\alpha_1}, e^{i\alpha_2}, \dots, e^{i\alpha_{d-1}}, e^{-i\sum_{k=1}^{d-1}\alpha_k}) \end{gathered} \tag{7.22}$$

where Λ is a diagonal matrix (its elements are shown between brackets). It is finally possible to obtain the decomposition of W in $\frac{d(d-1)}{2}$ Planar Rotations by reverting Eq. 7.22:

$$\begin{gathered} W = \Lambda(e^{i\alpha_1}, e^{i\alpha_2}, \dots, e^{i\alpha_{d-1}}, e^{-i\sum_{k=1}^{d-1}\alpha_k}) \\ U_{1,2}(\theta_1,\beta_1)U_{1,3}(\theta_2,\beta_2)U_{2,3}(\theta_3,\beta_3)\cdots\times \\ U_{1,d}(\theta_{\frac{(d-1)(d-2)}{2}+1}, \beta_{\frac{(d-1)(d-2)}{2}+1})\cdots\times \\ U_{d-2,d-1}(\theta_{\frac{(d-1)(d-2)}{2}+2}, \beta_{\frac{(d-1)(d-2)}{2}+2})\cdots\times \\ U_{d-1,d}(\theta_{\frac{d(d-2)}{2}}, \beta_{\frac{d(d-2)}{2}}) \end{gathered} \tag{7.23}$$

Each PR (Eq. 7.22) between a pair of eigenstates $|\mu\rangle$ and $|\nu\rangle$ connected by a dipole matrix element ($\propto \sum_j g_j^\alpha s_j^\alpha$) is implemented by a applying a transverse magnetic pulse, with a frequency in resonance with the selected transition. Now, the diagonal matrix Λ needs to be decomposed in a sequence of phase gates

$$P_{\mu\nu}(\alpha) = |\mu\rangle\langle\mu|e^{i\alpha} + |\nu\rangle\langle\nu|e^{-i\alpha} + \sum_{l\neq\mu,\nu}|l\rangle\langle l| \tag{7.24}$$

where each $P_{\mu\nu}(\alpha)$ is implemented by properly detuning the pulse frequency, obtaining a semi-resonant pulse between the selected eigenstates [176]. It is worth noting that the PR decomposition can always be implemented on quantum systems with different inter-level connectivity: if a direct transition between $|\mu\rangle$ and $|\nu\rangle$ is not allowed, the relative $U_{\mu\nu}$ can be decomposed by implementing a series of π pulses, acting as SWAP between levels, bringing the two levels near each other. This however increases definitely the length of the pulse sequence.

7.3.2 Quantum Householder Reflections

While I mainly focused on Planar Rotations approach, as a comparison we consider also Quantum Householder Reflections. Both approaches have been exploited for the following simulations. The QHR approach requires a specific inter-level connectivity (pod connectivity) between energy levels, exploiting an auxiliary level $|e\rangle$ connected to all the other states, as depicted in Fig. 7.4(b). This decomposition method can be applied only on C-systems, as the DMI term has the effect to mix the low-energy doublets allowing

a pod or even a full connectivity between the considered eigenstates. Below we outline the algorithm for the decomposition of an arbitrary $W \in SU(d)$ using Quantum Householder Reflection.

- Each step is represented by the QHR, defined as:

$$M(v,\phi) = \mathbb{I} + (e^{i\phi} - 1)|v\rangle\langle v| \tag{7.25}$$

  where $|v\rangle$ is a $d-$dimensional normalized complex vector and ϕ is an arbitrary phase.

- The calculation of v_i and ϕ_i can be done using an iterative process:

  - the parameter of the first QHR $M_1 = M(v_1, \phi_1)$ are defined as

$$\begin{aligned} \phi_1 &= 2\ \arg(1 - w_{11}) - \pi \\ v_1 &= \frac{1}{e^{-i\phi_1} - 1}\sqrt{\frac{2\ \sin(\phi_1/2)}{|1 - w_{11}|}}(|w_1\rangle - |e_1\rangle) \end{aligned} \tag{7.26}$$

    where w_1 is the first column of W matrix, w_{11} is the fist element of the w_1 vector and $|e_1\rangle$ = [1,0,...,0]^T;

  - next, apply $M(w_1, -\phi_1)$ on the left side of the initial matrix defining a new matrix $W_1 = M(w_1, -\phi_1)W$, with all zeros on the first row and first column, apart from the diagonal one;

  - moving on from W_1 and defining w_2, ϕ_2 and $|e_2\rangle$ as performed for w_1, ϕ_1 and $|e_1\rangle$, the parameters for M_2 can be found.

  All v_i vectors and ϕ_i phases can be determined by repeating this procedure.

- With all the computed parameters, we obtain the final QHR decomposition of an arbitrary W:

$$W = \prod_{i=1}^{d} M(v_i, \phi_i) \tag{7.27}$$

It is possible to implement QHR by using a set of parallel semi-resonant transverse magnetic rectangular pulses, detuned from the addressed gap by a value Δ, as reported in Fig. 7.4(b), between each eigenstate $|\mu\rangle$ and the auxiliary level $|e\rangle$. The amplitude of these pulses is $\propto \langle\mu|v_i\rangle$ and the phase is $\arg\langle\mu|v_i\rangle$. It is worth noting that, differently from PR decomposition, all these pulses are implemented in parallel, starting and ending at the same time. The pulse duration is τ and the detuning is Δ, common to all simultaneous pulses: these values depend on pulses amplitude and on ϕ_i as

$$\tau = \sqrt{\frac{\phi_i(2\pi - \phi_i)}{\Omega_{1e}^2 + \cdots + \Omega_{de}^2}}$$
$$\Delta = \pm\frac{\pi - \phi_i}{\tau} \tag{7.28}$$

where $\Omega_{\mu e}$ are the Rabi frequencies of the transitions.

With the above introduced decomposition methods, it is now possible to create an universal set of quantum gates on a multi-level qudit architectures by combining single-qudit rotations and two-qudit operations.

7.4 Single-qudit gates

The above introduced decomposition methods and the inter-level connectivity of the considered MNM systems lead to the implementation of a general single-qudit unitary gate.

7.4.1 Generalized Hadamard

Here we show the implementation of the Generalized Hadamard gate H_d, defined as:

$$\mathrm{H}_d = \frac{1}{\sqrt{d}} \sum_{\mu,\nu=1}^{d} e^{i\frac{2\pi}{d}(\mu-1)(\nu-1)} |\mu\rangle\langle\nu| \tag{7.29}$$

where d is the dimension of the qudit. It is worth noting that the Generalized Hadamard is the Quantum Fourier Transform (QFT) on a d-dimensional Hilbert space (see Appendix B). In the following paragraph we present the details of the gate decomposition in both PR and QHR, showing that a large number of elementary pulses are involved.

- **Details on Planar Rotations decomposition**

  In Tab. B.1, Tab. B.2 and Tab. B.3 (see Appendix B) the parameter of the sequence needed to implement H_4, H_6 and H_8 in PR are reported, assuming a full connectivity between eigenstates (i.e. when implemented on C-systems), that I computed. Parameters θ and β are the $U_{\mu\nu}$ rotation pulse parameters of Eq. 7.21, and α is the $P_{\mu\nu}$ phase pulse parameter of Eq. 7.24. In case of a linear connectivity between eigenstates (i.e. when implemented on S-systems), proper π pulses need to be added to the sequence. For H_4, the entire sequence is reported in Eq. B.5, resulting in 14 pulses; for H_6 is reported in Eq. B.6, resulting in 38 pulses; for H_8 is reported in Eq. B.7, resulting in 75 pulses. I specifically computed the above mentioned Planar Rotation parameters, reported in the Appendix B.

- **Details on Quantum Householder Reflections decomposition**

  In Tab. B.4 (see Appendix B) the parameters of the sequence of pulses needed to implement H_3, H_4, H_6 and H_8 in QHR are reported, assuming a pod connectivity between eigenstates, that have been computed in our joint research.

7.4.2 Generalized Hadamard gate on $d = 4$ qudits

Now we investigate the efficiency of the two decomposition approaches on different molecular systems, starting from a Generalized Hadamard gate implemented on $d = 4$ qudit with a **C1** system showing a full inter-level connectivity (i.e. the Cu^3 multi-spin $s_i = 1/2$ triangular molecule with competing interaction, considering only the four states of the two lowest doublets) and with a single-ion **S1** system with spin $S = 3/2$ showing a linear inter-level connectivity (i.e. a Cr^{7+} ion).

First, I contributed to highlight that the number of subsequent pulses (i.e. the depth of the calculation) to be implemented to simulate the Generalized Hadamard on a d-sized qudit show a different power scaling with the qudit space dimension; as reported in Fig. 7.5, a comparison between PR on a linearly interconnected qudit (blue data), PR on a fully interconnected qudit (red data) and QHR (green data) requiring at least a pod connectivity, shows that the QHR is much more efficient. In particular, QHR requires at most d subsequent pulses to compute H_d, while PR requires $\sim d^2/2$ in case of a fully interconnected system, and a additional $(d-1)(d-2)$ pulses in case of a linearly interconnected system. This is due to the fact that on QHR the pulses can be performed in parallel, while on PR (especially on linearly interconnected systems) must be performed in series. Hence, a higher connectivity of eigenstates makes the decomposition more efficient.

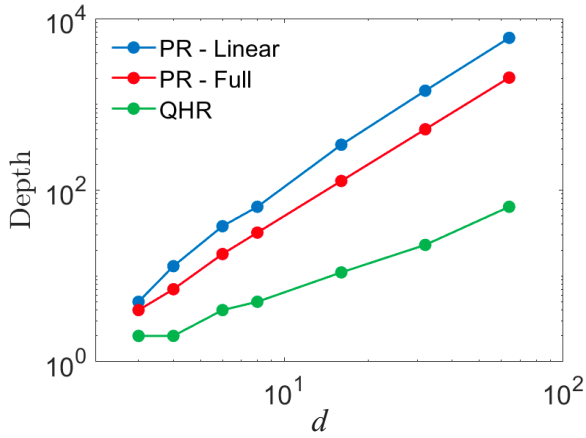

Figure 7.5: Depth (i.e. number of subsequent pulses) to implement H_d as a function of qudit space dimension d. PR on linearly interconnected systems (blue) and on fully interconnected systems (blue) require a number of pulses $\sim d$, while QHR requires a number of pulses $\sim d$. QHR represent a more efficient way to decompose quantum gates in elementary pulses. Reproduced from Ref. [46] with permission from Phys. Rev. Research (available under the terms of the Creative Commons Attribution 4.0 International license).

In Fig. 7.6 are reported the errors $\varepsilon = 1 - \langle\psi_0|H_d\rho H_d|\psi_0\rangle$ after the implementation of Hadamard gates on different configurations; the initial state $|\psi_0\rangle$ is defined as a super-

position of 30 initial states with different phases for the main panels; a superposition of 30 initial states with different amplitudes and phases are considered for the insets. These states are very error-prone, as contain an uniform superposition of eigenstates.

In Fig. 7.6(a) we report the error ε after the implementation of a single Hadamard on 4 levels qudit (H_4) using PR decomposition on the **C1** and on the **S1**, as a function of the external driving field B_1, from 10 G to 100 G, considered the upper limit of current technology [177]. The sequence of rectangular pulses implemented is reported in Appendix B, and two different values of T_2 (3 μs and 10 μs) are considered to emulate the effect of decoherence. In particular, for Cr^{3+} with $S = 3/2$ and for Cr^{3+} with $S = 5/2$ compounds, a T_2 of 3 μs has already been reached at low temperatures ($\sim$ 5 K) [178]; these values are obtained by chemically engineering the molecules [78][179][85], and values up to $\sim$ 100 μs can be reached [82][180]. The same considerations are valid for multi-spin systems with competing interactions, as the nuclear spin bath is the same.

Both molecular systems show a similar time required to implement the Hadamard gate at fixed B_1, in particular between 210 ns and 20 ns; while **S1** and **C1** have different transition matrix elements, impacting on gate time, the full connectivity of the C-system allows a more efficient decomposition as additional $\pi^{\pm}$ pulses are not needed (see Appendix B). The error ε show an almost monotonic trend as a function of B_1.

As described in Sec. 7.2, pure dephasing is the lead contributor to the decoherence on considered MNM systems; the intrinsic suppression of decoherence in **C1** system leads to a gain $\mathcal{R} \sim 3 - 4$ (defined as the ratio between ε_{S_1} and ε_{C_1}), almost constant in the entire B_1 range. This gain is independent by B_1 and T_2.

In Fig. 7.6(b) we report the results of the application of a series of Hadamard gates on a $d = 4$ qudit, implemented with **S1** and **C1** systems, with a fixed $T_2 = 3$ μs [178] and a $B_1 = 100$ G, close to the optimal value. As expected, the error ε increases by increasing the number of gates; however, system **C1** (red and green data) show an overall best quality compared to system **S1** (blue data). The green line is related to the application of QHR on a H_3 gate (the first three are the lowest energy levels, and the fourth level is the auxiliary $|e\rangle$ of the required pod connectivity), showing a reduction of the error. C-systems can implement properly both gate decomposition methods (PR and QHR), being more flexible with respect to S-systems.

7.4.3 Generalized Hadamard on larger qudits

Further numerical simulations are performed by increasing the size of the qudit, implementing the Generalized Hadamard on $d = 4, 6, 8$, defined in the basis of the lowest energy d eigenstates of single spin ions $S = 3/2$ **S1**, $S = 5/2$ **S2** and $S = 7/2$ **S3**, and on multi-spin with competing interaction system **C2** (double tetrahedron). In particular, in order to achieve up to 8 computational levels with the proper connectivity to implement QHR on the latter system, we consider the lowest eight $m = -1/2$ states, with the first $m = +1/2$ acting as the additional level required for the pod connectivity. All the transitions between the computational space and the auxiliary state $|e\rangle$ are allowed by the

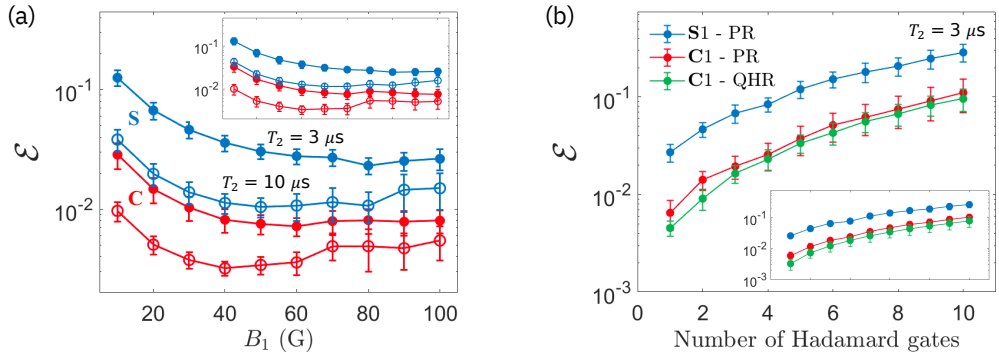

Figure 7.6: (a) Error $\varepsilon = 1 - \langle\psi_0|\mathrm{H}_d\rho\mathrm{H}_d|\psi_0\rangle$ after the implementation of a single Hadamard gate on an initial state $|\psi_0\rangle$ on a $d = 4$ qudit for two different T_2 (3 μs and 10 μs), using PR decomposition, as a function of external B_1 field. Red data represent the results obtained with the **C1** system (Cu^3 triangle), while the blue data the results obtained with the **S1** system (Cr^{3+} single spin $S = 3/2$ ion). We see that C-systems have a more efficient decomposition in terms of error by changing the driving field B_1, for fixed T_2 values. (b) Error ε after the implementation of a series of Hadamard gates, with a fixed $T_2 = 3$ μs and $B_1 = 100$ G. Red data represent the results obtained on a $d = 4$ **C1** system implementing H_4 with PR decomposition; green data represent the results obtained on the same system implementing H_3 with QHR decomposition (the fourth level is the auxiliary $|e\rangle$); blue data represent the results obtained on the **S1** system, with PR decomposition. We see that competing interaction systems are less affected by error for both PR and QHR by increasing the number of H gates applied in series. In both cases, we have a gain of competing interaction systems over single spin systems of $\sim 3 - 4$. Initial states $|\psi_0\rangle$ considered: main panels, 30 initial states superposition $|\psi_0\rangle = \sum_\mu e^{i\varphi_\mu}|\mu\rangle/\sqrt{d}$ with different phases φ_μ; insets, average over a set of 30 random initial states with different amplitudes and phases. Errorbars are the standard deviation. Reproduced from Ref. [46] with permission from Phys. Rev. Research (available under the terms of the Creative Commons Attribution 4.0 International license).

axial DMI (Eq. 7.2), inducing inter-multiplet mixing between states with $\Delta m = 0$: in this way, a transverse field will induce only $\Delta = \pm 1$ transitions. As outlined in Sec. 7.2.2, with C-systems it is possible to suppress decoherence by choosing the eight computational states with the same $\langle S_z\rangle$.

First, we study the effect of errors on State Fidelity by considering the implementation of H_6 on a mid-sized **S2** qudit, decomposed using Planar Rotations, as worst case.

Pulses can be set to have a certain amplitude in terms of magnetic field B_1: low amplitude pulses, with long overall execution time, can have better results respect to strong pulses, where each transition could interfere with other levels, causing leakage. Considering also decoherence, it is important to understand the best trade-off between B_1 and T_2: a long circuit with low B_1 pulses could have lower fidelity in presence of decoherence. In general, fidelity takes into account two aspects:

- **leakage**, due to errors on pulse implementation, that is lowered by lowering B_1, as slower pulses are more accurate in terms of induction of the right transition;

- **decoherence**, that is lowered by increasing B_1, thus reducing the overall gate time.

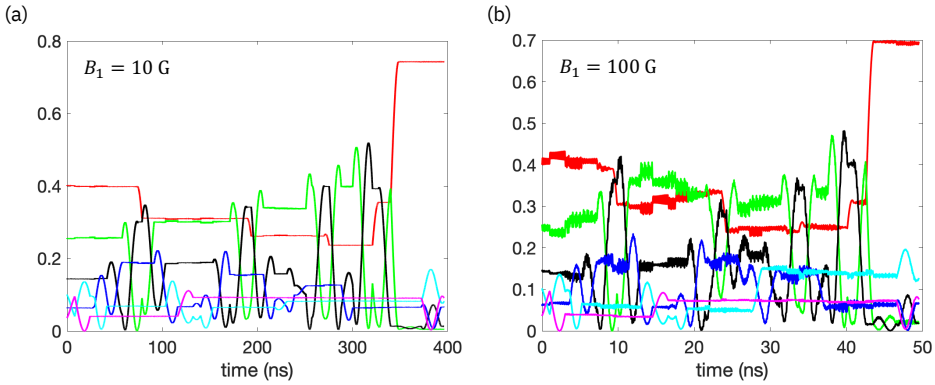

Figure 7.7: H_6 pulse sequence implemented with PR on **S2** system, assuming linear connectivity between levels, without considering decoherence ($T_2 = \infty$). (a) Pulses with $B_1 = 10$ G. (b) Pulses with $B_1 = 100$ G: high pulse amplitude can cause leakage, lowering the State Fidelity of the operation.

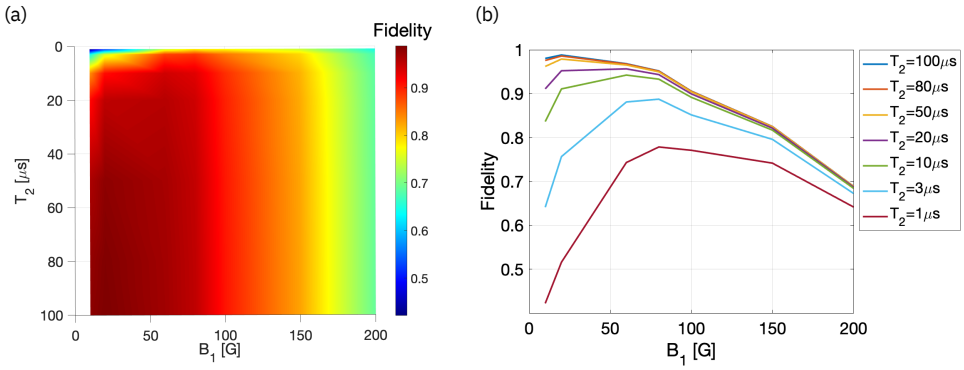

Figure 7.8: H_6 State Fidelity implemented with PR on **S2** system, assuming linear connectivity between levels, considering decoherence. (a) Heatmap of State Fidelity as a function of both T_2 and B_1. (b) State Fidelity as a function of B_1 for different T_2 values. In both panels, the maximum of State Fidelity moves to greater B_1 for lower T_2.

Fig. 7.7 shows the implemented pulse sequence for PR considering a linear connectivity between levels with $T_2 = \infty$: an high B_1 driving field can induce leakage between the selected transitions and other energy levels, lowering the State Fidelity. In Fig. 7.8(a) we report the State Fidelity as a function of both B_1 and T_2; in Fig. 7.8(b) we report the calculation of State Fidelity as a function of B_1 for different T_2 values. In both cases the maximum of State Fidelity moves to greater B_1 as T_2 lowers; a similar behaviour is noted for **S1** and **S3** qudits. Hence, a trade-off between B_1 and T_2 is required.

Given the study of decoherence and State Fidelity shown above, in Fig. 7.9 we report the results of the implementation of Generalized Hadamard gate H_d, where H_4 results

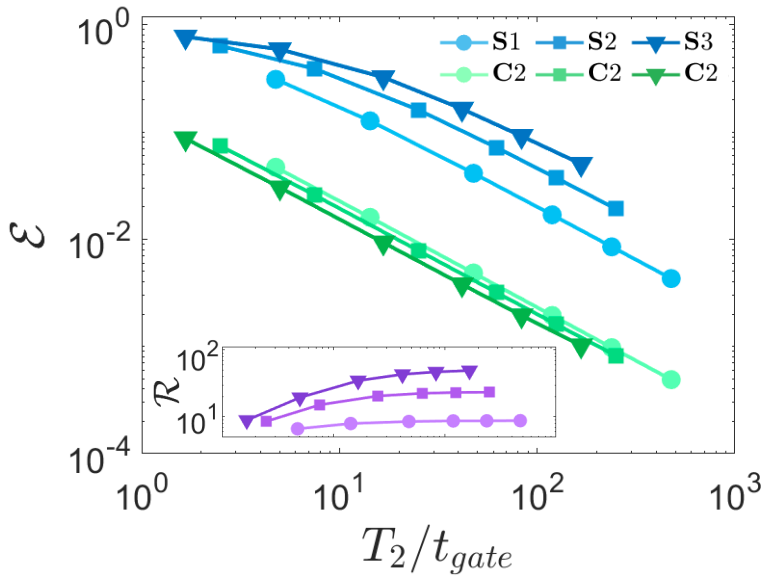

Figure 7.9: Error $\varepsilon = 1 - \langle\psi_0|\mathrm{H}_d\rho\mathrm{H}_d|\psi_0\rangle$ implementing Generalized Hadamard gate H_4 (dots), H_6 (squares) and H_8 (triangles) on $d = 4, 6, 8$ levels as a function of T_2/t_{gate}. Blue shades represent **S1**, **S2** and **S3** systems, green shades represent **C2**, where respectively $d = 2, 4, 8$ computational levels are used. Leakage is neglected due to low driving field $B_1 = 10$ G. C-systems show a lower error than S-systems, and the error does not increase with qudit size, as the green shades are almost superimposed. A single initial state $|\psi_0\rangle = 1/\sqrt{d}\sum_l e^{i2\pi/\mu}|\mu\rangle$ is considered in order to reduce the computational effort. Inset: gain between errors on S-systems and C-systems using $d = 4, 6, 8$-sized qudit, reaching a maximum value of $\mathcal{R} \sim 50$ for $d = 8$. Reproduced from Ref. [46] with permission from Phys. Rev. Research (available under the terms of the Creative Commons Attribution 4.0 International license).

are represented by dots, H_6 by squares and H_8 by triangles, as a function of T_2/t_{gate}. We compare the performances of **S1**, **S2** and **S3**, depicted with blue shades, with **C2** (considering 4, 6 and 8 computational levels), depicted in green shades. The qudit is initialized using a single initial state $|\psi_0\rangle = 1/\sqrt{d}\ \sum_l e^{i2\pi/\mu}|\mu\rangle$: this is an error-prone state, in which each component has the same absolute amplitude, as in the previous Section calculations. We used a single initial state also to reduce the computational effort to simulate the Hadamard gate, especially for **S3**, where only Planar Rotations with a linear connectivity between eigenstates can be used, increasing the number of subsequent pulses involved (see Appendix B). Here we need to focus on decoherence effects, so the leakage must be negligible. It can be reduced by implementing pulse engineering [181][47] or quantum control techniques [182], but an higher amount of computational resources would be required to implement them, together with being system specific; hence, we perform all simulations with a low driving field $B_1 = 10$ G making leakage negligible above the lowest $d + 1$ states.

The T_2 values explored are $T_2 = 1, 3, 10, 25, 50, 100$ μs. We notice that **C2** systems less affected by decoherence, as the computational error ε is lower with respect to S-systems;

we reach a maximum gain of $\mathcal{R} \sim 50$ for a qudit size $d = 8$ (Fig. 7.9 inset). We notice that the effect of decoherence does not increase with qudit size in C-system, i.e. by increasing the number of levels: the green-shaded curves are almost superimposed, while the error increases with qudit size in case of S-systems (blue-shaded curves). This result, combined with the remarkable gain reached, proves the power of multi-spin molecules with competing exchange interactions as optimal units for quantum computation. Moreover, the more efficient QHR decomposition method allows to reduce the t_{gate} required to implement the H_d: even if C-systems have a smaller transition matrix elements rather than S-systems, the higher efficiency of QHR leads to a t_{gate} comparable to the one obtained with PR. In particular, $t_{gate\mathrm{H}_4} \sim 200$ ns, $t_{gate\mathrm{H}_6} \sim 400$ ns and $t_{gate\mathrm{H}_8} \sim 600$ ns with B_1 set to 10 G.

7.5 Two-qudit gates

The next step is to introduce the implementation of two-qudit gates, in order to complete the universal gate set. As introduced in Sec. 4.3.3, two d-sized qudits are linked together with an effective $s = 1/2$ ion, acting as switch enabling and disabling the intra-qudit interaction [90][91][86]: this is a crucial feature to enable the two qudits interacting together only when needed, leading to the possibility to implement controlled gates. Moreover, unwanted time evolutions of the two-qudit system are significantly suppressed. Eq. 7.30 represents the spin Hamiltonian of the system consisting of two qudits and the switch:

$$\mathcal{H}_{2q} = \mathcal{H}_1 + \mathcal{H}_2 + \frac{\mathcal{D}\sigma_z}{2} + \mathcal{H}_{1-\sigma} + \mathcal{H}_{2-\sigma} \tag{7.30}$$

where $\mathcal{H}_1$ and $\mathcal{H}_2$ are the single qudit Hamiltonians, σ are the Pauli matrices of the switch, $\mathcal{D}$ is the switch Zero-Field Splitting and $\mathcal{H}_{1-\sigma}$, $\mathcal{H}_{2-\sigma}$ are the qudit-switch couplings, respectively for qudit 1 and qudit 2.

In order to build a well-working switch, we need a good factorization between qudit and switch eigenstates: $|\mu_1 m_\sigma \mu_2\rangle \equiv |\mu_1\rangle \otimes |m_\sigma\rangle \otimes |\mu_2\rangle$, where $|\mu_i\rangle$ are the qudit eigenstates, while $|m_\sigma\rangle$ are the switch eigenstates (eigenstates of σ_z).

The factorization of the eigenstates is required to generate a proper computational basis in the idle phase: if there is entanglement between the qudit and the switch, the system would evolve in time and the quantum registry would change, making it not useful as quantum computing platform. This is achieved when the transverse part (xy) of the interaction between the qudit and the switch is small compared to the single-body energy gaps (i.e. the energies needed to excite the qudit and to excite the switch). This condition is theoretically achievable with a spin $1/2$ switch characterized by a large g; however, realistic systems are based on transition metals like Ni (with incomplete $3d$ shell) or rare earths like Yb (with incomplete $4f$ shell). Transition metals are characterized by $g \sim 2$ and $T_2 \sim 1$ μs; a significant spin-orbit interaction increases this value, but makes coherence times are shorter. Rare earths, instead, are characterized by $g \sim 4$ and $T_2 \sim 1$ μs.

A spin 1 system is however not only characterized by its g value, but also by its ZFS,

representing another degree of freedom. A transition metal Ni^{2+} ion in an octahedral field (i.e. the structure of ligands surrounding the core ion) has a ZFS parameter $\mathcal{D} = 0.2 - 0.3$ meV (meaning tens of GHz in energy), meaning that one of the three levels can be easily selected and excluded from the Hamiltonian, obtaining an overall effective spin $1/2$ (with two well distinct levels) that can be represented by Pauli matrices notation.

As conservative choice, we adopt in this work a Ni^{2+} ions as switch, with spin $s = 1$, characterized by the parameters reported below. By applying an external magnetic field of ~ 1 T parallel to the z axis (easy axis), the resulting energy gap $\Delta E_{|m_\sigma=-1,0\rangle}$ (between $m_\sigma = -1$ and $m_\sigma = 0$) is very different from the energy gap $\Delta E_{|m_\sigma=0,+1\rangle}$ (between $m_\sigma = 0$ and $m_\sigma = +1$) due to the effect of the ZFS: it is thus possible to choose $|m_\sigma = -1, 0\rangle$ states only to define an effective two-levels system acting as switch, where $\mathcal{D} = d_\sigma - g_\sigma \mu_B B_0$. Most importantly, the couplings J_i must be much smaller than the difference between switch and qudit energy gaps in order to maintain states factorization between qudit and switch states.

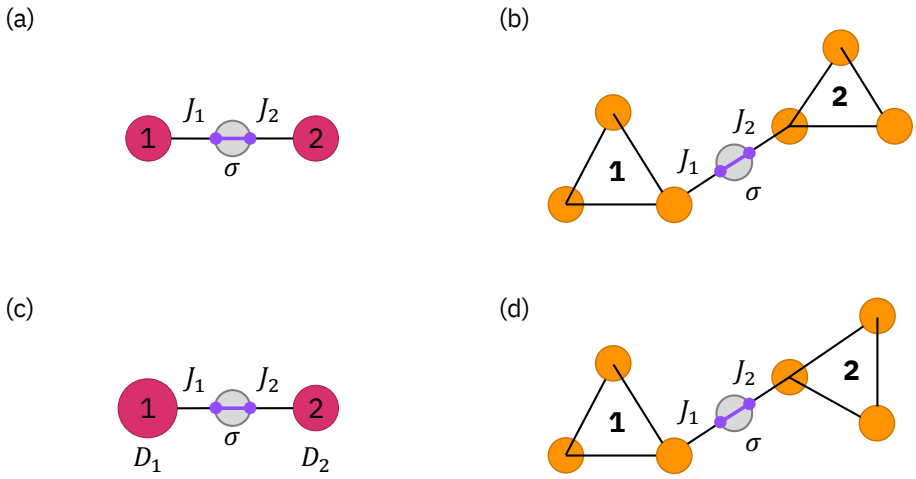

Figure 7.10: Two different implementations of the two-qudit with switch architecture. (a) Two **S1** qudits, coupled with the switch. (b) Two **C1** triangles, coupled with the switch via a single vertex. Panels (c) and (d) show the strategy implemented to make the two qudits distinguishable each other, i.e. by choosing different D_i for the two **S1** qudits, and by tilting one of the two **C1** triangles on the y axis (since it is an existing system and parameters cannot be chanced). Reproduced from Ref. [46] with permission from Phys. Rev. Research (available under the terms of the Creative Commons Attribution 4.0 International license).

- System **S1**+σ+**S1**: in Fig. 7.10(a) a sketch of the two-qudit with switch architecture is represented considering two S-systems, in particular **S1** with $S = 3/2$, and a $S = 1$ switch, acting as an effective $S = 1/2$. The qudit coupling terms of the spin Hamiltonian are $\mathcal{H}_{i-\sigma} = J_i \mathbf{S}_i \cdot \sigma$, with $i = 1, 2$. The system parameters are: $\mathcal{D}_1 = 30 \cdot 10^{-3}$ meV, $g_1 = 2.05$, $J_1 = 5 \cdot 10^{-3}$ meV, $\mathcal{D}_2 = 24 \cdot 10^{-3}$ meV, $g_1 = 1.95$, $J_1 = 7 \cdot 10^{-3}$ meV, $g_\sigma = 2.2$, $d_\sigma = -0.3$ meV. The two qudits are made distinguishable by setting different parameters, in particular $\mathcal{D}_1 \neq \mathcal{D}_2$ (Fig. 7.10(c)). In this case, I

specifically focused my effort on such systems architecture.

- System **C1**+σ+**C1**: in Fig. 7.10(b) a sketch of the same two-qudit with switch architecture is represented, but the qudits are in this case C-systems, in particular **C1** triangles: the coupling with the switch is implemented using a single vertex for each qudit, and the triangles are rotate by 90° each other around y axis, to make them nonequivalent due to their intrinsic anisotropy (Fig. 7.10(d)) [2]. The system parameters are the same of the **C1** system introduced in the previous Sections; switch parameters are: $g_\sigma = 2.2$, $d_\sigma = -0.3$ meV, $J_1 = 1 \cdot 10^{-2}$ meV, $J_2 = 1.4 \cdot 10^{-2}$ meV. I gave my contribution to study also on this system architecture.

The switchable qudit-qudit coupling can be achieved in the following way. First, the idle phase where the state of the two qudits is decoupled is obtained by keeping the switch in $m_\sigma = -1$ state: the J_i interaction between each qudit and the switch (always on) is diagonal and fixed, due to the chosen parameters range. Secondly, to turn on the effective qudit-qudit interaction, an 2π excitation pulse depending on the state of the two qudits is sent to the switch. As an example, in Fig. 7.11 the energy levels of the system **S1**+σ+**S1** are reported: black levels are related to states with $m_\sigma = -1$, where the switch is open; purple ones are excited states used to dynamically turn on the interaction (switch closed); the system **C1**+σ+**C1** follows a similar approach. In order to control the state of the switch, a conditional excitation of the switch itself is required; this is possible due to the $\mathcal{H}_{i-\sigma}$ terms of Eq. 7.30, making the transition energies of the switch dependent on the state of the two qudits to first order. For S-system based qudit-switch architecture, the transition energies of the switch can be calculated as $\delta(m_1, m_2) = g_\sigma \mu_B B_0 + J_1 m_1 + J_2 m_2$, where m_i are the eigenvalues of S_i^z and J_i are the couplings between the qudits and the switch. The chosen coupling range, where J_i are larger than the frequency broadening of the pulses, leads to the possibility to well distinguish the gaps [3]. We note, in turn, that proper pulse engineering techniques [181][47] could significantly improve the results that can be obtained with such systems.

It is worth noting that larger B_1 would speed up the implementation of two-qudit gates, reducing the effect of decoherence; a side effect is however an higher leakage, so higher J_i values are needed to better distinguish the states. We reached < 25 ns as gate time, and we accordingly optimized the driving field B_1 (as reported in Fig. 7.12).

7.5.1 Controlled-Phase

With the above introduced architecture, we implement a Controlled-Z gate, as a resonant 2π pulse is able to add a π phase to a given component of the wave function. A proper detuning of the pulse frequency from the energy gap $\delta(m_1, m_2)$ can lead to the application of a specific phase: this is achieved by implementing semi-resonant transitions [183]. This scheme is implemented on both Fig. 7.10(a) and Fig. 7.10(b) systems, where

[2] This is an existing system, so it is not possible to change the parameters to make the qudit distinguishable each other like the S1 system (i.e. we made the two D nonequivalent): a way to make distinguishable the two qudits is to rotate one of the two triangles on the y axis.

[3] For $J_1 = J_2$ only a subset of gaps are non-degenerate. While combined with universal single qudit rotations, this constitutes a universal set.

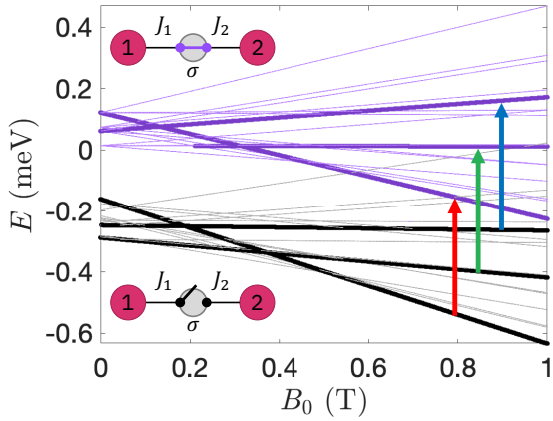

Figure 7.11: Energy levels of the **S1**+σ+**S1** system. Black: levels with switch spin expectation value $m_\sigma = -1$; purple: levels with switch spin expectation value $m_\sigma = 0$. The two sketch represent the open (black) and closed (purple) switch between the two qudits. Colored arrows represent the transitions involved in a two-qudit gate implementation, as a 2π pulse is applied to the switch depending on the states of the two qudits, in order to turn on the qudit-qudit interaction. Reproduced from Ref. [46] with permission from Phys. Rev. Research (available under the terms of the Creative Commons Attribution 4.0 International license).

the considered parameters are reported in the above Section. Results of the Controlled-Phase are shown in Fig. 7.12(a) and Fig. 7.12(a), respectively for S-system and C-system qudits; the initial state has been set to a uniform superposition of all the two-qudits wavefunction components, where each qudit has size $d = 4$, and where the switch is set in $m_\sigma = -1$ (switch closed). The chosen initial state is very error-prone, as in particular all components are taken into account, not only the three selected for the actual implementation of the gate: this choice leads to an overall higher effect of decoherence. Fig. 7.12(c) shows the tests performed with different B_1 values for the C-system qudits gate: the best B_1 value (considering leakage and decoherence effects) has been identified at 20 G. This value has been confirmed also for S-system qudits gate. As the duration of the gate is proportional to the phase we want to add [183], a proper rescaling of B_1 has been applied to have the three Controlled-Phase gates with the same length, where $B_1 = 20$ G is set to be the maximum amplitude.

T_2 is set to 3 μs for both qudits in both S-system and C-system cases, and 3 μs for the Ni^{2+} switch [184].

Similarly to the implementation of the Generalized Hadamard gate, the main outcome of the implementation of Controlled-Phase gate on qudit systems is the clear advantage of using C-systems rather than S-systems: the suppression of decoherence allows, at fixed B_1, to reduce the error from 4.2% to 1.7%. Even if the overall error is lower, we noticed an higher leakage on C-systems qudits, but it can be reduced with a proper pulse engineering strategy, or by incrementing J_i. Higher values of switch coherence can also lead to improvements on results. The parameters for both qudits and

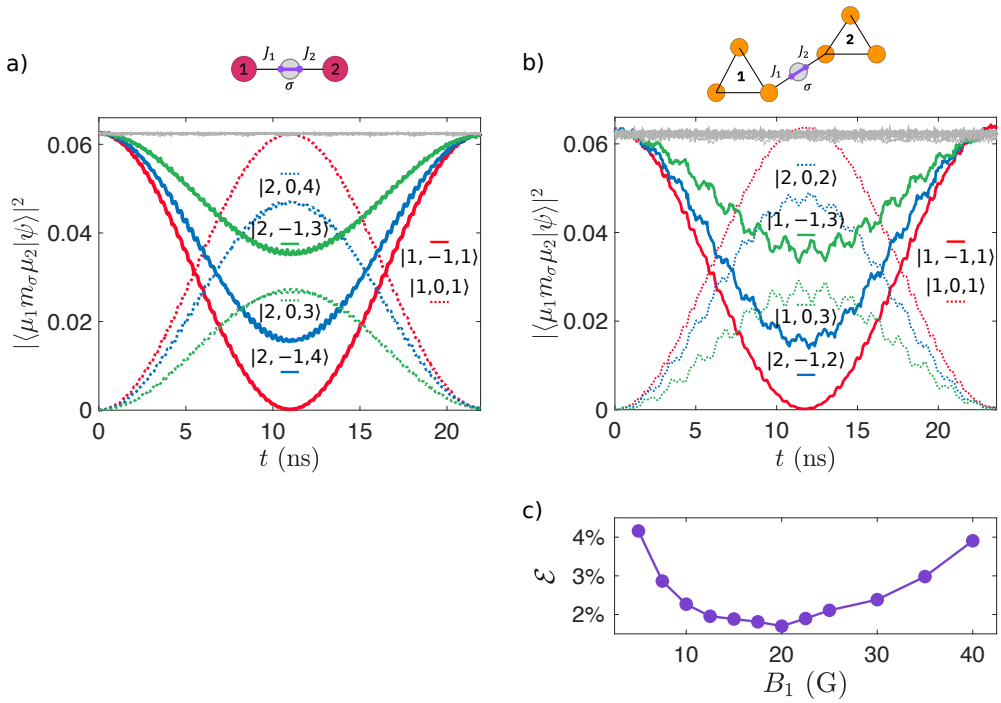

Figure 7.12: Simulation of the time evolution of the three selected components of the two-qudit wavefunction for the Controlled-Phase gate. Implemented phases are: π (red), $\pi/2$ (blue) and $\pi/4$ (green). Solid and dotted lines represent states where the switch is respectively in $m_\sigma = -1$ and $m_\sigma = 0$. Gray lines are the other energy levels of the system, thus not evolving. The initial state is set to be $|\psi_0\rangle = \sum_{\mu_1\mu_2} |\mu_1, m_\sigma = -1, \mu_2\rangle/d$, where $d = 4$ is the size of the each qudit. (a) Results of **S1**+σ+**S1** system. The error I computed is $\sim 4.2\%$. (b) Results of **C1**+σ+**C1** system. While leakage is larger in this case rather than in (a), the actual error on phase implementation is lower: $\sim 1.7\%$. (c) Error as a function of B_1, computed for C-system qudits (analogous for S-system qudits): the best working field is $B_1 = 20$ G, value used in both simulations reported in (a) and (b). T_2 has been set to 3 μs for both qudits and 3 μs for the Ni^{2+} switch [184]. Reproduced from Ref. [46] with permission from Phys. Rev. Research (available under the terms of the Creative Commons Attribution 4.0 International license).

switch are however set to realistic values; proper chemical engineering and synthesis must be performed to tune the parameters of these molecular systems.

Finally, when all transitions are well resolved, this scheme can be exploited to implement a Controlled-Phase gate leveraging on all available levels.

7.6 Conclusions

Molecular Nanomagnets consisting of multi-spin systems with competing exchange interactions have been investigated and proven as optimal qudit units for the implementation of an universal set of quantum gates. These molecules, rather than single spin S qudits, are characterized by a set of low energy multiplets where decoherence is strongly

suppressed [162]. Their Hamiltonian structure, in particular the anisotropic and asymmetric terms, introduce dipole matrix elements between most of these multiplets: this allows to optimize the number of sequential pulses required to implement unitary transformations. This is supported by the possibility to chemically engineering complex multi-spin molecules with properly tuned interactions; MNMs with competing interactions are hence a very competitive platform to implement qudits [185][186][100].

The implemented universal gate set on these MNMs can be relevant for the near-term next generation of quantum computing platforms, as current devices are limited by connectivity and, in particular, two-bodies operations are very slow and more error-prone.

Part of the content of this Chapter has been published in Phys. Rev. Research 4, 043135 (Ref. [46]).

CHAPTER 8

Quantum Error Correction with molecular spin qudits

Results reported in Chap. 7 show how Molecular Nanomagnets with a large number of accessible levels, especially in presence of competing exchange interactions, are protected from decoherence; universal sets of quantum gates can thus be implemented with a remarkable fidelity [46] with proper electro-magnetic pulses [187][184][180]. These kind of molecular systems, considered a promising unit of the future generations of Quantum Computers [100][14][188][109][141][189], can be exploited to implement complex algorithms and information encoding [171][190][176][191]; indeed, they can also be exploited for a simple implementation of Quantum Error Correction: the QEC codes can be embedded within the MNMs themselves [192][193]. Thus, exploiting molecular qudits could be the best way to achieve Quantum Error Correction.

The QEC scheme suppressing pure dephasing (dominant source of error in molecular qubits/qudits) proposed in Ref. [95] can be implemented on $S > 1$ qudits coupled to an ancilla with $S = 1/2$ qubit, allowing to flag errors without corrupting the encoded logical states. In this work we analyze the performance of this QEC scheme on specific molecular spin qudits, and we also explored the possibility to improve its performances by pulse-shaping techniques such as DRAG (Derivative Removal by Adiabatic Gate) [194][181].

8.1 Introduction

As introduced in Sec. 1.3, Quantum Error Correction is a crucial feature that needs to be addressed in order to build scalable and faithful Quantum Computing platforms, able to reach the so called quantum advantage, i.e. the ability to overcome classical computers to solve specific class of problems. Currently available Quantum Computing platforms need a huge number of physical qubits to encode logical qubits for Quantum Error Correction purposes, making the achievement of this feature still impossible; Molecular Nanomagnets, on the other hand, provide a multi-level structure [167] with remarkable coherence [77][82][180][195] allowing to embed Quantum Error Correction within a single computational unit (qudit) [192][193] in an easier and promising way [196], by reducing the number of units to be controlled and thus facilitating a practical implementation.

The Quantum Error Correction scheme proposed in Ref. [95], and here exploited, allows to suppress pure dephasing, identified as the most important source of errors in

molecular spin qudits (see Sec. 4.4) [95][96][197]. This scheme is based on a molecular qudit with $S > 1$, with $2S + 1$ accessible energy levels that can be exploited to encode the protected states $|0_L\rangle$, $|1_L\rangle$; the detection of the error (without corrupting the state) is made possible with an additional $S = 1/2$ ancilla qubit, similarly to the basic QEC schemes introduced in Sec. 1.5.2.

In this Chapter we present two different approaches for the implementation of this scheme on realistic molecular systems. Even if the QEC is still a long-term achievement, considered as important as *"the first nation to land the Moon"* [198], we identified a roadmap to implement the first proof of concept of QEC embedding in qudits, in particular on chemical details and pulse shaping techniques required.

8.2 Molecular systems and methods

Here we report the two different molecular systems used for the aforementioned QEC scheme.

- **Electronic spin qudit**, called e-system from now on, is an electronic spin dimer described by the following spin Hamiltonian:

$$H_e = \mu_B B_0 \Big(g_z S_z + g_z^A s_z^A \Big) + \mathcal{D} S_z^2 + \mathbf{S} \cdot \underline{\mathbf{J}} \cdot \mathbf{s}^A \tag{8.1}$$

  where the terms between brakets represent the Zeeman interaction with the external magnetic field along z axis, μ_B is the Bohr magneton and $\mathcal{D}$ is the axial ZFS term; lastly, $S > 1$ is the spin of the qudit, $s^A = 1/2$ is the spin of the ancilla qubit and $\underline{\mathbf{J}}$ is the exchange tensor between them. Working in a weak coupling regime is required to obtain eigenstate factorization: this is achieved by choosing $|J_{x,y}| \ll |(g_z - g_z^A)\mu_B B_0 + \mathcal{D}(2M+1)|$ [1], i.e. much smaller than the difference of excitation energies of two adjacent levels of both qudit and qubit ancilla. In this case, the difference between Zeeman energies is minimal. With this condition satisfied, and by applying an external field $B_0 > 0.1$ T, the eigenstates of the spin Hamiltonian in Eq. 8.1 are practically factorized: they can thus be labelled with $|M, m\rangle$, the eigenvalues of S_z and s_z^A.

- **Nuclear spin qudit**, called n-system from now on, is a single magnetic ion coupled by hyperfine interaction to the magnetic nucleus, described by the following spin Hamiltonian:

$$H_n = B_0 \Big(g_N \mu_N I_z + g_z^A \mu_B s_z^A \Big) + Q I_z^2 + \mathbf{I} \cdot \underline{\mathbf{A}} \cdot \mathbf{s}^A \tag{8.2}$$

  where the terms between brakets represent the interaction of the nuclear and electronic spins driven by an external magnetic field, with μ_N the nuclear magneton; lastly, $\mathbf{I}$ is the nuclear isospin, Q is the nuclear quadrupole coupling and $\underline{\mathbf{A}}$ is the hyperfine tensor. In order to achieve eigenstates factorization (weak coupling

[1] Where $\underline{\mathbf{J}}$ is assumed to be a diagonal tensor, so for simplicity we write J_x as J_{xx}, etc.

regime) of the spin Hamiltonian in Eq. 8.2, a condition similar to the e-system case is required. In this case, however, we have $\mu_N \ll \mu_B$, making the nuclear Zeeman interaction practically negligible, and hence reaching the factorization is easier. By imposing $B_0 > 0.1$ T (very easy condition for current technology), it is possible to achieve $g_z^A \mu_B B_0 \gg A_{x,y}$ [2]: the eigenstates can thus be labelled with $|M, m\rangle$, the eigenvalues of I_z and s_z^A.

Both $\underline{\mathbf{A}}$ and $\underline{\mathbf{J}}$ are assumed diagonal for simplicity. Theoretically, in both systems transitions between adjacent eigenstates of the spin Hamiltonians introduced above are possible: this is due to the ZFS or quadrupole and interaction terms. Proper pulse shaping techniques help to practically implement them. An external magnetic field $b_1(t)$ (parallel to x axis) is able to drive $\Delta m = \pm 1$ transitions: it is coupled to each system with the two Hamiltonians

$$H_{1e} = \mu_B b_1(t)\Big(g_x^A s_x^A + g_x S_x\Big) \tag{8.3}$$

for e-system, and

$$H_{1e} = b_1(t)\Big(\mu_B g_x^A s_x^A + \mu_N g_N I_x\Big) \tag{8.4}$$

for n-system. It is possible to compute numerically the time evolution of the overall spin Hamiltonian of each system by solving the motion equation of the density matrix:

$$\begin{aligned}\Big(\frac{d\rho(t)}{dt}\Big)_e &= -\frac{1}{\hbar}[H_e + H_{1e}, \rho(t)] \\ &+ \frac{1}{T_2}\Big[2S_z\rho(t)S_z - S_z^2\rho(t) - \rho(t)S_z^2\Big] \\ &+ \frac{1}{T_2^A}\Big[2s_z^A\rho(t)s_z^A - s_z^{A2}\rho(t) - \rho(t)s_z^{A2}\Big]\end{aligned} \tag{8.5}$$

for e-system, and

$$\begin{aligned}\Big(\frac{d\rho(t)}{dt}\Big)_n &= -\frac{1}{\hbar}[H_n + H_{1n}, \rho(t)] \\ &+ \frac{1}{T_2}\Big[2I_z\rho(t)I_z - I_z^2\rho(t) - \rho(t)S_z^2\Big] \\ &+ \frac{1}{T_2^A}\Big[2s_z^A\rho(t)s_z^A - s_z^{A2}\rho(t) - \rho(t)s_z^{A2}\Big]\end{aligned} \tag{8.6}$$

for n-system. In both Eq. 8.5 and Eq. 8.6, the first term represents the coherent time evolution, while second and the third terms represent pure dephasing of the qudit (T_2) and of the ancilla qubit (T_2^A).

[2] Where also in this case $\underline{\mathbf{A}}$ is a tensor, so for simplicity we write A_x as A_{xx}, etc.

8.3 Quantum Error Correction scheme on qudits

8.3.1 Code words

Assuming small t/T_2 for the selected physical system, we have to face with a single error: to correct it, we can exploit a molecular system with four addressable levels, i.e. a single molecule with $S = 3/2$. The chosen code words to encode the logic states into the four levels are:

$$\begin{aligned} |0_L\rangle &= \frac{|\frac{3}{2}\rangle + \sqrt{3}|-\frac{1}{2}\rangle}{2} \\ |1_L\rangle &= \frac{\sqrt{3}|\frac{1}{2}\rangle + |-\frac{3}{2}\rangle}{2} \end{aligned} \tag{8.7}$$

The above defined code words must fulfill the Knill-Laflamme conditions in Eq. 4.11: the application of pure dephasing, modeled in this case as a single S_z error, transforms the code words (Eq. 8.7) in two states $|e_0\rangle$ and $|e_1\rangle$, both orthogonal to the original $|0_L\rangle$ and $|1_L\rangle$:

$$\begin{aligned} |e_0\rangle &= \frac{S_z|0_L}{\|S_z|0_L\|} = \frac{\sqrt{3}|\frac{3}{2}\rangle - |-\frac{1}{2}\rangle}{2} \\ |e_1\rangle &= \frac{S_z|1_L}{\|S_z|1_L\|} = \frac{|\frac{1}{2}\rangle - \sqrt{3}|-\frac{3}{2}\rangle}{2} \end{aligned} \tag{8.8}$$

The effect of the leading error is thus a symmetric translation of the original encoded state $\alpha|0_L\rangle + \beta|1_L\rangle$ into the state $\alpha|e_0\rangle + \beta|e_1\rangle$: as no distortion is performed, the coefficients α and β are not corrupted, and a proper QEC scheme can discriminate correct states from wrong ones, being able to implement a proper correction.

It is now worth mentioning that, while a first order error $E_1 \propto S_z$ can be corrected with a four-level system, the capacity of the QEC code can be expanded to cover higher powers of S_z [95] by exploiting molecular systems with a larger number of levels.

It is now worth noting that simulations reported in Fig. 4.4 are referred to ideal performances of the QEC scheme: ancilla states are perfectly factorized, and pulses are instantaneous and monochromatic. In the next Sections, we first describe the proposed QEC scheme, and then its possible implementation on realistic physical systems.

8.3.2 QEC scheme phases and pulse sequence

Here we describe the proposed QEC scheme proposed in Ref. [95] and its implementation on a $S = 3/2$ qudit with a $S = 1/2$ ancilla qudit, being able to detect and correct the first order error $E_1 \propto S_z$ (see Eq. 4.13), already identified as pure dephasing. Together with the nuclear spin qudit already discussed in Ref. [95], here we consider also an electronic qudit. We leave to Section 8.4 all the details related to a physical implementation on realistic systems. In Fig. 8.1 we show the overall pulse sequence required

to implement the QEC scheme, from the logical state encoding to the logical state recovery, where the qudit Hamiltonian eigenstates are represented with horizontal solid lines, labelled with the expectation value of S_z in case of e-system, and I_z in case of n-system.

- **State preparation**. First, the ancilla qubit is prepared in state $|\downarrow\rangle$, while the information is stored on the first two levels $|-3/2\rangle$ and $|-1/2\rangle$ of the qudit.
- **Encoding**. Four pulses are used to implement the state encoding in the protected logical state $|-3/2\rangle \rightarrow |0_L\rangle$ and $|-1/2\rangle \rightarrow |1_L\rangle$. Two out of these four pulses can be performed in parallel.
- **Memory Time**. The encoded state can evolve for a certain time t: here the decoherence (i.e. pure dephasing) is the only considered error error source.
- **Detection**.
  - The information is first decoded: each of the states $\{|0_L\rangle, |1_L\rangle, |e_0\rangle, |e_1\rangle\}$ is mapped on a different $|M\rangle$ state. Correct superposition (i.e. where no error has occurred) is mapped to $\alpha|-3/2\rangle + \beta|1/2\rangle$, while wrong superposition (i.e. where error has occurred) is mapped to $\alpha|-1/2\rangle + \beta|3/2\rangle$.
  - The qudit-ancilla interaction makes the excitation energy of the ancilla dependent on the state of the qudit. After a conditional excitation of the ancilla qubit with two parallel π pulses, one for qudit in state $|-3/2\rangle$ and one for $|1/2\rangle$ we are able to detect the occurrence of the errors by simply measuring the ancilla.
- **Recovery**. A final set of pulses is applied to restore the original encoded state, depending on the outcome of the measurement of the ancilla.

As mentioned above, the performance of the QEC code is limited by the finite duration of the pulses themselves. During Detection and Recovery phases, the system (which is not protected) is subject to errors due to leakage and decoherence: QEC scheme performances and costs must be both taken into account in order to achieve the best results. The correction capability of the scheme would be incremented by increasing the number of available levels; however, additional errors would raise during Detection and Recovery phases, decreasing the overall efficiency [95].

8.4 Physical implementation

Two different physical systems (i.e. the above introduced e-system and n-system) are now considered in order to simulate a real implementation of the proposed QEC scheme, by a numeric integration of Eq. 8.5 and Eq. 8.6. Decoherence is set to be always present, not only during Memory Time phase, but also during the implementation of each set of pulses depicted in Fig. 8.1. Possible working points in terms of driving field $b_1(t)$ and qudit parameters are here investigated, in order to have a realistic molecular platform simulation with proper trade-off between leakage and decoherence effects.

First of all, the simulation of a real implementation of this QEC scheme comes with significant deviations from the ideal conditions on which the analysis in Fig. 4.4 is based:

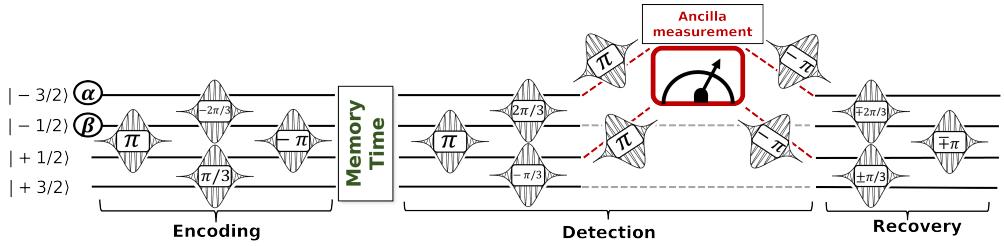

Figure 8.1: Quantum Error Correction scheme proposed to correct pure dephasing at first order with $S = 3/2$ qudit and an ancilla $S = 1/2$ qubit; the horizontal lines are the eigenstates of the qudit, labelled with the expectation value of S_z in case of e-system, and I_z in case of n-system. System initialization: logical states in the first two levels of the qudit, ancilla in $|\downarrow\rangle$ state. Pulse sketch represent actual resonalt pulses implemented, with the relative angles. During Encoding phase, the logic state is encoded to be protected; during Memory Time phase, the system is let evolving freely, and decoherence (pure dephasing) is affecting the states; Detection phase is where errors are detected with a proper conditional excitation/de-excitation of the ancilla qubit, after a first decoding of the information; finally, during the Recovery phase we use results from ancilla qubit measurements to reconstruct the information accordingly, thus recovering the original state. Reproduced from Ref. [47] with permission from the Royal Society of Chemistry (licensed under a Creative Commons Attribution-NonCommercial 3.0 Unported Licence).

ancilla states are not fully factorized, and pulses are not instantaneous and monochromatic.

- decoherence acting on the entire QEC procedure (where the state is not protected) and not only during Memory Time phase, due to the finite duration of the pulses;
- leakage to other levels not involved in transitions, due to unwanted frequencies in the pulses;
- measurement errors on ancilla, due to a mixing between ancilla qubit and qudit wavefunctions caused by the $J_{x,y}$ transverse coupling (with a probability to detect an error when no errors occurred, or not to detect an error when it occurred).

All these physical effects have an impact on the overall ε, slightly changing the behaviour depicted in Fig. 4.4 at short t/T_2 (where the additional error overcomes the incoherent error on which the QEC scheme is focused), while converging to the ideal behaviour for higher t/T_2.

Here the implementation of the proposed QEC scheme is simulated on the two identified systems in Sec. 8.2 (i.e. e-system and n-system).

8.4.1 Electronic spin qudit simulations

The first system considered in our joint research consists of two realistic dimers, where a Cr^{3+} ion, in an octahedral crystal field, with $S = 3/2$ acting as qudit is coupled (weakly) with an effective spin $1/2$ ion acting as the ancilla qubit. Two different ancilla ions are here considered: Cu^{2+} and Yb^{3+} complexes. It is possible to synthesize CrCu dimer

(namely e1-system) [176], and CrYb dimer (namely e2-system) is already existing [199]. Typical parameters for both dimers are described below:

- **CrCu dimer**: $g = 1.98$, $\mathcal{D} = -0.24$ cm^{-1}, with exchange interaction parameters $(J_x, J_y, J_z)/(A_x, A_y, A_z) = (1.7, 1.7, -3.3) \cdot 10^{-2}$ cm^{-1}, with $(g_x^A, g_y^A, g_z^A) = (2.1, 2.1, 2.3)$, and with coherence times $T_2 = 50$ μs and $T_2^A = 5$ μs [199][87].
- **CrYb dimer**: $g = 1.98$, $\mathcal{D} = -0.24$ cm^{-1}, with exchange interaction parameters $(J_x, J_y, J_z)/(A_x, A_y, A_z) = (1.7, 1.7, -3.3) \cdot 10^{-2}$ cm^{-1}, with $(g_x^A, g_y^A, g_z^A) = (2.9, 2.9, 4.2)$, and with coherence times $T_2 = 50$ μs and $T_2^A = 1 - 3$ μs [199][200].

We assumed $\underline{\mathbf{J}}$, $\underline{\mathbf{A}}$ and $\underline{\mathbf{g}}^A$ diagonal tensors, and we also assumed an axially anisotropic exchange interaction for both dimers, that can be obtained with a dipole-dipole coupling by properly positioning the ions at a distance of $5-6$ Å. Factorization between qudit and ancilla qubit is obtained by imposing $|J_{x,y}| \ll |(g - g_z^A)\mu_B B_0 + D(2M+1)|$.

Fig. 8.2(a) reports the energy levels of e2-system (CuYb dimer) as a function of the static external field B_0, with the eigenstates labelled by $|M, m\rangle$, the eigenvalues of S_z and s_z^A.

We report in Fig. 8.2(b) the performances of the QEC scheme in terms of the error $\varepsilon = 1 - \langle\psi(0)|\rho(t)|\psi(0)\rangle$ as a function of the memory time t/T_2 for both e1-system (CuCr dimer) and e2-system (CuYb dimer). The gray dashed line is the error for an uncorrected $s = 1/2$ subject to the effect of pure dephasing, while black solid line represents the ideal performances of this QEC scheme on a $S = 3/2$ qudit. Solid coloured lines represent the overall error where only ideal pulses are performed, but with measurement operators resulting from Hamiltonian diagonalization: unwanted ancilla-qudit interactions are considered, causing a not perfect factorization of the eigenstates. In this way, we highlighted the measurement errors coming from this imperfect factorization.

Considering the presence of the sole measurement error (solid coloured lines), we notice that ε is much larger for e1-system as it is characterized by a smaller $g_z^A - g_z$ (setting a restriction on the accuracy of the QEC scheme for these systems); for e2-system, characterized by an almost perfect factorization of eigenstates, one can neglect the measurement error, as the blue solid line is almost superimposed to the black solid line (i.e. the ideal behaviour, with no errors). Higher values of $B_0 > 1$ T can help to make e1-system behaviour similar to e2-system with $B_0 = 1$ T.

Including also real pulses (and hence both leakage and decoherence), we performed simulations with Gaussian-shaped pulses with the form

$$b_1(t) = B_1 e^{-(t-t_0)^2/2\tau^2} \cos \omega t \tag{8.9}$$

where ω is the frequency of each pulse, in resonance with the selected pair of energy levels for each transition of the QEC scheme of Fig. 8.1. In this case, we found that leakage is negligible for qudit transitions (the ZFS provides sufficiently large gaps between energy levels): it is thus possible to increase the driving field up to $B_1 = 100$ G, as shown in Fig. 8.2(b) inset: ε monotonically decreases (violet dots) by increasing B_1^Q (driving field for qudit transitions) at fixed t/T_2. The chosen $B_1^Q = 100$ G is thus only

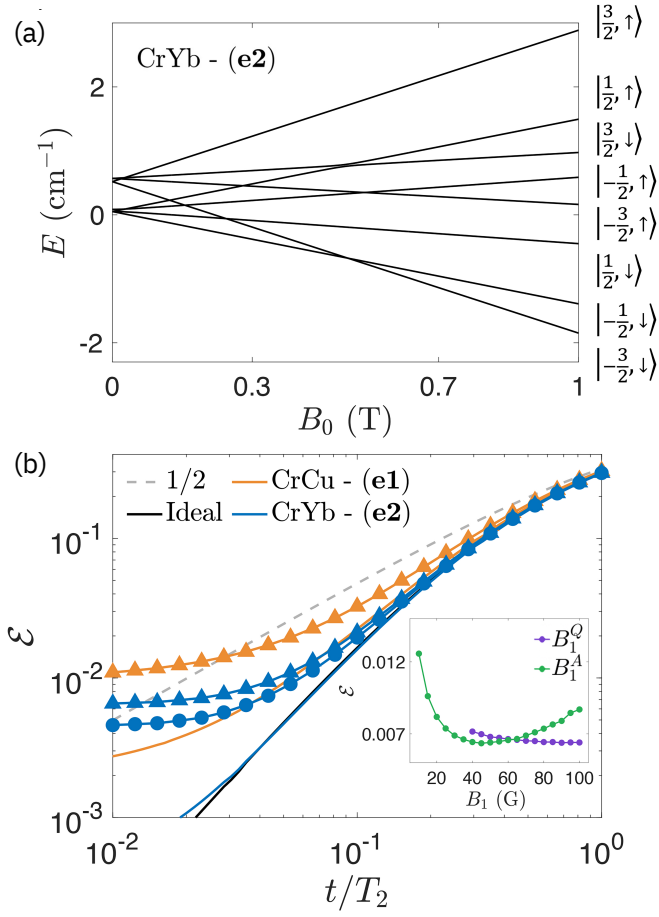

Figure 8.2: (a) Energy levels as a function of the external static B_0 magnetic field for e2-system. Note the practically factorized eigenstates labelled by $|S_z, s_z^A\rangle$. (b) Performances of QEC scheme (error $\varepsilon = 1 - \langle\psi(0)|\rho(t)|\psi(0)\rangle$) for both e1-system and e2-system, with a fixed $B_0 = 1$ T. Gray dashed line: error for an uncorrected $s = 1/2$ spin subject to pure dephasing. Black solid line: ideal performance on a $S = 3/2$ qudit. Solid coloured lines: measurement errors for the two e-systems (e1-system: orange, e2-system: blue) with $B_1^Q = 100$ G for the qudit and $B_1^A = 45$ G for the ancilla qubit. Related symbols are related to simulations including decoherence and leakage: in particular, regarding the ancilla coherence time, we set it to $T_2^A = 5$ μs for e1-system (orange triangles). On e2-system we compared two cases: blue triangles are related to $T_2^A = 1$ μs, while blue circles are related to $T_2^A = 3$ μs. Inset: the total error on e2-system as a function of the driving field B_1 with Gaussian-shaped pulses, for qudit (violet) and ancilla qubit (green) excitations, with fixed $t/T_2 = 0.035$ ($T_2^Q = 50$ μs and $T_2^A = 3$ μs). Reproduced from Ref. [47] with permission from the Royal Society of Chemistry (licensed under a Creative Commons Attribution-NonCommercial 3.0 Unported Licence).

limited by current technology [177]. On the other hand, J_z parameter is responsible for the energy level gaps of the ancilla qubit: since the gaps are smaller, a smaller B_1^A must

be used not to induce leakage of population to other neighbouring energy levels. The minimum of ε as a function of B_1^A is located at 45 G (green dots); lower values for the driving field would increase the duration of the pulses and hence decoherence, while higher values would increase leakage. With these B_1 values, and with $T_2 = 50$ μs for the qudit (realistic value in case of transition metal core ion and a chemically engineered organic ligand structure), we performed the simulations reported with triangular and circular symbols in the main panel.

Measurement error on the ancilla qubit compromises the performances of e1-system: the error ε on the orange triangles is the highest reported, very similar to the uncorrected $s = 1/2$ behaviour. On the other hand, measurement error is negligible for e2-system, as stated above. We finally note that, as the ancilla qubit is excited only during the Detection phase of the QEC procedure, it is possible to set $T_2^Q \gg T_2^A$: it has been set, for e1-system, to 5 μs [200] (orange triangles), while for e2-system, to 1 μs (blue triangles) and 3 μs (blue circles). The best performances have been obtained with e2-system with $T_2^A = 3$ μs, with $\varepsilon < 5 \cdot 10^{-3}$ for low t/T_2.

8.4.2 Nuclear spin qudit simulations

The second qudit-ancilla qubit system I specifically worked on is a nuclear spin qudit (n-system), consisting of a molecule [82] named $(PPh_4)_2[Cu(mnt)_2]$ containing a Cu^{2+} ion with an electronic spin $1/2$ coupled with the nuclear $I = 3/2$ spin via hyperfine interaction. Typical parameters for a ^{63}Cu ion are described below:

- **$(PPh_4)_2[Cu(mnt)_2]$**: $g = 1.48$, $Q = 1.7 \cdot 10^{-3}$ cm^{-1}, exchange interaction parameters $(J_x, J_y, J_z)/(A_x, A_y, A_z) = (0.4, 0.4, 1.7) \cdot 10^{-2}$ cm^{-1}, with $(g_x^A, g_y^A, g_z^A) = (2.0, 2.0, 2.1)$, and with coherence times $T_2 = 10^2 - 10^3$ μs and $T_2^A = 68$ μs [82].

As for the e-systems, we assumed $\underline{\mathbf{J}}$, $\underline{\mathbf{A}}$ and $\underline{\mathbf{g}}^A$ as diagonal tensors. The nuclear quadrupole Q reported value, that governs the energy gaps between adjacent nuclear spin levels, is set to $Q = 1.7 \cdot 10^{-3}$ cm^{-1} [83][201]. Fig. 8.3(a) shows the energy levels of n-system as a function of the static external field B_0, in which it is evident the separation of the two subspaces identified by the ancilla qubit in $|\downarrow\rangle$ and $|\uparrow\rangle$ states. In this case, the subspace identified by $|\psi_A\rangle = |\downarrow\rangle$ is used to encode the states to be protected, while the subspace with $|\psi_A\rangle = |\uparrow\rangle$ is used to detect the errors.

Simulations reported in Fig. 8.3(b) are performed with a low $B_0 = 0.1$ T: eigenstates are well factorized in this case, as the electronic and nuclear excitation energies are very different, giving a maximum states mixing of about 10^{-3}. This allows us to focus the investigation on decoherence and leakage only source of errors. Moreover, the matrix element of nuclear transitions is enhanced by a factor ~ 50 [45][160], speeding up the manipulation of nuclear levels, thanks to a slight mixing between electronic and nuclear spin wavefunction. Coherence times for n-system are not referenced in literature; in order to set a reasonable value for the T_2, compare with similar systems. The decoherence is mainly induced, at low B_0, by the coupling of the core ion with the surrounding magnetic nuclei, in which the electronic spins act as mediators: the T_2 (nuclear coherence time) has a direct relation with the T_2^A (electronic coherence time), in particular it is reasonable to assume it > 10 times larger [87][45], as reported in similar systems such as

Vanadyl tetraphenylporphyrinate. This system consists of a $I = 7/2$ nucleus coupled by hyperfine interaction with an electronic spin $1/2$: it is very similar to the considered n-system $(PPh_4)_2[Cu(mnt)_2]$. This complex has a $T_2^A = 68$ μs (at rather low temperature 5 K): a value 10 times larger for the nuclear coherence time $T_2 = 0.5$ ms is thus reasonable.

Black and blue triangles in Fig. 8.3(b) represent the error for different configuration of the driving field; the best results are achieved with an external driving field of $B_1^Q = 50$ G for the qudit and $B_1^A = 30$ G for the ancilla (black triangles). The inset represents the gain as the ratio between the uncorrected qubit error and the protected qudit. Higher B_1 would reduce the effect of decoherence, while increasing the leakage: $B_1 = 125$ G for the qudit (blue triangles) show an higher error ε.

8.5 Performance improvements with pulse-shaping techniques

In order to further improve the results depicted in Fig. 8.3(b), several pulse shaping techniques are existing, with the aim to reduce decoherence effect during QEC implementation while controlling leakage, by increasing the driving field; this is rather complicated, especially when the width of the pulse approaches the difference between the gaps, both in terms of frequency. We report here some of these techniques:

- Sideband-modulated "wah-wah" pulses [202][203];
- SWIPHT, namely *Speeding up Waveforms by Inducing Phases to Harmful Transitions* [204][205];
- DRAG, namely *Derivative Removal by Adiabatic Gate* [181][206][207].

8.5.1 DRAG: Derivative Removal by Adiabatic Gate

The chosen pulse shaping technique is the DRAG, as it allows to improve the speed of the implementation of two-level rotations with high fidelity (i.e. by suppressing leakage). A second pulse, simultaneous and orthogonal to the first one, is generated as the time derivative of the main pulse; the combination of these two pulses creates a spectral hole, that can be tuned and moved near to the frequency of the unwanted transitions. In this way, the leakage to that unwanted transition is significantly reduced. Therefore, the structure of the driving field $b_1(t)$ is:

$$b_1(t) = \begin{cases} \varepsilon_x(t)\cos\omega t + \varepsilon_y(t)\sin\omega t & \text{for } 0 < t < t_g \\ 0 & \text{otherwise} \end{cases} \tag{8.10}$$

where a single frequency ω is employed. More specifically, in case of a main driving field with a Gaussian shape, the x and y components become:

$$\begin{aligned} \varepsilon_x(t) &= \frac{B_1}{\sigma} e^{-(t-t_0)^2/2\sigma^2} \\ \varepsilon_y(t) &= \beta\lambda \frac{d\varepsilon_x(t)}{dt} \end{aligned} \tag{8.11}$$

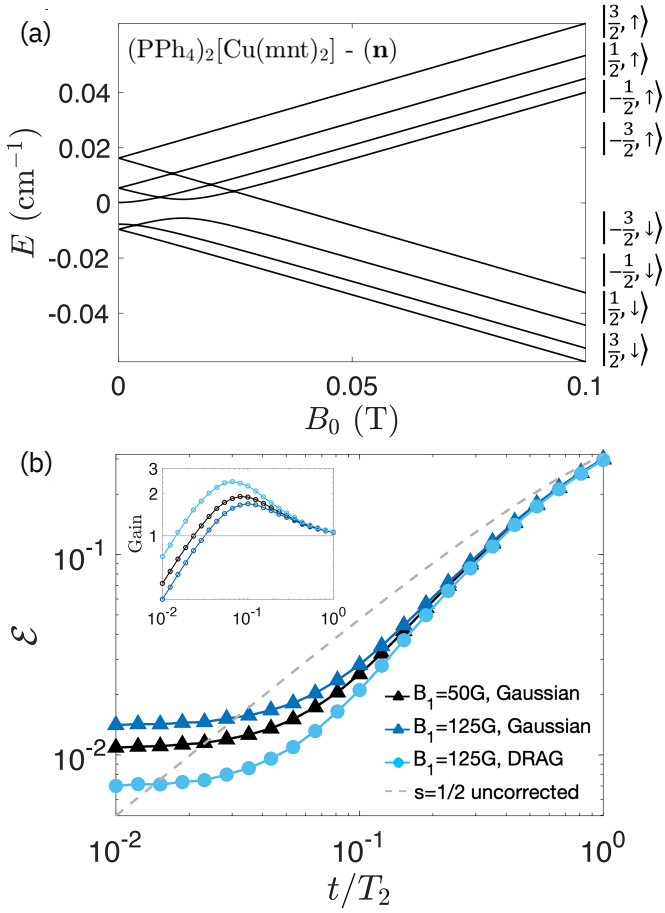

Figure 8.3: (a) Energy levels as a function of the external static field B_0 for n-system. The eigenstates are labelled by $|I_z, s_z^A\rangle$. (b) Performances of QEC scheme (error $\varepsilon = 1 - \langle\psi(0)|\rho(t)|\psi(0)\rangle$), with a fixed $B_0 = 0.1$ T, $T_2 = 0.5$ ms, $T_2^A = 68$ μs [82]. The driving field for the ancilla is set to $B_1^A = 30$ G, while different values and pulse shapes are employed for the B_1^Q: triangles are related to Gaussian-shaped pulses, while circles to DRAG-shaped pulses (see Section 8.5.1). The gray dashed line represents the error for an uncorrected $s = 1/2$ qudit subject to pure dephasing. Inset: gain as ratio between ε on protected and on unprotected qubits. Reproduced from Ref. [47] with permission from the Royal Society of Chemistry (licensed under a Creative Commons Attribution-NonCommercial 3.0 Unported Licence).

where B_1 is the maximum driving field amplitude, σ is the width of the Gaussian, λ is the relative strength between unwanted and desired transitions and β is a numerically optimized coefficient to tune the DRAG. The combination of pulses in Eq. 8.11 leads to the shaped pulse used to improve QEC performances, as reported in Fig. 8.4. The numerical optimization process to find the best β parameter is highlighted below:

- we consider a target transition e.g. between levels $(1 - 2)$ and the unwanted transition between levels $(2 - 3)$ which is the closest in energy;

- we compute the λ factor as the squared ratio between matrix elements of unwanted and target transitions, divided by the energy differences between levels;
- we perform the fidelity calculation with a set of β values between 0 and 1, finding the one that leads the best fidelity. This numerical optimization process has been performed for each B_1 value, as it depends on the leakage to the unwanted transitions.

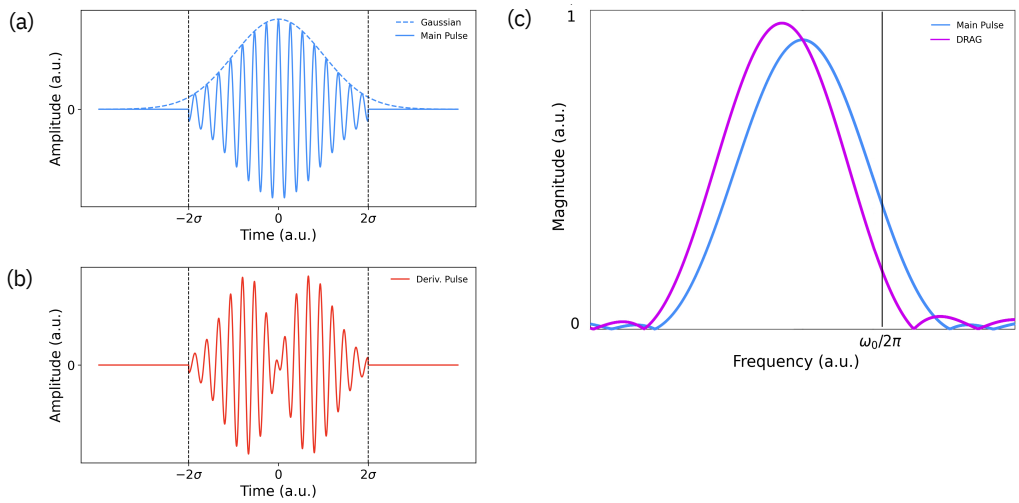

Figure 8.4: (a) Example of oscillating field with a Gaussian envelope, truncated outside $|2\sigma|$. (b) Time derivative of the Gaussian pulse represented in panel (a), truncated outside $|2\sigma|$. The overall DRAG pulse is the sum of the two pulses. (c) Frequency spectra comparison between Gaussian-shaped pulse (blue) and DRAG pulse (purple): on DRAG spectrum we note a shift on the peak to the left and a reduction of the frequency contribution to the unwanted transition $\omega_0/2\pi$.

The DRAG technique is here applied in its simplest form by considering a single unwanted transition disturbing the target one (while more complex implementations could handle many unwanted transitions [208][209]); on n-system, we use DRAG to select the following qudit transitions:

- $|3/2\rangle \leftrightarrow |1/2\rangle$ from $|1/2\rangle \leftrightarrow |-1/2\rangle$
- $|-1/2\rangle \leftrightarrow |-3/2\rangle$ from $|1/2\rangle \leftrightarrow |-1/2\rangle$

As reported in Fig. 8.3(b), the application of DRAG leads to a significant improvement of error ε when an high B_1 is employed, in particular on the a system where the energy gaps are similar: leakage is here kept under control by reducing the contribution on the unwanted transition, while reducing decoherence effect. The inset of Fig. 8.3(b), representing the gain as the ratio between ε on protected and on unprotected qubits, lets us to identify the best t/T_2 spot; we compare the performance of the QEC code using Gaussian and DRAG pulses neat this spot, for different T_2 and B_1. Results are reported

in Fig. 8.5. Dark-shaded lines with triangular markers are related to Gaussian pulses, while light-shaded lines with circular markers are related to DRAG pulses. Different color shades represent different T_2 values. We opted to use B_1 values larger than the ones allowed by current technology (current maximum $\sim$ 120 G for nuclear magnetic resonance equipments [210]) for two reasons: the first one is to better appreciate the DRAG effect, and the second one is to guide future development showing the advantage of larger B_1 values.

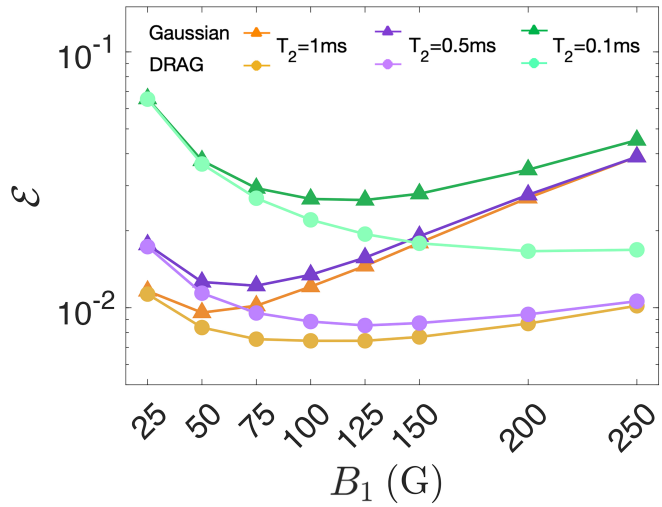

Figure 8.5: Performances of the DRAG technique on the proposed QEC scheme on n-system. Error ε is computed as a function of driving field B_1, for different T_2 values, near the t/T_2 maximum gain spot reported in Fig. 8.3(b) inset. Dark-shaded lines with triangular markers are related to Gaussian pulses, while light-shaded lines with circular markers are related to DRAG pulses. Different colors are related to different T_2 values. DRAG performances are maximized to intermediate B_1 and long T_2, while are maximized to larger B_1 when lowering T_2. Reproduced from Ref. [47] with permission from the Royal Society of Chemistry (licensed under a Creative Commons Attribution-NonCommercial 3.0 Unported Licence).

Gaussian pulses show a minimum in the error distribution for intermediate B_1 values: long Gaussian pulses (with low B_1) make decoherence the leading error source, while shorter Gaussian pulses (with high B_1) make leakage the leading error source. Higher T_2 values shift the error minimum to lower B_1, as the effect of decoherence is reduced. DRAG pulse shaping technique reduces the effect of leakage on results: ε behaviour is always below the one related to Gaussian pulses. In case of $T_2 = 0.1$ ms, the minimum of ε is positioned on $B_1 > 250$ G; by increasing T_2, the position of the minimum is shifted to lower B_1, as in case of Gaussian pulses, but the effect is less evident. We can see that the DRAG pulse shaping technique can significantly improve the performances of the proposed QEC scheme.

8.6 Conclusions

In this Chapter we considered two realistic molecular spin qudits as candidates for the embedding of QEC, with the aim to correct pure dephasing errors: the first one is a realistic system based on a $S = 3/2$ qudit coupled with an ancilla qubit with effective spin $1/2$, while the second one is an existing nuclear spin qudit with $I = 3/2$ coupled with an ancilla qubit (electronic) by hyperfine interaction. In both cases, the role of the ancilla qubit is to give an extension of the Hilbert space to detect errors without making the quantum state to collapse, being able to proceed with the calculations. Performances of the proposed QEC scheme have been investigated and optimized by selecting the proper driving field range, reaching values below 10^{-2} for both systems. DRAG pulse-shaping technique has been applied to further reduce the error. Other methods to improve the QEC scheme performances can be applied [182], together with different classes of molecular qudits consisting of multi-spin molecules [211][212].

Part of the content of this Chapter has been published in Phys. Chem. Chem. Phys., 2022,24, 20030-20039 (Ref. [47]).

Conclusions and future perspectives

In this work we had the opportunity to access and use the first prototype superconducting Quantum Computers, in particular the ones available on IBM Quantum platform, and to simulate realistic new architectures for possible next generation devices based on molecular spin qudits. We also followed IBM Quantum devices evolution during the last three years (2019-2022) as we performed several benchmarks and characterizations, and we highlighted the improvements of performances in terms of error rates and qubit calibrations.

We exploited current Quantum Computers and Simulators to study small-sized physical systems such as molecular spin chains, considered one of the first areas where Quantum Computation could bring an advantage, even with a rather small amount of qubits. We applied the Variational Quantum Eigensolver algorithm, hybrid quantum-classical method, to study the static properties of spin $1/2$ molecular chains with a leading Heisenberg interaction and subject to an external magnetic field. Starting from a spin $1/2$ dimer test model, we moved on to more complex systems like four spins and six spins closed chains: a proper Hamiltonian encoding on the qubits and a well studied variational ansatz strategy, allowed us to compute the ground state energies for different magnetic field values, together with the magnetization and the expectation value of the total spin. Two different ansatz approaches have been compared: an Hardware Heuristic Ansatz approach, able to be natively adapted to the hardware configuration, and a Physically Motivated Ansatz approach, that takes in consideration properties and symmetries of the target model. While both have similar performances on computing the ground state static properties of the studied systems on noisy simulations, we noted that the latter shows a better and faster convergence, in particular when scaling up the target model complexity (i.e. the number of spins in the chain), and it is able to reconstruct the local spin expectation values symmetries, making it the better choice to study molecular spin systems with proper error mitigation techniques like Qiskit Measurement Error Mitigation. This ansatz approach has been then exploited to study parity effects on even-odd open-closed chains. We then further complicated the target systems by adding a Dzyaloshinskii-Moriya interaction, to study the VQE performances in presence of anticrossings between different total spin states for a trimer and a four spin closed chain.

We were able to perform noiseless simulations with a proper ansatz strategy to well reconstruct the ground state energy, the magnetization and the torque in proximity of the anti-crossings, consisting of a rather small gap between the ground state and the first excited state. We finally studied the dynamic properties of these model systems by computing the spin-spin Dynamic Correlation functions on a real IBM Quantum chip, with a remarkable fidelity with respect to exact results after application of proper error mitigation techniques.

IBM Quantum devices have been also exploited to study strongly correlated quantum systems like the Fermi-Hubbard model, in order to validate the previously developed approaches like the Physically Motivated Ansatz and the error mitigation techniques. Differently from spin systems, fermionic systems Hamiltonian require more complex mapping like Jordan-Wigner Transformation, which increases the number of required qubits and the depth of the resulting circuits. We studied static properties of the ground state with VQE noisy simulations, and we simulated the time evolution on IBM Quantum real hardware with the Suzuki-Trotter decomposition on a dimer. In both cases, the results well fit with the expected behaviour, especially with the application of error mitigation techniques, such as a custom Post selection technique for real hardware time evolution. We demonstrated that current quantum devices can nowadays be reliably used to simulate rather small but interesting physical systems; we are confident that the future technological improvements will make these devices even more reliable and useful for practical computation.

Results obtained with IBM Quantum are remarkable, but still limited to a small amount of qubits and small circuit depth: to take a significant step forward, a change of perspective could be useful, for example exploiting a qudit logic. We focused on exploring new approaches to Quantum Computation with the dual objective to handle some intrinsic limitations of current devices (in particular decoherence) and to increment the computing power (e.g. to embed Quantum Error Correction inside the fundamental unit of computation). We studied different molecular systems called Molecular Nanomagnets to achieve both these objectives, as they can represent key candidates to implement multi-level (qudit) logic with many engineerable and coherent levels: in fact, Molecular Nanomagnets are molecules consisting of core magnetic ions surrounded by a ligand cage, and can be chemically engineered and properly tuned to create multi-level systems. From a technological point of view, a recently proposed work [48] has shown how to integrate such molecules into superconducting circuits already used to control transmon qubits. This clearly indicates a future possible hybrid and integrated architecture, leveraging on existing and already advanced superconducting technology, to be exploited to create and control platforms consisting of molecular spin qudits. Therefore, a physical implementation of the proposed Molecular Nanomagnet compounds can be considered realistic.

Two different Molecular Nanomagnets have been exploited: single spin systems and multi-spin systems with competing interactions. We demonstrated that multi-spin systems with competing interactions are protected by decoherence rather than single spin systems. On these realistic MNMs, Universal set of quantum gates were simulated by

implementing multi-level Hadamard gate up to 8 levels and a Controlled-Phase gate, with proper external driving and static magnetic fields. The competing interactions protection from decoherence allowed us to reach a gain of ~ 50 in terms of gate fidelity with respect to single spin MNMs on 8 levels Hadamard gate, and a ~ 3 times fidelity gain on Controlled-Phase. Even more remarkably, in case of competing interaction MNMs the error does not increase with system size, making them very effective candidates to build the fundamental logic of the future qudit-based devices, in particular considering the proposed qudit-switch architecture enabling scalability.

We exploited similar molecular systems to implement a qudit capable to embed a recently proposed Quantum Error Correction scheme to detect and correct pure dephasing errors, considered the leading errors on such systems. The investigated molecular systems are based on an electronic or nuclear spin S qudit, both coupled with an ancilla qubit to expand computational space to implement the QEC scheme. The scheme has been implemented by choosing the best driving and static fields: performances have been investigated on both systems, reaching errors below 10^{-2}. On the nuclear spin qudit, a pulse-shaping technique named DRAG has been applied to further increase the performances of the scheme in terms of error.

With the introduced schemes to implement gates on molecular spin qudits with remarkable fidelity, one of the first steps towards the practical realization of such platform is to implement some quantum algorithms; the first identified algorithm is the Quantum Simulation of a Fermi-Hubbard system. To do this, we already started to implement and simulate some other quantum gates, e.g. the iSWAP gate, and we are investigating the composition of gates on the proposed qudit platforms.

The race towards production-ready Quantum Computers is still open, and represents one of the most challenging and revolutionary technological improvements of this century. In the next decade the scientific community will for sure continuously pursue this goal; this work aims to help towards direction, from enabling the first uses of near-term devices on chemical and physical research, to giving a possible roadmap for the implementation of next generations of Quantum Computers.

Appendices

APPENDIX A

The Qiskit framework

Qiskit [12] is an open-source quantum development framework (namely an SDK, that stands for *Software Development Kit*) created to work with quantum computers at many levels, from pulses and circuits, to pre-build libraries and application modules.

A.1 Introduction to Qiskit

Qiskit has been released in 2016, and it is developed by IBM and by the open-source community. Based on Python, it allows to exploit sets of quantum gates and pre-built circuits and modules to let users, researchers and professionals to implement quantum applications.

The developed code can be translated into properly configured circuits to be run on the Qiskit simulators or on real Quantum Computers, like for example IBM Quantum; the Transpiler [23] has the role to convert the code into circuits, taking in consideration the characteristics of the simulator or the hardware itself, letting the users to automate the deployment on different platforms. These transpiled circuits can be run either on real QPUs, or on simulated QPUs using CPUs or GPUs. The management of the jobs life cycle can be achieved with the provided tools.

Qiskit modules currently (early 2023) consist of the Core functions, the Providers (Qiskit Aer, IBM Quantum Runtime and other Partners like IonQ [213]), the Applications (Nature, Finance, Optimization and Machine Learning) and the Extensions (Experiments, Dynamics and Metal [214]).

Qiskit has been used extensively in this work, especially in the analysis reported in Chap. 5 and Chap. 6, where IBM Quantum chips have been used to simulate spin and fermionic systems behaviour and characteristics, and to perform the search for systematic errors reported here in Sec. A.3.

A.2 Gates composition using Qiskit

In Chap. 1, Sec. 1.1.2, we introduced the main quantum logic gates to perform single-qubit and multi-qubit operations; here we present in more details how to implement combinations of single- and two-qubit gates to create some of the most common building blocks used in Digital Quantum Simulations.

We already introduced the generalized single-qubit rotation in $SU(2)$ space in Eq. 1.10:

$$U(\theta,\phi,\lambda) = \begin{pmatrix} \cos\frac{\theta}{2} & -e^{i\lambda}\sin\frac{\theta}{2} \\ e^{i\phi}\sin\frac{\theta}{2} & e^{i(\phi+\lambda)}\cos\frac{\theta}{2} \end{pmatrix} \tag{A.1}$$

This gate depends on 3 angles θ, ϕ and λ. A proper choice of the angles leads to the implementation of single-qubit rotations like:

$$\begin{aligned} R_x(\theta) &= U(\theta, -\pi/2, \pi/2) \\ R_y(\theta) &= U(\theta, 0, 0) \\ R_z(\lambda) &= U(0,0,\lambda) = e^{-i\lambda/2}\Phi(\lambda) \end{aligned} \tag{A.2}$$

where $\Phi(\lambda) = \begin{pmatrix} 1 & 0 \\ 0 & e^{i\lambda} \end{pmatrix}$ is the Phase gate. As the Qiskit platform is able to implement single-qubit rotation gates, is also able to implement generic $U_3 = U(\theta,\phi,\lambda) = R_z(\phi)R_x(\theta)R_z(\lambda)$ rotations. Given the single-qubit rotations introduced above, we now introduce the implementation of two-qubit operations.

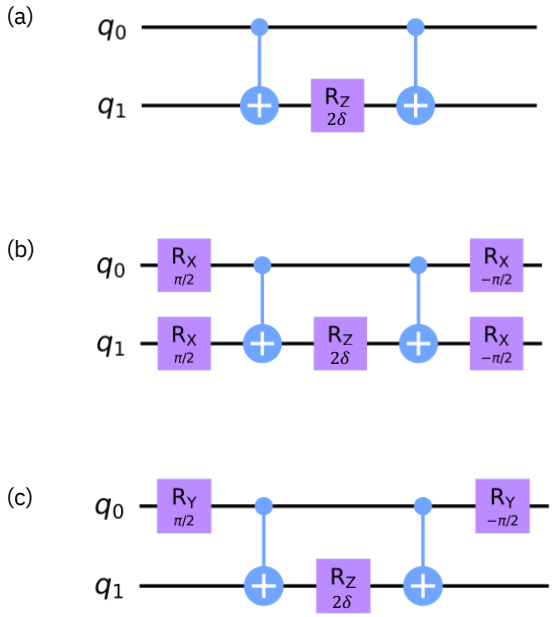

Figure A.1: Composition of two-qubit gates with elementary quantum gates. (a) $ZZ(\delta) = e^{-i\delta\sigma_z\otimes\sigma_z}$. (b) $YY(\delta) = e^{-i\delta\sigma_y\otimes\sigma_y}$, built using the identity $R_x(\pi/2)\sigma_z R_x - \pi/2$. (c) $XX(\delta) = e^{-i\delta\sigma_x\otimes\sigma_x}$, built using the identity $R_y(\pi/2)\sigma_z R_y(-\pi/2)$.

When considering the Digital Quantum Simulation of physical systems, for example a Fermi-Hubbard model (see Chap. 6), the interaction between different spins is described by these two-qubit operations. In order to implement a useful set of building blocks on the Qiskit framework for IBM Quantum platform, we must consider a typical Universal gate set for superconducting transmon qubits, consisting of the single-qubit

rotations and the entangling gate CNOT. In particular, one can verify the gates compositions [11] depicted in Fig. A.1, implementing ZZ, YY and XX. It is possible to select other Universal gate sets used to build the two-qubit building blocks, by choosing e.g. C-$\Phi(\delta)$ gate instead of CNOT gate, equally implementable on a superconducting quantum processor [14][215][216][217].

The building blocks reported in Fig. A.1 have been extensively used to build the time evolution circuits for the Fermi-Hubbard model (see Sec. 6.5.1 and Sec. 6.5.2), in particular the YY and XX building blocks for the hopping term, and the ZZ building block for the interaction term.

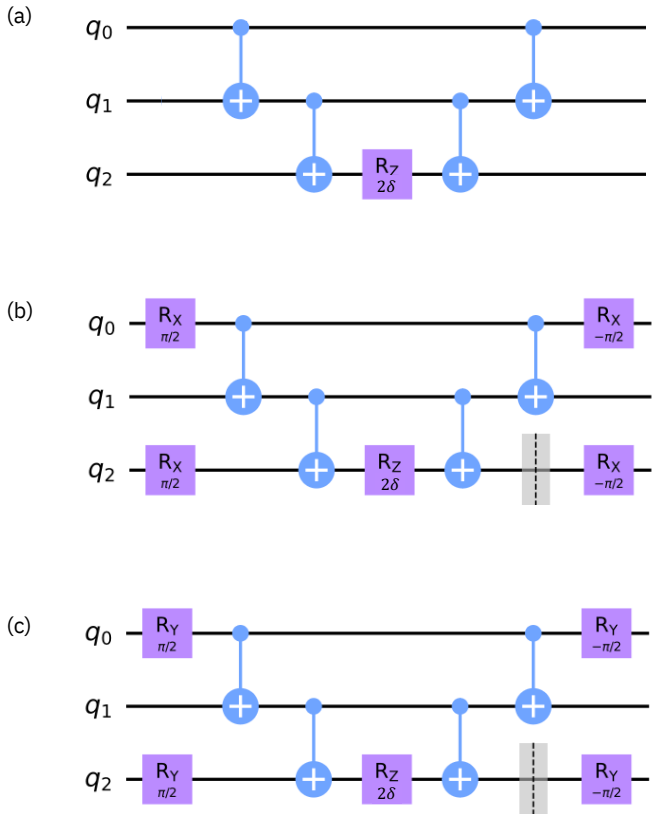

Figure A.2: Composition of three-qubit gates with elementary quantum gates. (a) $ZZZ(\delta) = e^{-i\delta\sigma_z\otimes\sigma_z\otimes\sigma_z}$. (b) $YZY(\delta) = e^{-i\delta\sigma_y\otimes\sigma_z\otimes\sigma_y}$. (c) $XZX(\delta) = e^{-i\delta\sigma_x\otimes\sigma_z\otimes\sigma_x}$. The barriers have been inserted for a better circuit visualization only. The above circuit shapes are generalizable to N-qubits.

The two-qubit gates composition can be extended to a multi-qubit approach, with the objective to create N-qubit building blocks using single- and two-qubit elementary operations from the Universal gate set consisting of single-qubit rotations and two-qubit CNOTs. Fig. A.2 shows the building blocks using 3 qubits, implementing ZZZ, YZY and XZX; however, this can be generalized in case of N-qubits [11].

A.3 Search for systematic errors of quantum gates on IBM Quantum

As introduced in Chapter 1, quantum errors affecting current QC platforms can be divided in two categories: coherent errors and incoherent errors. While incoherent errors, the most dangerous for the computation, must be handled with proper techniques, coherent errors can be categorized as an incorrect application of quantum gates: they can be considered systematic errors. These errors can thus be characterized and, eventually, corrected by a proper tuning of the quantum gates themselves.

A.3.1 Single-qubit rotations state tomography

Single-qubit rotation gates R_x and R_y should perform rotations respectively on x and y axes; an effect of the *gates error* is that single qubit rotations act on tilted angles. An ε_z tilt angle affects the R_x and R_Y accuracy at the maximum rotation (π) , while ε_x and ε_y affect the real and imaginary part of the rotation. The following equations represent generic rotations along x and y axes affected by coherent errors, corrected with the tilt angles ε_x, ε_y and ε_z [11]:

$$R_{\hat{n}_x}(\theta) = R_z(\varepsilon_y)R_y(-\varepsilon_z + \frac{\pi}{2})R_z(\theta)R_y(\varepsilon_z - \frac{\pi}{2})R_z(-\varepsilon_y) \tag{A.3}$$

$$R_{\hat{n}_y}(\theta) = R_z(-\varepsilon_x)R_x(\varepsilon_z + \frac{\pi}{2})R_z(-\theta)R_x(-\varepsilon_z - \frac{\pi}{2})R_z(\varepsilon_x) \tag{A.4}$$

where $\hat{n}_x = (\cos\varepsilon_y \cos\varepsilon_z, \cos\varepsilon_y \sin\varepsilon_y, \sin\varepsilon_z)$, $\hat{n}_y = (\cos\varepsilon_z \cos\varepsilon_x, \cos\varepsilon_x \sin\varepsilon_z, \sin\varepsilon_z)$.

Although the Qiskit Noisy Simulator is not meant to exactly reproduce the behaviour of the related quantum hardware, it is possible to have a good representation of the calibration at the time of the simulation; given that, in Fig. A.3 and Fig. A.4 are reported the single-qubit R_x and R_y rotations characterization, in which the hardware behaviour has been reproduced with a parametric noisy simulation following the relations reported in Eq. A.3 and Eq. A.4. The best ε parameters set that reproduces the hardware behaviour is reported in Table A.1 and in Table A.2.

We note that, as the Quantum Volume increases, the systematic errors are lowered as the tilt angles needed to correct them become smaller. Compared to `ibmq_yorktown` QV8 device, the best ε set for `ibmq_montreal` QV128 device consists of values almost one order of magnitude smaller. This is due to the increment of quality of IBM Quantum devices during time (in this case from late 2019 to mid 2020), reflecting on a larger QV through the various quantum hardware generations released.

ε_x	ε_y	ε_z
$\sim \pi/20$	$\sim \pi/26$	$\sim \pi/19$

Table A.1: Parameters set to correct systematic errors for IBM Quantum Yorktown QV8 quantum chip (late 2019).

Together with results reported in Fig. A.3 and Fig. A.4, we performed another test on QV8 device `ibmq_yorktown` (late 2019) by correcting a series of subsequent X gates:

ε_x	ε_y	ε_z
$\sim \pi/130$	$\sim \pi/100$	$\sim \pi/100$

Table A.2: Parameters set to correct systematic errors for IBM Quantum Montreal QV128 quantum chip (mid 2020).

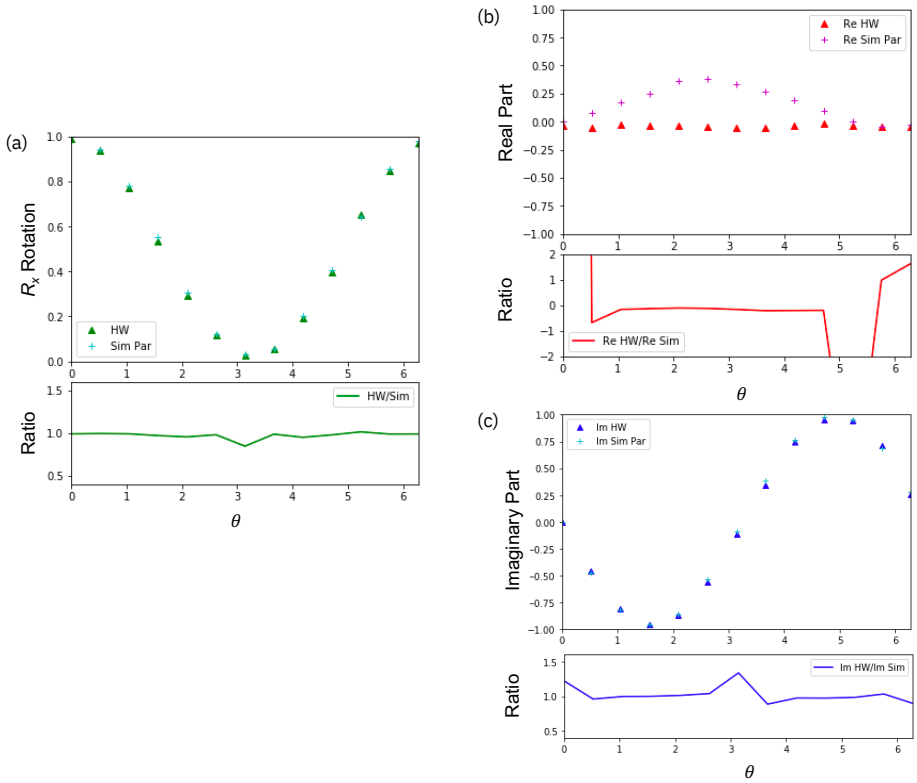

Figure A.3: (a) Behaviour of an hardware rotation R_x from 0 to 2π on a single qubit of IBM Quantum Yorktown QV8 chip reproduced with the noiseless simulator following Eq. A.3. (b) Real and (c) Imaginary parts with ratio plots between hardware and parametrized simulations. We note that the hardware real part is zero, so the simulation struggles to reconstruct it.

while we note an increasing error from 1.7% to 8.9% for 1 to 15 subsequent X hardware gates (odd steps) on a single qubit, a parametrized rotation $U_x(\pi)$ built as the following (and based on Eq. A.3 and Eq. A.4)

$$U_x(\pi) = \begin{pmatrix} -i\sin\varepsilon_y & -(\sin\varepsilon_z + i\cos\varepsilon_z)\cos\varepsilon_y \\ (\sin\varepsilon_z - i\cos\varepsilon_z)\cos\varepsilon_y & i\sin\varepsilon_y \end{pmatrix} \tag{A.5}$$

with $\varepsilon_y = \pi/26$ and $\varepsilon_z = \pi/19$ (see Table A.1, late 2019), shows no increasing trend in error, leaving the State Fidelity constant.

This method can be leveraged to correct the systematic error of the QV8 hardware rotations by properly tilting the rotation axes; however, we note that the computed ε set

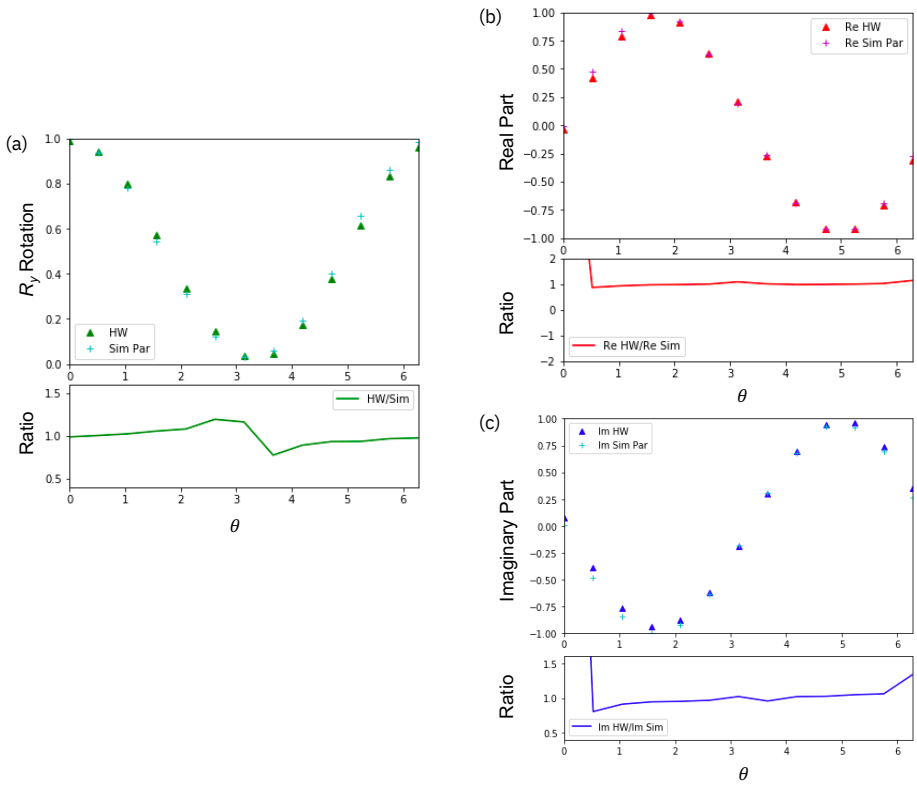

Figure A.4: (a) Behaviour of an hardware rotation R_y from 0 to 2π on a single qubit of IBM Quantum Yorktown QV8 chip reproduced with the noiseless simulator following Eq. A.4. (b) Real and (c) Imaginary parts with ratio plots between hardware and parametrized simulations. The hardware behaviour of the rotation itself and both real and imaginary parts are well reconstructed by the parametrized noiseless simulations, as confirmed by the ratio plots.

for QV128 hardware starts to become negligible, as reported in Table A.2 (mid 2020): as the IBM Quantum devices quality continues to be improved, this method would become less impacting on quantum hardware computed results.

A.3.2 Two-qubit CNOT state tomography

We now perform the state tomography of a CNOT gate performed on two qubits with IBM Quantum `ibmq_yorktown` QV8 chip (mid 2020). The CNOT density matrix ρ_{CNOT} has been built starting from the four Bell states [11] as initial states:

$$\frac{|0\rangle + |1\rangle}{\sqrt{2}} \otimes |0\rangle \rightarrow \begin{pmatrix} 1 \\ 0 \\ 1 \\ 0 \end{pmatrix} \text{ on basis } \begin{matrix} |00\rangle \\ |01\rangle \\ |10\rangle \\ |11\rangle \end{matrix} \tag{A.6}$$

$$\frac{|0\rangle - |1\rangle}{\sqrt{2}} \otimes |0\rangle \rightarrow \begin{pmatrix} 1 \\ 0 \\ -1 \\ 0 \end{pmatrix} \text{ on basis } \begin{matrix} |00\rangle \\ |01\rangle \\ |10\rangle \\ |11\rangle \end{matrix} \tag{A.7}$$

$$\frac{|0\rangle + |1\rangle}{\sqrt{2}} \otimes |1\rangle \rightarrow \begin{pmatrix} 0 \\ 1 \\ 0 \\ 1 \end{pmatrix} \text{ on basis } \begin{matrix} |00\rangle \\ |01\rangle \\ |10\rangle \\ |11\rangle \end{matrix} \tag{A.8}$$

$$\frac{|0\rangle - |1\rangle}{\sqrt{2}} \otimes |1\rangle \rightarrow \begin{pmatrix} 0 \\ 1 \\ 0 \\ -1 \end{pmatrix} \text{ on basis } \begin{matrix} |00\rangle \\ |01\rangle \\ |10\rangle \\ |11\rangle \end{matrix} \tag{A.9}$$

By properly measuring the circuit related to the above states on the selected quantum hardware (or performing a noisy simulation), it is possible to compute the following observables:

$$\begin{aligned} \langle \sigma_z \otimes \sigma_z \rangle, \langle \sigma_x \otimes \sigma_x \rangle, \langle \sigma_y \otimes \sigma_y \rangle \\ \langle I \otimes \sigma_x \rangle, \langle \sigma_x \otimes I \rangle, \langle I \otimes \sigma_y \rangle, \langle \sigma_y \otimes I \rangle \\ \langle \sigma_z \otimes \sigma_x \rangle, \langle \sigma_z \otimes \sigma_y \rangle \\ \langle \sigma_x \otimes \sigma_z \rangle, \langle \sigma_y \otimes \sigma_z \rangle \\ \langle \sigma_x \otimes \sigma_y \rangle, \langle \sigma_y \otimes \sigma_x \rangle \end{aligned} \tag{A.10}$$

Observables reported in Eq. A.10 can be finally used to compose the CNOT density matrix as follows:

$$\rho_{CNOT} = \begin{pmatrix} |\alpha|^2 & \alpha^*\beta & \alpha^*\gamma & \alpha^*\delta \\ \beta^*\alpha & |\beta|^2 & \beta^*\gamma & \beta^*\delta \\ \gamma^*\alpha & \gamma^*\beta & |\gamma|^2 & \gamma^*\delta \\ \delta^*\alpha & \delta^*\beta & \delta^*\gamma & |\delta|^2 \end{pmatrix} \tag{A.11}$$

where the in-diagonal elements are

$$\text{In-diagonal} \rightarrow \begin{cases} |\alpha|^2 = ZZ[00] \\ |\beta|^2 = ZZ[01] \\ |\gamma|^2 = ZZ[10] \\ |\delta|^2 = ZZ[11] \end{cases} \tag{A.12}$$

and the off-diagonal elements are

$$\text{Off-diagonal} \rightarrow \begin{cases} XX + YY \propto \Re(\beta\gamma) \\ XY - YX \propto \Im(\beta\gamma) \\ IX + ZX \propto \Re(\alpha\beta) \\ IY + ZY \propto \Im(\alpha\beta) \\ XI + XZ \propto \Re(\alpha\gamma) \\ YI + YZ \propto \Im(\alpha\gamma) \\ XY + YX \propto \Re(\alpha\delta) \\ XX - YY \propto \Im(\alpha\delta) \\ IX + ZX \propto \Re(\delta\gamma) \\ IY + XY \propto \Im(\delta\gamma) \\ XI + XZ \propto \Re(\beta\delta) \\ YI + YZ \propto \Im(\beta\delta) \end{cases} \tag{A.13}$$

We report in Fig. A.5 and in Fig. A.6 the result of the CNOT tomography performed on `ibmq_yorktown` QV8 device in late 2019 for the four qubits used for the first tests of the Fermi-Hubbard model time evolution reported in Chap. 6, in particular the qubit pairs 0-1 and 2-3. The State Fidelity provides a comparison between noiseless simulations and real hardware runs.

The computed State Fidelity for CNOTs on QV 8 devices is above 0.9: considering a further increase on higher QV devices, it is possible to consider the two-qudit gate implementation reliable.

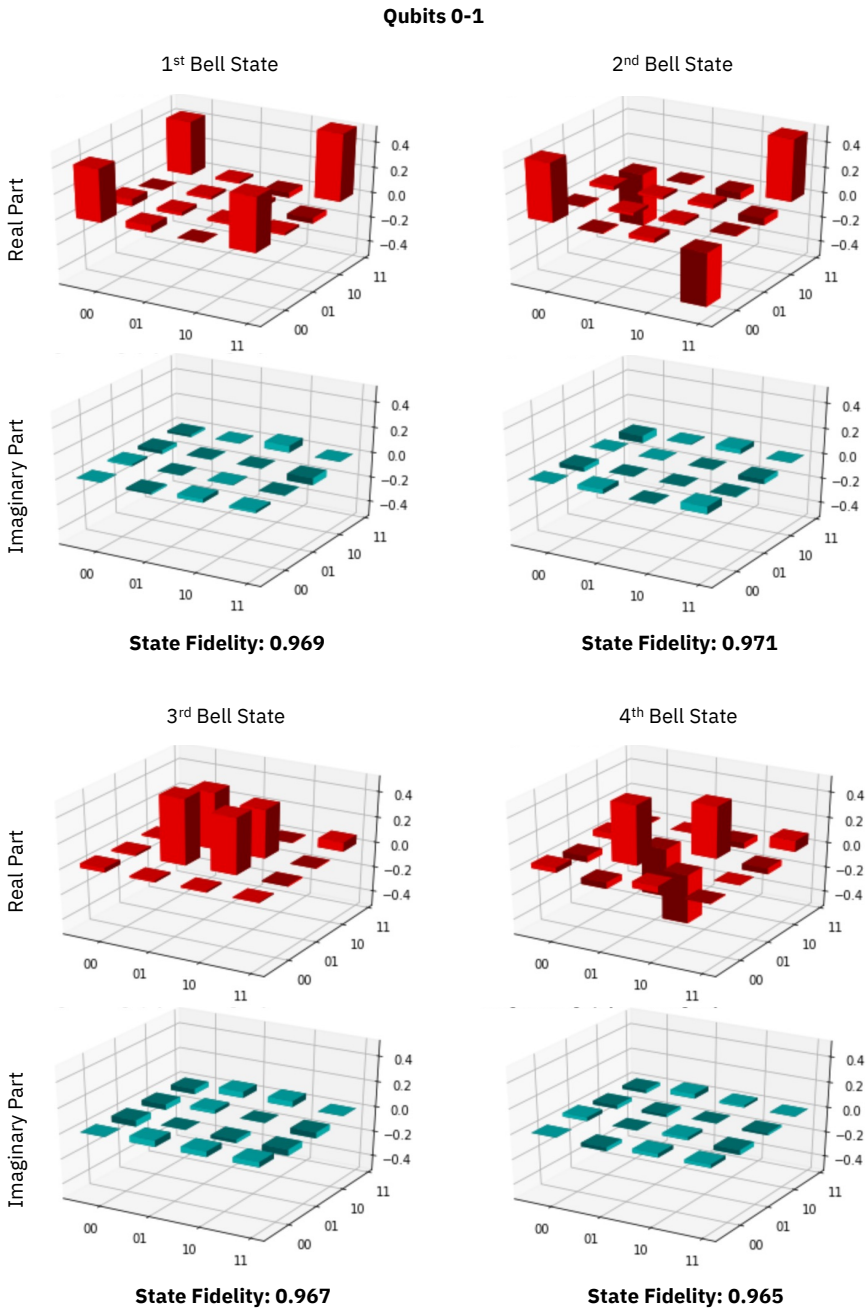

Figure A.5: CNOT tomography for IBM Quantum Yorktown QV8 device (late 2019), for the first tests of the Fermi-Hubbard model time evolution reported in Chap. 6 for qubits 0-1, built using the ρ_{CNOT} relation in Eq. A.11. The State Fidelity gives a comparison between noiseless simulations and real hardware runs.

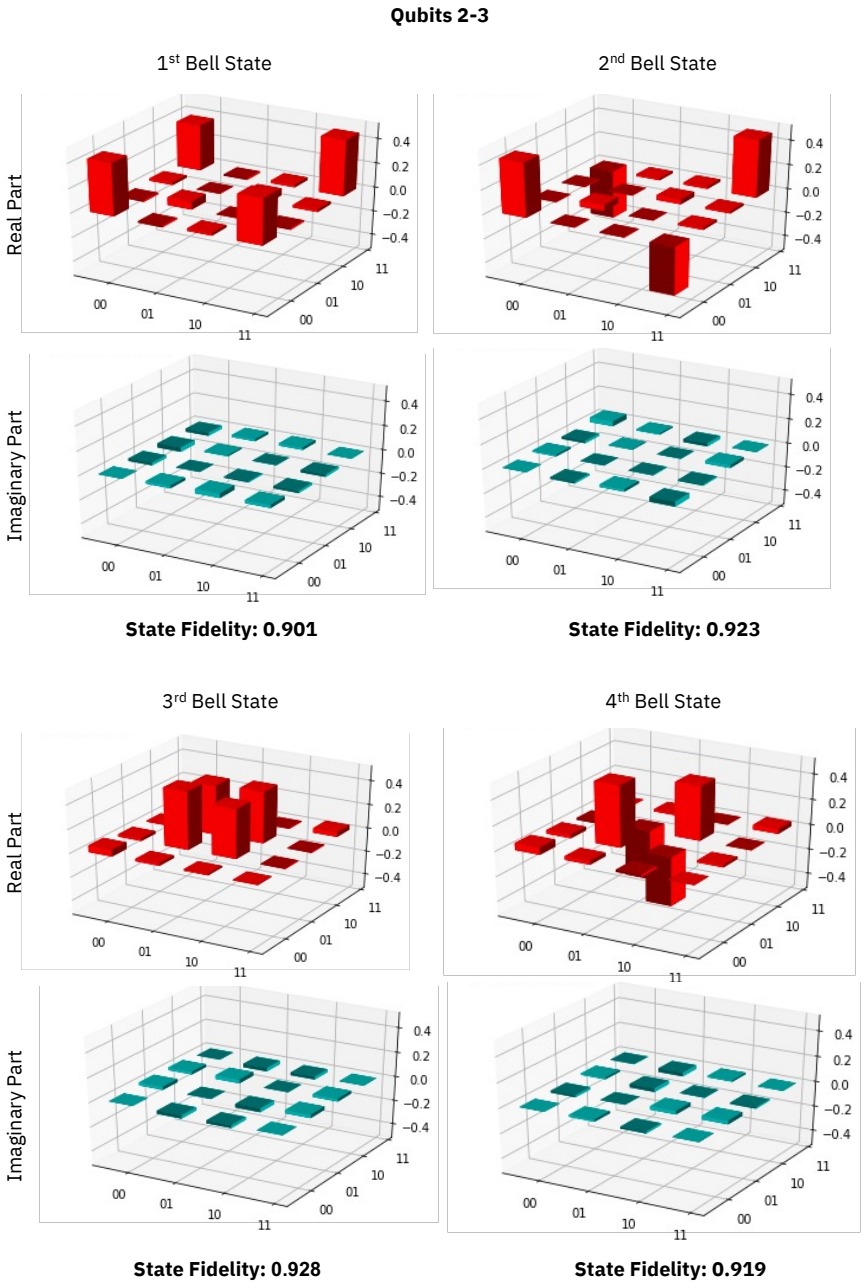

Figure A.6: CNOT tomography for IBM Quantum Yorktown QV8 device (late 2019), for the first tests of the Fermi-Hubbard model time evolution reported in Chap. 6 for qubits 2-3, built using the ρ_{CNOT} relation in Eq. A.11. The State Fidelity gives a comparison between noiseless simulations and real hardware runs.

A.4 Qiskit Measurement Error Mitigation

Qiskit provides an automatic feature to correct the measurement error, called Measurement Error Mitigation (MEM) [142]. It consists in the computation of a calibration matrix that can help to determine the effect of the measurement operation on the results: this is performed by preparing all the possible basis states, then by measuring them and looking for the probability distribution. In particular, given

$$P_x = \mathrm{Tr}\left(\langle x|\rho|x\rangle\right) \tag{A.14}$$

where ρ is the density matrix, and given P_ρ the ideal probability distribution, $\tilde{P}_\rho$ the experimental probability distribution and A the calibration matrix, one can compute:

$$\begin{aligned} \tilde{P}_\rho &= A \cdot P_\rho \\ P_\rho &= A^{-1} \cdot \tilde{P}_\rho \end{aligned} \tag{A.15}$$

The calibration matrix A translates the ideal probability distribution into the experimental probability distribution; errors due to the measurement can be mitigated by applying an inverted calibration matrix to the final result.

This method is applied *a posteriori* on the computed results:

$$|\psi\rangle \rightarrow |\tilde{\psi}\rangle = R|\psi\rangle \rightarrow |\tilde{\psi}_{mitigated}\rangle = A^{-1}|\tilde{\psi}\rangle \tag{A.16}$$

we start from a certain initial state $|\psi\rangle$ and we perform a rotation on it, then we can apply the inverted calibration matrix to mitigate the error coming from the measurement operation. Fig. A.7 shows the application of Qiskit Measurement Error Mitigation on a R_x rotation on `ibmq_armonk` chip (mid 2020). It is finally worth noticing that this method performs very well when the error due to the measurement process is relevant with respect to the other errors, i.e. when the circuit consists of a rather small amount of gates (as the case of Eq. A.16), or when a large amount of measurement gates are performed (as the case of specific algorithms like VQE).

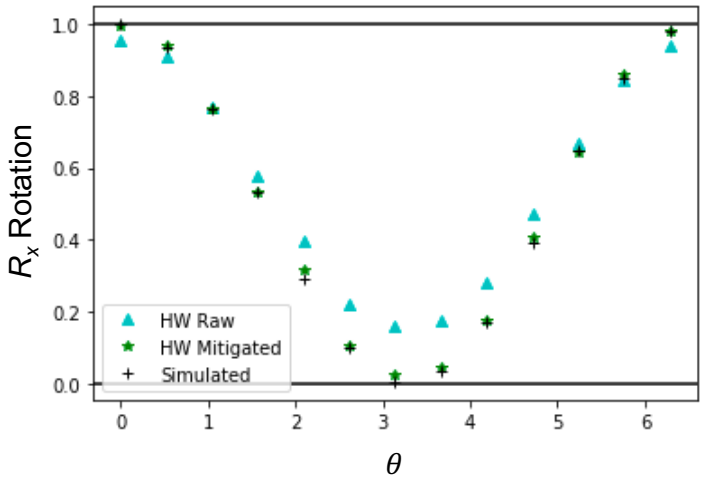

Figure A.7: Qiskit Measurement Error Mitigation (MEM) example on a single rotation gate on IBM Quantum Armonk device (mid 2020). Light blue triangles represent a R_x rotation from 0 to 2π performed on IBM Quantum Armonk hardware, black crosses represent the noiseless simulation of the rotation, and the green stars are the above hardware results mitigated with Qiskit Measurement Error Mitigation. We notice that green stars and black crosses are almost superimposed: this means that the Measurement Error Mitigation is able to mitigate the leading error coming from the measurement process. Other errors, i.e. the *gate error* of the rotation itself, are still present and not corrected by the Qiskit MEM, slightly drifting the mitigated results from the noiseless behaviour.

APPENDIX B

Quantum gates decomposition on qudits

Here we demonstrate how the Hadamard Transform is the Quantum Fourier Transform (QFT) for a single qubit, and how can be generalized in case of a qudit of size d [165].

B.1 Hadamard Transform and QFT

The QFT for a registry of n qubits is defined:

$$U_{QFT}|x\rangle_n = \frac{1}{\sqrt{2^n}} \sum_{y=0}^{2^n-1} e^{2\pi i x y/2^n} |y\rangle_n \tag{B.1}$$

Equation B.1 can be generalized in case of a d-sized qudit as the following:

$$U_{QFT}|x\rangle = \frac{1}{\sqrt{d}} \sum_{y=0}^{d-1} e^{2\pi i x y/d} |y\rangle \tag{B.2}$$

where $|x\rangle, |y\rangle \in \{|0\rangle, |1\rangle, ..., |d-1\rangle\}$.

The effect of Hadamard Transformation is to map $H|0\rangle \leftarrow |+\rangle$ and $H|1\rangle \leftarrow |-\rangle$, so a compact form can be expressed as $H = |+\rangle\langle 0| + |-\rangle\langle 1|$. In order to generalize the Hadamard Transformation to a d-level system, we nee first to generalize the X and Z operators, since H transforms Z eigenvectors in X eigenvectors:

$$\begin{cases} \mathrm{X}_d|x\rangle = |x \oplus 1\rangle \\ \mathrm{Z}_g = \sum_{x=0}^{d-1} e^{2\pi i x/d} |x\rangle\langle x| \end{cases} \tag{B.3}$$

Hence, the X_d and Z_d eigenvectors can be expressed as:

$$\begin{cases} |\tilde{z}\rangle = \{|x\rangle\}_{x=0}^{d-1} \\ |\tilde{x}\rangle = \frac{1}{\sqrt{d}} \sum_{y=0}^{d-1} e^{2\pi i x y/d} |y\rangle \end{cases} \tag{B.4}$$

Finally, considering Eq. B.4, the Hadamard Transformation can be written as $\mathrm{H}_d|x\rangle = |\tilde{x}\rangle = \frac{1}{\sqrt{d}} \sum_{y=0}^{d-1} e^{2\pi i x y/d} |y\rangle$, that is the QFT reported in Eq. B.2.

■

B.2 Details of decomposition methods

In this Section are reported the details for the implementation of single-qudit quantum gates for both Planar Rotations and Quantum Householder Reflections decomposition methods. The reported parameters are used to implement the Generalized Hadamard gate, following the algorithm outlined in Sec. 7.4.

B.2.1 Planar Rotations

Here we report all the parameters of the decomposition of a Generalized Hadamard gate using Planar Rotations, in case of a "linear" connectivity between levels (S-systems) and in case of a "full" connectivity between levels (C-systems).

The $\pi^{\pm}_{\mu\nu}$ pulses are properly used to swap up or down the eigenstates, in order to perform U rotations on adjacent eigenstates $|\mu\rangle$, $|\nu\rangle$.

$$\begin{aligned} H_4 = {} & P_{1,2}P_{3,4}\times \\ & \times U_{1,2} \times \pi^{+}_{1,2}U_{1,3}\pi^{-}_{1,2}U_{2,3} \times \pi^{+}_{3,4}\pi^{+}_{2,3}U_{1,4}\pi^{-}_{2,3}U_{2,4}\pi^{-}_{3,4}U_{3,4} \end{aligned} \tag{B.5}$$

$$\begin{aligned} H_6 = {} & P_{5,6}P_{3,4}P_{2,3}\times \\ & \times U_{1,2} \times \pi^{+}_{2,3}U_{1,3}\pi^{-}_{2,3}U_{2,3} \times \pi^{+}_{3,4}\pi^{+}_{2,3}U_{1,4}\pi^{-}_{2,3}U_{2,4}\pi^{-}_{3,4}U_{3,4}\times \\ & \times \pi^{+}_{4,5}\pi^{+}_{3,4}\pi^{+}_{2,3}U_{1,5}\pi^{-}_{2,3}U_{2,5}\pi^{-}_{3,4}U_{3,5}\pi^{-}_{4,5}U_{4,5}\times \\ & \times \pi^{+}_{5,6}\pi^{+}_{4,5}\pi^{+}_{3,4}\pi^{+}_{2,3}U_{1,6}\pi^{-}_{2,3}U_{2,6}\pi^{-}_{3,4}U_{3,6}\pi^{-}_{4,5}U_{4,6}\pi^{-}_{5,6}U_{5,6} \end{aligned} \tag{B.6}$$

$$\begin{aligned} H_8 = {} & P_{7,8}P_{6,7}P_{5,6}P_{3,4}P_{1,2}\times \\ & \times U_{1,2} \times \pi^{+}_{2,3}U_{1,3}\pi^{-}_{2,3}U_{2,3} \times \pi^{+}_{3,4}\pi^{+}_{2,3}U_{1,4}\pi^{-}_{2,3}U_{2,4}\pi^{-}_{3,4}U_{3,4}\times \\ & \times \pi^{+}_{4,5}\pi^{+}_{3,4}\pi^{+}_{2,3}U_{1,5}\pi^{-}_{2,3}U_{2,5}\pi^{-}_{3,4}U_{3,5}\pi^{-}_{4,5}U_{4,5}\times \\ & \times \pi^{+}_{5,6}\pi^{+}_{4,5}\pi^{+}_{3,4}\pi^{+}_{2,3}U_{1,6}\pi^{-}_{2,3}U_{2,6}\pi^{-}_{3,4}U_{3,6}\pi^{-}_{4,5}U_{4,6}\pi^{-}_{5,6}U_{5,6} \\ & \times \pi^{+}_{6,7}\pi^{+}_{5,6}\pi^{+}_{4,5}\pi^{+}_{3,4}\pi^{+}_{2,3}U_{1,7}\pi^{-}_{2,3}U_{2,7}\pi^{-}_{3,4}U_{3,7}\pi^{-}_{4,5}U_{4,7} \times \pi^{-}_{5,6}U_{5,7}\pi^{-}_{6,7}U_{6,7}\times \\ & \times \pi^{+}_{7,8}\pi^{+}_{6,7}\pi^{+}_{5,6}\pi^{+}_{4,5}\pi^{+}_{3,4}\pi^{+}_{2,3}U_{1,8}\pi^{-}_{2,3}U_{2,8}\pi^{-}_{3,4}U_{3,8}\times \\ & \times \pi^{-}_{4,5}U_{4,8}\pi^{-}_{5,6}U_{5,8}\pi^{-}_{6,7}U_{6,8}\pi^{-}_{7,8}U_{7,8} \end{aligned} \tag{B.7}$$

A "full" connectivity between levels does not require the additional $\pi^{\pm}_{\mu\nu}$ pulses, as no swap are needed. Thus, the amount of required pulses is lowered, and Eq. B.5, Eq. B.6 and Eq. B.7 are modified accordingly. With the above reported gate decomposition in elementary pulses, we can now report the parameters to create each $U_{\mu\nu}$ and each P_{α}. In Tab. B.1, Tab. B.2 and Tab. B.3 are reported the values, keeping three significant digits when a numeric form is needed (due to a complex arithmetic expression).

μ, ν	$\theta/2$	β	α
3,4	$-\pi/4$	$\pi/2$	
2,4	$\arctan(1/\sqrt{2})$	0	
1,4	$\arctan(1/\sqrt{3})$	$\pi/2$	
2,3	0.912	-0.464	
1,3	$\arctan(-1/\sqrt{2})$	$-\pi/4$	
1,2	$\pi/4$	$\pi/4$	
3,4			$\pi/8$
1,2			$3\pi/8$

Table B.1: Parameters to decompose H_4 gate into PR (keeping three significant digits), assuming full connectivity.

B.2.2 Quantum Householder Reflection

Here are reported the parameters for the Quantum Householder Reflection for the Generalized Hadamard decomposition in elementary pulses, following the algorithm outlined in Sec. 7.4. In Tab. B.4 are reported the values of the parameters v_i and ϕ_i, keeping three significant digits when a numeric form is needed (due to a complex arithmetic expression).

μ, ν	$\theta/2$	β	α
5,6	$\pi/4$	$-2\pi/3$	
4,6	$\arctan(1/\sqrt{2})$	$-\pi/3$	
3,6	$\pi/6$	2π	
2,6	$\arctan(1/2)$	$\pi/3$	
1,6	$\arctan(1/\sqrt{5})$	$2\pi/3$	
4,5	$(\sqrt{3/7})$	$-\arctan(3\sqrt{3})$	
3,5	$(2\sqrt{5/19})$	$(4/\sqrt{3})$	
2,5	$\arctan(\sqrt{31/65})$	$\pi - \arctan(5\sqrt{3}/7)$	
1,5	$\arctan(1/2)$	$-2\pi/3$	
3,4	$\arctan(\sqrt{37/13})$	$-\arctan(2\sqrt{3}/5)$	
2,4	$(2\sqrt{5/19})$	$1/2(\pi + \arctan(8\sqrt{3}/13))$	
1,4	$\pi/6$	$-\pi/2$	
2,3	$\arctan(\sqrt{7/3})$	$\arctan(1/3\sqrt{3})$	
1,3	$\arctan(1/\sqrt{2})$	$-5\pi/6$	
1,2	$\pi/4$	1.047	
5,6			$-\pi/3$
3,4			$\pi/2$
2,3			$2\pi/3$

Table B.2: Parameters to decompose H_6 gate into PR (keeping three significant digits), assuming full connectivity.

μ,ν	$\theta/2$	β	α
7,8	$\pi/4$	$-3\pi/4$	
6,8	$\arctan(1/\sqrt{2})$	$-\pi/2$	
5,8	$\pi/6$	$-\pi/4$	
4,8	$2\arctan(1/2)$	0	
3,8	$\arctan(1/\sqrt{5})$	$\pi/4$	
2,8	$(\sqrt{6})$	$\pi/2$	
1,8	$\arctan(1/\sqrt{7})$	$3\pi/4$	
6,7	1.016	4.457	
5,7	0.824	-0.5	
4,7	0.687	0.843	
3,7	0.573	2.213	
2,7	0.474	-2.657	
1,7	0.388	-1.178	
5,6	1.093	-1.249	
4,6	0.895	0.655	
3,6	0.731	2.585	
2,6	0.573	-1.714	
1,6	0.421	0.393	
4,5	1.113	-0.663	
3,5	0.895	1.834	
2,5	0.687	-1.906	
1,5	0.464	0.785	
3,4	1.093	-0.071	
2,4	0.824	3.034	
1,4	0.524	0	
2,3	1.016	0.530	
1,3	0.615	-1.963	
1,2	0.785	1.178	
7,8			$\pi/16$
6,7			π
5,6			$7\pi/16$
3,4			$11\pi/16$
1,2			$5\pi/16$

Table B.3: Parameters to decompose H_8 gate into PR (keeping three significant digits), assuming full connectivity.

	H_3 v_i	ϕ_i
1	$\frac{1}{2}\sqrt{1+\frac{1}{\sqrt{3}}}[1-\sqrt{3},1,1]^T$	π
2	$\frac{1}{\sqrt{2}}[0,1,-1]^T$	$\pi/2$

	H_4 v_i	ϕ_i
1	$\frac{1}{2}[-1,1,1,1]^T$	π
2	$\frac{1}{\sqrt{2}}[0,1,0,-1]^T$	$\pi/2$

	H_6 v_i	ϕ_i
1	$[0.544i,-0.375i,-0.375i,-0.375i,-0.375i,-0.375i]^T$	$-\pi$
2	$[0,0.575+0.220i,0.244-0.261i,0.071+0.103i,-0.331+0.135i,-0.559-0.197i]^T$	1.937
3	$[0,0,-0.490+0.626i,0.113-0.466i,0.352-0.055i,0.025-0.105i]^T$	-2.478
4	$[0,0,0,-0.322+0.537i,0.395-0.657i,-0.073+0.121i]^T$	-2.601

	H_8 v_i	ϕ_i
1	$[0.569i,-0.311i,-0.311i,-0.311i,-0.311i,-0.311i,-0.311i,-0.311i]^T$	$-\pi$
2	$[0,0.432+0.384i,0.230-0.305i,0.238-0.048i,0.062+0.139i,-0.194+0.146i,-0.381-0.030i,-0.388-0.286i]^T$	2.297
3	$[0,0,0.174+0.819i,-0.228+0.008i,-0.097-0.316i,0.159-0.231i,0.060-0.056i,-0.067-0.22i]^T$	2.932
4	$[0,0,0,0.233+0.568i,-0.146+0.133i,-0.336-0.475i,0.352-0.320i,-0.103+0.094i]^T$	2.752
5	$[0,0,0,0,0.046+0.355i,0.032+0.251i,-0.110-0.856i,0.032+0.251i]^T$	3.014

Table B.4: Parameters to decompose H_3, H_4, H_6 and H_8 gate into QHR (keeping three significant digits).

APPENDIX C

Technological innovation

Conducting a research process based on Quantum Computing implying the simulation of complex systems or the execution of hybrid algorithm, e.g. the Variational Quantum Eigensolver, could be very demanding in terms of computational resources and execution time. Simulations reported in Chap. 5, Chap. 6 and in Ref. [127] fall in this category, in particular by increasing the complexity of the target system (i.e. number of spins of an open/closed Heisenberg chain).

C.1 Automatic computation framework for quantum algorithms

In order to overcome the large amount of time and resources required to perform simulations, together with dealing with the overall process complexity, we built the following computational framework able to exploit HPC resources and databases technologies.

This framework consists of three different parts: enabling the parallel computation on a proper environment, managing the input and output data by providing access to a database in which to store experiments data and metadata, and implementing a dashboard to display results, along with the development environment. The high level architecture is reported in Fig. C.1.

C.1.1 Data calculation: the computational environment

Required and intensive numerical computation effort, for both classical simulation of quantum devices and the classical part of hybrid quantum-classical algorithms, can be demanded to High Performance Computing (HPC) or Cloud environments. A proper parallelisation of jobs has been exploited, i.e. splitting the overall process in a set of independent calculations sent to the available resources in the environment: in particular, a significant speed up in the VQE process on Ref. [127] has been reached (~ 200 times for the most complex calculations) with respect to the same computation performed locally without parallelisation.

C.1.2 Data collection: the data storage

All the computed results, together with the related metadata and input configurations, are then stored into a NoSQL database. Specifically for Ref. [127] calculations, we in-

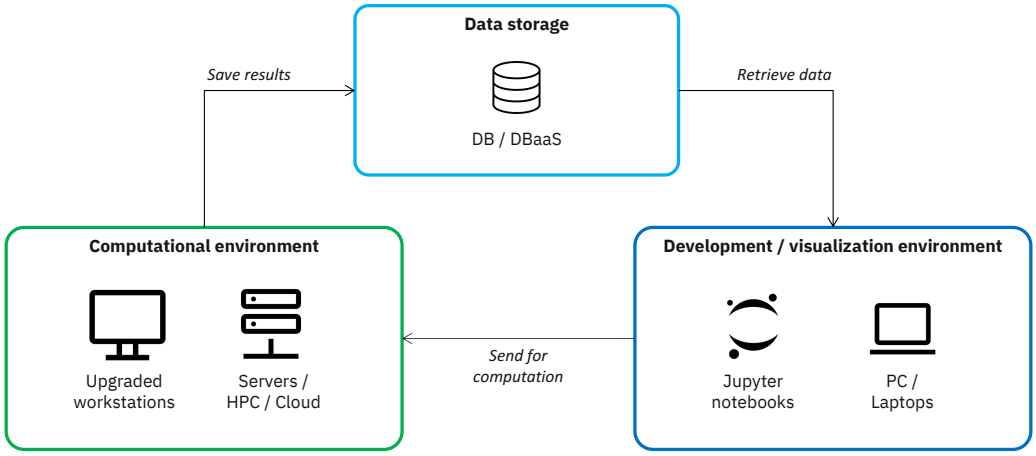

Figure C.1: Computation framework developed to handle IBM Quantum / Qiskit jobs and results. A local development environment is used to develop algorithms and view / consolidate data plots. A remote computational environment allows to access computational resources to perform high demanding simulation jobs in parallel. Computed results are securely stored and reliably in a database, together with all the metadata and input configurations. Queries are performed on the database to retrieve data in order to consolidate plots.

cluded in the database collection the following main metadata for each computation (i.e. one for each point in each plot):

- **physical parameters**: J_x, J_y, J_z, D, and the number of spins composing the chain;
- **external parameters**: magnetic field B_x and B_z components, together with the tilt angle θ;
- **VQE configuration**: ansatz identifier, ansatz depth, optimization algorithm, maximum number of optimization iterations;
- **quantum run configuration**: number of gates (pre and post transpiling), number of shots, quantum backend or simulator, measurement error mitigation flag (on/off);
- **results**: best energy value and counts, ground state components, ground state parametrized circuit, ground state density matrix components, parallel and perpendicular magnetization values and counts, torque;
- **run information**: initial timestamp, final timestamp, computational time taken, together with the database entry id (unique).

C.1.3 Data Plot: development and visualization environment

The last part has the aim to retrieve the data from the database by performing queries, in order to collect all data related to a single experiment, i.e. all the series of points to be put in the same plot. Some specific functions perform data retrieval and print the plots.

Considering that the data storage and data retrieval process are performed in near real time, this set of functions can be used to create a live dashboard to showcase the results.

Details of this framework has been reported on Read The Docs (Ref. [218]).

C.2 A new framework for integrating Quantum into existing software architectures

C.2.1 Introduction

The recent improvements on Quantum Computing technology made possible to everyone to access and use real QC prototypes: this will lead quickly to the possibility to include quantum-based workloads into current software architectures. Startups and corporations could soon begin using quantum computers to enhance software applications in fields like finance and the materials sciences, but to reach that point, it is not sufficient to just build quantum systems and hope industry developers figure out how to integrate their workloads with this new technology. The design of such software on distributed systems is based on a couple of essential best practices and pillars, such as the loose-coupling of components (i.e. the modularity of the software), the use of open-source frameworks, and the reusability of assets and components; a software application typically consists of logical layers, allowing the developers and maintainers to work on specific components in a decoupled way. Nowadays it is still very difficult to perform an hybrid quantum-classical computation in an integrated way, exploiting a classical computer and a quantum computer to perform some specific tasks or workloads inside the same software application.

We present here an open-source software architecture, following the above mentioned best practices, that can be used as a pre-built pattern to create hybrid applications: this framework allows the developers to quickly create workloads able to receive user requests, sending them to a Quantum Computer, and receiving the results back, while making sure all data handling occurs in the right order and format.

Quantum Computing services released via the Cloud can currently be accessed in two main different ways, either using a web-based interface to graphically create and run circuits, or via REST API. In both cases, all jobs sent to the quantum devices and simulators are executed exploiting several queue processes (e.g. fairshare). The software development for quantum algorithms is not currently integrated with traditional development on classical resources: the objective of this proposed framework is to provide a reference architecture and a set of blueprints to close the gap between the classical and the quantum computation fields. Considering the latest trend of innovation about QCs, we imagine that enterprises and researchers will soon start using such platforms almost daily, and integration with classical applications will be desirable and, in the next future, required, to support and improve computing capacity for existing and new workloads.

C.2.2 Challenges

We identified two challenges to be overcome to achieve this integration. The first takes in consideration the requested upskilling and theoretical knowledge to embrace quantum computation: currently, an integration between classical and quantum applications is possible, but requires a low level approach using the available quantum SDKs (i.e. Qiskit). In particular, some details can be highlighted: currently, most of the quantum SDKs are available for Python, and a proper decoupling logic must be available to integrate quantum workloads with non-Pyton classical workloads. Fortunately, these decoupling logics are arising, like for example the REST API interface provided by Qiskit Runtime [219], available in different programming languages. However, a developer having to integrate classical-quantum backends needs to know at least the basics of quantum computation, like for example the quantum circuit composition, or the pre-built Qiskit libraries or applications [220]. Using Qiskit basic features to integrate applications could therefore be difficult to achieve, especially within the complexity of an enterprise application stack. The second identified challenge lies on the similarity between Quantum Computing and HPC environments in terms of resource accessibility: they share some peculiarities such as the computation complexity, the long processing time, the concurrent resource access and the scalability.

C.2.3 Proposed architecture, requirements and data flow

In order to overcome these challenges, we proposed on Ref. [51] a proprietary framework based on IBM Cloud technologies; this framework has been improved over time and has been in particular refactored leveraging on open-source technologies, ready for an enterprise or production environment. Red Hat OpenShift Container Platform [221] has been chosen as the core solution to achieve the best portability and to exploit the extended number of services in terms of data storage, hosting, middleware and queuing services.

We decided exploit RedHat OpenShift, one of the leader platforms to manage and orchestrate containers, that provides a significant number of functionalities to design and monitor almost any workload; to make the development straightforward, we decided to adopt a managed database solution (DBaaS) to store the configurations. We also focused on major improvements in terms of workload management: in the previous version of the framework (Ref. [51]) we exploited HTTP invocations to trigger the Functions components, introducing the risk of failure and the need to set up a retry mechanism to properly handle those failures. Now the Functions trigger is delegated to Kafka [222], the most adopted platform for event streaming that ensures the delivery of properly configured messages. The serverless component is demanded to Knative [223], the native technology when OpenShift Container Platform is adopted.

Lastly, we introduced an automation script that allows to install all the framework components needed with a one-click, taking an elapsed time of a couple of minutes, giving yet another boost in terms of ease of usability and automation. In terms of data flow, the mechanism to trigger a function after an end user interaction with the UI has been improved, as the very same payload sent over HTTP is now sent on a Kafka topic.

This triggers the Knative Eventing subcomponents, that delivers the message from the Kafka Topic to the Knative Service component.

C.2.4 Integrating Quantum with existing Enterprise workloads

The proposed framework aims to standardize the interaction of an existing infrastructure with Quantum Computing platforms, in our case IBM Quantum, leveraging the most used open-source technologies. The general idea implemented is to decouple all the components of the framework and isolate, using containers, the components which interact with IBM Quantum. In addition to this, as introduced above, we automated the provisioning process accordingly to the latest *Infrastructure-as-Code* (IaC) trends. Fig. C.2 reports the proposed integration flow.

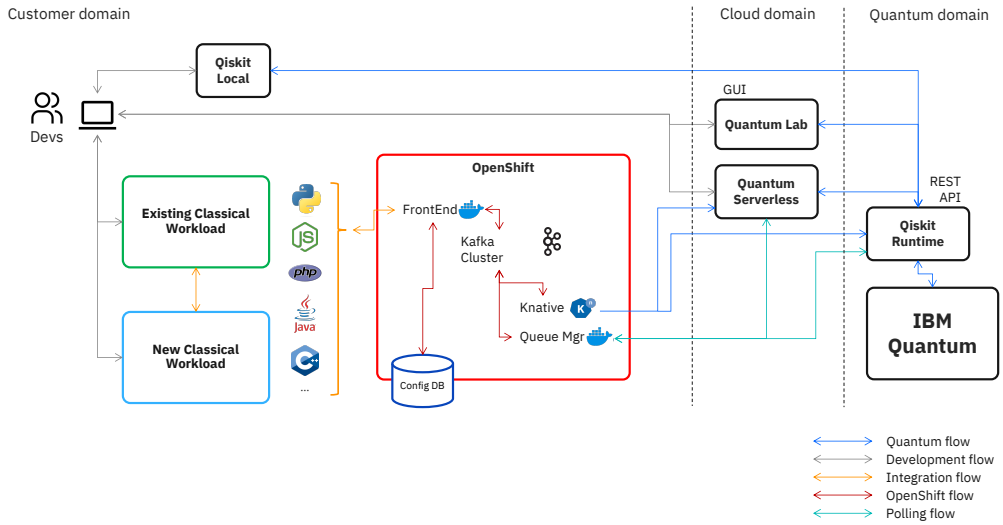

Figure C.2: Positioning of the proposed integration framework in the Qiskit technological environment. *Customer domain* refers to all private environments, that can be positioned on a Customer premises, a Public Cloud or a Hybrid/Multi Cloud environment. The *Cloud domain* refers to the Qiskit environment located on IBM Cloud. As *Quantum domain* we refer to the Quantum Datacenter inside IBM facilities. Our framework (in red) can help integrating classical applications or workloads with a quantum backend, to expand the computational possibilities.

C.2.5 Framework components

We developed a quantum application framework that aims to standardize the interaction of pre-existing software infrastructure with IBM Quantum resources, using common open-source technologies like RedHat OpenShift Container Platform and Apache Kafka. The framework consists of five main components, outlined below:

- **Frontend**: this is the primary entry point for this framework, where the user inputs the request to run a certain quantum algorithm, specifies whether the circuit will

run on a simulator or real quantum device, and receives a client ID and job ID for tracking. The main role of this component is to gather these inputs and transform them into a standard file format that will interact with the rest of the framework components. In the demo deployed on IBM Cloud, the frontend is just a simple Java [1] application with some static HTML [2] and JS resources that provide a web interface for users. Once the user input has been processed by the quantum system, the result of the computation is sent back to the frontend for the user to see.

- **Kafka Cluster**: built by Apache Kafka [222], a distributed open-source system for creating real-time streaming data pipelines and streaming applications, the Kafka Cluster is the heart of the communication that occurs between each of the framework components. Whenever we need to move information from one component to another, we write it onto a Kafka Topic categories that allow us to organize the messages to be send across the framework. For example, we use a Kafka Topic to send the user's request for a quantum circuit off for processing, and we use a different Kafka Topic to send the result of a quantum computation back to the frontend for the user to see.

- **Knative Functions**: Knative Functions [223] are a useful tool for building and deploying event-driven *functions*, self-contained modules of code dedicated to a specific task, with minimal overhead. In this framework, the Knative Functions component is responsible for building the quantum algorithm, and sending the corresponding quantum circuit to the IBM Quantum provider choosing either the appropriate simulator or the least busy quantum device available. Once the simulator or device has been chosen, the Knative Functions components defines a Qiskit job and sends it off for execution.

- **Queue Manager**: it is responsible for polling the computational results from the IBM Quantum device or simulator, and then writing those results onto a Kafka Topic [222] that goes back to the frontend component for the user to see.

- **Cloudant DB**: a database solution that can store the configuration of the framework for future use. We chose to use Cloudant DB [224], a managed solution for data storage. The data model consists of one collection, named *Config*, that contains the parameters that allow the frontend to call the backend. This approach makes possible to add other quantum applications by simply adding multiple *Config* files to the database.

C.2.6 Conclusions

The proposed quantum application framework addresses many of the challenges that developer organizations may face when attempting to integrate quantum computation

[1] Programming language released in 1996, designed to be used within the Java Platform, suite of programs facilitating the development and the deployment of softwares.

[2] The *HyperText Markup Language* is the standard markup language to develop browser-based user interfaces. It can be integrated by other formatting languages like Cascading Style Sheets (CSS) and scripting languages such as JavaScript (JS).

into classical software architectures. The general idea behind our strategy was to decouple all the framework's components, and then use containers to isolate the components that interact with quantum resources. This separation allows us to easily get around the limitations of various quantum providers.

The use of Knative Functions also helps us mitigate some of the challenges of working with quantum systems, such as their large processing times. This makes it easier to process multiple user inputs in quick succession. Our flexible architecture allows developers to focus exclusively on the logic of their application without worrying about preparing runtimes, managing deployment, or directly facing underlying infrastructure. An approach like this could be vital in order to allowing quantum adoption in the next years.

This framework is the successor to a similar project first proposed by our team (Ref. [225]), which was published as disclosure in 2019 (Ref. [226]).

Part of the content of this work has also been published in arXiv:2107.02007 (Ref. [51]).

Bibliography

[1] *Meet two of the most powerful supercomputers on the planet*, Tech. Rep. (IBM, 2018).

[2] *IBM Quantum Computing*, IBM Quantum (2023).

[3] *IBM Quantum Computing Platform*, IBM Quantum (2023).

[4] A. W. Cross, L. S. Bishop, S. Sheldon, P. D. Nation, and J. M. Gambetta, "Validating quantum computers using randomized model circuits," Phys. Rev. A **100**, 032328 (2019).

[5] R. P. Feynman, "Simulating physics with computers," International Journal of Theoretical Physics **21** (1982).

[6] G. E. Moore, "Cramming more components onto integrated circuits, reprinted from electronics," IEEE Solid-State Circuits Society Newsletter **11**, 33 (2006).

[7] S. Kumar, "Fundamental limits to moore's law," (2015).

[8] J. P. Dowling and G. J. Milburn, "Quantum technology: The second quantum revolution," (2002).

[9] D. P. DiVincenzo, "The physical implementation of quantum computation," (2000).

[10] J. Bird, *Engineering mathematics* (Newnes, 2007) p. 532.

[11] M. A. Nielsen and I. L. Chuang, *Quantum Computation and Quantum Information: 10th Anniversary Edition* (Cambridge University Press, 2010).

[12] *Qiskit: Open-Source Quantum Development*, Qiskit (2023).

[13] A. J., A. Adedoyin, J. Ambrosiano, P. Anisimov, W. Casper, G. Chennupati, C. Coffrin, H. Djidjev, D. Gunter, S. Karra, N. Lemons, S. Lin, A. Malyzhenkov, D. Mascarenas, S. Mniszewski, B. Nadiga, D. O'malley, D. Oyen, S. Pakin, L. Prasad, R. Roberts, P. Romero, N. Santhi, N. Sinitsyn, P. J. Swart, J. G. Wendelberger, B. Yoon, R. Zamora, W. Zhu, S. Eidenbenz, A. Bärtschi, P. J. Coles, M. Vuffray, and A. Y. Lokhov, "Quantum algorithm implementations for beginners," ACM Transactions on Quantum Computing **3**, 1 (2022).

[14] F. Tacchino, A. Chiesa, S. Carretta, and D. Gerace, "Quantum computers as universal quantum simulators: State-of-the-art and perspectives," Advanced Quantum Technologies **3**, 1900052 (2019).

[15] P. Santini, S. Carretta, F. Troiani, and G. Amoretti, "Molecular nanomagnets as quantum simulators," Phys. Rev. Lett. **107**, 230502 (2011).

[16] I. M. Georgescu, S. Ashhab, and F. Nori, "Quantum simulation," Rev. Mod. Phys. **86**, 153 (2014).

[17] S. Lloyd, "Universal quantum simulators," Science **273**, 1073 (1996).

[18] N. Hatano and M. Suzuki, "Finding exponential product formulas of higher orders," in *Quantum Annealing and Other Optimization Methods* (Springer Berlin Heidelberg, 2005) pp. 37–68.

[19] J. Preskill, *Quantum*, Vol. 2 (2018) p. 79.

[20] H.-P. Breuer and F. Petruccione, "Concepts and methods in the theory of open quantum systems," (2003).

[21] Y. C. Cheng and R. J. Silbey, "Markovian approximation in the relaxation of open quantum systems," The Journal of Physical Chemistry B **109**, 21399 (2005).

[22] A. Kossakowski, "On quantum statistical mechanics of non-hamiltonian systems," Reports on Mathematical Physics **3**, 247 (1972).

[23] *Qiskit Transpiler: qiskit.transpiler*, Qiskit (2023).

[24] L. F. Richardson, "The approximate arithmetical solution by finite differences of physical problems involving differential equations, with an application to the stresses in a masonry dam," Philosophical Transactions of the Royal Society A **210** (1911).

[25] E. Knill, R. Laflamme, and L. Viola, "Theory of quantum error correction for general noise," Physical Review Letters **84**, 2525 (2000).

[26] S. J. Devitt, K. Nemoto, and W. J. Munro, "Quantum error correction for beginners," (2009).

[27] M. D. Reed, L. DiCarlo, S. E. Nigg, L. Sun, L. Frunzio, S. M. Girvin, and R. J. Schoelkopf, "Realization of three-qubit quantum error correction with superconducting circuits," Nature **482**, 382 (2012).

[28] P. W. Shor, "Scheme for reducing decoherence in quantum computer memory," Phys. Rev. A **52**, R2493 (1995).

[29] P. Aliferis, "Level reduction and the quantum threshold theorem," (2007).

[30] D. Gottesman, "Stabilizer codes and quantum error correction," (1997).

[31] B. Jacob, W. Peter, P. Nicola, R. Patrick, W. Nathan, and L. Seth, "Quantum machine learning," Nature **549**, 195–202 (2017).

[32] Y. Zhang and Q. Ni, "Recent advances in quantum machine learning," Quantum Engineering **2**, e34.

[33] L. K. Grover, "A fast quantum mechanical algorithm for database search," (1996).

[34] P. W. Shor, "Polynomial-time algorithms for prime factorization and discrete logarithms on a quantum computer," SIAM Journal on Computing **26**, 1484 (1997).

[35] V. Mavroeidis, K. Vishi, M. D., and A. Jøsang, "The impact of quantum computing on present cryptography," International Journal of Advanced Computer Science and Applications **9** (2018).

[36] *Announcing IBM z16: Real-time AI for Transaction Processing at Scale and Industry's*

First Quantum-Safe System, Tech. Rep. (IBM Newsroom, 2022).

[37] *IBM Reveals Next-Generation IBM POWER10 Processor*, Tech. Rep. (IBM Newsroom, 2020).

[38] *IBM Unveils Breakthrough 127-Qubit Quantum Processor*, Tech. Rep. (IBM Newsroom, 2021).

[39] A. Steane, "The ion trap quantum information processor," Applied Physics B: Lasers and Optics **64**, 623 (1997).

[40] D. Loss and D. P. DiVincenzo, "Quantum computation with quantum dots," Physical Review A **57**, 120 (1998).

[41] J. Koch, T. M. Yu, J. Gambetta, A. A. Houck, D. I. Schuster, J. Majer, A. Blais, M. H. Devoret, S. M. Girvin, and R. J. Schoelkopf, "Charge-insensitive qubit design derived from the cooper pair box," Phys. Rev. A **76**, 042319 (2007).

[42] U. L. Andersen, "Photonic chip brings optical quantum computers a step closer," Nature **591** (2021).

[43] C. Wang, L. Li, J. Gong, and Y. Liu, "Arbitrary entangled state transfer via a topological qubit chain," (2021).

[44] H. Loïc, B. Lucas, S. Adrien, L. Thierry, B. Antoine, R. Georges-Olivier, and J. Christophe, "Quantum computing with neutral atoms," Quantum **4**, 327 (2020).

[45] R. Hussain, G. Allodi, A. Chiesa, E. Garlatti, D. Mitcov, A. Konstantatos, K. S. Pedersen, R. De Renzi, S. Piligkos, and S. Carretta, "Coherent manipulation of a molecular ln-based nuclear qudit coupled to an electron qubit," Journal of the American Chemical Society **140**, 9814 (2018).

[46] M. Chizzini, L. Crippa, A. Chiesa, F. Tacchino, F. Petiziol, I. Tavernelli, P. Santini, and S. Carretta, "Molecular nanomagnets with competing interactions as optimal units for qudit-based quantum computation," Phys. Rev. Research **4**, 043135 (2022).

[47] M. Chizzini, L. Crippa, L. Zaccardi, E. Macaluso, S. Carretta, A. Chiesa, and P. Santini, "Quantum error correction with molecular spin qudits," Phys. Chem. Chem. Phys. **24**, 20030 (2022).

[48] V. Rollano, M. C. de Ory, C. D. Buch, M. Rubín-Osanz, D. Zueco, C. Sánchez-Azqueta, A. Chiesa, D. Granados, S. Carretta, A. Gomez, S. Piligkos, and F. Luis, "High cooperativity coupling to nuclear spins on a circuit quantum electrodynamics architecture," Communications Physics **5**, 246 (2022).

[49] *Quantum Circuits: qiskit.circuits*, Qiskit (2023).

[50] A. W. Cross, L. S. Bishop, J. A. Smolin, and J. M. Gambetta, "Open quantum assembly language," (2017).

[51] M. Grossi, L. Crippa, A. Aita, G. Bartoli, V. Sammarco, E. Picca, N. Said, F. Tramonto, and F. Mattei, "A serverless cloud integration for quantum computing," (2021).

[52] J. Kahn, *IBM unveils ambitious plan for quantum computing software*, Tech. Rep. (Fortune, 2021).

[53] *Measuring Quantum Volume*, Qiskit (2023).

[54] F. Arute, K. Arya, and R. Babbush, .

[55] D. M. J. G. Edwin Pednault, John Gunnels, "On "quantum supremacy"," IBM Research Blog (2019).

[56] C. Rossetti, *Rudimenti di Meccanica Quantistica* (Levrotto & Bella, 2011).

[57] H. Devoret, "Quantum fluctuations in electrical circuits," in *Quantum Fluctuations: Les Houches Session LXIII* (North-Holland/Elsevier, 1997).

[58] M. H. Devoret, A. Wallraff, and J. M. Martinis, "Superconducting qubits: A short review," (2004).

[59] J. Bardeen, L. N. Cooper, and J. R. Schrieffer, "Theory of superconductivity," Phys. Rev. **108**, 1175 (1957).

[60] J. Clarke and F. Wilhelm, "Superconducting quantum bits," Nature **453**, 1031–1042 (2008).

[61] D. Dew-Hughes, "The critical current of superconductors: an historical review," Low Temperature Physics **27**, 713 (2001).

[62] M. Tinkham, *Introduction to Superconductivity* (Krieger, Malabar, 1985).

[63] Y. Makhlin, G. Scöhn, and A. Shnirman, "Josephson-junction qubits with controlled couplings," Nature **398**, 305 (1999).

[64] M. Göppl, A. Fragner, M. Baur, R. Bianchetti, S. Filipp, J. M. Fink, P. J. Leek, G. Puebla, L. Steffen, and A. Wallraff, "Coplanar waveguide resonators for circuit quantum electrodynamics," Journal of Applied Physics **104**, 113904 (2008).

[65] A. Blais, R.-S. Huang, A. Wallraff, S. M. Girvin, and R. J. Schoelkopf, "Cavity quantum electrodynamics for superconducting electrical circuits: An architecture for quantum computation," Phys. Rev. A **69**, 062320 (2004).

[66] M. Zemlicka, E. Redchenko, M. Peruzzo, F. Hassani, A. Trioni, S. Barzanjeh, and J. M. Fink, "Compact vacuum gap transmon qubits: Selective and sensitive probes for superconductor surface losses," (2022).

[67] A. Megrant, C. Neill, R. Barends, B. Chiaro, Y. Chen, L. Feigl, J. Kelly, E. Lucero, M. Mariantoni, P. J. J. O'Malley, D. Sank, A. Vainsencher, J. Wenner, T. C. White, Y. Yin, J. Zhao, C. J. Palmstrøm, J. M. Martinis, and A. N. Cleland, "Planar superconducting resonators with internal quality factors above one million," Applied Physics Letters **100**, 113510 (2012).

[68] *The Physics of Computation Conference*, Tech. Rep. (MIT Endicott House, 2018).

[69] C. B. Olivia Lanes, *Celebrating the 40-year anniversary of the Physics of Computation Conference*, Tech. Rep. (IBM Newsroom, 2021).

[70] "Flickr ibm research, collection: Ibm quantum," (2023).

[71] C. N. Hugh Collins, *IBM Unveils 400 Qubit-Plus Quantum Processor and Next-Generation IBM Quantum System Two*, Tech. Rep. (IBM Newsroom, 2022).

[72] A. Wack, H. Paik, A. Javadi-Abhari, P. Jurcevic, I. Faro, J. M. Gambetta, and B. R. Johnson, "Quality, speed, and scale: three key attributes to measure the performance of near-term quantum computers," (2021).

[73] J. Gambetta, "Expanding the ibm quantum roadmap to anticipate the future of quantum-centric supercomputing," IBM Research Blog (2022).

[74] S. Bravyi, O. Dial, J. M. Gambetta, D. Gil, and Z. Nazario, "The future of quantum

computing with superconducting qubits," Journal of Applied Physics **132**, 160902 (2022).

[75] A. N. Cleland, "An introduction to the surface code," SciPost Phys. Lect. Notes , 49 (2022).

[76] A. G. Fowler, M. Mariantoni, J. M. Martinis, and A. N. Cleland, "Surface codes: Towards practical large-scale quantum computation," Phys. Rev. A **86**, 032324 (2012).

[77] M. Atzori, L. Tesi, E. Morra, M. Chiesa, L. Sorace, and R. Sessoli, "Room-temperature quantum coherence and rabi oscillations in vanadyl phthalocyanine: Toward multifunctional molecular spin qubits," Journal of the American Chemical Society **138**, 2154 (2016).

[78] M. Atzori, E. Morra, L. Tesi, A. Albino, M. Chiesa, L. Sorace, and R. Sessoli, "Quantum coherence times enhancement in vanadium(iv)-based potential molecular qubits: the key role of the vanadyl moiety," Journal of the American Chemical Society **138**, 11234 (2016).

[79] G. F. S. Whitehead, J. Ferrando-Soria, L. Carthy, R. G. Pritchard, S. J. Teat, G. A. Timco, and R. E. P. Winpenny, "Synthesis and reactions of n-heterocycle functionalised variants of heterometallic Cr7Ni rings," Dalton Trans. **45**, 1638 (2016).

[80] D. Gatteschi, R. Sessoli, and J. Villain, *Molecular Nanomagnets* (Oxford Scholarship Online, 2006).

[81] F. Troiani, A. Ghirri, M. Affronte, S. Carretta, P. Santini, G. Amoretti, S. Piligkos, G. Timco, and R. E. P. Winpenny, "Molecular engineering of antiferromagnetic rings for quantum computation," Phys. Rev. Lett. **94**, 207208 (2005).

[82] K. Bader, D. Dengler, S. Lenz, B. Endeward, S. Jiang, P. Neugebauer, and J. van Slageren, "Room temperature quantum coherence in a potential molecular qubit," Nature Communications **5** (2014).

[83] M. Fujii, F. Wakai, H. Abe, and A. Hirai, "63cu and 65cu nmr in a single crystal of k2cuf4," Journal of the Physical Society of Japan **50**, 1109 (1981).

[84] C.-J. Yu, M. J. Graham, J. M. Zadrozny, J. Niklas, M. D. Krzyaniak, M. R. Wasielewski, O. G. Poluektov, and D. E. Freedman, "Long coherence times in nuclear spin-free vanadyl qubits," Journal of the American Chemical Society **138**, 14678 (2016).

[85] C. J. Wedge, G. A. Timco, E. T. Spielberg, R. E. George, F. Tuna, S. Rigby, E. J. L. McInnes, R. E. P. Winpenny, S. J. Blundell, and A. Ardavan, "Chemical engineering of molecular qubits," Phys. Rev. Lett. **108**, 107204 (2012).

[86] M. Atzori, A. Chiesa, E. Morra, M. Chiesa, L. Sorace, S. Carretta, and R. Sessoli, "A two-qubit molecular architecture for electron-mediated nuclear quantum simulation," Chem. Sci. **9**, 6183 (2018).

[87] S. J. Lockyer, A. Chiesa, G. A. Timco, E. J. L. McInnes, T. S. Bennett, I. J. Vitorica-Yrezebal, S. Carretta, and R. E. P. Winpenny, "Targeting molecular quantum memory with embedded error correction," Chem. Sci. **12**, 9104 (2021).

[88] F. Troiani, M. Affronte, S. Carretta, P. Santini, and G. Amoretti, "Proposal for quantum gates in permanently coupled antiferromagnetic spin rings without need of local fields," Phys. Rev. Lett. **94**, 190501 (2005).

[89] S. Carretta, P. Santini, G. Amoretti, F. Troiani, and M. Affronte, "Spin triangles as optimal units for molecule-based quantum gates," Phys. Rev. B **76**, 024408 (2007).

[90] A. Chiesa, G. Whitehead, S. Carretta, L. Carthy, T. Grigore, S. Teat, G. Amoretti, E. Pavarini, R. Winpenny, and P. Santini, "Molecular nanomagnets with switchable coupling for quantum simulation," Nature **4** (2014), doi.org/10.1038/srep07423.

[91] J. Ferrando-Soria, E. Moreno Pineda, A. Chiesa, A. Fernanzez, S. Magee, S. Carretta, P. Santini, I. Vitorica-Yrezabal, F. Tuna, G. Timco, E. McInnes, and R. Winpenny, "A modular design of molecular qubits to implement universal quantum gates," Nature Communications **7**, 11377 (2016).

[92] S. Paolo, C. Stefano, and A. Giuseppe, *Molecular Magnetic Materials: Concepts and Applications*, Vol. 5 (Wiley Online Library, 2016).

[93] S. Takahashi, I. Tupitsyn, J. van Tol, C. Beedle, D. Hendrickson, and P. Stamp, "Decoherence in crystals of quantum molecular magnets," Nature **476** (2011).

[94] F. Troiani, V. Bellini, and M. Affronte, "Decoherence induced by hyperfine interactions with nuclear spins in antiferromagnetic molecular rings," Phys. Rev. B **77** (2008).

[95] A. Chiesa, E. Macaluso, F. Petiziol, S. Wimberger, P. Santini, and S. Carretta, "Molecular nanomagnets as qubits with embedded quantum-error correction," The Journal of Physical Chemistry Letters **11**, 8610 (2020).

[96] F. Petiziol, A. Chiesa, S. Wimberger, P. Santini, and S. Carretta, "Counteracting dephasing in molecular nanomagnets by optimized qudit encodings," npj Quantum Information **7**, 133 (2021).

[97] A. M. Childs, D. Maslov, Y. Nam, N. J. Ross, and Y. Su, "Toward the first quantum simulation with quantum speedup," Proceedings of the National Academy of Sciences **115**, 9456 (2018).

[98] P. Krantz, M. Kjaergaard, F. Yan, T. P. Orlando, S. Gustavsson, and W. D. Oliver, "A quantum engineer's guide to superconducting qubits," Applied Physics Reviews **6**, 021318 (2019).

[99] A. D. Córcoles, A. Kandala, A. Javadi-Abhari, D. T. McClure, A. W. Cross, K. Temme, P. D. Nation, M. Steffen, and J. M. Gambetta, "Challenges and opportunities of near-term quantum computing systems," Proceedings of the IEEE **108**, 1338 (2020).

[100] C. D. Bruzewicz, J. Chiaverini, R. McConnell, and J. M. Sage, "Trapped-ion quantum computing: Progress and challenges," Applied Physics Reviews **6**, 021314 (2019).

[101] Y. Li and S. C. Benjamin, "Efficient variational quantum simulator incorporating active error minimization," Phys. Rev. X **7**, 021050 (2017).

[102] T. Guidi, B. Gillon, and S. Mason, "Direct observation of finite size effects in chains of antiferromagnetically coupled spins," Nature Communications **6** (2015).

[103] R. Schmidt, J. Richter, and J. Schnack, "Frustration effects in magnetic molecules," Journal of Magnetism and Magnetic Materials **295**, 164 (2005).

[104] O. Waldmann, "Spin dynamics of finite antiferromagnetic heisenberg spin rings,"

Phys. Rev. B **65**, 024424 (2001).

[105] A. Peruzzo, J. McClean, and P. Shadbolt, "A variational eigenvalue solver on a photonic quantum processor," Nature Communications **5** (2014).

[106] A. Kandala, A. Mezzacapo, K. Temme, M. Takita, M. Brink, J. M. Chow, and J. M. Gambetta, "Charge-insensitive qubit design derived from the cooper pair box," Nature **549** (2017).

[107] N. Moll, P. Barkoutsos, L. S. Bishop, J. M. Chow, A. Cross, D. J. Egger, S. Filipp, A. Fuhrer, J. M. Gambetta, M. Ganzhorn, A. Kandala, A. Mezzacapo, P. Müller, W. Riess, G. Salis, J. Smolin, I. Tavernelli, and K. Temme, "Quantum optimization using variational algorithms on near-term quantum devices," Quantum Science and Technology **3**, 030503 (2018).

[108] K. Bharti, A. Cervera-Lierta, T. H. Kyaw, T. Haug, S. Alperin-Lea, A. Anand, M. Degroote, H. Heimonen, J. S. Kottmann, T. Menke, W.-K. Mok, S. Sim, L.-C. Kwek, and A. Aspuru-Guzik, "Noisy intermediate-scale quantum algorithms," Reviews of Modern Physics **94** (2022).

[109] A. Chiesa, F. Tacchino, M. Grossi, P. Santini, I. Tavernelli, D. Gerace, and S. Carretta, "Quantum hardware simulating four-dimensional inelastic neutron scattering," Nat. Phys. , 455–459 (2019).

[110] P. K. Barkoutsos, G. Nannicini, A. Robert, I. Tavernelli, and S. Woerner, "Improving variational quantum optimization using CVaR," Quantum **4**, 256 (2020).

[111] S. Mangini, F. Tacchino, D. Gerace, D. Bajoni, and C. Macchiavello, "Quantum computing models for artificial neural networks," Europhysics Letters **134**, 10002 (2021).

[112] J. J. Sakurai, *Modern quantum mechanics; rev. ed.* (Addison-Wesley, Reading, MA, 1994).

[113] Y. Cao, J. Romero, J. P. Olson, M. Degroote, P. D. Johnson, M. Kieferová, I. D. Kivlichan, T. Menke, B. Peropadre, N. P. D. Sawaya, S. Sim, L. Veis, and A. Aspuru-Guzik, "Quantum chemistry in the age of quantum computing," Chemical Reviews **119**, 10856 (2019).

[114] *Qiskit Optimizers: cobyla*, Qiskit (2023).

[115] *Qiskit Optimizers: spsa*, Qiskit (2023).

[116] M. Cerezo, A. Sone, and T. Volkoff, "Cost function dependent barren plateaus in shallow parametrized quantum circuits," Nature Communications **12** (2021).

[117] J. Mcclean, J. Romero, R. Babbush, and A. Aspuru-Guzik, "The theory of variational hybrid quantum-classical algorithms," New Journal of Physics **18** (2016).

[118] *Qiskit Operators: opflow*, Qiskit (2023).

[119] G. Aleksandrowicz, T. Alexander, P. Barkoutsos, L. Bello, Y. Ben-Haim, D. Bucher, F. J. Cabrera-Hernández, J. Carballo-Franquis, A. Chen, C.-F. Chen, J. M. Chow, A. D. Córcoles-Gonzales, A. J. Cross, A. Cross, J. Cruz-Benito, C. Culver, S. D. L. P. González, E. D. L. Torre, D. Ding, E. Dumitrescu, I. Duran, P. Eendebak, M. Everitt, I. F. Sertage, A. Frisch, A. Fuhrer, J. Gambetta, B. G. Gago, J. Gomez-Mosquera, D. Greenberg, I. Hamamura, V. Havlicek, J. Hellmers, Łukasz Herok, H. Horii, S. Hu, T. Imamichi, T. Itoko, A. Javadi-Abhari, N. Kanazawa, A. Karazeev, K. Kr-

sulich, P. Liu, Y. Luh, Y. Maeng, M. Marques, F. J. Martín-Fernández, D. T. McClure, D. McKay, S. Meesala, A. Mezzacapo, N. Moll, D. M. Rodríguez, G. Nannicini, P. Nation, P. Ollitrault, L. J. O'Riordan, H. Paik, J. Pérez, A. Phan, M. Pistoia, V. Prutyanov, M. Reuter, J. Rice, A. R. Davila, R. H. P. Rudy, M. Ryu, N. Sathaye, C. Schnabel, E. Schoute, K. Setia, Y. Shi, A. Silva, Y. Siraichi, S. Sivarajah, J. A. Smolin, M. Soeken, H. Takahashi, I. Tavernelli, C. Taylor, P. Taylour, K. Trabing, M. Treinish, W. Turner, D. Vogt-Lee, C. Vuillot, J. A. Wildstrom, J. Wilson, E. Winston, C. Wood, S. Wood, S. Wörner, I. Y. Akhalwaya, and C. Zoufal, *Qiskit: An Open-source Framework for Quantum Computing*, Zenodo (2019).

[120] A. Kandala, K. Temme, and A. Córcoles, "Error mitigation extends the computational reach of a noisy quantum processor," Nature **567** (2019).

[121] *Qiskit Simulators: Building Noise Models*, Qiskit (2023).

[122] B. Gard, L. Zhu, and G. Barron, "Efficient symmetry-preserving state preparation circuits for the variational quantum eigensolver algorithm," npj Quantum Inf **6** (2020).

[123] K. Seki, T. Shirakawa, and S. Yunoki, "Symmetry-adapted variational quantum eigensolver," Phys. Rev. A **101**, 052340 (2020).

[124] L. Pauling, "The calculation of matrix elements for lewis electronic structures of molecules," The Journal of Chemical Physics **1**, 280 (1933).

[125] P. Fazekas and P. W. Anderson, "On the ground state properties of the anisotropic triangular antiferromagnet," The Philosophical Magazine: A Journal of Theoretical Experimental and Applied Physics **30**, 423 (1974).

[126] *Qiskit Simulators: statevector*, Qiskit (2023).

[127] L. Crippa, F. Tacchino, M. Chizzini, A. Aita, M. Grossi, A. Chiesa, P. Santini, I. Tavernelli, and S. Carretta, "Simulating static and dynamic properties of magnetic molecules with prototype quantum computers," Magnetochemistry **7** (2021).

[128] S. Wang, E. Fontana, and M. Cerezo, "Noise-induced barren plateaus in variational quantum algorithms," Nature Communications **12** (2021).

[129] J. C. Spall, "An overview of the simultaneous perturbation method for efficient optimization," Johns Hopkins Apl Technical Digest **19**, 482 (1998).

[130] S. Bravyi, S. Sheldon, A. Kandala, D. C. Mckay, and J. M. Gambetta, "Mitigating measurement errors in multiqubit experiments," Phys. Rev. A **103**, 042605 (2021).

[131] X. Bonet-Monroig, R. Sagastizabal, M. Singh, and T. E. O'Brien, "Low-cost error mitigation by symmetry verification," Phys. Rev. A **98**, 062339 (2018).

[132] S. McArdle, X. Yuan, and S. Benjamin, "Error-mitigated digital quantum simulation," Phys. Rev. Lett. **122**, 180501 (2019).

[133] W. Huggins, J. McClean, and N. Rubin, "Efficient and noise resilient measurements for quantum chemistry on near-term quantum computers," npj Quantum Inf **7** (2021).

[134] P. Jurcevic, D. Zajac, J. Stehlik, I. Lauer, and R. Mandelbaum, *Pushing quantum performance forward with our highest Quantum Volume yet*, Tech. Rep. (IBM Research Blog, 2022).

[135] V. Shende, S. Bullock, and I. Markov, "Synthesis of quantum-logic circuits," IEEE

Transactions on Computer-Aided Design of Integrated Circuits and Systems **25**, 1000 (2006).

[136] *Qiskit Initialize*, Qiskit (2023).

[137] J. S. Pedernales, R. Di Candia, I. L. Egusquiza, J. Casanova, and E. Solano, "Efficient quantum algorithm for computing n-time correlation functions," Phys. Rev. Lett. **113**, 020505 (2014).

[138] R. Kubo, "Statistical-mechanical theory of irreversible processes. i. general theory and simple applications to magnetic and conduction problems," Journal of the Physical Society of Japan **12**, 570 (1957).

[139] D. Wecker, M. B. Hastings, N. Wiebe, B. K. Clark, C. Nayak, and M. Troyer, "Solving strongly correlated electron models on a quantum computer," Phys. Rev. A **92**, 062318 (2015).

[140] C. Cade, L. Mineh, A. Montanaro, and S. Stanisic, "Strategies for solving the fermi-hubbard model on near-term quantum computers," Phys. Rev. B **102**, 235122 (2020).

[141] F. Arute, K. Arya, R. Babbush, D. Bacon, J. C. Bardin, R. Barends, A. Bengtsson, S. Boixo, M. Broughton, B. B. Buckley, D. A. Buell, B. Burkett, N. Bushnell, Y. Chen, Z. Chen, Y.-A. Chen, B. Chiaro, R. Collins, S. J. Cotton, W. Courtney, S. Demura, A. Derk, A. Dunsworth, D. Eppens, T. Eckl, C. Erickson, E. Farhi, A. Fowler, B. Foxen, C. Gidney, M. Giustina, R. Graff, J. A. Gross, S. Habegger, M. P. Harrigan, A. Ho, S. Hong, T. Huang, W. Huggins, L. B. Ioffe, S. V. Isakov, E. Jeffrey, Z. Jiang, C. Jones, D. Kafri, K. Kechedzhi, J. Kelly, S. Kim, P. V. Klimov, A. N. Korotkov, F. Kostritsa, D. Landhuis, P. Laptev, M. Lindmark, E. Lucero, M. Marthaler, O. Martin, J. M. Martinis, A. Marusczyk, S. McArdle, J. R. McClean, T. McCourt, M. McEwen, A. Megrant, C. Mejuto-Zaera, X. Mi, M. Mohseni, W. Mruczkiewicz, J. Mutus, O. Naaman, M. Neeley, C. Neill, H. Neven, M. Newman, M. Y. Niu, T. E. O'Brien, E. Ostby, B. Pató, A. Petukhov, H. Putterman, C. Quintana, J.-M. Reiner, P. Roushan, N. C. Rubin, D. Sank, K. J. Satzinger, V. Smelyanskiy, D. Strain, K. J. Sung, P. Schmitteckert, M. Szalay, N. M. Tubman, A. Vainsencher, T. White, N. Vogt, Z. J. Yao, P. Yeh, A. Zalcman, and S. Zanker, "Observation of separated dynamics of charge and spin in the fermi-hubbard model," (2020).

[142] *Qiskit Measurement Error Mitigation: Textbook*, Qiskit (2023).

[143] E. Fradkin, "Jordan-wigner transformation for quantum-spin systems in two dimensions and fractional statistics," Phys. Rev. Lett. **63**, 322 (1989).

[144] G. Ortiz, J. E. Gubernatis, E. Knill, and R. Laflamme, "Quantum algorithms for fermionic simulations," Phys. Rev. A **64**, 022319 (2001).

[145] R. Somma, G. Ortiz, J. E. Gubernatis, E. Knill, and R. Laflamme, "Simulating physical phenomena by quantum networks," Physical Review A **65** (2002), 10.1103/physreva.65.042323.

[146] G. Brassard, P. Høyer, and A. Tapp, "Quantum counting," in *Automata, Languages and Programming* (Springer Berlin Heidelberg, 1998) pp. 820–831.

[147] J.-M. Reiner, F. Wilhelm-Mauch, G. Schön, and M. Marthaler, "Finding the ground state of the hubbard model by variational methods on a quantum computer with

gate errors," Quantum Science and Technology **4**, 035005 (2019).

[148] Z. Cai, "Resource estimation for quantum variational simulations of the hubbard model," Physical Review Applied **14** (2020).

[149] N. Vogt, S. Zanker, J.-M. Reiner, M. Marthaler, T. Eckl, and A. Marusczyk, "Preparing ground states with a broken symmetry with variational quantum algorithms," Quantum Science and Technology **6**, 035003 (2021).

[150] G. Mazzola, P. J. Ollitrault, P. K. Barkoutsos, and I. Tavernelli, "Nonunitary operations for ground-state calculations in near-term quantum computers," Physical Review Letters **123** (2019).

[151] A. J. Daley, I. Bloch, C. Kokail, S. Flannigan, N. Pearson, M. Troyer, and P. Zoller, "Practical quantum advantage in quantum simulation," Nature **607**, 667 (2022).

[152] A. Miessen, P. J. Ollitrault, F. Tacchino, and I. Tavernelli, "Quantum algorithms for quantum dynamics," Nature Computational Science (2022).

[153] S. Flannigan, N. Pearson, G. H. Low, A. Buyskikh, I. Bloch, P. Zoller, M. Troyer, and A. J. Daley, "Propagation of errors and quantitative quantum simulation with quantum advantage," (2022).

[154] A. Heinrich, W. Oliver, L. Vandersypen, A. Ardavan, R. Sessoli, D. Loss, A. Bleszynski-Jayich, J. Fernandez-Rossier, and A. Morello, "Quantum-coherent nanoscience," Nature Nanotechnology **16**, 1318–1329 (2021).

[155] D. Aguilà, L. A. Barrios, V. Velasco, O. Roubeau, A. Repollés, P. J. Alonso, J. Sesé, S. J. Teat, F. Luis, and G. Aromí, "Heterodimetallic [lnln] lanthanide complexes: Toward a chemical design of two-qubit molecular spin quantum gates," Journal of the American Chemical Society **136**, 14215 (2014).

[156] J. Liu, J. Mrozek, A. Ullah, Y. Duan, J. Baldoví, E. Coronado, G.-A. A., and A. Ardavan, "Quantum coherent spin–electric control in a molecular nanomagnet at clock transitions," Nature Physics **17**, 1205–1209 (2021).

[157] Y. Bae, K. Yang, P. Willke, T. Choi, A. J. Heinrich, and C. P. Lutz, "Enhanced quantum coherence in exchange coupled spins via singlet-triplet transitions," Science Advances **4**, eaau4159 (2018).

[158] P. Vorndamme and J. Schnack, "Decoherence of a singlet-triplet superposition state under dipolar interactions of an uncorrelated environment," Phys. Rev. B **101**, 075101 (2020).

[159] I. Gimeno, W. Kersten, M. C. Pallarés, P. Hermosilla, M. J. Martínez-Pérez, M. D. Jenkins, A. Angerer, C. Sánchez-Azqueta, D. Zueco, J. Majer, A. Lostao, and F. Luis, "Enhanced molecular spin-photon coupling at superconducting nanoconstrictions," ACS Nano **14**, 8707 (2020).

[160] S. Chicco, A. Chiesa, G. Allodi, E. Garlatti, M. Atzori, L. Sorace, R. De Renzi, R. Sessoli, and S. Carretta, "Controlled coherent dynamics of [vo(tpp)], a prototype molecular nuclear qudit with an electronic ancilla," Chem. Sci. **12**, 12046 (2021).

[161] M. L. Baker, G. A. Timco, S. Piligkos, J. S. Mathieson, H. Mutka, F. Tuna, P. Kozłowski, M. Antkowiak, T. Guidi, T. Gupta, H. Rath, R. J. Woolfson, G. Kamieniarz, R. G. Pritchard, H. Weihe, L. Cronin, G. Rajaraman, D. Collison,

E. J. L. McInnes, and R. E. P. Winpenny, "A classification of spin frustration in molecular magnets from a physical study of large odd-numbered-metal, odd electron rings," Proceedings of the National Academy of Sciences **109**, 19113 (2012).

[162] A. Chiesa, F. Petiziol, M. Chizzini, P. Santini, and S. Carretta, "Theoretical design of optimal molecular qudits for quantum error correction," The Journal of Physical Chemistry Letters **13**, 6468 (2022).

[163] K.-Y. Choi, Y. H. Matsuda, H. Nojiri, U. Kortz, F. Hussain, A. C. Stowe, C. Ramsey, and N. S. Dalal, "Observation of a half step magnetization in the Cu_3-type triangular spin ring," Phys. Rev. Lett. **96**, 107202 (2006).

[164] E. Garlatti, S. Carretta, M. Affronte, E. C. Sañudo, G. Amoretti, and P. Santini, "Magnetic properties and relaxation dynamics of a frustrated ni7 molecular nanomagnet," Journal of Physics: Condensed Matter **24**, 104006 (2012).

[165] M. M. Wilde, "Preface to the second edition," in *Quantum Information Theory* (Cambridge University Press, 2016) pp. xi–xii.

[166] B. B. A. Abragam, *Electron Paramagnetic Resonance of Transition Ions* (OUP Oxford, 1970).

[167] Y.-S. Ding, Y.-F. Deng, and Y.-Z. Zheng, "The rise of single-ion magnets as spin qubits," Magnetochemistry **2** (2016).

[168] A. Caneschi, A. Dei, D. Gatteschi, C. A. Massa, L. A. Pardi, S. Poussereau, and L. Sorace, "Evaluating the magnetic anisotropy in molecular rare earth compounds. gadolinium derivatives with semiquinone radical and diamagnetic analogues," Chemical Physics Letters **371**, 694 (2003).

[169] H. Breuer and F. Petruccione, *The theory of open quantum systems* (OUP Oxford, 2010).

[170] A. Bencini and D. Gatteschi, *Electron Paramagnetic Resonance of Exchange Coupled Systems* (Springer Verlag, 1990).

[171] Y. Wang, Z. Hu, B. C. Sanders, and S. Kais, "Qudits and high-dimensional quantum computing," Frontiers in Physics **8** (2020).

[172] S. G. Schirmer, A. D. Greentree, V. Ramakrishna, and H. Rabitz, "Constructive control of quantum systems using factorization of unitary operators," Journal of Physics A: Mathematical and General **35**, 8315 (2002).

[173] P. J. Low, B. M. White, A. A. Cox, M. L. Day, and C. Senko, "Practical trapped-ion protocols for universal qudit-based quantum computing," Phys. Rev. Research **2**, 033128 (2020).

[174] L. E. Fischer, D. Miller, F. Tacchino, P. K. Barkoutsos, D. J. Egger, and I. Tavernelli, "Ancilla-free implementation of generalized measurements for qubits embedded in a qudit space," Physical Review Research **4** (2022).

[175] D. D'Alessandro, *Introduction to Quantum Control and Dynamics* (Chapman Hall/CRC Applied Mathematics Nonlinear Science, CRC Press, 2007).

[176] F. Tacchino, A. Chiesa, R. Sessoli, I. Tavernelli, and S. Carretta, "A proposal for using molecular spin qudits as quantum simulators of light–matter interactions," J. Mater. Chem. C **9**, 10266 (2021).

[177] P. A. S. Cruickshank, D. R. Bolton, D. A. Robertson, R. I. Hunter, R. J. Wylde, and

G. M. Smith, "A kilowatt pulsed 94 ghz electron paramagnetic resonance spectrometer with high concentration sensitivity, high instantaneous bandwidth, and low dead time," Review of Scientific Instruments **80**, 103102 (2009).

[178] M. J. Graham, J. M. Zadrozny, M. Shiddiq, J. S. Anderson, M. S. Fataftah, S. Hill, and D. E. Freedman, "Influence of electronic spin and spin–orbit coupling on decoherence in mononuclear transition metal complexes," Journal of the American Chemical Society **136**, 7623 (2014).

[179] M. Atzori and R. Sessoli, "The second quantum revolution: Role and challenges of molecular chemistry," Journal of the American Chemical Society **141**, 11339 (2019).

[180] J. M. Zadrozny, J. Niklas, O. G. Poluektov, and D. E. Freedman, "Millisecond coherence time in a tunable molecular electronic spin qubit," ACS Central Science **1**, 488 (2015).

[181] J. M. Gambetta, F. Motzoi, S. T. Merkel, and F. K. Wilhelm, "Analytic control methods for high-fidelity unitary operations in a weakly nonlinear oscillator," Phys. Rev. A **83**, 012308 (2011).

[182] A. Castro, A. García Carrizo, S. Roca, D. Zueco, and F. Luis, "Optimal control of molecular spin qudits," Phys. Rev. Applied **17**, 064028 (2022).

[183] A. Chiesa, P. Santini, D. Gerace, J. Raftery, A. Houck, and S. Carretta, "Digital quantum simulators in a scalable architecture of hybrid spin-photon qubits," Scientific Reports **5** (2015).

[184] M. K. Wojnar, D. W. Laorenza, R. D. Schaller, and D. E. Freedman, "Nickel(ii) metal complexes as optically addressable qubit candidates," Journal of the American Chemical Society **142**, 14826 (2020).

[185] J. H. Yulin Chi, "A programmable qudit-based quantum processor," Nature Communications **13** (2022).

[186] M. Ringbauer, M. Meth, L. Postler, R. Stricker, R. Blatt, P. Schindler, and T. Monz, "A universal qudit quantum processor with trapped ions," Nature Physics **18**, 1053–1057 (2022).

[187] M. S. Fataftah, J. M. Zadrozny, S. C. Coste, M. J. Graham, D. M. Rogers, and D. E. Freedman, "Employing forbidden transitions as qubits in a nuclear spin-free chromium complex," Journal of the American Chemical Society **138**, 1344 (2016).

[188] I. Pogorelov, T. Feldker, C. D. Marciniak, L. Postler, G. Jacob, O. Krieglsteiner, V. Podlesnic, M. Meth, V. Negnevitsky, M. Stadler, B. Höfer, C. Wächter, K. Lakhmanskiy, R. Blatt, P. Schindler, and T. Monz, "Compact ion-trap quantum computing demonstrator," PRX Quantum **2**, 020343 (2021).

[189] A. Blais, A. L. Grimsmo, S. M. Girvin, and A. Wallraff, "Circuit quantum electrodynamics," Rev. Mod. Phys. **93**, 025005 (2021).

[190] C. Cafaro, F. Maiolini, and S. Mancini, "Quantum stabilizer codes embedding qubits into qudits," Phys. Rev. A **86**, 022308 (2012).

[191] C. Godfrin, A. Ferhat, R. Ballou, S. Klyatskaya, M. Ruben, W. Wernsdorfer, and F. Balestro, "Operating quantum states in single magnetic molecules: Implementation of grover's quantum algorithm," Phys. Rev. Lett. **119**, 187702 (2017).

[192] S. J. Devitt, W. J. Munro, and K. Nemoto, "Quantum error correction for begin-

ners," Reports on Progress in Physics **76**, 076001 (2013).

[193] B. M. Terhal, "Quantum error correction for quantum memories," Rev. Mod. Phys. **87**, 307 (2015).

[194] M. Werninghaus, D. J. Egger, F. Roy, S. Machnes, F. K. Wilhelm, and S. Filipp, "Leakage reduction in fast superconducting qubit gates via optimal control," npj Quantum Information **7**, 14 (2021).

[195] M. Shiddiq, D. Komijani, Y. Duan, A. Gaita-Ariño, E. Coronado, and S. Hill, "Enhancing coherence in molecular spin qubits via atomic clock transitions," Nature **531**, 348 (2016).

[196] S. Carretta, D. Zueco, A. Chiesa, Gómez-León, and F. Luis, "A perspective on scaling up quantum computation with molecular spins," Applied Physics Letters **118**, 240501 (2021).

[197] A. Chiesa, F. Petiziol, E. Macaluso, S. Wimberger, P. Santini, and S. Carretta, "Embedded quantum-error correction and controlled-phase gate for molecular spin qubits," AIP Advances **11**, 025134 (2021).

[198] *Strategic Research Agenda*, Tech. Rep. (European Quantum Flagship, 2020).

[199] T. Sanada, T. Suzuki, T. Yoshida, and S. Kaizaki, "Heterodinuclear complexes containing d- and f-block elements: synthesis, structural characterization, and metal-metal interactions of novel chromium(iii)lanthanide(iii) compounds bridged by oxalate," Inorganic Chemistry **37**, 4712 (1998).

[200] K. S. Pedersen, A.-M. Ariciu, S. McAdams, H. Weihe, J. Bendix, F. Tuna, and S. Piligkos, "Toward molecular 4f single-ion magnet qubits," Journal of the American Chemical Society **138**, 5801 (2016).

[201] C. Mazzoli, G. Allodi, G. Guidi, R. De Renzi, and P. Ghigna, "Nmr-nqr of orbitally ordered kcuf 3," Journal of Magnetism and Magnetic Materials - J Magn Magn Mater **272**, 106 (2004).

[202] R. Schutjens, F. A. Dagga, D. J. Egger, and F. K. Wilhelm, "Single-qubit gates in frequency-crowded transmon systems," Phys. Rev. A **88**, 052330 (2013).

[203] L. S. Theis, F. Motzoi, and F. K. Wilhelm, "Simultaneous gates in frequency-crowded multilevel systems using fast, robust, analytic control shapes," Phys. Rev. A **93**, 012324 (2016).

[204] S. P. Premaratne, J.-H. Yeh, F. C. Wellstood, and B. S. Palmer, "Implementation of a generalized controlled-not gate between fixed-frequency transmons," Phys. Rev. A **99**, 012317 (2019).

[205] S. E. Economou and E. Barnes, "Analytical approach to swift nonleaky entangling gates in superconducting qubits," Phys. Rev. B **91**, 161405 (2015).

[206] F. Motzoi, J. M. Gambetta, P. Rebentrost, and F. K. Wilhelm, "Simple pulses for elimination of leakage in weakly nonlinear qubits," Phys. Rev. Lett. **103**, 110501 (2009).

[207] A. De, "Fast two-quadrature adiabatic quantum gates for weakly nonlinear qubits: a tight-binding approach," Quantum Information Processing **18**, 165 (2019).

[208] L. S. Theis, F. Motzoi, S. Machnes, and F. K. Wilhelm, "Counteracting systems of diabaticities using DRAG controls: The status after 10 years," EPL (Europhysics

Letters) **123**, 60001 (2018).

[209] F. Motzoi and F. K. Wilhelm, "Improving frequency selection of driven pulses using derivative-based transition suppression," Phys. Rev. A **88**, 062318 (2013).

[210] K. J. Sanders, A. J. Pell, S. Wegner, C. P. Grey, and G. Pintacuda, "Broadband mas nmr spectroscopy in the low-power limit," Chemical Physics Letters **697**, 29 (2018).

[211] M. L. Baker, T. Lancaster, A. Chiesa, G. Amoretti, P. J. Baker, C. Barker, S. J. Blundell, S. Carretta, D. Collison, H. U. Güdel, T. Guidi, E. J. L. McInnes, J. S. Möller, H. Mutka, J. Ollivier, F. L. Pratt, P. Santini, F. Tuna, P. L. W. Tregenna-Piggott, I. J. Vitorica-Yrezabal, G. A. Timco, and R. E. P. Winpenny, "Studies of a large odd-numbered odd-electron metal ring: Inelastic neutron scattering and muon spin relaxation spectroscopy of cr8mn," Chemistry – A European Journal **22**, 1779 (2016).

[212] R. J. Woolfson, G. A. Timco, A. Chiesa, I. J. Vitorica-Yrezabal, F. Tuna, T. Guidi, E. Pavarini, P. Santini, S. Carretta, and R. E. P. Winpenny, "[crf(o2ctbu)2]9: Synthesis and characterization of a regular homometallic ring with an odd number of metal centers and electrons," Angewandte Chemie International Edition **55**, 8856 (2016).

[213] *IonQ: Trapped Ion Quantum Computing*, Tech. Rep. (IonQ, 2023).

[214] *Qiskit Metal: quantum device design*, Qiskit (2023).

[215] U. L. Heras, A. Mezzacapo, L. Lamata, S. Filipp, A. Wallraff, and E. Solano, "Digital quantum simulation of spin systems in superconducting circuits," Phys. Rev. Lett. **112**, 200501 (2014).

[216] F. Tacchino, A. Chiesa, M. D. LaHaye, S. Carretta, and D. Gerace, "Electromechanical quantum simulators," Phys. Rev. B **97**, 214302 (2018).

[217] D. C. McKay, S. Filipp, A. Mezzacapo, E. Magesan, J. M. Chow, and J. M. Gambetta, "Universal gate for fixed-frequency qubits via a tunable bus," Phys. Rev. Appl. **6**, 064007 (2016).

[218] A. Aita, L. Crippa, and M. Grossi, *Automatic Computation Framework*, Read The Docs (2021).

[219] *Qiskit Runtime overview*, IBM Quantum (2023).

[220] *Qiskit Algorithms for Applications*, Qiskit (2023).

[221] *Red Hat OpenShift*, Tech. Rep. (Red Hat, 2023).

[222] *Apache Kafka*, Apache Software Foundation (2023).

[223] *Knative is an Open-Source Enterprise-level solution to build Serverless and Event Driven Applications*, Knative (2023).

[224] *IBM Cloudant*, IBM Cloud (2023).

[225] M. Grossi, A. Aita, and L. Crippa, *Build and deploy Quantum-based web Applications using Qiskit & Python Flask on IBM Cloud*, Medium (2019).

[226] M. Grossi, A. Aita, L. Crippa, F. Mattei, and F. Accetta, *Method and system to create and deploy Cloud containerized quantum-based web applications using API-exposed quantum computers as back-end*, Prior Art Database (2019).

Publications and Communications

As of January 2023

List of publications

Referred publications

- M. Chizzini (*), L. Crippa (*), A. Chiesa, F. Tacchino, F. Petiziol, I. Tavernelli, P. Santini and S. Carretta, *Molecular nanomagnets with competing interactions as optimal units for qudit-based quantum computation*, Phys. Rev. Research 4, 043135 , Ref. [46]
(*) Equally contributed

- M. Chizzini, L. Crippa, L. Zaccardi, E. Macaluso, S. Carretta, A. Chiesa and P. Santini, *Quantum error correction with molecular spin qudits*, Phys. Chem. Chem. Phys., 2022,24, 20030-20039, Ref. [47]

- L. Crippa, F. Tacchino, M. Chizzini, A. Aita, M. Grossi, A. Chiesa, P. Santini, I. Tavernelli and S. Carretta, *Simulating Static and Dynamic Properties of Magnetic Molecules with Prototype Quantum Computers*, Magnetochemistry 2021, 7(8), 117, Ref. [127]

- M. Grossi (*), L. Crippa (*), A. Aita (*), G. Bartoli, V. Sammarco, E. Picca, N. Said, F. Tramonto and F. Mattei, *A Serverless Cloud Integration For Quantum Computing* arXiv:2107.02007, 2021, Ref. [51]
(*) Equally contributed

Publications in preparation

- M. Chizzini, A. Chiesa, L. Crippa, F. Tacchino, I. Tavernelli, P. Santini and S. Carretta, *Simulation of fermionic systems with molecular spin qudits*

Communications

Conferences

- L. Crippa, F. Accetta, A. Aita, G. Bartoli, M. Grossi, F. Mattei and V. Sammarco, *A Containerized Quantum Application Software Architecture Framework*, Talk - Quantum Computing @ INFN, Bologna (It), 15/11/2022
- L. Crippa, M. Chizzini, A. Chiesa, F. Tacchino, F. Petiziol, I. Tavernelli, P. Santini and S. Carretta, *Molecular Nanomagnets with Competing Interactions as Optimal Units for Qudit-Based Quantum Computation*, Poster - European Conference of Molecular Magnetism (ECMM) 2022, Rennes (Fr), 4-7/7/2022
- L. Crippa, A. Aita, G. Bartoli, M. Grossi, E. Picca, V. Sammarco and F. Mattei, *Integrating applications with Qiskit Runtime*, Talk - CASCON x EVOKE 2021, Toronto (Ca), remote, 23/11/2021

Courses and events

- *Molecular nanomagnets with competing interactions as optimal units for qudit-based quantum computation*, Talk - Quantum Technology Initiative Journal Club, CERN openlab, remote, 26/1/2023
- *Introduction to Quantum Computing using Qiskit*, Lecture - National University of Singapore, remote, 19/5/2020
- *Digital quantum simulation and time evolution*, Talk – University of Heidelberg, remote, 6/5/2020
- *Quantum computing in depth*, Quantum Practitioner Course, Lecture - IBM T. J. Watson Research Center, Yorktown (NY, USA), 18/12/2019

Copyright Permissions

- Figure 3.7, 3.8(a) and 3.9 are reproduced with permission from IBM Flickr, IBM Research, Collection: IBM Quantum (Ref. [70]), open access photo collection distributed under the terms and conditions of the Creative Commons Attribution 2.0 International (CC BY-ND 2.0).

- Figure 4.2 is reproduced with permission from Royal Society of Chemistry, Dalton Trans., 2016, 45, 1638 (Ref. [79]), licensed under the terms and conditions of the Creative Commons Attribution 3.0 Unported Licence (CC BY 3.0).

- Figure 5.7, 5.8, 5.10, 5.11, 5.14 and 5.23 are reproduced with permission from MDPI, Magnetochemistry 2021, 7(8), 117 (Ref. [127]), open access article distributed under the terms and conditions of the Creative Commons Attribution 4.0 International (CC BY 4.0).

- Figure 7.2, 7.3, 7.4, 7.5, 7.6, 7.9, 7.10, 7.11 and 7.12 are reproduced with permission from Phys. Rev. Research, Phys. Rev. Research 4, 043135 (Ref. [46]), available under the terms and conditions of the Creative Commons Attribution 4.0 International (CC BY 4.0).

- Figure 4.4, 8.1, 8.2, 8.3 and 8.5 are reproduced with permission from Royal Society of Chemistry, Phys. Chem. Chem. Phys., 2022,24, 20030-20039 (Ref. [47]), licensed under the terms and conditions of the Creative Commons Attribution-NonCommercial 3.0 Unported (CC BY-NC 3.0).

Acknowledgments

The last three years, during which I came back to Physics after more than five years of an amazing journey in the enterprise, have meant for me a return to my origins, where my curiosity about how really things work started to be fulfilled. I had the unique opportunity to continuously jump between two different worlds - business and research, as I carried on my PhD while working for IBM - that actually take advantages from each others in a rich way. No real progress is possible without fundamental research, as no practical and large scale implementation and distribution of developed technology is usually possible without enterprises. I will for sure keep this in mind during all my future activities.

I would like to thank all the people who believed in this collaboration between Parma University and IBM, who believed in me, supported me, and who shared with me at least a part of this path. Part of this Thesis work has been performed within the European Union's Horizon 2020 program under Grant Agreement No. 862893 (FET-OPEN project FATMOLS).

My special thanks start from my Tutor, Prof. Stefano Carretta, who warmly welcomed me in the Molecular Magnetism group, constantly supported me and reintroduced me to Physics after a couple of years with his advices, reading recommendations, and patience. Speaking about patience, I want to thank Prof. Alessandro Chiesa, for guiding me in everyday work, answering my continuous questions and for sharing his knowledge. His precious contribution made for sure possible this achievement, helping me also to close the unavoidable gap I had with theory. I thank also Prof. Paolo Santini, for constantly encouraging me doing my best, on both Physics and Graphics: the first page cover of PCCP Journal paper has been a great achievement!

I would like to deeply thank my IBM Manager Francesca Bonifazi, who pushed a lot to let me follow this research path, together with my previous Managers Adele and Maurizio (and upward), allowing me to invest part of my time at IBM, and my whole Team. The ROI will be huge in the next years for IBM and in particular for our IBM Cloud quantum services! I want to thank also my IBM supervisor Dr. Ivano Tavernelli, with whom we shared almost all publications achieved in this work, for inspiring me

to pursue this research path while working for IBM. With him, I thank also Francesco Tacchino for his advices and experience, especially on quantum simulations.

Now, I would like to thank the people who shared with me a significant part of this path. I spent together with Mario Chizzini a lot of time doing joint research, debugging, raising doubts and questions, on almost every paper published for this thesis. We managed to parallelize work, giving each one our own contribution, and helping each other. We converged in the overall paper analysis with joint plots, comparing different molecules and ansatzes, finding and reporting the best characteristics from each approach. So, thank you! I thank also my other colleagues at University of Parma, in particular Simone Chicco and Emilio Macaluso: the remote working did not allow to share many time together, but we had evenly significant experiences together. I'm very grateful to my colleagues and friends Antonello Aita and Michele Grossi: we started together to explore the quantum world years ago, and now we found ourselves involved in great projects and opportunities. Moreover, our work on the two developed computational framework had a tremendous impact on our publications. So, thank you a lot for your help and friendship! My last special thanks go to the IBM Quantum Ambassador team, both Italian and International - in particular Federico Mattei and Robert Loredo - for supporting and encouraging me during these years; and of course to the Italian Quantum Community people, especially Vito Sammarco and Giacomo Bartoli, whose professional experience in software development helped me to build better code.

And finally, I'm really thankful to my entire family: my dad and mom, my sister Laura with Lorenzo, my grandmother, my grandparents in Heaven, my father/mother/brothers and sister in law, and all my other relatives. Doing this double job was not so easy, but your encouragement through these three years helped me a lot. And I'm of course really grateful to my wife Alessia and to my daughter Sofia, that God donated me both: thank you for your lovely presence in my life, and for your support and patience. Without you, I wouldn't have been able to say yes every day to this adventure!